Quality Assessment of Cardiovascular Cells and Tissues by Raman Microspectroscopy and Imaging

Dissertation

der Mathematisch-Naturwissenschaftlichen Fakultät

der Eberhard Karls Universität Tübingen

zur Erlangung des Grades eines

Doktors der Naturwissenschaften

(Dr. rer. nat.)

vorgelegt von

Dipl. Pharm. Julia Marzi

aus Freiburg im Breisgau

Tübingen 2019

Gedruckt mit Genehmigung der Mathematisch-Naturwissenschaftlichen Fakultät der Eberhard Karls Universität Tübingen.

Tag der mündlichen Qualifikation:	18.06.2019
Dekan:	Prof. Dr. Wolfgang Rosenstiel
1. Berichterstatter:	Prof. Dr. Katja Schenke-Layland
2. Berichterstatter:	Prof. Dr. Ulrich A. Stock
3. Berichterstatter:	Prof. Dr. Liliana Schaefer

Das Leben muss nicht einfach sein, vorausgesetzt es ist nicht leer.

Lise Meitner

Table of Contents

Abstract

The increasing lifespan of the human population has been accompanied by a higher prevalence of cardiovascular diseases. It has been more than 50 years since the first heart valve was transplanted in a human patient and many new approaches in cardiovascular transplantation and tissue engineering (TE) have been evolving ever since. However, the availability of human donor tissues is limited. Ideal, vital, durable, non-immunogenic heart valve or cardiovascular replacements are not yet commercially available. Thus, a better understanding of developmental and regulating mechanisms of cardiovascular tissues is essential to develop new implant materials. Moreover, cardiovascular tissue transplants or tissue-engineered grafts need to be monitored before transplantation. This thesis aimed to establish Raman microspectroscopy and Raman imaging as marker-independent, non-destructive technique for quality assessment of cardiovascular transplants and tissue-engineered products. Towards this aim, the influence of an ice-free cryopreservation technique (IFC) on tissue integrity and immunogenicity of heart valves was analyzed. The extracellular matrix (ECM) structures of standard cryopreserved (FC) and IFC allograft leaflets were compared to native leaflets after long-term implantation in sheep. Moreover, the mid-term immunogenic effects on IFC treated xenografts were assessed. Quantitative monitoring of interstitial cryoprotectant (CPA) concentrations was performed for quality control of cryopreserved heart valves. Furthermore, phenotype and tissue origin of human smooth muscle cells (SMCs) that are applied in cardiovascular TE, were analyzed. The ECM remodeling of SMC ring constructs under different culture conditions was monitored. In addition to Raman measurements, routine techniques such as immunocytochemistry, quantitative polymerase chain reaction and histological staining were performed. The results demonstrate the superiority of Raman microspectroscopy and Raman imaging as marker-independent, non-destructive and sensitive method, which is also time- and cost efficient when compared to routine techniques. Raman analysis combined with multivariate data analysis tools allowed for the determination and characterization of structural ECM changes in FC heart valves and real-time quantification of residual CPAs. These techniques enabled the identification and discrimination of single human SMCs based on their tissue origin and phenotype. Moreover, ECM remodeling in tissue-engineered SMC rings was non-invasively monitored. This work affirms the potential of Raman techniques for future applications in in situ quality assessment in cardiovascular research.

Zusammenfassung

Die steigende Lebenserwartung der Bevölkerung geht mit einer erhöhten Prävalenz kardiovaskulärer Erkrankungen einher. Seit der ersten Transplantation einer humanen Herzklappe vor über 50 Jahren entwickelt sich der Bereich der kardiovaskulären Transplantationen und des Tissue Engineerings (TE) stets weiter. Allerdings besteht nur eine begrenzte Verfügbarkeit menschlicher Spendergewebe und bisher sind keine kommerziell erhältlichen künstlichen Ersatzgewebe verfügbar, die vital sowie nicht-immunogen sind und eine langfristige Implantation überdauern. Für die Entwicklung neuer Gewebe ist ein besseres Verständnis der entwicklungsbiologischen und regulierenden Mechanismen erforderlich. Außerdem ist die Kontrolle der kardiovaskulären Transplantate und künstlich hergestellten Gewebe vor der Transplantation von großer Relevanz. Das Ziel der folgenden Studie war die Etablierung von Raman Mikrospektroskopie und Raman-Bildgebung für die Marker-freie, nicht-destruktive Qualitätssicherung im Bereich der kardiovaskulären Transplantation und des kardiovaskulären TE. Zunächst wurde der Einfluss eines eisfreien Kryokonservierungsverfahrens (IFC) auf die Gewebeintegrität und Immunogenität von Herzklappen analysiert. Der strukturelle Aufbau der extrazellulären Matrix (EZM) von standard-kryokonservierten (FC) und IFC Allograft Herzklappensegeln wurde nach Langzeitimplantation in einem Schafmodel mit native Herzklappensegeln verglichen. Zusätzlich wurden mittelfristige immunogene Effekte IFC-behandelter Xenografts bewertet. Zur Qualitätskontrolle der kryokonservierten Herzklappen, wurden die Konzentrationen der verwendeten Cryoprotectiva (CPAs) im Gewebe bestimmt. Weiterhin wurden der Phänotyp und Gewebeursprung glatter Muskelzellen, die in verschiedenen TE-Ansätzen Anwendung finden, analysiert. Die EZM Reorganisation in Geweberingen aus glatten Muskelzellen wurde auf den Einfluss unterschiedlicher Kultivierungsbedingungen untersucht. Ergänzend zu den Raman Messungen wurden Protein- und Genexpression analysiert und histologische Färbungen ausgeführt. Die Ergebnisse dieser Studie demonstrieren die Vorteile der Raman-Mikrospektroskopie und Raman-Bildgebung gegenüber Routineanwendungen bezüglich Marker-unabhängigkeit, Zerstörungsfreiheit und Sensitivität, als auch Zeit- und Kostenersparnis. Raman-Analysen in Kombination mit multivariater Datenanalyse ermöglichten die Ermittlung und Charakterisierung molekularer struktureller EZM-Änderungen in FC Herzklappensegeln sowie die Echtzeit-Quantifizierung von CPA Residuen im Gewebe. Des Weiteren konnten mit diesen Methoden humane glatte Muskelzellen anhand ihres Phänotyps und Gewebeur-

sprungs identifiziert und unterschieden werden, sowie die Entstehung und Reorganisation der EZM in TE Geweberingen beobachtet werden. Diese Arbeit bestärkt das Potential der Raman Spektroskopie für zukünftige Anwendung in der in situ Qualitätssicherung von neuen Implantatmaterialien in der kardiovaskulären Forschung.

Abbreviations

ACTA2	alpha smooth muscle actin
ANOVA	analysis of variance
CALD1	caldesmon
CARS	coherent anti-Stokes Raman spectroscopy
CCD	charge-coupled device
CNN1	calponin
COL1	collagen 1
CPA	cryoprotective agent
DMSO	dimethyl sulfoxide
DNA	deoxyribonucleic acid
EC	Euro-Collins
ECM	extracellular matrix
EZM	extrazelluläre Matrix
FC	frozen cryopreservation
FMD	formamide
GAG	glycosaminoglycan
HAoSMC	human aortic smooth muscle cell
HCASMC	human coronary artery smooth muscle cell
HPASMC	human pulmonary artery smooth muscle cell
HTSMC	human trachea smooth muscle cell
HUtSMC	human uterus smooth muscle cell
ICC	immunocytochemistry
IFC	ice-free cryopreservation
NIR	near infrared
M	molar [mol/L]
mM	millimolar [mmol/L]
MYH11	smooth muscle myosin heavy chain 11
MP	multiphoton
MVA	multivariate data analysis
PC	principal component
PCA	principal component analysis
PG	propylene glycol
QM	quiescence medium
SD	standard deviation
SERS	surface-enhanced Raman spectroscopy
SHG	second harmonic generation
α-SMA	alpha smooth muscle actin
SMC	smooth muscle cell
TCA	true component analysis
TE	tissue engineering
TEVG	tissue-engineered vascular graft
TGFβ	transforming growth factor beta
TPEF	two-photon excited fluorescence

List of Figures

List of Publications

Accepted Manuscripts

1. **J Marzi**, E.M. Brauchle, D.A. Carvajal Berrio, S.L. Layland, K Schenke-Layland; *Raman Spectroscopy*, Comprehensive Biomaterials II, Elsevier, Oxford, Paul Ducheyne, 2017; 108-127

2. A.C. Biermann, **J Marzi**, E.M. Brauchle, M Schneider, A Kornberger, S Abdelaziz, J.L. Wichmann, C.T. Arendt, E Nagel, K.G.M. Brockbank, M Seifert, K Schenke-Layland, U.A. Stock; *Impact of T-cell-mediated immune response on xenogeneic heart valve transplantation: short-term success and mid-term failure*, European Journal of Cardiothoracic Surgery, 2018; 53(4): 784-792

3. A.C. Biermann* & **J. Marzi***, E.M. Brauchle, J.L. Wichmann, C.T. Arendt, V. Puntmann, E. Nagel, S. Abdelaziz, A.G. Winter, K.G.M. Brockbank, S.L. Layland, K. Schenke-Layland, U.A. Stock; *Improved long-term durability of allogeneic heart valves*, European Journal of Cardiothoracic Surgery, 2019; 55(3): 484-493
*authors contributed equally

4. **J. Marzi**, A.C. Biermann, E.M. Brauchle, K.G.M Brockbank, U.A. Stock, K. Schenke-Layland; *Marker-independent in situ quantitative assessment of residual cryoprotectants in cardiac tissues*, Analytical Chemistry, 2019; 91(3): 2266-2272

5. **J. Marzi**, E.M. Brauchle, K. Schenke-Layland, M. Rolle; *Non-invasive functional molecular phenotyping of human smooth muscle cells utilized in cardiovascular tissue engineering,* Acta Biomaterialia, 2019; 85: 193-205

6. A. Zbinden, **J. Marzi**, K. Schlünder, C. Probst, M. Urbanczyk, S. Black, E.M. Brauchle, S.L. Layland, U. Kraushaar, G. Duffy, K. Schenke-Layland, P. Loskill; *Non-invasive marker-independent high content analysis of a microphysiological human pancreas-on-a-chip model,* Matrix Biology, 2019; in press

Submitted Manuscripts

7. D. Shendi, **J. Marzi**, W.H. Linthicum, A.J. Rickards, D. Dolivo, S. Keller, T. Dominko, T.C. McDevitt, Q. Wen, K. Schenke-Layland, M.W. Rolle; *Hyaluronic acid as a macromolecular crowding agent for increased production of cell-derived matrices*

8. R. M. Spiers, **J. Marzi**, E. M. Brauchle, S. E. Cross, R. H. Vaughan, P. Bateman, S. J. Hughes, K. Schenke-Layland, P. R. V. Johnson; *Raman Microspectroscopy for determining donor age related differences in extracellular matrix protein digestion for human islet isolation*

In Preparation

9. K. Sugyiama, **J. Marzi**, E.M. Brauchle, Y. Yamashiro, K. Schenke-Layland, H. Yanagisawa; *Label-free Raman imaging of elastic fibers and collagen fibers in diseased and healthy mouse aortic tissues*

Chapter 1

Introduction

1 Introduction

1.1 Cardiovascular Diseases

The growth and ageing of the western population is accompanied with an increased prevalence of cardiovascular and metabolic events that affect the vasculature as well as the human heart. Cardiovascular diseases are the leading cause of death worldwide [1, 2]. Heart valve diseases occur predominantly as age-related valve deteriorations causing regurgitation or stenosis [3]. However, congenital and rheumatic heart diseases are also still relevant. The annual rate of heart valve replacement surgeries worldwide is expected to increase to over 800.000 interventions by the year 2050 [4]. Furthermore, preponderance of metabolic diseases such as diabetes, obesity or hypertension and other cardiovascular risk factors cause a constantly increasing incidence of cardiovascular diseases. 16% among the western population of 55 years and older suffer from peripheral artery disease and coronary artery disease is the most common cause of death [5, 6]. The first heart valve replacement surgery was performed more than 50 years ago [7]. Autologous and synthetic materials that replace heart valves as well as vessels have been applied in clinics for several decades now. However, all procedures bare risks or fail in long-term performance and the ideal durable heart valve or vascular replacement that is capable to grow and remodel within the patient has not been established.

1.1.1 Heart Valve Replacement

Heart valve replacement surgeries are required if there is no option for a minimally invasive treatment of a valvular disease. Fresh human allogeneic donor valves (homovitals) provide optimal hemodynamics and immunogenicity. However, their application is limited by donor organ scarcity [8, 9]. Therefore, mechanical or bioprosthetic tissue valves are commonly applied. Bioprosthetic valves comprise of preserved and sterilized xenogeneic or allogeneic donor valves or constructs from animal tissues such as bovine pericardium. Mechanical valves vary in material, shape and size and are the standard replacement for younger patients up to an age of 70 [10]. Mechanical valves circumvent immunogenic risk factors, however, to avoid blood clotting and thrombosis the patients need life-long medication with anticoagulants. Anticoagulation therapy limits the patients activity and lifestyle by the risk of severe bleeding [11] and involves complications especially in younger patients and women in the childbearing age [12, 13]. Application

of bioprosthetic valves increased in the last years. However, their implantation is mainly indicated for patients older than 65, because these valves have a limited life-span within the patient [10]. Thromboembolic events are avoided, however long-term failure of bioprosthetic valves appears due to valve deterioration and structural degeneration [14, 15]. In a long-term study by Hammermeister et al. no significantly different outcome was observed between patients with a mechanical and a bioprosthetic valve, however different complications occurred in the two groups [11].

All of the heart valve replacements that are available on the market are avital implants. One approach for valve grafts is the generation of tissue-engineered viable heart valves. The basic paradigm of tissue engineering (TE) includes the isolation and culture of specific cells from the patient and the culture of these cells on a three dimensional synthetic or natural scaffold to form a biomaterial. This constructed *neotissue* can then be implanted in the desired site within the patient for repair, replacement or regeneration purposes [16]. Although, there is tremendous scientific input and efforts in the establishment of functional, durable tissue-engineered heart valves, many promising approaches are still in clinical trials [17].

1.1.2 Heart Valve Leaflet Macro- and Microstructure

A major issue in heart valve replacement is to sustain the complex heart valve leaflet extracellular matrix (ECM) structures that are essential for the physiological function of the heart valve. The semilunar leaflet consists of three structural layers determining the leaflets long-term durability and biomechanical properties [18] (Figure 1). The layered architectural pattern forms a flexible and soft leaflet in the unloaded state that, at the same time, stays inelastic under pressure [19]. The fibrosa is located on the outflow side of the leaflet and mainly consists of circumferentially aligned collagen fibers that support the leaflet's stiffness and strength and bear the load of blood pressure [19]. The crimped structured collagen bundles in the fibrosa cause corrugation during systole that are released in diastole [20] (Figure 1 A, B). Collagen fiber architecture determines the biomechanical sustainability of the leaflets. Highly hydroxylated collagen I fibers in the heart valve are mainly stabilized and strengthened by trivalent hydroxylysyl pyridinoline cross-links [21]. The degree of cross-links determines the resistance to enzymatic degradation and the stability and load-bearing capability of the leaflet [22, 23]. Changes in collagen fiber architecture or remodeling of collagen fibers occur in cellular response to mechanical or biochemical triggers or traction forces and result in altered synthesis and degradation of collagens [24, 25]. The inflow side, ventricularis, is dominated by a radially

aligned elastic fiber network that enables the elasticity of the leaflet and reconditions the contracted state during systole [19, 26]. In between these two layers resides the spongiosa. This layer contains solvable ECM proteins such as glycosaminoglycans (GAGs), proteoglycans and few loosely arranged fibrous structures [27, 28]. GAGs absorb water and form a gel-like structure that allows the retention of frictional stress and stabilizes the leaflets [27, 29]. The valves are outlined by valvular endothelial cells (VECs) forming a monolayer. Within the three layers so-called valvular interstitial cells (VICs) are located. Depending on environmental conditions, VICs influence ECM modulation by dynamic phenotypic switching from quiescent fibroblast-like cells to activated myofibroblasts or smooth muscle-like cells [30, 31]. Preserving the ECM structures is crucial for long-term performance of the cryopreserved and implanted leaflets. In contrary, it is controversially discussed whether the implants need to be viable or can be decellularized [17, 32-35].

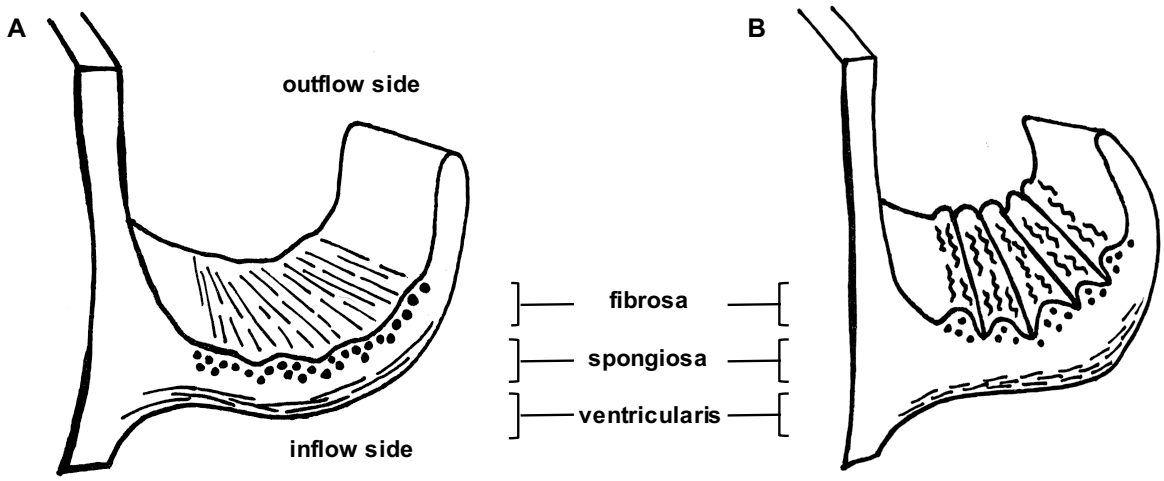

Figure 1. Schematic microstructure of the heart valve leaflet during diastole (A) and systole (B). The layered leaflet consists of the collagen-rich fibrosa on the outflow side and the elastin-rich ventricularis on the inflow side. In between resides the spongiosa that mainly consists of proteoglycans. Modified from Schoen and Levy [20].

1.1.3 Cryopreservation of Heart Valve Tissue

Organ scarcity is a limiting factor in heart valve replacement. Cryopreservation and tissue banking enable long-term storage of heart valve tissues and allow for tissue accessibility at any time. Tissues are decontaminated and frozen down in specific cryomedia that contain cryoprotective agents (CPAs), such as dimethyl sulfoxide (DMSO), propylene glycol (PG) or ethane diol [36-38]. CPAs limit the damaging effects of osmosis and diffusion on cells during freezing and stabilize the tissue while interstitial water is removed [39]. There exist different methods of cryopreservation. Conventionally applied

frozen cryopreservation (FC) is the standard procedure in clinics, but needs to follow defined cooling parameters to control the inevitable ice-formation [40]. Alternative approaches, such as vitrification, avoid interstitial ice-formation [41, 42].

To date, FC is the standard protocol for allograft tissue preservation and applies a mixture of 10% DMSO and medium [43, 44]. However, those valves lack long-term sustainability within the patient. After 12-15 years the implants undergo structural degradation, lack functionality and need to be removed [9, 45]. In pediatrics leaflet durability is even shorter [46, 47] and due to the extended life expectation of the population an additional replacement surgery is often necessary, although there is a high risk of complications and failure [48]. FC, which has been applied since more than three decades, showed ice-crystal formation in heart valve tissues, causing tissue deterioration and leading to irreversible tissue damages, that limit the leaflet's lifetime in vivo[15, 49, 50]. Due to these issues there does not exist a gold standard protocol for heart valve cryopreservation and there is a need for continuous improvement. TE approaches have not evolved in the expected speed either. Among the many TE attempts that have been developed in the last years, earlier approaches failed in clinics [51] and so far only few materials and procedures showed promising outcomes in preclinical studies [17]. Thus, a protocol for an alternative cryomedium and cryopreservation technique was established that was proposed to avoid ice formation and destruction of the tissue [52, 53]. Ice-free cryopreservation (IFC) of allografts applies VS83 medium that contains high amounts of CPAs, which allow the medium to approach a vitrification-like state instead of freezing and forming ice crystals [54]. VS83 allows for cryopreservation below the glass-transition temperature of the combined CPAs (-124°C), without the formation of ice crystals. Preserving tissues in VS83 medium supports storage at higher temperatures. Storage at -80 °C instead of storage in the liquid phase of nitrogen (-197 °C) is possible, making ice-free cryopreservation an economically beneficial procedure. Storage at -80 °C requires less equipment and energy and would therefore be easier accessible in less developed countries. Preclinical data and a mid-term (7 months) in vivo study in a sheep model already showed a superior outcome in IFC tissue matrix integrity and heart valve functionality when compared to FC leaflets [50, 55]. As a last step before approving IFC treated tissues in clinical trials, a long-term in vivo study of 12 months needed to be performed in a juvenile sheep model to assess the long-term durability. The ovine model is the gold standard for preclinical cardiovascular studies. Mechanical and hemodynamic parameters are similar to human heart valves, due to the enhanced calcium metabolism the ovine model presents the

'worst-case-scenario' for calcifications and the ovine development is much faster than in humans. 12 months in sheep equal an implantation duration of around 18 years in human [14, 56, 57].

Another question that needs to be addressed before implementing ice-free cryopreservation in a clinical trial is cytotoxicity of the CPAs in the VS83 cryomedium. The influence of CPAs on tissues and cells has broadly been discussed [58-60]. CPA permeation kinetics depend on various factors. Temperature and concentration as well as the origin of the treated tissue and the chemical composition of the CPA itself influence the cryopreservation procedure. Still, trial and error experiments have to be conducted to determine cytotoxicity in every cryopreservation approach [59]. Highly concentrated CPAs as applied in VS83 medium were shown to be cytotoxic, although combination of several CPAs did not show an increased cytotoxic effect in comparison to individually applied CPAs [61]. Regardless of the fact that decellularization by VS83 medium cryopreservation might be a beneficial side-effect, for safe clinical use of VS83 medium, its effects on the recipient's or migrating remodeling cells need to be investigated.

1.1.4 Vascular Tissue Engineering

Hypertension, cardiovascular risk factors and atherosclerotic plaques strain the vasculature, cause thromboembolic occlusions and minimize their lifetime. For several decades blood vessels have been harvested from saphenous veins, radial arteries or internal mammary arteries which is the standard for both, coronary and peripheral artery autologous graft bypass surgeries [62]. Nevertheless, autografts are not always available due to previous diseases or the lack of accessible vessels. Moreover, graft failure can occur after implantation [63, 64]. The alternative for autologous grafts is the implantation of synthetic materials such as Dacron® or polytetrafluoroethylene [65, 66]. However, those grafts showed infection or thrombosis, especially in the application as small diameter (<6 mm) grafts [67]. Therefore, there is a high demand for new graft substitutes. Tissue engineered vascular grafts (TEVG) are designed to provide a low immune response and inflammation potential, an anti-thrombotic surface, long-term patency, the capability to remodel within the patient, and could replace damaged vessels in the future [68, 69]. Current approaches in TEVGs apply biodegradable natural or synthetic scaffold materials, which are mostly electrospun and either seeded with cells before transplantation or constructed to be cellularized in vivo [68]. Moreover, there are scaffold-free approaches, which are based on the formation of so-called tissue rings by self-assembly of cells in specific agarose or polymer molds (Figure 2) [70, 71]. Isolated smooth muscle cells (SMCs) or stem-

cell derived SMCs are utilized in cardiovascular TE approaches [72, 73]. Vascular SMCs play a crucial role in structural integrity and contractile regulation of blood vessels [74]. SMCs appear and can be classified as contractile or synthetic phenotype. The contractile phenotype SMC has a low proliferation rate, expresses mainly contractile filaments and has a spindle-shaped morphology. The synthetic phenotype of SMCs has an increased proliferation rate, expresses dominantly ECM proteins and has a rhomboid, fibroblast-like morphology [75, 76]. However, there are also intermediate SMC phenotypes, which share features of both subtypes. Whereas manufacturing of scaffold materials for TEVGs can be well controlled and characterized, the characterization of SMCs and the detection and regulation of phenotypic switching remain a major obstacle [77]. Despite the enormous effort to produce 'off-the-shelf' cardiovascular conduits and various clinical trials, commercially available TEVGs for clinical use do not exist to date [78-80]. Moreover, feasibility of costs and manufacturing times as well as potential immune response of TEVGs remain an unanswered question [68]. An important factor to understand and assess remodeling processes and to accelerate the application of potential TEVG scaffolds in clinics is the establishment of reliable methods to characterize and monitor the scaffold materials or involved cells [81, 82].

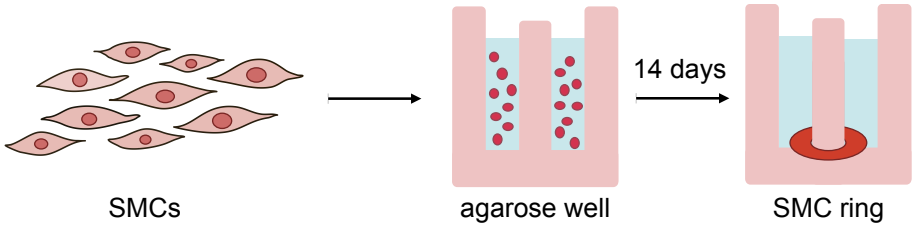

Figure 2. Self-assembly of SMCs to SMC ring constructs. Isolated primary or stem cell-derived SMCs are seeded in agarose wells, cultured in medium for 14 days and form SMC rings**.** Modified from Dikina et al. [83]

1.2 Raman Spectroscopy

Quality control and quality assurance of biomaterials and viable tissues remain major challenges in the field of biomedical research and TE [84, 85]. There is a high demand for the evaluation of biomaterial degradation behavior and cell-matrix interactions as well as for real-time techniques to monitor these processes. Raman spectroscopy has gained relevance as an analytical tool, whereas its related technique near infrared spectroscopy has lost importance [86, 87]. Raman spectroscopic methods are based on the detection of molecular vibrations in a sample induced by an incident light source. The acquisition of chemically-sensitive, highly-resolved Raman spectra allows for the identification of intra- and intermolecular changes and modifications. Raman spectroscopy enables fast, marker independent, non-destructive and potentially non-invasive data acquisition and is highly sensitive on a molecular level.

1.2.1 The Principle of Raman Scattering

The interaction of photons of an incoming light source and the molecules of a sample results in the induction of different energetic effects and frequency shifts. Depending on the wavelength of the incident light and the sample properties fluorescence (ultraviolet wavelength range), scattering (visible wavelength range) or light absorption (infrared wavelength range) occur [88]. Incident photons of visible light can be scattered elastically or inelastically. Mostly, photons are scattered back at the same energy as the incident light. Only 1 out of 10^7 photons is changed in frequency and scatters inelastically [89]. Elastic scattering is called Rayleigh scattering and can be observed in the blue color of the sky, where blue sunlight is scattered stronger than red light [90, 91]. In inelastic scattering, also known as Raman scattering, energy is transferred between photons and molecules by the induction of a rotational or vibrational vector within the molecule. A frequency shift occurs in relation to the incident wavelength. This effect has first been theoretically predicted in 1923 by Smekal [92] and is called the ‘Raman effect’, named after the Indian physicist and Nobel prize laureate C.V. Raman, who first described the effect experimentally in 1928 [93-95]. Raman scattering can result in emitted photons of either higher or lower energy levels than the incident photons. Stokes scattering results in the loss of energy and a frequency shift to higher wavelength ranges (red-shifted). The molecules absorb light and are transferred to a higher virtual energy level. Photons of a lower energy level are emitted when the molecules relapse to the ground state. In

anti-Stokes scattering, a frequency shift to lower wavelength ranges (blue-shifted) is observed [88] (Figure 3).

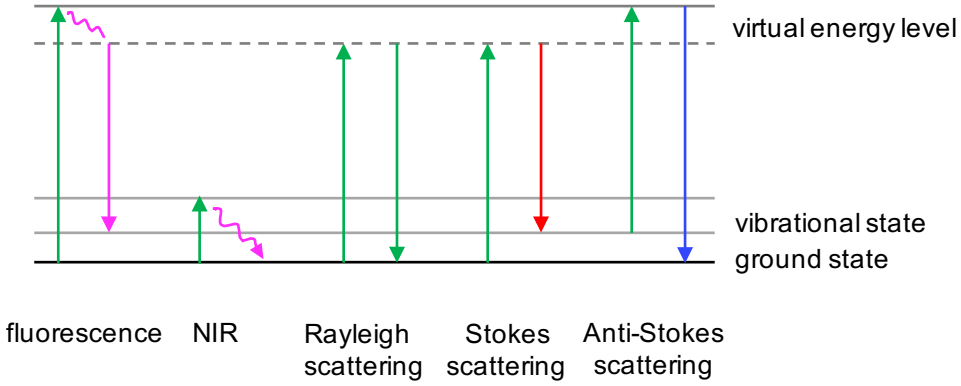

Figure 3. Principles of photon-molecule interactions. Energy levels of molecules excited by incident photons. Anti-stokes and Stokes scattering are the two events of Raman scattering. Modified from Mishchenko et al.[88]

1.2.2 Raman Microspectroscopy and Raman Imaging

In most biological applications, Raman spectroscopy is combined with light and sometimes fluorescence microscopy [96, 97], referred to as Raman microspectroscopy, and especially allows the targeting of small structures. Both Raman scattering effects are used in Raman devices. Stokes Raman scattering is applied in spontaneous Raman microspectroscopy (Figure 4). The sample is excited through the microscopic objective with a laser, after focusing on the region of interest over the camera of the microscope. Molecular vibrations due to photon-molecule interactions result in a loss of energy of the emitted photons. The resulting frequency shift is specific for every molecular bond. A notch filter splits frequency-shifted Raman scattering from backscattered light of the same wavenumber as the incident light or higher. The grating of the charge-coupled device (CCD) camera of the spectrograph converts the photons into a Raman spectrum that is comparable to a biochemical fingerprint of the sample. The Raman spectrum is defined by the frequency shift in wavenumber [cm^{-1}], so-called Raman shift and the count of scattered photons (intensity). Instead of the acquisition of spectra of preselected single points within the sample, it is also possible to scan a whole area at a defined pixel resolution and generate a spectral map in which every pixel is defined by a separate spectrum. This technique enables to acquire Raman images of a defined area.

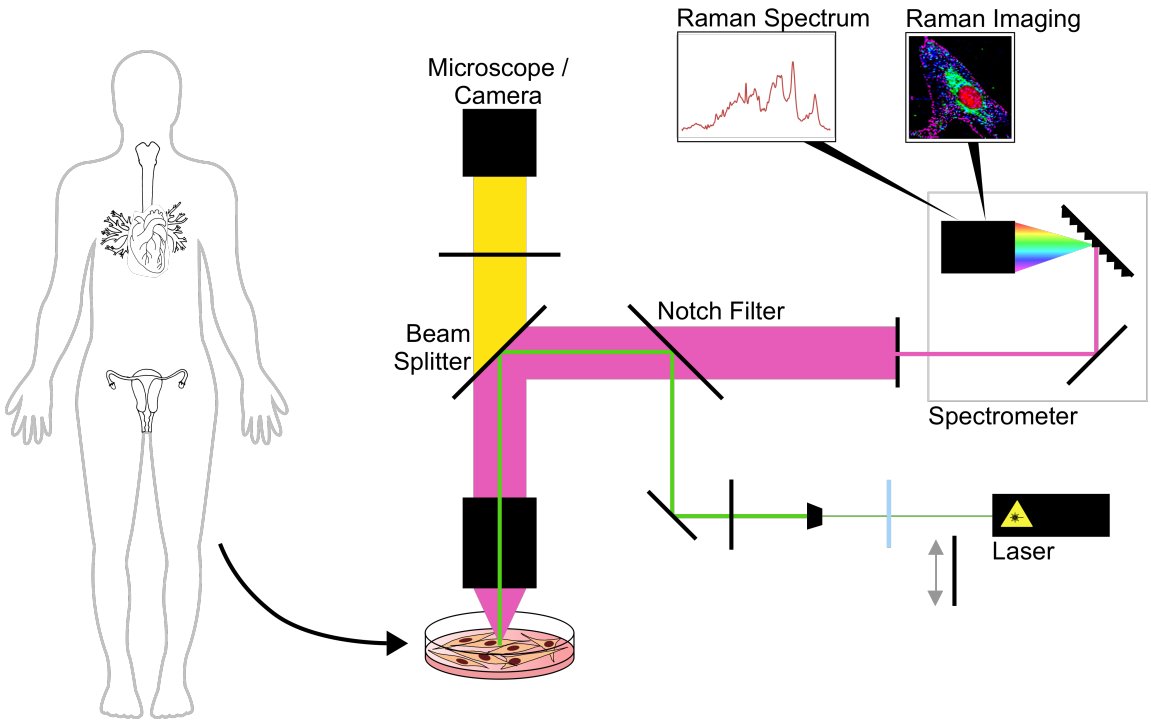

Figure 4. Technical setup of Raman spectroscopic measurements. Tissue or isolated cells placed on the sample holder are excited by a green (532 nm) or near infrared (785 nm) laser (green light path). Photons of lower frequency are emitted, separated from Rayleigh or higher frequency scattering by a notch filter and detected by the CCD camera in the spectrograph (pink light path). The bright field microscope setup allows for targeting the region of interest for Raman acquisition (yellow light path). Single point spectral acquisition or Raman imaging can be performed. Adapted from Marzi et al. (Acta Biomaterialia, in revision).

Raman spectra provide qualitative and quantitative information on defined molecular bonds and the Raman fingerprint is specific for a certain structure. However, whereas small molecules and chemicals provide singular specific and defined peaks, large biomolecules in cells or tissues mostly represent a higher number of molecular vibrations and assigned peaks. Different proteins or lipids that predominantly exhibit similar functional groups can show small spectral differences. Thus, multivariate data analysis (MVA) tools [98, 99], such as principal component analysis (PCA), linear discriminant analysis, cluster analysis or regression models, can be applied to identify minor spectral differences and analyze complex and large data sets. PCA was the method of choice for the analysis of the Raman measurements presented in this work. PCA is a vector-based approach to reduce dimensionality [100, 101] and is commonly applied in chemometrics. A PCA is based on the following assumption [102]:

$$[X] = [T][P^T] + [E] \quad (1)$$

X: data matrix

T: scores matrix

P^T: matrix of loadings

E: residuals

A data matrix (X) consists of the most dominating principal component scores (T) and their corresponding loadings matrix (P^T). The matrix E are residuals that are irrelevant for the variability or represent noise [103]. In PCA the spectral information is reduced to eigenvectors, so-called principal components (PCs), that explain the variance between the spectral data and are orthogonal towards each other [103]. Thus, PC1 explains the main spectral differences, PC2 the next relevant variability and so on. However, depending on the data pretreatment and measurement conditions, PC1 of spectral data often describes discrepancies in the baseline and does not describe sample-specific information. To visualize the spectral data analyzed by PCA the scores plot allows to show each spectrum as a score value in a two-dimensional scatter defined by two selected PCs. The scores plot defines whether there is a separation between two or more data sets. Another output of the PCA, that helps to interpret the data is the loadings plot. The loadings plot explains spectral differences that are indicated by the corresponding PC [99]. Positive peaks in the loadings plot refer to spectral information that are predominantly found in spectra of a positive score value. Negative peaks in the loadings correlate to spectral information of data points with negative score values.

Raman imaging is dominantly applied to visualize the distribution and localization of defined structures in a sample. For in-depth analysis of the overall data set and to assess information of a region of interest within the measured area, techniques for data reduction and preselection are required. Data analysis of Raman images is more complex than single point measurement analysis due to the big data sets. Spectral maps allow to construct Raman images and can be evaluated by creating intensity heat maps of a defined Raman shift bandwidth or by MVA [104]. An additional approach similar to PCA is true component analysis (TCA) that originates from the image analysis of the WiTec Project FIVE software (WiTec GmbH, Ulm, Germany). TCA creates an intensity distribution image by either manual selection of a spectrum of interest in the spectral map or a reference spectrum or by defining the most prevalent spectral components by basis analysis. A measured spectrum (S_i) is described based on a linear combination of known spectra (B).

(2)
$$\vec{S}_i = \hat{B}\vec{H}_i + E$$

$\vec{S}_i$: spectrum from the spectral data set

$\hat{B}$: matrix of basis spectra

$\vec{H}_i$: mixing values spectrum i

E: error spectrum

1.2.3 Approaches of Raman Microspectroscopy in Biomedical Research

Raman microspectroscopy and imaging have certain advantages that overcome the limitations of commonly used optical or histochemical techniques. In comparison to NIR spectroscopy this technique is not significantly affected by water [86] and is advantageous for the analysis of samples in aqueous solutions. Moreover, it enables an adequate spatial resolution as well as real-time acquisition times. Different than in fluorescence microscopy and histochemistry, no specific labeling is required which allows for non-destructive measurements. Raman techniques are well-established for qualitative and quantitative applications in pharmaceutical and material science [105-108]. Although early approaches already introduced Raman spectroscopy for biological applications to investigate molecular orientation and arrangement in polymers or proteins [109-111] and for bioanalytics [112, 113], Raman microspectroscopy still needs to further evolve in the analysis of complex biomolecular composites such as tissues and cells as well as in biomedical approaches.

In the biomedical field, Raman techniques are popular in the distinction between healthy and diseased tissues in cancer research [114-116]. Furthermore, variable cells such as bone cells, cancer cells, stem cells [117-120] as well as cardiomyocytes differentiation [121, 122] and cell death stages [97, 123] have been analyzed and characterized by Raman spectroscopy. Due to its broad usability Raman spectroscopy offers constantly increasing fields of applications. However, in the research area of cardiovascular tissues and cells only few Raman-based studies were performed. Most of the studies focused on the detection of calcifications in vessels or heart valve tissues. The phosphate in apatite provides a strong and specific Raman signal at 960 cm^{-1} that indicates calcific lesions and atherosclerosis [124-126]. Analysis of heart valve collagen structures has first been investigated by Votteler et al., who monitored tissue degradation by collagenases [127]. Besides the applications in tissues, Raman spectroscopy can be applied in the analysis of coatings of mechanical heart valves due to its properties in material characterization [128, 129]. In TE, Raman microspectroscopy is well-recognized for biomaterial characterization [87, 130], whereas the potential to detect neo-tissue formation, degradation and cell-biomaterial interaction requires further investigation.

Another advantage of Raman microspectroscopy are the comparably high penetration depths. Thus, it can be applied for permeation studies of strong scattering drugs, chemicals or carbon nanotube (CNT)-coupled substrates that present a high vibrational contrast into weaker scattering tissue [131]. In vivo imaging of drug delivery through skin

[132, 133] or the assessment of skin penetration depths of sunscreen [134] have been performed using Raman microspectroscopy. Semi-quantitative assessment of chemicals such as DMSO and PG that are applied as well as CPAs in cryopreservation medium were demonstrated in skin penetration studies [135-137].

1.3 Multiphoton Imaging

Laser-induced multiphoton excitation imaging is a non-linear optical process. Non-linear optics refer to a higher-order response of the dielectric polarization to the electrical field of the light and are based on pulsed lasers [138]. Multiphoton microscopy provides several advantages for biological imaging, such as reduced photobleaching of the sample, an increased confocal penetration depth due to the application of femtosecond NIR lasers and fast, label-free imaging of intrinsic fluorescent or multiphoton-active molecules in ECM and cells [139, 140].

In multiphoton microscopy, it can be distinguished between two-photon excited fluorescence (TPEF), also referred to as multiphoton-induced autofluorescence, and second harmonic generation (SHG). TPEF is based on simultaneous absorption of two photons of the same frequency and results in the non-linear excitation of fluorescence in molecules. In TPEF, the emission wavelength is higher than half of the incident frequency ($>\lambda/2$). Originally, it was introduced to overcome strong scattering light in fluorescence microscopy of tissues and in combination with fluorescent dyes [141]. However, label-free imaging is accessible for endogenous fluorescent molecules in tissues and cells such as NAD(P)H, elastin or flavins [139, 142]. SHG imaging is based on the simultaneous excitation with two photons of the same frequency, resulting in a sharp emitted signal of exactly half of the incident wavelength ($=\lambda/2$) [143]. In SHG the input energy remains constant, whereas in TPEF a loss of energy caused by the relaxation of the excited state is observed [144]. SHG imaging requires non-centrosymmetric molecules to achieve an interaction with the laser photons. Collagen, microtubules and skeletal muscle have been reported to be SHG-active [145-147]. Assessment of ECM structures is of major interest in multiphoton microscopy. Collagen fibers and elastic fibers in tissues can be imaged simultaneously by inducing TPEF signal of elastic fibers and SHG in collagen fibrils [142, 148]. Signals can be separated by two different band-pass filters and detectors [146].

Multiphoton imaging evolved quickly and has widely been applied to study collagens in diverse tissues. Multiphoton imaging is well-established in imaging of skin or cancer tissues [144, 149, 150]. Furthermore, it has been shown to be suitable as an in vivo device due to the penetration depth as well as in an endoscopic format [151-153]. Moreover, multiphoton microscopy demonstrated the detection of structural deteriorations in collagen fibers of heart valve leaflets [154]. Multiphoton imaging, which was already established

for collagen and elastic fiber imaging in cryopreserved heart valve tissues [50, 55] was applied in addition to Raman microspectroscopy as proof of principle technique. Imaging of the collagen-rich fibrosa and the elastin-rich ventricularis allows to characterize changes in the ECM structures. Collagen fibers in the fibrosa of fresh native heart valve leaflets show parallel alignment (Figure 5 A, C), confirming the circumferential alignment of collagen fibers described in literature [50, 155, 156]. Collagen bundles in the ventricularis are less oriented and loosely arranged (Figure 5 B, D). Elastic fibers in the fibrosa are aligned in parallel to the collagen fibers, whereas in the ventricularis elastic fibers form a fiber network. In addition, cells are detectable in the elastic fiber signal channel by endogenously fluorescent NADPH (Figure 5 A, C). Ovine and porcine leaflets are commonly used as animal heart valve replacement tissues. Both leaflet structures are comparable in their multiphoton signal intensity. Similar structural collagen and elastic fiber patterns are found in fibrosa and ventricularis. Slightly thicker fibrosa collagen bundles are shown in porcine tissues.

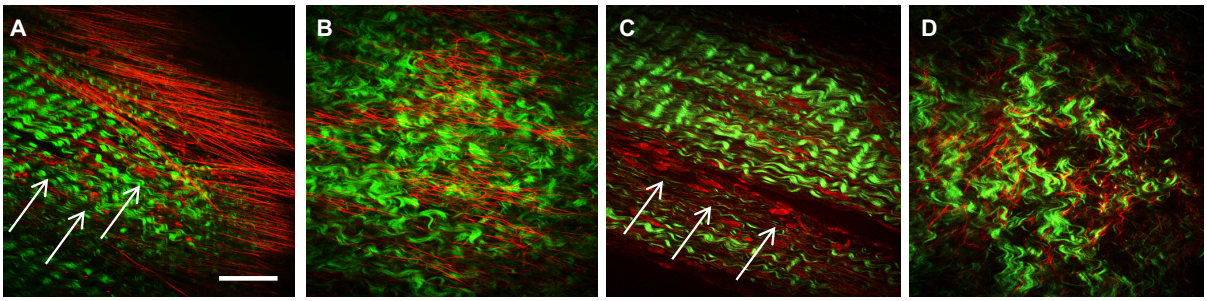

Figure 5. Multiphoton imaging of a native heart valve leaflets. Merged multiphoton images of collagen (green) and elastic fibers (red) in fibrosa **(A, C)** and ventricularis **(B, D)** layer of native ovine **(A, B)** and porcine **(C, D)** pulmonary leaflets. Cells were detectable in the elastin channel (indicated by arrows). Scale bar equals 60 µm

Chapter 2

Objectives of the Thesis

2 Objectives of the Thesis

This thesis focuses on the application of Raman microspectroscopic methods for the quality assessment and monitoring of cardiovascular cells and tissues. The aim was to establish Raman imaging and Raman single point measurements in cardiovascular research to provide molecular information on extracellular matrix (ECM) and cellular composition. Conventional techniques to determine gene or protein expression lack marker-independence and non-destructiveness. Thus, the usability of Raman microspectroscopy as non-invasive quality control tool to identify and distinguish cardiovascular cells, tissues and tissue-engineered constructs, according to their specific Raman fingerprint, was explored. In particular, Raman microspectroscopy was applied in two different approaches of cardiovascular replacements. The quality assessment of an alternative ice-free cryopreservation (IFC) procedure in transplantation of heart valve leaflets and the characterization and monitoring of SMCs that are applied in various vascular tissue engineering approaches were addressed.

IFC leaflets showed better preserved ECM structures and immunogenicity in vitro when compared to frozen cryopreserved (FC) leaflets. Therefore, this work attempted the investigation of long-term (12 months) in vivo sustainability of IFC- and FC-treated heart valve leaflets and the monitoring of IFC treated porcine xenograft performance in a sheep model. Collagen fibers, as a major ECM protein and load-bearing component, were in the focus of the analyses of structural deteriorations. In addition, a quantitative approach to monitor potentially toxic cryoprotective agents (CPAs) of the IFC medium in heart valve tissues was investigated. The sensitivity of Raman microscopy and imaging to detect interstitial CPA concentrations was assessed based on a multivariate calibration model.

Moreover, Raman imaging and Raman single point measurements were established to characterize human smooth muscle cells (SMCs). The goal was to identify and monitor phenotypic switching in SMCs by Raman microspectroscopy and to determine the sensitivity to distinguish SMCs of different tissue origins and compare the results to standard techniques such as immunohistochemistry and quantitative PCR. Finally, Raman spectroscopy was tested as quality control tool in tissue engineering of vascular SMC rings to determine the influence of different culture conditions on ECM remodeling and to compare the designed constructs to the structures of native vascular tissue.

Chapter 3

Results I: Characterization and Analysis of Heart Valve ECM Structures

The contents of this chapter are based on

A.C. Biermann & J. Marzi, E.M. Brauchle, J.L. Wichmann, C.T. Arendt, V. Puntmann, E. Nagel, S. Abdelaziz, A.G. Winter, K.G.M. Brockbank, S.L. Layland, K. Schenke-Layland, U.A. Stock, *Improved long-term durability of allogeneic heart valves*, European Journal of Cardiothoracic Surgery, 2019; 55(3): 484-493

and

A.C. Biermann, J Marzi, E.M. Brauchle, M Schneider, A Kornberger, S Abdelaziz, J.L. Wichmann, C.T. Arendt, E Nagel, K.G.M. Brockbank, M Seifert, K Schenke-Layland, U.A. Stock, *Impact of T-cell-mediated immune response on xenogeneic heart valve transplantation: short-term success and mid-term failure*, European Journal of Cardiothoracic Surgery, 2018; 53(4): 784-792

3 Results I: Characterization of Heart Valve ECM Structures

Standard cryopreservation of heart valves has been shown to result in a distinct immune response, inflammation and ECM degradation [15]. Thus, transplants are predisposed to calcification and lack long-term performance, which is particularly critical in pediatric patients. IFC is an alternative cryopreservation technique that avoids ice-crystal formation. A previous short-term study provided preliminary results on IFC leaflet performance [55]. In comparison to FC leaflets, IFC tissues showed superiority in hemodynamics and preserved ECM structures, detected by multiphoton imaging and histochemical staining [55]. For in-depth analysis of molecular changes in the leaflet's ECM, Raman microspectroscopy was established as a marker-independent, non-invasive technique. All tissues samples for the analyses were acquired within sheep studies, conducted to assess long-term performance and immunogenicity of IFC treated pulmonary allografts (ovine) and xenografts (porcine). Explanted, treated non-transplanted tissues as well as native tissues of the replacement surgeries were analyzed.

3.1 Raman Spectrum of the Heart Valve Leaflet's ECM

Standard histochemical techniques allow for the identification and localization of ECM structures. However, these techniques do not enable characterization on the molecular level. Raman microspectroscopy was established to define biochemical changes of the ECM. Before assessing the influence of cryopreservation and implantation on heart valve leaflets, Raman spectra of native ovine and porcine pulmonary leaflets were acquired as reference spectra to later be compared with xenographic and allographic implants. The ECM and its diverse components are essential for the leaflet's integrity, function and durability. Collagens present a major component of the heart valve's ECM and are crucial for the leaflet's biomechanical strength and durability [22, 154]. Therefore, spectral acquisition focused on the collagen bundles in the fibrosa layers of the heart valve leaflets, that could be targeted over the bright field camera function of the Raman microscope. Compared to a collagen I (Col I) reference spectrum, both spectra showed assignments to the most characteristic Col I peaks, confirming Col I as major collagen in the leaflets ECM. Minor differences were detected in the spectral fingerprint of ovine and porcine collagen fibers (Figure 6 A). PCA revealed a clear clustering between the two animals (Figure 6 B). Spectral discrepancies were mainly identified as an intensity difference at 872 cm^{-1} and peak shifts at 942, 1243 and 1454 cm^{-1} (Figure 6 C). Positive peaks in the loadings plot showed a major influence on data in the positive score range,

negative peaks explained characteristic peaks of data defined in the negative score range of the PC. Ovine data, which clustered in the positive PC1 range, showed higher ratios in the hydroxyproline peak at 872 cm^{-1}. Hydroxy groups in hydroxyproline form stereoelectronic bonds and are essential for the constitutional stability in collagen 3D structure [157, 158]. This might indicate a stronger collagen fiber folding in ovine compared to porcine tissues and correlates to mechanical testing data of ovine and porcine aortic leaflets reported by Martin et al that demonstrated a higher degree of extensibility for ovine leaflets [159]. Other minor differences were visible in peak shifts in porcine tissue in the amide III region (1243 cm^{-1}) and in the collagen backbone (942 and 1454 cm^{-1}).

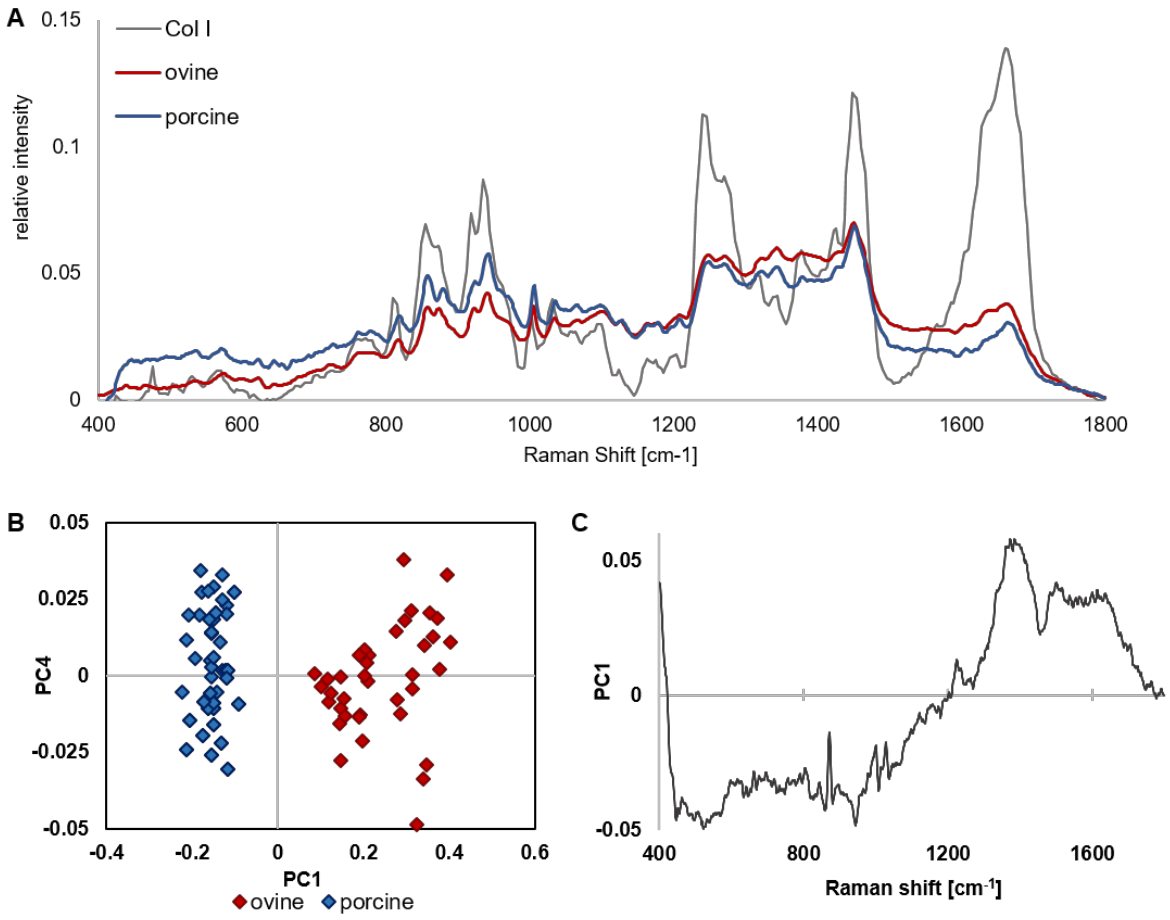

Figure 6. Raman microspectroscopy on native heart valve leaflets. (A) Average Raman spectra of the collagen structures of the fibrosa layer of native ovine (red) and porcine (blue) tissues. The reference spectrum of collagen I is shown in grey. **(B)** PCA showed a clear separation of porcine and ovine data, explained by alterations in the indicated peaks in the PC1 loadings plot **(C)**.

3.2 Long-term Performance of IFC and FC Treated Leaflets

Preclinical as well as mid and short-term studies could show superior performance and persistence of IFC treated tissues in comparison to FC tissues [52, 55]. A long-term animal study was conducted to assess the effects of implantation on cryopreserved allografts and their in vivo durability over time. Leaflets preserved by FC or IFC procedure were implanted in sheep for 12 months. To evaluate and compare the effects of FC and IFC treatment in long-term transplantation, leaflets were explanted after 12 months in vivo and analyzed. 6 FC and 5 IFC heart valves, respectively, were analyzed by standard histochemical staining for immune response (CD3, chloroacetate esterase), calcification (van Kossa), cellularity and morphology (Movat-Pentachrome, Hematoxylin-Eosin), as well as echocardiography for functional testing of the valves as described before [50, 55, 160]. In addition, Raman microspectroscopy was applied as novel approach to non-invasively and marker-independently analyze changes in the leaflets ECM structures.

Histochemical analysis revealed inflamed, T-cell infiltrated and thickened leaflets in 3 of 6 FC tissues. Cardiovascular imaging showed excellent hemodynamic data for IFC leaflets (Biermann and Marzi et al., **Appendix I**). For fast assessment of ECM condition, multiphoton images of each explant and native controls were acquired. Collagen bundles are SHG-active and by separating two detector channels with different band-pass filters elastic fibers were simultaneously detectable due to their auto-fluorescence. Native and explanted IFC and FC leaflets were compared. Collagen and elastic fibers were imaged in all tissues. In comparison to the analysis of non-transplanted porcine pulmonary leaflets and a mid-term sheep study, that both reported significantly weaker collagen and elastin signals in FC leaflets [50, 55], long-term implanted FC leaflets showed clearly detectable collagen and elastin structures. Qualitative differences in collagen and elastin expression were not identified in the ventricularis for any of the treatments. Alterations in the collagen fiber structures were of major interest. For qualitative analysis, crimp amplitude and crimp period of the collagen fibers were defined in the SHG images. Crimp structure is an indicator for collagen fiber durability. Worn-out, stretched and elongated collagen fibers that show a reduced extensibility have been reported in relation to failure in withstanding biomechanical stress and heart valve aging [155, 161, 162]. No significant difference was detected in native and IFC crimp period and amplitude. Explanted FC tissues exhibited a significant decrease in crimp amplitude and an increase in crimp period (Biermann and Marzi et al., **Appendix I**, Figure 5), indicating an elongation and degeneration of the collagen fibers as shown as well for elongated and stretched mitral

valve leaflets by Lee et al. [163]. Altered crimp structures in FC explants were a result of the incapability of the leaflets to withstand biomechanical strain leading to long-term failure.

Multiphoton imaging assessed collagen fiber deterioration and structural changes. Raman measurements and analysis helped to identify changes on a molecular level. No spectral intensity differences in the overall Raman fingerprint were found in native, IFC and FC tissues. In comparison to induced degradation of porcine heart valves with collagenase performed by Votteler et al [127], the overall collagen content in ovine tissue did not decrease due to the FC treatment. PCA of the spectral data of five or six heart valves per group could identify spectral differences between FC and native data. IFC data did not cluster significantly from the native ECM data (Biermann and Marzi et al. **Appendix I**, Figure 6). PC2 described the separation between native, IFC and FC data. Comparison and statistical analysis of the PC2 score values showed a significant difference between native and FC data. Major peaks involved in the spectral differences were described by the PC2 loadings plot and were assigned to defined molecular bonds within the collagen molecule correlating to structural reorganization in crosslink and 3D structure (Biermann and Marzi et al., **Appendix I**, Figure 6). PC3 indicated a minor, however not significant separation of IFC and native data. Relevant peaks in the PC3 loadings plot were 817, 863 and 941 cm^{-1} that referred to C-C bonds of the collagen backbone. Increased peak intensities in IFC tissues might indicate changes in the secondary structure and in the alignment of the collagen fibers [164]. These findings correlated to histological results that presented condensed fiber structures in IFC explants. In-depth spectral analysis revealed a peak shift in the amide I peak region. The average Raman fingerprint spectrum of FC leaflets had a maximum peak around 1664 cm^{-1}, whereas native and IFC leaflets had a maximum at 1666/1667 cm^{-1}, comparable to the amide I peak in Col I. Similar findings were reported in studies on tendon and bone, describing a decrease in collagen amide I Raman shift wavenumber with increasing mechanical or thermal strain [165, 166].

We conclude, that FC leaflets, due to the deteriorations caused by the cryopreservation, do not sustain the biomechanical stress in vivo, resulting in structural reorganization in the triple helical collagen structures, which were shown by altered crimp structures in multiphoton imaging and amide I peak shift in Raman spectra. Over the long term, this led to functional failure of the implants. Collagen in FC ovine heart valves was

more restructured and remodeled than degraded. Supportively, Collagen I ELISA of homogenized IFC and FC tissues did only show a minimal, but not significant decrease in FC collagen content compared to collagen in IFC leaflets (Biermann and Marzi et al., **Appendix I**, Figure 6). An additional ELISA on metalloproteinase 9 (MMP 9), a gelatinase that is involved in collagen degradation [167], did not show a significant increase in FC tissue homogenates compared to IFC leaflets and confirmed our conclusion that FC matrix changes occur as mechanically-induced deteriorations rather than collagen degradation. Although there is no indication for an overall matrix degeneration in FC leaflets, deteriorations might have an essential influence on the functionality of the implants, as it has been reported previously that alterations in collagen crosslink have a stronger impact on mechanical strength of heart valve tissue than the collagen content itself [22].

Notably, FC functional and hemodynamic results showed a similar or even slightly better outcome than in short and mid-term studies, indicating a partially reversible recovery in vivo. An additional PCA comparing native, non-transplanted leaflets and long-term explants confirmed this hypothesis. PCAs for IFC and FC data, showed a separation of non-transplanted and native tissue spectral data for both, FC and IFC treated leaflets (Figure 7). Whereas, IFC tissues recovered in vivo and presented ECM spectral information overlapping the data of native leaflets (Figure 7 B), FC explant data only slightly shifted towards native ECM score values in PC2 (Figure 7 A). ECM damages caused by the cryopreservation method were irreversible and did not fully recover. Moreover, a distinction between native and long-term implanted FC tissues appeared in PC3, indicating additional occurrence of matrix deteriorations during implantation, which might influence the long-term performance of FC leaflets.

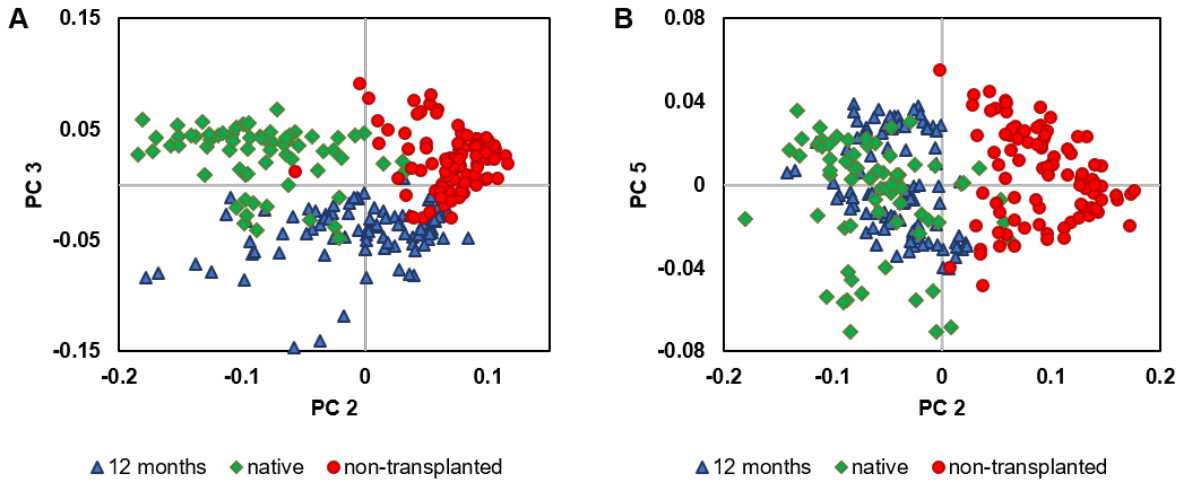

Figure 7. PCA of native, treated non-transplanted and long-term implanted FC and IFC tissues. Both FC and IFC treatments induced significant tissue alteration that were irreversible in FC tissues **(A)** and reversible in IFC implants **(B)**.

Diverse analyses confirmed that IFC resulted in acellular, fully functional leaflets with reduced immunogenicity and well-preserved matrix structures after 12 months in vivo. Raman microspectroscopy and multiphoton imaging could confirm that IFC treated ECM structures of the implants obtained an integrity and architecture comparable to native valves. In contrary, FC treated leaflets presented deteriorations and degeneration of their collagen fiber structures, that might cause a limited biomechanical strength and shortened lifetime in vivo. Moreover, Raman microspectroscopy enabled in-depth analysis of structural changes in FC leaflets on a molecular level, allowing for a better understanding of the damaging effect of the FC method on heart valve tissue.

3.3 Detection of Inflammation-driven Changes in Xenografts

Transplantation of cryopreserved allografts or homografts is commonly applied in clinics. However, there is limited availability of donor tissues, especially in pediatrics [168]. Xenotransplantation might be an alternative option to overcome this obstacle and prevent donor organ scarcity. Therefore, IFC that previously showed improved tissue preservation in allografts, was applied on xenografts to evaluate their in vivo performance and immune responsiveness. A large animal study was conducted over a period of 12 weeks. IFC treated allografts or xenografts (porcine) were implanted in 12 juvenile merino sheep. Leaflets were explanted after six different time points between 1 and 12 weeks. In order to determine IFC xenograft immune response and acceptance, immunohistochemistry, ex vivo CT and a transforming growth factor beta (TGFβ) release assay were conducted.

Allografts were acellular at all time points of explantation. In contrary, xenografts which were acellular in the first explants, were infiltrated by T-cells and evolved a distinct thickening and inflammation over time. Severe immune responses were detectable in xenogeneic leaflets from 4 weeks on. TGFβ release was slightly increased in xenografts, but no significant time-dependent release was shown (Biermann et al., **Appendix II,** Figure 4-6).

Moreover, multiphoton imaging and Raman microspectroscopy were employed for additional assessment of ECM integrity. Multiphoton imaging of native ovine and porcine tissues and xenografts and allografts explanted after 2 and 12 weeks showed similar collagen and elastin structures (Biermann et al., **Appendix II**, Figure 7). No deterioration or changes in ECM structures were detectable in either sample. Multiphoton imaging did not detect any visible effects of IFC treatment on the xenograft matrix. However, in contrary to allografts, xenografts showed cells in the multiphoton images, indicating a migration of immune cells.

Raman microspectroscopy was applied to assess detailed molecular changes in the xenogeneic leaflets. It was shown that native ovine and porcine leaflets differed in their Raman biochemical fingerprint. Therefore, prior to the analysis of the explants, IFC treated but non-transplanted ovine and porcine tissues were measured. Comparison of these xenografts and allografts with native porcine and ovine tissues indicated different effects of the cryopreservation procedure on porcine and ovine tissues. PCA analysis showed a clustering of all four groups (Biermann et al., **Appendix II**, Figure 8). Besides the differences in native ovine and porcine tissue described by PC3, differences were

shown between treated non-transplanted and native leaflets within xenografts and allografts in PC2. Interestingly, clustering between porcine tissues was more significant than the separation of treated and untreated ovine data. PC2 loadings described a spectral assignment similar to the general heart valve collagen spectrum. Thus, differences in native and IFC treated leaflets were explained by intensity differences in collagen. IFC treated leaflets clustered in the negative PC2 range correlating to higher collagen contents. IFC eliminated interstitial water based on the cryopreservative effect and caused shrinking of the leaflet and condensation of the fiber structures, as shown in histochemical analysis (Biermann and Marzi et al., **Appendix I,** Figure 2). Accordingly, the overall collagen content did not increase due to IFC treatment, but as a consequence of the fiber condensation the relative spectral intensity of collagen fibers increased. This effect seemed to be stronger in porcine than in ovine leaflets. Those results postulate that porcine tissues are more sensitive to structural alterations caused by the cryopreservation procedure than ovine tissues. These findings were confirmed by previous results of Votteler et al [127] and Schenke-Layland et al [52], who described collagen degradation in FC treated porcine heart valve tissues by Raman microspectroscopy as well as multiphoton imaging. In contrary, ovine FC treated tissues only showed collagen deterioration, but no decrease in overall collagen signal intensity (Biermann and Marzi et al., **Appendix I,** Figure 5). Peaks of the PC3 loadings plot that caused the separation of ovine and porcine spectral data were similar to the assignments already described in the PCA of only native porcine and ovine tissues.

For analysis of xenograft immune response, leaflets were explanted after time points of 1, 2, 3, 4, 8 and 12 weeks in vivo and measured by Raman microspectroscopy within 48 h after excision. One allograft (4 weeks) required explantation after 2.5 weeks due to a severe inflammation (pneumonia) in the animal. Xenograft and allograft spectra were compared separately to detect time-dependent changes in each graft type. PCA of allograft samples showed spectral differences in PC3 (Biermann et al., **Appendix II**, Figure 6). Comparison and statistical analysis of the PC3 scores plot showed significant differences between native leaflets and tissues within the first 3 weeks after transplantation. Allografts implanted for 8 and 12 weeks did not differ in their Raman data from native tissues (Biermann et al., **Appendix II**, Figure 6). Allografts underwent reversible matrix changes that might correlate to the condensation caused be the cryopreservation and recovered during implantation time. These results were equally shown for long-term implanted allografts, as described above (Figure 7 B).

PCA of xenografts demonstrated time-dependent spectral differences in PC1 (Biermann et al., **Appendix II**, Figure 6). Score values of the explants differed significantly from native porcine tissue with decreasing score values over time. While non-transplanted and leaflets explanted within the first week showed higher score values than native leaflets, leaflets explanted after 3 weeks or later demonstrated negative score values. Differences within the first weeks were dominated by higher collagen signals explained by the condensed ECM structures. Differences of mid-term explants are related to immune reaction-triggered matrix degradation. The shift in PC score values at a time point between 3-4 weeks correlated to the reported T-cell-mediated immune response and tissue degeneration in xenografts after 4 weeks.

Immunohistochemical staining and Raman analysis results showed that IFC treated xenografts demonstrated an initially unremarkable immunogenicity, but failed in mid-term performance and were actively rejected. Raman spectra of the xenografts ECM identified significant alterations at the same time point as severe T-cell infiltration and inflammation were detected. An association of ECM degeneration and T-cell infiltration in bioprosthetic xenografts has been previously reported [169]. Raman results of treated but non-transplanted xenografts and allografts indicated a significantly higher effect of the cryopreservation procedure on porcine tissue. Xenogeneic leaflets exhibited inferior ECM integrity before transplantation and could not recover fast enough in vivo before exposure to additional stress by infiltrating immune cells.

Chapter 4

Results II:
Quantitative Assessment of Cryoprotective Agents in Heart Valve Tissues

The contents of this chapter are based on

J. Marzi, A.C. Biermann, M. Haensel, E.M. Brauchle, K.G.M Brockbank, U.A. Stock, K. Schenke-Layland, *In situ quantitative assessment of residual cryoprotectant effects on cardiac tissues*, Analytical Chemistry, 2019; 91(3): 2266-2272

4 Results II: Quantitative Assessment of CPAs in Heart Valve Tissues

IFC treatment of heart valves has been shown to improve leaflet ECM preservation compared to standard cryopreservation. The main difference between the two treatments is the cryopreservation media. FC medium contains 10% DMSO (1.4 M), while IFC medium (VS83) consists of 4.65 M DMSO, 4.65 M FMD and 3.31 M PG in Euro-Collins buffer (EC). CPA concentration in IFC medium is almost about 10 times higher than in the standard freezing solution and therefore enables ice-free cryopreservation and storage below the glass-transition temperature of the CPAs. Despite the advantages of highly concentrated CPAs in IFC medium that sustain the leaflets long-term integrity, the safety issue of CPAs needed to be addressed before releasing IFC treated heart valves for clinical trials. All CPAs in VS83 cryomedium, applied in IFC, are molecules that are potentially toxic [170-173] and could harm the patient directly or cardiovascular cells that should help to remodel the implanted tissue. Therefore, a complete removal of CPAs needed to be guaranteed by the washing protocol before implantation. To date, for quantitative assessment of CPAs or other drugs in tissues, complex quantitative techniques such as high performance liquid chromatography (HPLC) [174], tandem mass spectrometry (MS) [175, 176] or nanoparticle-coupled magnet resonance imaging [177] are established that would not allow for a marker-independent, non-invasive and real-time monitoring of chemicals or drugs in tissues. Raman microspectroscopy and Raman imaging were established for qualitative and quantitative in situ analysis of residual CPAs in IFC treated heart valve tissues. The washing procedure consists of 5 washing steps of 10 min in EC. To determine the CPAs in the washing solution, supernatants of the washing steps of the long-term study (see Chapter 3) were collected and measured. In addition, Raman imaging was performed on IFC treated leaflets directly after rewarming to monitor the CPAs that penetrated the tissue and their decrease due to the washing procedure. Moreover, in order to define the limit of detection of the CPAs in heart valve tissues, leaflets stored in different VS83 concentrations were measured by Raman microspectroscopy.

4.1 Raman Spectra of CPAs in VS83 Medium

In comparison to large biomolecules in tissues and cells that mostly consists of similar amino acids, chemicals and small molecules represent well-defined singular Raman peaks. Single components of the VS83 solution were measured separately to identify the spectral assignments of DMSO, FMD and PG and their most significant specific peaks that could later be used for the establishment of a calibration model. The most significant peaks of VS83 spectrum were found at 677 and 711 cm^{-1} and correlated to the symmetric and asymmetric stretch of the C-S bonds in DMSO. Specific peaks for PG were found at 806 and 840 cm^{-1} and were assigned to CH_3–bending and C-C-O stretching in PG. CH rocking in FMD caused a characteristic peak at 1392 cm^{-1} (Marzi et al., **Appendix III**, Figure 1). The Raman spectrum of the EC medium did not show signals in the wavenumber range of DMSO. A slight shoulder appeared in the higher wavenumber region of the PG range and a weak peak slightly shifted to the maximum of the FMD peak was detectable. However, these peaks were of marginal importance, because the overall peak intensities of the pure CPAs were between 20 (compared to FMD) to 60 (compared to DMSO) fold higher than the intensities in EC. These specific peaks enabled a simultaneous monitoring of all CPAs.

4.2 CPA Quantification in Supernatants

The collected washing supernatants of the five washing steps and the storage solution of 6 IFC heart valves were measured. Average Raman spectra demonstrated significantly decreased CPA intensities after the first washing. For quantitative assessment of the CPAs and the establishment of a calibration model, fresh VS83 solution was diluted with 1xEC. Calibration solutions ranged between 100% and 0.2% VS83, corresponding to concentrations of 0.009-4.65 mol/l for DMSO and FMD and 0.007-3.31 mol/l for PG. A partial least square regression model allowed for the prediction of the overall VS83 concentration. However, in order to consider different wash-out kinetics of the three CPAs a separate calibration for every CPA was established according to their specific Raman shift ranges (Marzi et al., **Appendix III**, supplementary figure 1). The concentrations of each CPA within the supernatants were predicted over the calibration model. Results showed a significant decrease for DMSO, PG and FMD after the first and between the first and the second washing step. After the third washing step initial DMSO and PG concentrations in the supernatants decreased by 99.2% and FMD decreased by 98.9%. The following washing steps did not indicate a further change in CPA

content. Final concentrations in the supernatants of the last washing step represented 0.02 M DMSO, 0.01 M PG and 0.04 M FMD (Marzi et al., **Appendix III**, Figure 2). The washing protocol showed sufficient efficacy to remove the CPAs. Quantitative analysis of CPA concentrations in the supernatants indicated no significant release of DMSO, FMD and PG after the third washing step. Thus, the results encouraged to shorten the protocol to 3 instead of 5 washing steps.

4.3 In situ CPA Detection in Tissue and Analysis of Tissue Permeability

Raman microspectroscopy had the fidelity for the quantitative analysis of DMSO, FMD and PG in the washing supernatants up to concentrations in the single-digit mM range. There exist several techniques which allowed for the quantification of chemicals or drugs in liquids or were used to study CPA permeation kinetics in different tissues such as nuclear magnetic resonance, osmolality measurements or capillary zone electrophoresis [178-182]. However, for the establishment of an in situ tool to non-invasively monitor chemical residuals within tissues, all of these techniques lacked in either specificity, non-destructiveness or sensitivity. In addition, the previous studies showed that permeation kinetics strongly depended on concentration, temperature, the applied CPA as well as the treated tissue. To circumvent these variables and avoid the mathematical modeling of penetration kinetics, an in situ quality control tool for direct assessment of CPA concentration in tissues would be beneficial. Therefore, Raman techniques were applied. To test the applicability for CPA detection within tissues, single Raman spectra acquisition and Raman imaging were performed. The Raman fingerprint of IFC treated tissues prior and after the washing procedure was compared. Freshly rewarmed IFC-treated leaflets demonstrated peaks in their biochemical fingerprint, that did not correlate to the leaflets ECM structures, but were assigned to the previously defined peaks of DMSO and FMD. PG was not clearly detectable due to the overlap with peaks assigned to the leaflets ECM (Marzi et al., **Appendix III**, Figure 3A). For in-depth analysis and monitoring of the washing procedure, the washing process was simulated and continuously imaged by Raman microspectroscopy. Image acquisition at very low resolution allowed for fast scanning of a large area. Within 3 min, it was possible to collect an overview image of an area of 2000 x 2000 µm. Detailed tissue structures were not detectable at the low pixel resolution of 100 x 100 µm, however it was sufficient for specific identification of the CPA spectra. Efflux of every CPA could be monitored in the intensity heat maps at the characteristic Raman shift regions of 640-740 cm^{-1} for DMSO, 780-860

cm^{-1} for PG and 1280-1400 cm^{-1} for FMD. Significant signals from CPAs were not detected after the third washing step (Marzi et al., **Appendix III**, Figure 4). However, within the first washing step different efflux kinetics for DMSO, FMD and PG were detected. For the next washing steps a highly significant decrease was detected for all CPAs. Significant differences between the different CPAs within a washing step were only detected between DMSO and PG (Figure 8). In summary, DMSO was washed out the fastest, followed by FMD and then PG. Those results corresponded to the room temperature penetration kinetics of IFC medium into fresh leaflet tissue reported by Vasquez-Rivera et al. [183].

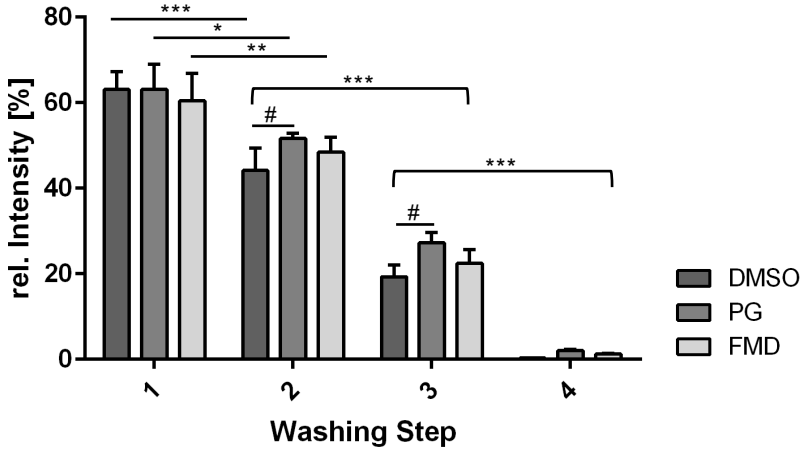

Figure 8. Raman monitoring of the CPA efflux. Statistical analysis of the normalized spectral intensities of the CPAs at the different washing steps showed a significant decrease after each washing step. A significant difference in the kinetics of the different CPAs was observed between DMSO and PG. n=3; *p≤0.5, **p≤0.05, ***p≤0.01 for differences between the washing steps; #p≤0.5 for differences between the CPAs

A PCA of the images of each washing step could identify both CPAs and tissue structures (Marzi et al., **Appendix III**, Figure 5A). Raman images of the freshly rewarmed leaflets and the leaflets after the first washing step were dominated by spectral information in the positive PC range that was assigned to the CPAs. Contrarily, Raman images after the second washing steps mainly provided spectral information relating to the leaflets ECM (Marzi et al., **Appendix III**, Figure 5B). Raman imaging results confirmed the outcome of the quantitative analysis of the supernatants and the proposal to shorten the washing procedure.

An additional experiment was conducted to determine the limit of detection of CPAs in tissues. Therefore, single leaflets, obtained from the replacement surgeries, were preserved in different concentrations of IFC medium, rewarmed and measured by single spectra acquisition. Concentrations varied between 100% VS83 with the known

CPA concentrations and 5% VS83 corresponding to CPA concentrations of 0.23 M DMSO and FMD and 0.17 M PG. Significant interstitial DMSO peaks were detectable for all concentrations as well as minor FMD peaks. PG was not detectable in the lower VS83 concentrations due to the overlap with the collagen peaks of the tissue. Notably, no proportional relation between VS83 concentration and peak intensities was found. While CPA peaks in tissues preserved in pure VS83 correlated to the peak intensities of tissues preserved in 25% VS83, tissues preserved in 50% and 75% VS83 showed much higher CPA peak intensities (Marzi et al., **Appendix III**, Figure 3B). It was concluded that the cryopreservative effect of the CPAs caused this phenomenon. Highly concentrated CPAs eliminated the interstitial water in the cryopreserved tissue, which avoids ice-crystal formation and destruction of the tissues. However, this does not result in a complete replacement of water by CPAs but the dehydration of the tissue, demonstrated in shrunk leaflets with condensed ECM structures (Biermann and Marzi et al., **Appendix I**). In high concentrations and the absence of water, all CPAs seem to rather undergo self-association [184-187] than binding to proteins or other tissue structures. Intermolecular interactions might dominate in comparison to interactions with the tissue and formation of big complexes reduced the permeability [59]. Thus, highly concentrated CPAs did not permeate into the tissue in the same amount as if in dilution. Raman imaging of unwashed leaflets confirmed this hypothesis. Unwashed leaflets did not show interstitial CPA concentrations that were as concentrated as in the surrounding VS83 medium (Marzi et al., **Appendix III**, Figure 4). Less concentrated CPAs only provide negligible self-associating effects and are not capable to push out all of the interstitial water. In this case, tissues do not condense, water stays within the tissue and enables a deeper penetration of the CPAs into the tissue, resulting in the detection of higher concentrations within the tissue. A better understanding of the cryopreservative effect of VS83 was provided. Additionally, the necessity for highly concentrated CPAs, that enabled elimination of water but at the same time caused less toxic interstitial CPA concentrations, was demonstrated.

Chapter 5

Results III: Identification and Discrimination of Vascular and Non-vascular Smooth Muscle Cells and their Phenotypes

The contents of this chapter are based on

J. Marzi, E.M. Brauchle, K. Schenke-Layland, M. Rolle, *Non-invasive functional molecular phenotyping of human smooth muscle cells utilized in cardiovascular tissue engineering,* Acta Biomaterialia, 2019, 89: 193-205

5 Results III: Identification and Discrimination of Vascular and Non-vascular SMCs and their Phenotypes

Susceptibility of current applied synthetic as well as autologous grafts to thrombosis, pseudoaneurysms and infections [188] requires the development of new materials for the replacement of vessels. TEVGs derived from decellularized materials, biodegradable scaffolds or engineered cell-sheets are the major approaches in cardiovascular tissue-engineering [78, 189-191]. Biomaterial design itself has strongly evolved, the remaining problem is cell source and the control and characterization of cells applied in vascular graft constructs. SMCs represent a very heterogeneous group and easily transform between the two major phenotypes – contractile and synthetic SMC. Maintenance of the functional, contractile SMC phenotype is required in both isolated donor vessel SMCs as well as stem cell derived SMCs when aiming for a functional persisting graft. Regulation and mechanisms of phenotypic switching are well described [75, 76], however to transfer and control phenotypic switching in TE remains difficult [77]. The following study aimed to established Raman microspectroscopy as quality assessment tool in cardiovascular TE. Control and understanding of SMC development and characteristics are essential to develop tissue-engineered biomaterials based on nature's blueprint. Thus, the work included the characterization and discrimination of native smooth muscle tissues and cells as well as the monitoring of phenotypic switching in cultured SMCs and the assessment of ECM remodeling in tissue-engineered SMC constructs.

5.1 Raman Imaging of Vascular and Non-vascular Smooth Muscle Tissues

SMCs are present in tissues of vascular but also non-vascular origin. Aorta, arteries, uterus or trachea differ in their anatomic appearance and function. Embedded and fixed tissue sections of human aorta, pulmonary artery, uterus and trachea were analyzed to define characteristic Raman fingerprints for smooth muscle tissues and to localize distinct tissue structures. Raman mapping was performed on defined areas in tissue sections. TCA of the spectral data provided intensity heat maps, indicating all pixels with similar spectral information and their localization in the sample. The molecular information of the identified structures could be analyzed by the average spectra of the components.

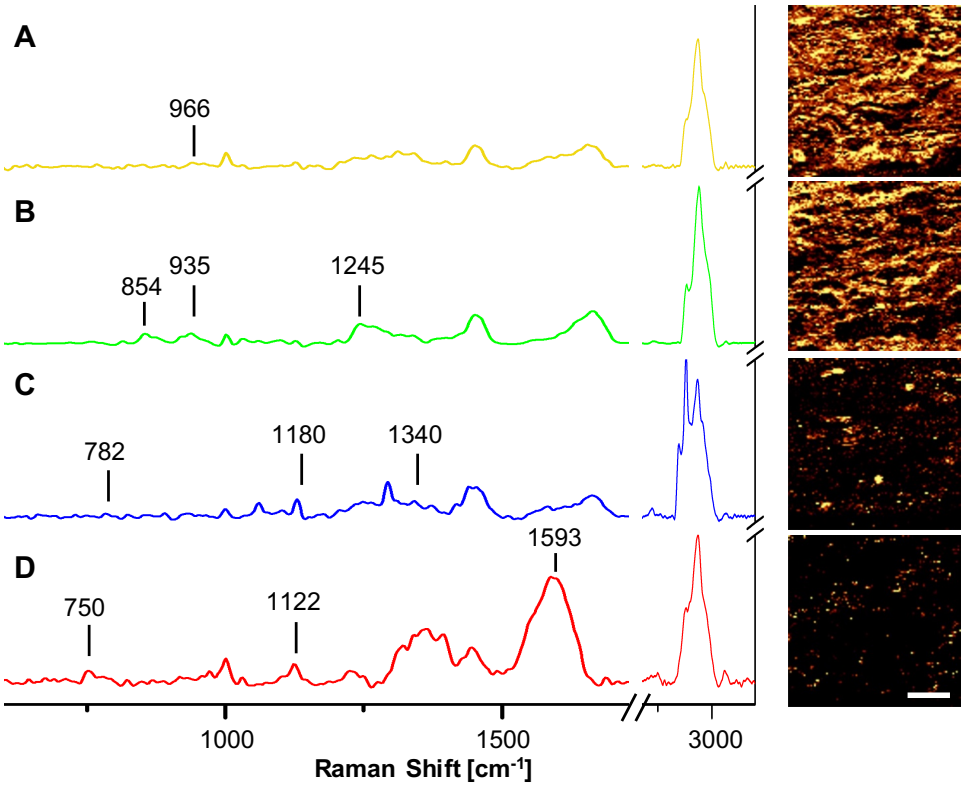

Figure 9. Raman imaging of human aortic tissue. (A-D) Main spectral components were extracted. Component 1 **(A)** showed specific peaks for elastin. Component 2 **(B)** was assigned to collagens. Component 3 **(C)** described cells and nucleic acids and component 4 **(D)** identified red blood cells. The localization of these components within the aortic tissue was displayed in intensity heat maps. Scale bar equals 20 µm.

For the imaging of the smooth muscle tissues, four main components were selected according to the map of the aortic tissue sample (Figure 9 A-D). Component 1 (Figure 9 A) had a spectral signature for elastin. Peaks distinguishing elastin from collagen were found at 526 and 966 cm^{-1} correlating to desmosine/isodesmosine. Spectral assignment of component 2 (Figure 9 B), with characteristic peaks at 854, 935 and 1245 cm^{-1} correlated to hydroxyproline and the C-C backbone in collagen. Component 3 (Figure 9 C) showed peaks at 782, 1180 and 1340 cm^{-1} indicating nucleic acids and the presence of cells. Component 4 (Figure 9 D), which was only present in some tissues, visualized red blood cells with characteristic bands at 750, 1122 and 1593 cm^{-1}, assigned to porphyrin and the quinoid ring. The peak at 1001 cm^{-1} was present in all samples and is assigned to the highly Raman active C-C ring breathing of the amino acid phenylalanine [192], which is present in numerous biological samples. A detailed summary of all characteristic peaks and their molecular assignments is provided in supplementary table I (**Appendix V)**.

These components were applied as reference spectra for the TCA of the other samples to compare different smooth muscle tissues. Intensity heat maps of these components showed the localization and distribution of the molecules within the uterine tissue, trachea and pulmonary artery (Figure 10). Merging of all components was shown in an overlay image for each tissue. Each of the investigated smooth muscle tissues showed the presence of all components, but a different distribution of the ECM structures. Vascular smooth muscle tissues had less collagen and more elastin than non-vascular tissues.

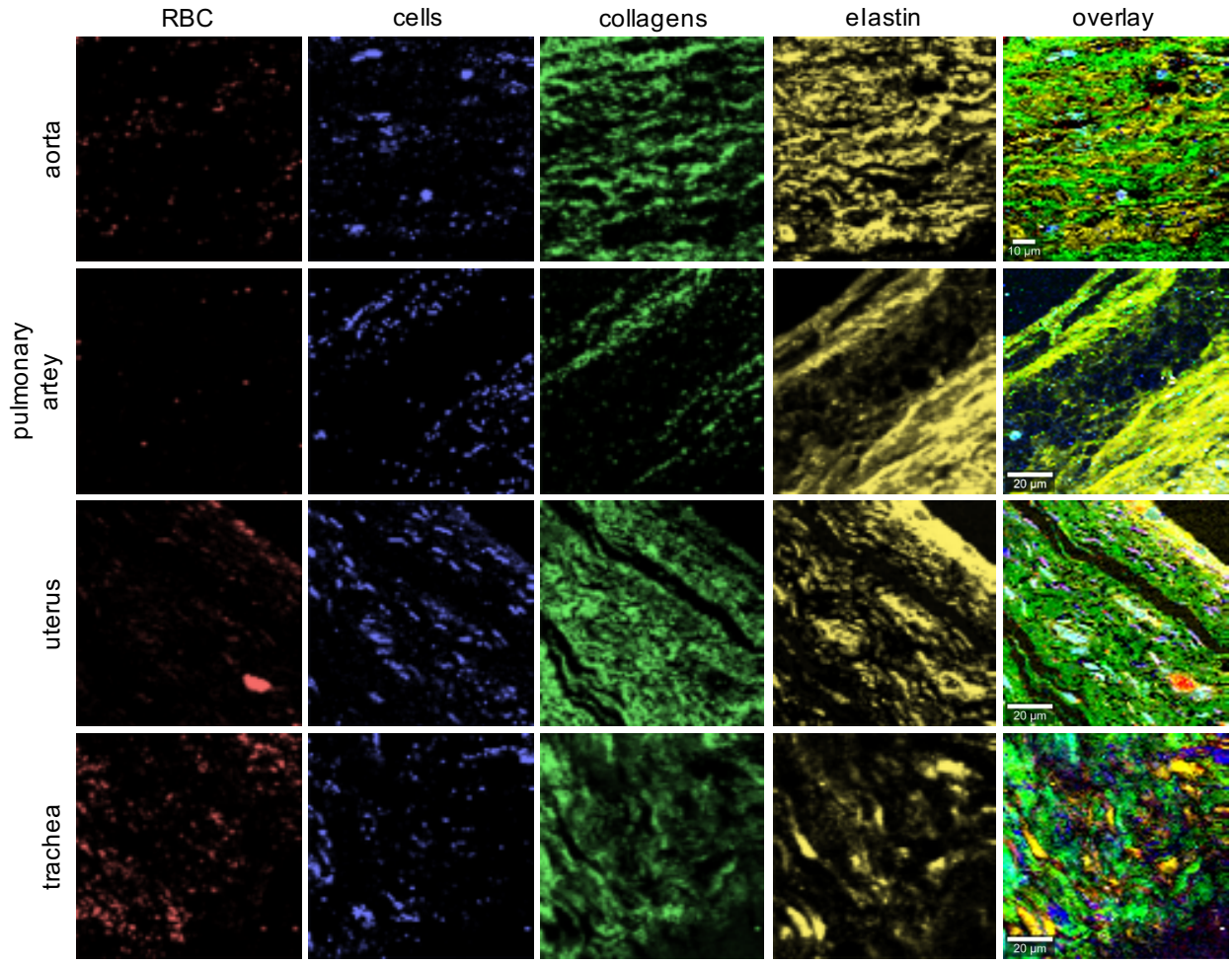

Figure 10. Intensity heatmaps and overlay images of the TCA analysis. The aortic tissue components served as reference. The overlay images show the red blood cell (RBC) component in red, the collagen component in green, cells in blue and elastin in yellow.

In comparison to Raman imaging, routine histochemical analyses on ECM tissue structures were performed. Movat-Pentachrome staining (Figure 11 A-D) identified nuclei and elastic fibers (black), collagen fibers (yellow), ground substance and mucin (blue), muscle (red) and fibrin (bright red). SHG allowed for a label-free imaging of the collagen structures, which were detectable in all vascular tissues (Figure 11 E-H). In non-vascular tissues, collagen structures, ground substance and muscle tissue were dominating. In the bright field mode of the Raman microscope, collagen bundles were visible and targeted for single spectrum acquisition (Figure 11 I-L).

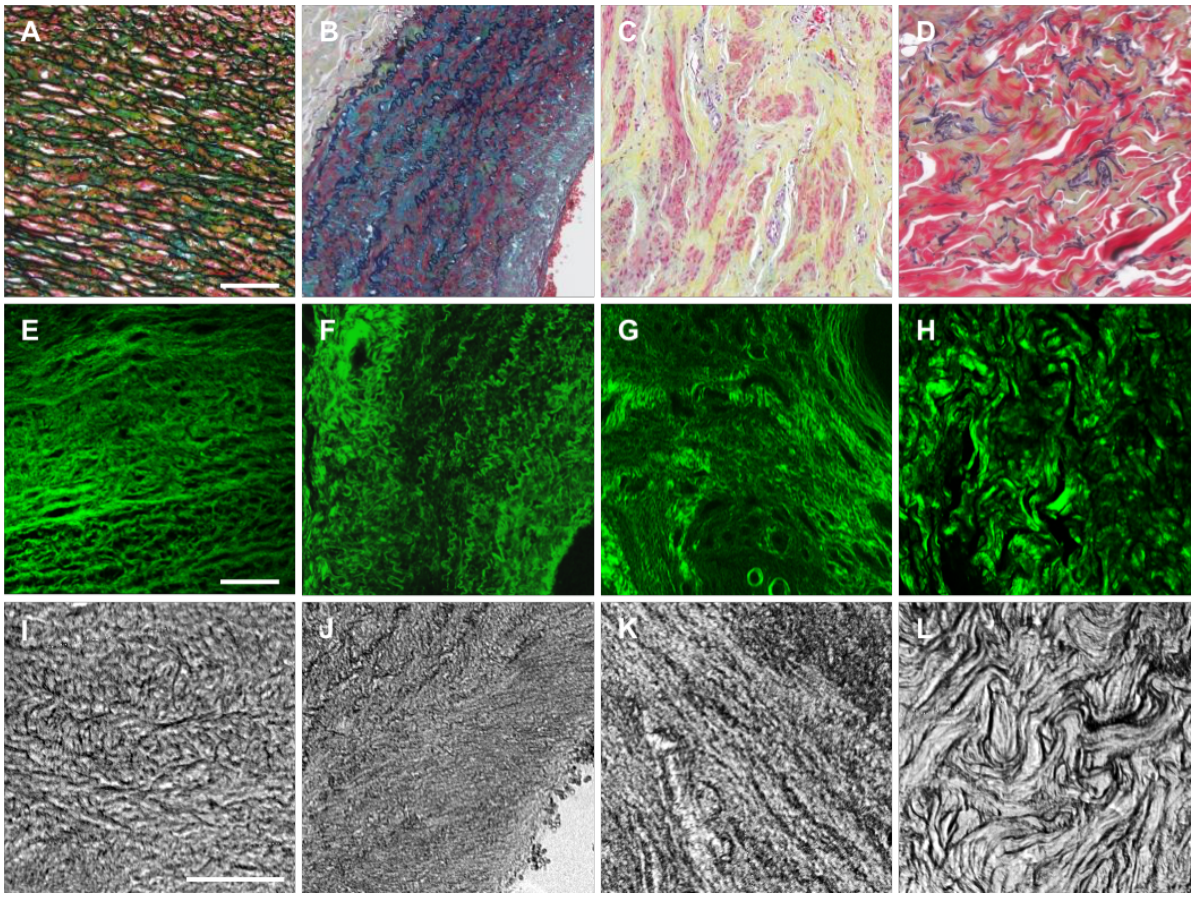

Figure 11. Routine histochemical analyses. Performed on aorta **(A, E, I)**, pulmonary artery **(B, F, J)**, uterus **(C, G, K)** and trachea **(D, H, L)** smooth muscle tissue sections. **(A-D)**, Movat-Pentachrome staining identified nuclei, elastic fibers (black), collagen fibers (yellow), glycosaminoglycans, mucin (blue), muscle (red) and fibrin (bright red). Scale bar equals 100 µm. **(E-H)** SHG imaging showed collagen structures (green). Scale bar equals 100 µm. **(I-L)** Contrast phase bright field Raman microscope images allowed for targeting larger collagen bundle structures for single Raman spectra acquisition. Scale bar equals 20 µm.

For detailed analysis, a PCA was performed on single spectra randomly acquired of the collagen structures of each tissue. The PC2/PC3 scores plot allowed for a separation of the investigated smooth muscle tissues. A separation of vascular and non-vascular tissues was found in PC2 based on collagen content. Aortic and pulmonary artery data as well as uterine and trachea data were separated due to spectral differences in

PC3, referring to differences in the architectural structure of collagen (Marzi et al., **Appendix IV**, Figure 7).

These results confirmed the different collagen quantities in smooth muscle tissues shown as well in Raman imaging, multiphoton imaging and Movat-Pentachrome staining (Figure 11). All methods identified high collagen contents in uterus and trachea tissue, followed by collagens in the aorta. Pulmonary artery tissue did not show much collagen. Raman microspectroscopy provided spectral maps with information on a molecular level and allowed to marker-independently image different structures. Routine immunostaining and histochemical analyses showed tissue structures and cellular components, but staining was time-consuming and only allowed assessment of a limited number of tissue structures for each staining method. Other label-free techniques such as multiphoton laser-induced SHG imaging were only applicable for the detection of collagen structures.

5.2 Raman Imaging of Vascular and Non-vascular SMCs

Smooth muscle tissues could be separated according to their Raman fingerprint. Clustering was mainly explained by differences in ECM structures, especially to collagen fibers. To further investigate differences in tissue origin on a cellular level, we aimed to analyze isolated human SMCs of different smooth muscle tissue origins. Human vascular SMCs isolated from aorta (HAoSMCs), pulmonary artery (HPASMCs) and coronary artery (HCASMCs), and non-vascular SMCs originating from uterus (HUtSMCs) and trachea (HTSMCs) were analyzed in vitro. Cells of passage 6 were cultured for 48 h, fixed in 4% paraformaldehyde and imaged. For the imaging of single SMCs of different tissue origins, four main components were selected in the TCA (Figure 12 A-D). Component 1 (Figure 12 A) described membrane structures and contained spectral information of phospholipids. Characteristic peaks for phospholipid bonds such as choline or C-N vibrations were present at 715, 875 and 1080 cm^{-1}. Component 2 (Figure 12 B) was related to lipids and lipid droplet peaks, representing the golgi apparatus [193]. Peaks different from phospholipids were found at 878 and 968 cm^{-1}. Most of the differences between phospholipids and lipids were peak shifts, but not the presence or absence of peaks. Additionally, in comparison to phospholipid bilayers, lipid droplets showed a stronger Raman signal in the area around 2800 cm^{-1} [194]. Component 3 (Figure 12 C) displayed proteins and had characteristic peaks at 1308 and 1660 cm^{-1} assigned to amide III and amide I. Component 4 (Figure 12 D) identified cell nuclei and had peaks at 786, 1251 and 1577 cm^{-1} correlating to DNA phosphate and bases. TCA allowed for the localization of these components in the cell. The defined components for HAoSMCs were used as reference spectra for the analysis of the other cell types (Figure 12E). Proteins, nucleic acids, lipids and phospholipids were detectable in HCASMCs, HPASMCs, HTSMC and HUtSMCs and different distribution patterns were shown. In the combined images of all components for all different cells the nucleus could clearly be identified but the proportion and localization of the other components differed in each SMC type. A detailed summary of all characteristic peaks and their molecular assignments is shown in supplementary table II (**Appendix VI**).

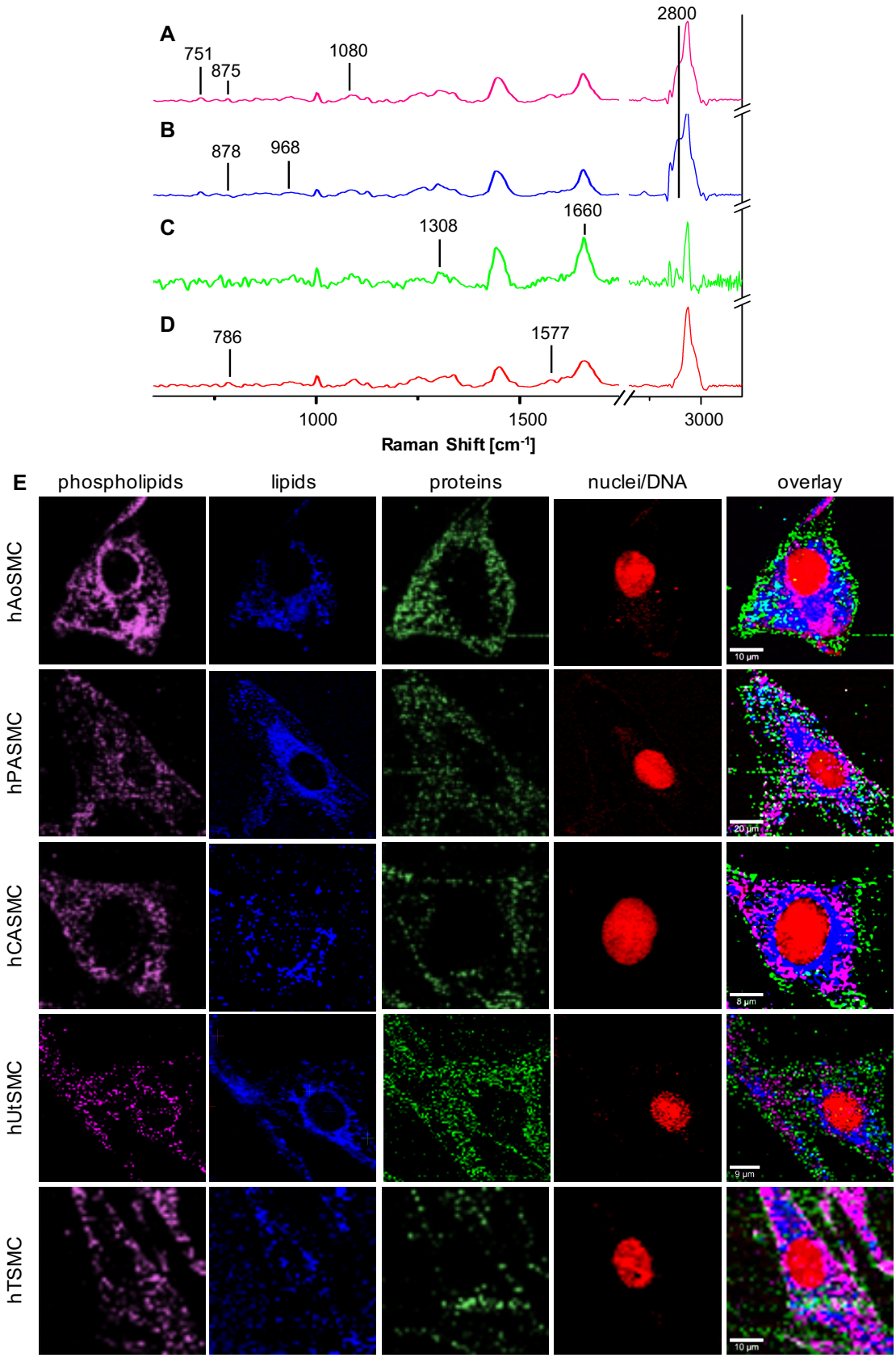

Figure 12. Raman imaging of single adherent hSMCs. (A-D) TCA identified four main spectral components in HAoSMCs. Component 1 **(A)** showed specific peaks for phospholipids and membrane. Component 2 **(B)** was assigned to lipids. Component 3 **(C)** described proteins and component 4 **(D)** identified nucleic acids. **(E)** HAoSMC components served as reference for TCA of the other cells. The intensity heat maps showed phospholipids in pink, the lipid component in blue, proteins in green and the nucleic acids component in red.

5.3 Discrimination of SMCs of Different Tissue Origins

Raman imaging of single adherent SMCs allowed for the identification and localization of distinct cellular components such as the nucleus, lipids and proteins. TCA allowed for the separation of the main cellular components. In relation to the overall data sets, small spectral differences such as a peak shift or intensity differences indicating intramolecular changes were barely detectable by TCA. Raman imaging can be applied to visualize the localization of cellular structures within the cell or to monitor physiological or triggered effects in real-time. However, for fast characterization of a larger batch of cells, this technique would be too time-consuming. The acquisition of an image of a single cell with a pixel size of 1x1 µm took about an hour. To develop a fast protocol with the further option and accessibility for cell sorting, single spectra acquisition of cells in suspension were performed. PCA was applied to check for spectral differences between the SMCs of different tissue origins. PC2/PC3 scores plot indicated a separation between the five different groups of SMC tissue origin (Marzi et al., **Appendix IV**, Figure 2). Each group demonstrated a specific Raman fingerprint. PC2 explained a separation within the SMCs of the vascular and non-vascular group. PC3 separated SMCs of non-vascular and vascular origin. The loadings plot of PC 2 described information related to the cell nuclei. Differences within vascular and non-vascular SMCs were determined by peaks assigned to DNA (720 cm^{-1}), nucleic bases (778 and 1294 cm^{-1}) and the phosphate backbone of the DNA (1090 and 1434 cm^{-1}). A separation of non-vascular and vascular SMCs according to PC 3 was depending on cellular structures. Peaks described by the loadings plot of PC3 correlated to lipids (1125 and 1339 cm^{-1}), proteins (1250 and 1650 cm^{-1}) and phosphatidylinositol (775 cm^{-1}) (Marzi et al, **Appendix IV**).

An additional PCA to elaborate smaller differences within the vascular group was conducted. Analysis of vascular SMCs (Figure 13) showed a clustering of all groups, however only HCASCMs differed significantly from the other cells in PC2 and HPASMCs in PC3. Spectral data from HAoSMC partly overlapped with HPASMC data in PC2 and with HCASMC data in PC3. PC2 explained a separation based on peaks at 788, 877 and 1438 cm^{-1}, referring to DNA, the C-N-N symmetric stretching in lipids and CH_2-CH_3 deformation vibrations in proteins. Peaks in PC3 loadings plot were found at 936, 1341 and 1447 cm^{-1} that correlated to the C-C backbone in proteins, the DNA bases adenine and guanine and CH_2 deformation in proteins.

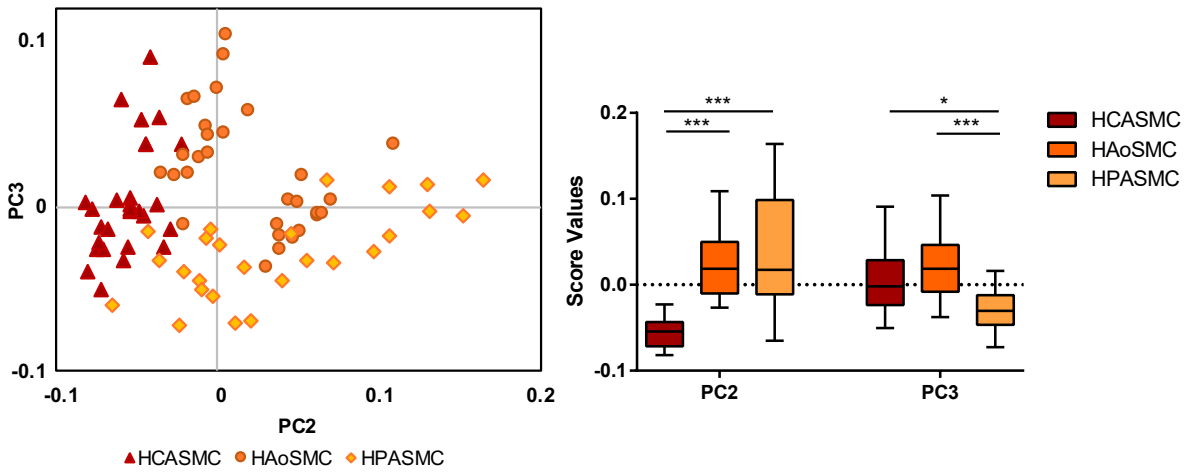

Figure 13. PCA of vascular SMCs. Detailed analysis of vascular SMCs showed a significant clustering of coronary smooth muscle cells (HCASMCs) in PC2 and a separation of pulmonary smooth muscle cells (HPASMCs) in PC3. n=30; *p<0.05, ***p<0.001

Moreover, standard techniques for protein and gene expression analysis were applied on passage 6 cells of all tissue origins. Immunocytochemistry (ICC) on smooth muscle myosin heavy chain 11 (*MYH11*) and calponin (*CNN1*) as well as quantitative polymerase chain reaction (qPCR) were performed. RNA expression of alpha smooth muscle actin (α-SMA, *ACTA2*), *CNN1*, caldesmon (*CALD1*), *MYH11* and collagen I (*COL1A1*) and collagen III (*COL3A1*) were analyzed by qPCR. *MYH11*, *CNN1*, *ACTA2* and *CALD1* are proteins of the contractile apparatus and are reported to be specifically expressed in SMCs of the contractile phenotype [75, 195]. Col I and III were analyzed to assess ECM deposition and switching to the synthetic phenotype. Contractile marker expression did not differ significantly between all SMCs (Marzi et al., **Appendix IV**, Figure 3A-F). The results did not allow for the definition of a specific gene expression pattern that would distinguish and identify the SMCs of the different tissue origins as shown by PCA. Furthermore, significantly different gene expression levels were not detected in vascular and non-vascular SMCs. In ICC, all SMCs expressed MYH11 and CNN1, however there was no significant difference in protein deposition patterns that could help to discriminate HAoSMCs, HCASMCs, HPASMCs, HTSMCs and HUtSMCs (Marzi et al., **Appendix IV**, Figure 3G).

This work showed that SMCs of vascular and non-vascular tissues differ in their molecular composition. Moreover, also within the group of vascular SMCs a separation was indicated by PCA. Although SMCs are highly diverse in their phenotype, differences between SMCs of distinct tissue origin were shown in a clear separation in the PCA, indicating that spectral differences due to SMC heterogeneity are less influencing within

the same passage than inter-populational differences of SMCs of different tissues. For in-depth analysis of SMC heterogeneity and phenotype variability within one population, Raman analysis of more than 30 cells might be needed to have a representative number of phenotype intermediates.

The biochemical Raman fingerprint of the cells of all different SMC origins varied. Monitoring and identification of SMCs isolated from different tissue origins has not been thoroughly investigated. Most studies focused on the distinction of contractile and synthetic SMC phenotype within the same tissue [196, 197]. Gabbiani et al analyzed different vascular SMCs and non-vascular SMCs in various mammals by gel electrophoresis and immunofluorescence microscopy [198]. Intermediate-size filaments were examined. Vimentin and αSMA were reported to be dominantly expressed in vascular SMCs, whereas in non-vascular SMCs the major filament was desmin and γSMA was mostly expressed instead of αSMA [198].

These features make Raman microspectroscopy and Raman imaging into a valuable tool to characterize and identify SMCs as it has already been shown before for other cell types such as stem cells [121, 122]. Hereby we showed a technique superior to marker-based routine techniques that did not enable a discrimination of SMCs of different tissue origins.

5.4 Discrimination of SMC Phenotypic Switching

SMCs represent a very heterogeneous cell population within one tissue. Whereas cellular differences between different smooth muscle tissues have not been investigated before, phenotypic changes in one SMC population are well described [75]. Functional SMCs usually express characteristics of the contractile phenotype. Phenotypic switching to the synthetic phenotype was often reported in relation to development and diseases such as atherosclerosis or aneurysms [199-201]. Moreover, many physiological and external triggers inducing phenotypic switching have been described [195, 202-204]. Several genes and proteins are dominantly expressed in either the contractile or synthetic phenotype [75, 195, 204]. However, it is hard to define a single marker gene or protein identifying a SMC as clearly contractile or synthetic phenotype. Most of these markers are also transiently expressed in the other phenotype as well as in other cell types, another difficulty is the presence of intermediate states of the phenotypes [75].

This work aimed to apply Raman microspectroscopy to monitor changes in primary isolated SMCs in culture. Therefore, SMCs of a vascular (coronary artery) and a non-vascular (uterus) origin were cultured for 20 passages and measured by Raman microspectroscopy. Additionally, ICC was performed. PCA indicated a shift in spectral information over the period of culture in both populations (Marzi et al., **Appendix IV**, Figure 4C, D). Both SMC types showed a significant difference between low and high passages. For HUTSMCs a first phenotypic alteration was detectable after passage 6, whereas for HCASMC a significant change of the cell composition was not detected before passage 10. SMCs appeared to differ in their phenotypic switching.

In parallel to Raman measurements, standard ICC was performed (Marzi et al., **Appendix IV**, Figure 5). Morphological alterations throughout culture time were visible in bright field images. Low passage HUtSMCs clearly showed the spindle-shaped morphology of contractile SMCs. However, low passage HCASMCs were less differentiated in their morphology. HUtSMCs represented a significant shift in morphology to a rhomboid, fibroblast-like shape in high passage. HCASMCs also depicted a synthetic phenotype in higher passages. Cells of low (4 & 6) and high (20) passage were stained for the contractile phenotype marker CNN1 and three other markers related to the synthetic phenotype. Connexin 43 (CX43), COL1 and Syndecan-4 (SYN4) are mainly expressed in SMCs of the synthetic phenotype [75, 205] and have been reported in relation to phenotypic switching in coronary artery SMCs [206, 207], ECM production [208] and aortic aneurysms [209, 210]. ICC for CNN1 showed a decrease of protein expression over passaging in

HUtSMCs. Cells of low passages stained positive for CNN1, in passage 20 only few cells expressed the contractile marker protein. In HCASMCs no significantly different CNN1 expression patterns between high and low passage cells were found. ICC for synthetic SMC phenotype proteins was positive in vascular and non-vascular SMCs in low and high passage. However, COL1 was stronger expressed in HCASMCs of higher passage, indicating a switch to the synthetic SMC phenotype (Marzi et al., **Appendix IV**, Figure 5).

ICC results complied with the results of the Raman measurements. For both cell types cellular alterations were detected over passage time. In addition, it was shown that uterine SMCs underwent a more significant phenotypic switch, while HCASMC indicated a smooth transition to the synthetic phenotype. Biomolecular changes were unambiguously detectable and definable in the Raman results, whereas in ICC and PCR a clear infallible marker was lacking. There exists a large number of markers that are dominantly expressed in either the synthetic or contractile SMC phenotype [75]. However, this does not imply that those markers are not completely missing in the other phenotype and can also be expressed in other cell types such as fibroblast or other cardiovascular cells [30, 154, 211]. Standard techniques demonstrated the difficulty to rely on one single marker to define the phenotypic state of a SMC. Moreover, transition states exist in between the synthetic and contractile phenotype. In contrary, Raman microspectroscopy provided the overall biomolecular fingerprint of the cell, containing molecular information describing the overall composition of single cells and enabling the detection of cellular changes and the definition of the time point of differentiation. This might also be of particular interest for stem-cell derived tissue-engineering approaches.

According to our results, we conclude that SMCs applied for TE should be of passage 6 - 7 or below to guarantee the dominance of SMCs of functional, contractile phenotype. A comparable study by Timraz et al. investigated the behavior of HAoSMCs in culture and reported a similar result [212]. Based on the analysis of cell morphology, ICC on MYH11, αSMA, COL1 and COL3 and marker gene expression passage 7 was identified as the intermediate state between contractile and synthetic phenotype.

5.5 Analysis of Tissue-Engineered Vascular Rings

A major obstacle for rapidly evolving TE approaches is to control and monitor the development, degeneration and functionality of the biomaterial [213, 214]. An additional aspect in cell-based approaches is the assessment of cell differentiation states. This is of major interest for stem cell-based approaches, which provide the advantage of being differentiable to various kinds of cells, however it needs to be guaranteed that they differentiate exactly into the required type of cell [72]. However, also for smooth muscle cells, there exists a broad populational heterogeneity and the risk of phenotypic switching, as it was described before [77]. Therefore, Raman analyses were applied to compare the tissue structure of tissue-engineered SMC rings to native smooth muscle tissue. SMC rings are scaffold-free tissue constructs formed in agarose wells by self-assembly of primary or stem cell-derived SMCs [71, 215, 216]. SMC rings can be assembled to a vascular graft tube with the option to incorporate microspheres or microbeads to allow supplementation with drugs or growth factors [83, 217]. Moreover, these constructs provide optimal features to be applied for ex vivo drug testing and disease modeling. Raman spectroscopic measurements were performed on rings formed by primary human vascular SMCs in order to non-invasively analyze the tissue structures. First, SMC rings that were cultured under different conditions were compared. The influence of quiescence and growth medium and TGF-β supplementation on ECM remodeling was investigated. Raman data were acquired from three different groups of rings constructed out of passage 7 HCASMCs that were cultured for 14 days. The SMC rings were cultured in i) growth medium (GM), ii) quiescence medium (QM) or iii) GM supplemented with TGF β (GM+TGFβ). Raman imaging and TCA identified and localized nuclei as wells as two further components (Marzi et al., **Appendix IV**, Figure 6A). Peaks related to DNA could define the nuclei structures, that were detected in one of the TCA components. The second component contained peaks referring to contractile proteins [218, 219] and the third component identified by TCA, showed peak assignments related to a dissolved and dried aggrecan proteoglycan reference (Marzi et al., **Appendix IV**, Figure 6B) and to peaks reported before in proteoglycans and glycosaminoglycans [220]. Structures related to the Raman signature of contractile proteins showed a strong deposition in QM-cultured rings and a modest deposition in GM-cultured rings. TGFβ supplementation to GM increased the expression of the contractile proteins, as observed before in SMC culture and other cell types [75, 217, 221]. The proteoglycan component was distinctively expressed in rings in GM culture, TGFβ supplementation did not induce a significant alteration in

the expression pattern. SMC rings cultured in QM only showed minor proteoglycan deposition. Proteoglycans seemed to play an important role in vascular SMC-derived ECM expression. These findings were confirmed by the results of previous studies that reported higher expression of lipoprotein-binding proteoglycans in proliferative vascular SMCs compared to quiescent SMCs [222] and the relevance of proteoglycans (hyaluronan and versican) for vascular SMC migration and proliferation [223]. Suna et al described the impact of aggrecan in ECM remodeling in vasculature and reported aggrecan gene expression specifically in vascular SMCs, whereas vascular endothelial cells lacked aggrecan expressing genes [224]. Moreover, extensive aggrecan and versican deposition have been reported in aortic aneurysm tissue [225].

A PCA was performed on single point measurements of the rings structures for detailed analysis of spectral differences and to search for specific Raman fingerprints, identifying the SMC rings of QM, GM and GM+TGF culture conditions. A distinct clustering for each culture condition was demonstrated (Marzi et al., **Appendix IV**, Figure 6C). While PC3 allowed for a significant separation between each group, PC 5 allowed for a separation of the rings cultured in QM from the rings cultured in GM (Marzi et al., **Appendix IV**, Figure 6D). PC3 indicated differences in amino acids and amides in proteins. PC5 explained alterations in collagen. In addition, PC3 and PC5 both showed a proteoglycan specific peak at 1008 cm^{-1} in the positive range of their loadings plots. GM and GM+TGF data were mainly described by positive PC3 values and GM data as well by positive PC5 data, indicating higher proteoglycan levels in tissue samples of those culture conditions (Marzi et al., **Appendix IV**, Figure 6E). PCA results of ECM protein expression in the differently cultured rings correlated to the Raman imaging data. Raman imaging and single spectrum acquisition results lead to the conclusion that GM induced an increased matrix production, while QM helped to maintain the SMCs contractile phenotype with little ECM remodeling and proteoglycan expression. Combination of GM and TGFβ supported both, a stable matrix and synthesis of functional, contractile proteins. These culture conditions were found to be ideal to form a tissue ring that develops intact ECM structures which are necessary to sustain the physiological demands of a native vessel. Tissue-engineered rings grown in medium with TGFβ supplementation or incorporated with gelatin beads containing TGFβ have already been shown to comply with the biomechanical properties of native tissue [217].

In addition, tissue rings formed by HAoSMCs were compared to native aortic tissue to identify molecular and structural differences or similarities between native tissue

and the tissue-engineering approach. While smooth muscle tissues of different anatomical origins differed in their Raman information no significant difference was detectable between HAoSMC rings and aortic tissue. Except for PC1 that indicated a difference in the baseline of the Raman spectra, similarities in the spectral assignment of native aorta and tissue-engineered HAoSMC rings were described by the PCA (Marzi et al., **Appendix IV**, Figure 8G). The tissue-engineered constructs resembled the molecular Raman fingerprint of the corresponding native aortic tissue, leading to the conclusion that the applied protocol to form and culture SMC rings led to a tissue-engineered graft with matrix structures comparable to those of native human aorta. In addition to the successful characterization of the tissue-engineered SMC rings, the results demonstrated the potential of Raman imaging and microspectroscopy as quality control tool in TE.

Chapter 6

General Discussion & Outlook

6 General Discussion & Outlook

6.1 Quality Assessment in Cardiovascular Cells and Tissues

Raman microspectroscopy combined with MVA was established for diverse applications in the analysis of cardiovascular implant materials. The assessment of ECM changes on a molecular level, the discrimination of SMCs of different tissue origin and phenotype, the monitoring of ECM remodeling in tissue-engineered vascular SMC rings as well as successful interstitial quantification of cytotoxic chemicals were demonstrated. Raman analysis provided relevant additional information compared to standard techniques and is an easy, accessible technique for diverse sample conditions. Little sample preparation and no destructive labeling is required.

Compared to previous preclinical and mid-term studies on cryopreserved heart valve leaflets [15, 50, 55] that only applied multiphoton imaging and standard histochemistry techniques, Raman microspectroscopy provided additional input on the character of the cryopreservation-induced structural ECM damages, which was not previously accessible. It was shown that FC-induced deterioration, but no degradation of the collagen fibers in ovine pulmonary leaflets. In contrary, collagen degradation was reported in FC porcine tissues. Raman measurements of ovine and porcine control tissues led to the hypothesis that ovine and porcine tissues show minor alterations in their ECM composition that cause a different sensitivity to cryopreservation. Whereas for the assessment of SMCs several cellular and tissue components were compared, the heart valve study mainly focused on collagen structures. However, Raman microspectroscopy has also been shown to assess lipids, proteins and GAGs as demonstrated in a study that quantified the influence of two different decellularization procedures on aortic implants [226]. Moreover, Raman spectroscopy was not only applicable to non-invasively monitor and quantify CPAs in supernatants and tissues, which so far was only demonstrated by NIR spectroscopy [183], but supported the evaluation of the underlying mechanism of CPA action.

Many attempts in heart valve and vascular TE failed in preclinics or clinics [17, 68]. There is an urgent need in cardiovascular tissue-engineering to assess detailed preclinical information. The results of this study showed the sensitivity of Raman techniques to detect mechanically and immunologically induced structural ECM changes. Moreover, another study reported a Raman signature for the prediction of cardiac allograft rejection [227]. In addition to the analysis of allografts and xenografts, as performed in this work,

Raman microspectroscopy and imaging would be of further interest for the quality assessment in evolving field of tissue-engineered heart valves. The comparison of newly formed tissue structures within native tissues or the characterization of implanted biomaterials itself, but also the monitoring of the degradation of the biomaterials and cell-biomaterial interactions are promising future applications. Furthermore, this approach could equally be applied for the real-time monitoring of tissue-engineered heart valves or vascular grafts in bioreactors as it has been applied for cell culture before [228]. In addition to the potential application in bioreactors, Raman spectroscopy provides the ideal properties for non-invasive monitoring in microfluidic systems. Microfluidic systems, so-called organ-on-a-chip models, recapitulate the microstructure and function of living organs and would allow for animal-free drug testing. Cardiovascular organ-on-a-chip approaches such as 'heart-on-a-chip' or setups with iPSC-derived cardiomyocytes [229, 230] would benefit from a marker-free in situ monitoring tool as it could be shown for the assessment of glucose stimulation in a pancreas-on-a-chip model (Zbinden, Marzi et al., in preparation).

However, prior to pre-implant control and in situ monitoring of tissue-engineered grafts it is of major importance to characterize and identify the applied cells, especially if stem cell-derived cells are utilized. An enhanced molecular understanding of SMC biology could facilitate the design of more potent cell-based biomaterials and regulate SMC differentiation behavior in vascular TE [77]. SMC analysis was based on the acquisition of one specific Raman fingerprint per cell defining the overall cellular composition and enabling fast identification and discrimination by PCA. According to the Raman fingerprint it was possible to distinguish phenotypic switching in SMCs, which is a widely investigated phenomenon in SMCs [75, 202, 204], but has never been reported to be assessed non-destructively and label-free. Moreover, a marker-independent separation of SMCs of different smooth muscle tissue origins was demonstrated. A significant difference was shown between vascular and non-vascular SMCs, but also SMCs of aorta, coronary artery and pulmonary artery showed differences in their overall cellular composition. Inter-populational differences between different tissue origins had a higher relevance than intra-populational heterogeneity within one passage of SMCs. In contrary to the conclusion by Huber et al. [231] who stated that SMC origin plays a negligible role in TE, the results indicated a relevance for the selection of passage as well as SMC origin for tissue-engineering approaches. Previously, only few studies compared SMCs of different origins and except for one study by Gabbiani et al only vascular and non-

vascular cells were compared [198]. For detailed mechanistic investigations and the specific assessment of defined cellular proteins, Raman instrumentation and data analysis might still need further development and are not superior to the selectivity of established techniques such as immunofluorescence labeling or gene expression analysis. It is essential to harmonize and normalize Raman applications for a successful introduction in standardized cell culture screening or Raman activated cell sorting (RACS) [232, 233] or clinical applications. Nevertheless, these results are a promising indicator towards establishing Raman microspectroscopy as non-destructive quality control tool in cell-based TE approaches for real-time monitoring of the material formation as well as for the preselection and characterization of the applied cells.

6.2 Data Assessment in Multiphoton Microscopy and Raman Microspectroscopy

Similar to Raman microspectroscopy, multiphoton imaging can be applied label-free, is non-invasive and does not require complex sample preparation. In contrast, it is only accessible to a limited number of endogenous fluorescent or SHG-active molecules, otherwise it has to be applied in combination with immunofluorescent dyes [234]. Due to the rare event of Raman scattering in only 1 of 10^7, multiphoton imaging is more efficient and requires shorter acquisition times than spontaneous Raman scattering imaging. Multiphoton images allowed for the fast assessment of qualitative characteristics of collagen and elastic fibers, such as localization, distribution and appearance of fiber structures. In addition, it has been shown that also paraffin-embedded and fixed smooth muscle tissues provided multiphoton collagen signals, as demonstrated before for fixed skin and heart valve tissue [235]. This study showed that multiphoton microscopy is well-suited for fast, non-invasive assessment of the influence of biomechanical stress on heart valve leaflet ECM structures as it has been reported previously for coronary artery microstructure [236]. However, more detailed analysis is not possible in multiphoton microscopy. In particular, deterioration in FC leaflet collagen structures were visualized and could be qualified according to crimp structure properties, but detailed information on molecular changes induced by the cryopreservation method were only accessible by Raman microspectroscopic measurements. Moreover, in multiphoton imaging no differences were detected between allogeneic and xenogeneic ECM structures, except for the infiltrating cells, whereas Raman microspectroscopy revealed inflammation-dependent structural differences. The same outcome applied accordingly for collagen detection in smooth muscle tissues. A determination of collagen quantities in different smooth muscle tissues was possible. However, no further differences could be defined by qualitative multiphoton imaging. Quantitative multiphoton approaches combined with MVA or the calculation of signal ratios and the combination of SHG and TPEF imaging [237] might allow for a more detailed data output. A further approach would be fluorescence lifetime imaging (FLIM). FLIM is based quantification and has recently been reported to allow for the determination of collagen/elastin ratios in vascular grafts and biochemical imaging of coronary arteries and atherosclerotic plaques [238-241].

While Raman imaging assesses the molecular information by acquiring a broadband spectrum in every single pixel and therefore requires more time to achieve a res-

olution enabling imaging of defined structures, multiphoton imaging allowed for fast label-free imaging of defined structures, comparable to coherent anti-Stokes Raman scattering microscopy (CARS) at a defined Raman shift wavenumber. In the future, multimodal imaging with a combination of multiphoton microscopy and Raman microspectroscopy would represent an advanced analysis tool for cardiovascular ECM structures. Recent studies already reported the combination of Raman and multiphoton imaging in investigations on skin and liver tissue [242, 243] and as pathological tool for the detection of skin melanoma [244].

6.3 Standard Techniques and Raman Spectroscopy for Characterization of ECM Structures and Cells

A major challenge in characterization of biomaterial or replacement tissue is the quantification of the properties compared to physiological or biomechanical properties of the native tissue [87]. The establishment of in vitro test systems that can access information on cell-biomaterial interaction, cellular processes and biocompatibility is still evolving regarding relevance to in vivo testing, cost-efficiency and reliability [245]. The results of this thesis showed that Raman microscopy and imaging could provide many of the required features for quality assessment in cardiovascular research that are still missing in standard techniques such as immunofluorescence microscopy, standard histochemistry or gene and protein expression assays.

Raman spectroscopy is highly precise and detects differences in molecular composition of ECM structures. Standard histochemical staining performed on smooth muscle tissues and in the heart valve long-term study was time-consuming, could not be performed on fresh tissues and only confirmed the results of previous studies [50, 55]. However, Raman microspectroscopy and MVA as well as the analysis of crimp structures by multiphoton imaging, provided quantitative as well as qualitative input on the remodeling and degeneration of FC heart valve leaflets on a molecular level that have not been shown before by any other method. Furthermore, PCA allowed for a fast classification of the state of ECM integrity in cryopreserved heart valve tissues or of the ECM composition in smooth muscle tissues. Schenke-Layland et al. applied Movat-Pentachrome staining, immunofluorescence labeling and multiphoton microscopy in a study comparing decellularized tissue-engineered heart valve leaflets with native ovine aortic and porcine pulmonary leaflets [154]. They demonstrated comparable ECM structures in tissue-engineered and native tissues and no remarkable difference between the two native tissues. In comparison, this study showed that Raman spectroscopy could identify minor structural differences in native ovine and porcine pulmonary leaflets that might be relevant for the different response of porcine and ovine tissues to the IFC and FC cryopreservation procedures.

Characterization and in situ monitoring of tissue growth in cell culture is also one of the issues in TE where no completely satisfying method has been developed so far [245]. Thus, Raman imaging and PCA demonstrated fast, non-invasive monitoring and characterization of ECM remodeling in tissue-engineered SMC rings of different culture

conditions and could confirm a similar matrix composition in the tissue-engineered constructs and native vessels without processing or destructing them.

Current methods for the assessment of cell function and gene expression like ELISA, ICC or PCR, are time consuming, destructive and inefficient [246]. The acquisition of the Raman fingerprint of SMCs was more efficient than ICC and qPCR on known phenotype markers. PCA demonstrated a significant discrimination of SMCs of different tissue origins, helped to monitor phenotypic switching and could be performed in situ. Furthermore, Raman Spectroscopy has been shown to be one of the few techniques that enabled the monitoring of cell cycle, differentiation, mineralization or metabolism in real time and without destructing the cells [247-249]. There exist several other imaging techniques, mainly applied in medical imaging, that are non-invasive and allow for 3D reconstruction of tissue structures [250-252]. However, optical coherence tomography, micro x-ray, computer tomography or magnetic resonance imaging are limited in their resolution and molecular sensitivity. Superior characteristics and analytical possibilities shown in this thesis, enable the application of Raman spectroscopy in cardiovascular bioprocess monitoring and quality control, which are important for end product design [87].

Nevertheless, spontaneous Raman scattering provides a relatively weak signal [89]. Especially low scattering molecules, such as biomolecules in a tissue environment, result in longer acquisition times and high laser powers than isolated molecules or molecules with high scattering vibrational states [253]. Therefore, principles to enhance the Raman scattering and reduce interferences were established. CARS is based on the stimulation of an anti-Stokes Raman scattering induced by two lasers of the same frequency. A strong, enhanced signal is generated, if the merged frequencies of the two lasers correspond to the frequency of the vibration of the Raman active molecule [254-256]. In general, this approach only considers the assessment of a defined spectral bandwidth, such as the CH-/OH- stretch region between 2700-3000 cm^{-1} [257], however new multiplex, broadband CARS systems have been developed [258, 259]. Another technology to access strong Raman spectra is surface-enhanced Raman spectroscopy (SERS). SERS provides up to 10^{11} fold increased signal intensities by signal-enhancing nanostructured surfaces [260, 261], first described for silver electrodes [262]. An adaption of SERS is tip-enhanced Raman spectroscopy, applying a metallic tip similar to the principle of atomic force microscopy [263]. Additionally, structures can be tagged with nanoparticles or CNTs that provide stronger Raman signals [264, 265]. In previous work, stimulated

Raman or CARS were applied to image SMCs [266, 267]. The peak near 2845 cm^{-1} is especially sensitive for lipids and often applied to image tissues or cells based on the intrinsic lipid contrast. These studies identified SMCs in a tissue or scaffold environment, but no detailed SMC subcellular structures were analyzed. Although CARS and SERS provide increased Raman signals, they are more complex in technical setup, sample preparation, and broadband application. Thus, the work included in this thesis predominantly focused on spontaneous Raman scattering techniques.

CARS and SERS provide advantages in sensitivity and acquisition time and should be considered in future approaches for analysis of cardiovascular cells and tissues. CARS might play an important role in real-time quality assessment. Once characteristic Raman shift ranges for a SMC phenotype or ECM deterioration are defined, CARS could be applied in the defined area for fast, routine imaging and discrimination in cardiovascular quality control. SERS enables enhanced signal intensities and higher spatial resolution and thus is relevant for the acquisition of singular structures in heterogeneously composed tissues or cells, described before in cancer tissues as immuno-SERS microscopy that can be performed on native tissues or Raman-actively labeled antigens [268, 269]. Another method of tracking is the application of CNT labeling. This method could be utilized to track cell metabolism or tissue-engineered grafts after implantation and can also be applied in in vivo approaches [131, 270].

6.4 Biochemical Raman Fingerprint and Reference Spectra

The Raman spectral fingerprint presents an overview of a sample and is not necessarily linked to only one defined structure, if not measuring an isolated substance but a cell or tissue. Due to the heterogeneously distributed structures in tissues and cells and the spatial resolution of about 1 µm in diameter, a Raman spectrum can be assigned to several structures such as proteins or lipids.

Single point measurement spectra and information defined by PCA can be evaluated according to reported peaks found in literature. Whereas there exist precise data bases of detailed molecular vibrations in small molecules [271], there is limited availability of reliable reference databases in biological molecules. There exist reviews that summarize peaks found in different studies on biological tissues and cells [272] and De Gelder et al measured various reference spectra of cellular molecules such as DNA, defined amino acids, fatty acids and saccharides and metabolites [273]. Single point measurements can aim for the analysis of a defined structure, but in quality assessment applications the overall fingerprint that provides a characteristic assignment for every cell or tissue structure is of major interest. The fingerprint does not define a single isolated molecule, but represents the general composition of the target and enables fast discrimination of different samples, as it was shown in this work for different SMCs.

However, in image analysis, due to the large number of different spectra, reference spectra can be beneficial to identify and localize certain structures within the matrix of many different assignments. The limiting factor in reference spectrum acquisition is not only the extreme diversity of cellular and extracellular molecules, but also the sensitivity of Raman microspectroscopy to structural alterations [274, 275]. An isolated, lyophilized commercially available protein can have another structural constitution than the same protein in a tissue, resulting in minor spectral differences [127]. Thus, the measurement of lyophilized, isolated molecules as reference standard might not be precise enough because Raman spectra of biological molecules of a similar structure only differ marginally. For example, the Raman spectra of different collagen types (Figure 14), measured as lyophilized reference substances, indicated spectral differences mainly in different peak ratios, peak intensities or peak shifts and barely in the presence or absence of a peak. Therefore, there is a need for a systemic evaluation of the variables influencing a possible reference substance. The most reliable, however time-consuming, option to establish a biomolecule database would be Raman measurements by targeting an immunofluorescence-labeled molecule in its native surrounding.

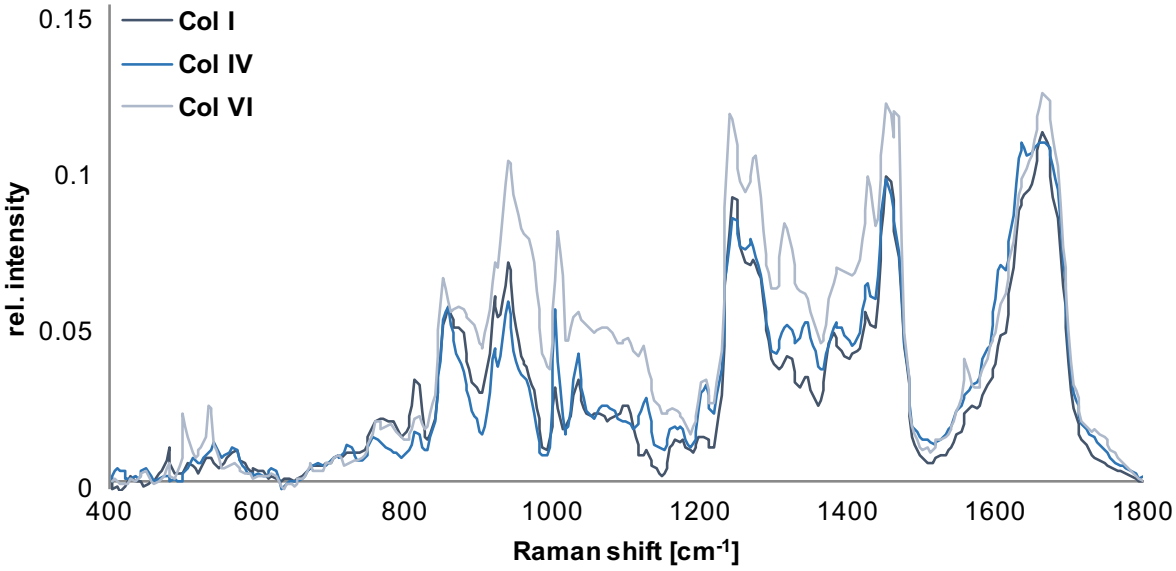

Figure 14. Raman spectra of different collagen types.

Depending on the experimental setup and hypothesis it should be considered whether a Raman fingerprint is sufficient or if reference spectra of defined molecules have to be obtained for the analysis. Whereas the Raman fingerprint is ideal for the characterization of spectral alterations and the separation of data sets or identification of a data point, as applied in MVA tools, deeper mechanistic or structural analyses and especially Raman image analysis would extremely benefit from a database of defined biomolecules. Previous studies reported TCA or Raman data analysis of cardiovascular tissues in combination with linear combination of basis spectra [218, 219, 276]. However, only a limited number of reference spectra was investigated and the acquisition of reference spectra was always a precondition of the study. In future work, a major goal should be the establishment of an accessible and standardized ECM reference database for cardiovascular and other tissue ECM characterization which allows for in-depth analysis and reliable identification of small molecules. A database would circumvent the analysis of unknown components determined by TCA by identification and fitting of defined reference spectra.

6.5 Single Spectrum Acquisition Versus Raman Imaging

Raman imaging and single point Raman measurements were applied for the analysis of SMCs and smooth muscle tissues as well as for the quantification of interstitial DMSO, PG and FMD concentrations. The choice of the method depended on the scientific question that should be addressed. Single point measurements allowed to preselect a defined structure and generate a Raman fingerprint that enables in-depth molecular characterization of the structure. However, reliable targeting is only possible if the region of interest is a clearly microscopically detectable structure or cell or if the data acquisition is combined with immunofluorescence labeling [97]. Raman imaging is more time-consuming, but enabled to access all the spectral information within a defined area. Furthermore, low-resolution imaging allows for fast monitoring of the distribution of strong scattering chemicals in weak scattering tissues. Large data sets are created that enable various analyses. Simple image generation by filter settings and intensity heat maps allow a fast, label-free visualization of higher scattering structures.

For in-depth analysis and the identification of the major spectral components in spectral maps, TCA, PCA or cluster analysis can be applied. In contrary to PCA, components defined by TCA depend on the number of selected components and only describe an approximation of the defined spectral information. Spectra identified in a component may vary from the actual spectral assignment to a certain degree. Thus, for some SMC types only noisy images could be achieved when employing the spectral components defined in HAoSMC as reference spectra in the analysis. Proteins, lipids, membrane lipids and DNA were identified as main components in the aortic SMCs. The nuclear component was found in all cells, regardless of tissue origin. However, for the protein and lipid structures, especially of the non-vascular cells, the reference spectrum of hAoSMC did not perfectly fit to image these structures in the other cells. An independent analysis showed a better fit to the cellular structures than the fitting with the HAoSMC reference spectra (Figure 15). HTSMC and HUtSMC were less noisy in the independent TCA (Figure 15 B, D) than in the TCA with the HAoSMC reference spectra (Figure 15 A, C). Comparison of the identified spectra with the HAoSMC spectra indicated slight differences in the lipid composition in HAoSMCs and HUtSMCs (Figure 15 E) and differences in protein composition in HAoSMCs, HUtSMC and HTSMCs (Figure 15 F). This implied not only a different distribution and quantity of lipids and proteins in the cells, but also a different composition of those molecular structures.

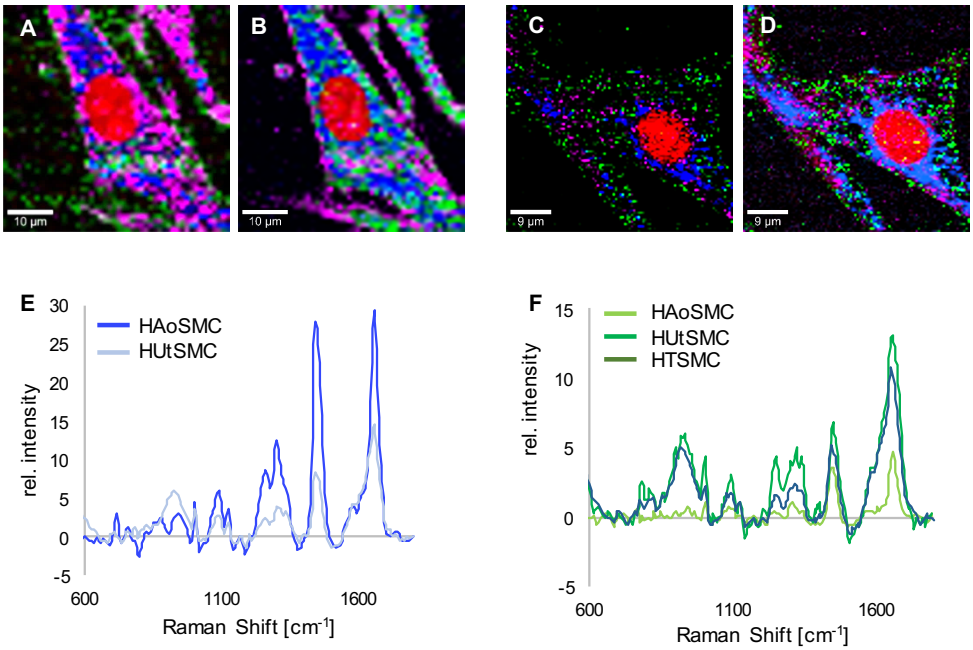

Figure 15. TCA of HSMCs. Independent TCA **(B, D)** on HTSMCs **(A, B)** and HUtSMCs **(C, D)** revealed precise imaging compared to the TCA with the identified spectra for proteins, lipids, phospholipids and nuclei in HAoSMCs **(A, C).** Comparison of the TCA components, described differences in the lipid spectrum of HAoSMCs and HUtSMCs **(E)** and differences in the protein spectrum between HAoSMCs, HTSMCs and HUtSMCs **(F).**

Moreover, also complex MVA can be performed on preselected, extracted regions of interest defined by TCA to determine minor structural differences within one of the structural components in the image. This would be comparable to MVA of single point measurements and was shown for the analysis of lipid composition before and after glucose stimulation in a pancreas-on-a-chip model (Zbinden, Marzi et al., in preparation) or the characterization of molecular changes in elastic and collagen fibers in the aortas of different murine genotypes (Sugiyama, Marzi et al., in preparation).

The choice regarding whether detailed molecular information of a certain structure is required or an overview image of a defined area with different structures is of major interest should be carefully considered. Single point Raman measurements allow for the fast assessment of the Raman fingerprint of a cell or tissue structure that enables detailed molecular characterization and would be sufficient information for a possible application for cell sorting. In contrary, Raman imaging allows the label-free image generation of a tissue or cell area and demonstrates the localization and quantitative distribution of several tissue or cell structures simultaneously.

6.6 Conclusion

In situ monitoring and characterization of cellular properties or cell-material interactions represents a major obstacle in the constantly evolving field of TE. This study reported the establishment of Raman microspectroscopy and Raman imaging combined with MVA tools for the quality assessment of tissues and cells applied in cardiovascular TE. It was successfully demonstrated, that Raman microspectroscopy allowed to identify cryopreservation-induced ECM changes in heart valve leaflets and to monitor and quantify CPAs in cardiac tissues. Moreover, SMCs of different tissue origins and phenotype were discriminated and classified by MVA according to their Raman fingerprint. Similarly, the matrix development in dependence of the culture medium could be monitored in tissue-engineered vascular SMC grafts by Raman imaging. In comparison to standard techniques such as gene and protein expression analyses, major advantages of the Raman techniques were the marker-independence, non-invasiveness and sensitivity on a molecular level, which allowed for real-time and in situ characterization and quantification. Single point Raman measurements combined with PCA were shown to be the preferred technique for a fast assessment of a characteristic Raman fingerprint that allows to discriminate and identify variable samples or cells and to analyze minor spectral differences in detail. Raman imaging enabled the marker-independent and simultaneous visualization of distinct cell, tissue or biomaterial structures and should be favored for descriptive studies of structural distributions patterns of different molecules. In addition, Raman imaging was highly efficient to study permeation kinetics in tissues. The results demonstrated the benefits of Raman techniques, that addressed the analytical needs in cardiovascular TE. Raman microspectroscopy and imaging are of great potential for future applications such as cell-sorting or in situ monitoring of various metabolic or developmental processes. Furthermore, the results encourage the application of Raman microspectroscopy as quality control tool for tissue-engineered grafts. Non-destructive discrimination of different cells or tissues by MVA and the Raman fingerprint is already advanced. In the future, more effort still needs to be dedicated to the establishment of Raman microspectroscopy for the characterization and identification of single molecules in complex biological samples. Whereas identification and monitoring of drugs and chemicals is well-established and applied in industry, Raman analysis of biomolecules lacks a comprehensive, reliable and standardized data base of references, that would facilitate the identification of a broader range of specific molecules.

References

1. Beckmann A, Funkat A-K, Lewandowski J, Frie M, Ernst M, Hekmat K, Schiller W, Gummert JF and Harringer W. German heart surgery report 2016: the annual updated registry of the German Society for Thoracic and Cardiovascular Surgery. *The Thoracic and cardiovascular surgeon*. 2017;65:505-518.
2. Group AW, Timmis A, Townsend N, Gale C, Grobbee R, Maniadakis N, Flather M, Wilkins E, Wright L and Vos R. European Society of Cardiology: cardiovascular disease statistics 2017. *European heart journal*. 2017;39:508-579.
3. Aikawa E and Schoen FJ. Calcific and degenerative heart valve disease *Cellular and Molecular Pathobiology of Cardiovascular Disease*: Elsevier; 2014: 161-180.
4. Yacoub M and Takkenberg J. Will heart valve tissue engineering change the world? *Nature Reviews Cardiology*. 2005;2:60.
5. Hanson MA, Fareed MT, Argenio SL, Agunwamba AO and Hanson TR. Coronary artery disease. *Primary Care: Clinics in Office Practice*. 2013;40:1-16.
6. Conte SM and Vale PR. Peripheral arterial disease. *Heart, Lung and Circulation*. 2017.
7. Harken DE, Taylor WJ, Lefemine AA, Lunzer S, Low HB, Cohen ML and Jacobey JA. Aortic valve replacement with a gaged ball valve. *American Journal of Cardiology*. 1962;9:292-299.
8. Tuna IC, Orszulak TA, Schaff HV and Danielson GK. Results of homograft aortic valve replacement for active endocarditis. *The Annals of thoracic surgery*. 1990;49:619-624.
9. O'brien M, Stafford E, Gardner M, Pohlner P and McGiffin D. A comparison of aortic valve replacement with viable cryopreserved and fresh allograft valves, with a note on chromosomal studies. *The Journal of thoracic and cardiovascular surgery*. 1987;94:812-823.
10. Baumgartner H, Falk V, Bax JJ, De Bonis M, Hamm C, Holm PJ, Iung B, Lancellotti P, Lansac E, Rodriguez Muñoz D, Rosenhek R, Sjögren J, Tornos Mas P, Vahanian A, Walther T, Wendler O, Windecker S, Zamorano JL and Group ESCSD. 2017 ESC/EACTS Guidelines for the management of valvular heart disease. *European Heart Journal*. 2017;38:2739-2791.
11. Hammermeister KE, Sethi GK, Henderson WG, Oprian C, Kim T and Rahimtoola S. A comparison of outcomes in men 11 years after heart-valve replacement with a mechanical valve or bioprosthesis. *New England Journal of Medicine*. 1993;328:1289-1296.
12. Dabbous MK, Sakr FR and Malaeb DN. Anticoagulant therapy in pediatrics. *Journal of basic and clinical pharmacy*. 2014;5:27.
13. Nishimura RA and Warnes CA. Anticoagulation during pregnancy in women with prosthetic valves: evidence, guidelines and unanswered questions. *Heart*. 2015:heartjnl-2014-306500.
14. Barnhart GR, Jones M, Ishihara T, Rose D, Chavez A and Ferrans V. Degeneration and calcification of bioprosthetic cardiac valves. Bioprosthetic tricuspid valve implantation in sheep. *The American journal of pathology*. 1982;106:136.
15. Brockbank K, Lightfoot F, Song YC and Taylor M. Interstitial ice formation in cryopreserved homografts: a possible cause of tissue deterioration and calcification in vivo. *The Journal of heart valve disease*. 2000;9:200-206.
16. Ikada Y. *Tissue engineering: fundamentals and applications*: Elsevier; 2011.
17. Fioretta ES, Dijkman PE, Emmert MY and Hoerstrup SP. The future of heart valve replacement: recent developments and translational challenges for heart valve tissue engineering. *Journal of tissue engineering and regenerative medicine*. 2018;12:e323-e335.
18. Gross L and Kugel M. Topographic anatomy and histology of the valves in the human heart. *The American journal of pathology*. 1931;7:445.
19. Schoen FJ. Evolving concepts of cardiac valve dynamics: the continuum of development, functional structure, pathobiology, and tissue engineering. *Circulation*. 2008;118:1864-1880.
20. Schoen FJ and Levy RJ. Tissue heart valves: current challenges and future research perspectives. *Journal of Biomedical Materials Research: An Official Journal of The Society for Biomaterials, The Japanese Society for Biomaterials, and The Australian Society for Biomaterials and the Korean Society for Biomaterials*. 1999;47:439-465.
21. Bailey AJ, Paul RG and Knott L. Mechanisms of maturation and ageing of collagen. *Mechanisms of ageing and development*. 1998;106:1-56.
22. Balguid A, Rubbens MP, Mol A, Bank RA, Bogers AJ, Van Kats JP, De Mol BA, Baaijens FP and Bouten CV. The role of collagen cross-links in biomechanical behavior of human aortic heart valve leaflets—relevance for tissue engineering. *Tissue engineering*. 2007;13:1501-1511.
23. Paul RG and Bailey AJ. Chemical stabilisation of collagen as a biomimetic. *The Scientific World Journal*. 2003;3:138-155.

24. Rabkin E, Aikawa M, Stone JR, Fukumoto Y, Libby P and Schoen FJ. Activated interstitial myofibroblasts express catabolic enzymes and mediate matrix remodeling in myxomatous heart valves. *Circulation*. 2001;104:2525-2532.
25. Weber KT, Sun Y, Tyagi SC and Cleutjens JP. Collagen network of the myocardium: function, structural remodeling and regulatory mechanisms. *Journal of molecular and cellular cardiology*. 1994;26:279-292.
26. Vesely I. The role of elastin in aortic valve mechanics. *Journal of biomechanics*. 1997;31:115-123.
27. Stephens EH, Chu C-K and Grande-Allen KJ. Valve proteoglycan content and glycosaminoglycan fine structure are unique to microstructure, mechanical load and age: Relevance to an age-specific tissue-engineered heart valve. *Acta Biomaterialia*. 2008;4:1148-1160.
28. Angel PM, Nusinow D, Brown CB, Violette K, Barnett JV, Zhang B, Baldwin HS and Caprioli RM. Networked-based characterization of extracellular matrix proteins from adult mouse pulmonary and aortic valves. *Journal of proteome research*. 2010;10:812-823.
29. Hinton Jr RB, Lincoln J, Deutsch GH, Osinska H, Manning PB, Benson DW and Yutzey KE. Extracellular matrix remodeling and organization in developing and diseased aortic valves. *Circulation research*. 2006;98:1431-1438.
30. Rabkin-Aikawa E, Farber M, Aikawa M and Schoen FJ. Dynamic and reversible changes of interstitial cell phenotype during remodeling of cardiac valves. *Journal of Heart Valve Disease*. 2004;13:841-847.
31. Liu AC, Joag VR and Gotlieb AI. The emerging role of valve interstitial cell phenotypes in regulating heart valve pathobiology. *The American journal of pathology*. 2007;171:1407-1418.
32. Cebotari S, Tudorache I, Ciubotaru A, Boethig D, Sarikouch S, Goerler A, Lichtenberg A, Cheptanaru E, Barnaciuc S and Cazacu A. Use of fresh decellularized allografts for pulmonary valve replacement may reduce the reoperation rate in children and young adults: early report. *Circulation*. 2011;124:S115-S123.
33. Hopkins RA, Bert AA, Hilbert SL, Quinn RW, Brasky KM, Drake WB and Lofland GK. Bioengineered human and allogeneic pulmonary valve conduits chronically implanted orthotopically in baboons: hemodynamic performance and immunologic consequences. *The Journal of thoracic and cardiovascular surgery*. 2013;145:1098-1107. e3.
34. Rüffer A, Purbojo A, Cicha I, Glöckler M, Potapov S, Dittrich S and Cesnjevar RA. Early failure of xenogenous de-cellularised pulmonary valve conduits—a word of caution! *European Journal of Cardio-thoracic Surgery*. 2010;38:78-85.
35. Schoen FJ. Morphology, clinicopathologic correlations, and mechanisms in heart valve health and disease. *Cardiovascular engineering and technology*. 2018;9:126-140.
36. Macfarlane DR and Forsyth M. Recent insights on the role of cryoprotective agents in vitrification. *Cryobiology*. 1990;27:345-358.
37. Meryman H. Cryoprotective agents. *Cryobiology*. 1971;8:173-183.
38. Brockbank KG. Cryoprotective agent and its use in cryopreservation of cellular matter. 1991.
39. Fuller BJ. Cryoprotectants: the essential antifreezes to protect life in the frozen state. *CryoLetters*. 2004;25:375-388.
40. Mazur P. Cryobiology: the freezing of biological systems. *Science*. 1970;168:939-949.
41. Brockbank KG, Chen Z, Greene ED and Campbell LH. Vitrification of heart valve tissues *Cryopreservation and freeze-drying protocols*: Springer; 2015: 399-421.
42. Rall WF and Fahy GM. Ice-free cryopreservation of mouse embryos at− 196 C by vitrification. *Nature*. 1985;313:573.
43. Angell W, Angell J, Oury J, Lamberti J and Grehl T. Long-term follow-up of viable frozen aortic homografts. A viable homograft valve bank. *The Journal of thoracic and cardiovascular surgery*. 1987;93:815-822.
44. O'Brien MF, Stafford G, Gardner M, Pohlner P, McGiffin D, Johnston N, Brosnan A and Duffy P. The viable cryopreserved allograft aortic valve. *Journal of cardiac surgery*. 1987;2:153-167.
45. Kirklin J, Smith D, Novick W, Naftel D, Kirklin J, Pacifico A, Nanda N, Helmcke F and Bourge R. Long-term function of cryopreserved aortic homografts. A ten-year study. *The Journal of thoracic and cardiovascular surgery*. 1993;106:154-65; discussion 165-6.
46. Rajani B, Mee RB and Ratliff NB. Evidence for rejection of homograft cardiac valves in infants. *The Journal of thoracic and cardiovascular surgery*. 1998;115:111-117.
47. Clarke D, Campbell D, Hayward A and Bishop D. Degeneration of aortic valve allografts in young recipients. *The Journal of thoracic and cardiovascular surgery*. 1993;105:934-41; discussion 941-2.

48. Ruel M, Chan V, Bédard P, Kulik A, Ressler L, Lam BK, Rubens FD, Goldstein W, Hendry PJ and Masters RG. Very long-term survival implications of heart valve replacement with tissue versus mechanical prostheses in adults< 60 years of age. *Circulation*. 2007;116:I-294-I-300.
49. Mitchell RN, Jonas RA and Schoen FJ. Pathology Of Explanted Cryopreserved Allograft Heart Valves: Comparison With Aortic Valves From Orthotopic Heart Transplants. *The Journal of Thoracic and Cardiovascular Surgery*. 1998;115:118-127.
50. Schenke-Layland K, Madershahian N, Riemann I, Starcher B, Halbhuber K-J, König K and Stock UA. Impact of Cryopreservation on Extracellular Matrix Structures of Heart Valve Leaflets. *The Annals of Thoracic Surgery*. 81:918-926.
51. Simon P, Kasimir M, Seebacher G, Weigel G, Ullrich R, Salzer-Muhar U, Rieder E and Wolner E. Early failure of the tissue engineered porcine heart valve SYNERGRAFT® in pediatric patients. *European journal of cardio-thoracic surgery*. 2003;23:1002-1006.
52. Schenke-Layland K, Xie J, Heydarkhan-Hagvall S, Hamm-Alvarez SF, Stock UA, Brockbank KG and MacLellan WR. Optimized preservation of extracellular matrix in cardiac tissues: implications for long-term graft durability. *The Annals of thoracic surgery*. 2007;83:1641-1650.
53. Fahy GM, Wowk B, Wu J, Phan J, Rasch C, Chang A and Zendejas E. Cryopreservation of organs by vitrification: perspectives and recent advances. *Cryobiology*. 2004;48:157-178.
54. Huber AJ, Brockbank KG, Aberle T, Schleicher M, Chen ZZ, Greene ED, Lisy M and Stock UA. Development of a simplified ice-free cryopreservation method for heart valves employing VS83, an 83% cryoprotectant formulation. *Biopreservation and biobanking*. 2012;10:479-484.
55. Lisy M, Pennecke J, Brockbank KG, Fritze O, Schleicher M, Schenke-Layland K, Kaulitz R, Riemann I, Weber CN and Braun J. The performance of ice-free cryopreserved heart valve allografts in an orthotopic pulmonary sheep model. *Biomaterials*. 2010;31:5306-5311.
56. Ali M, Kumar S, Bjornstad K and Duran C. The sheep as an animal model for heart valve research. *Cardiovascular Surgery*. 1996;4:543-549.
57. Rashid ST, Salacinski HJ, Hamilton G and Seifalian AM. The use of animal models in developing the discipline of cardiovascular tissue engineering: a review. *Biomaterials*. 2004;25:1627-1637.
58. Elliott GD, Wang S and Fuller BJ. Cryoprotectants: A review of the actions and applications of cryoprotective solutes that modulate cell recovery from ultra-low temperatures. *Cryobiology*. 2017;76:74-91.
59. Best BP. Cryoprotectant toxicity: facts, issues, and questions. *Rejuvenation research*. 2015;18:422-436.
60. Fahy GM. The relevance of cryoprotectant “toxicity” to cryobiology. *Cryobiology*. 1986;23:1-13.
61. Campbell L and Brockbank K. Cryopreservation of porcine aortic heart valve leaflet-derived myofibroblasts. *Biopreservation and biobanking*. 2010;8:211-217.
62. Veith FJ, Gupta SK, Ascer E, White-Flores S, Samson RH, Scher LA, Towne JB, Bernhard VM, Bonier P, Flinn WR, Astelford P, Yao JST and Bergan JJ. Six-year prospective multicenter randomized comparison of autologous saphenous vein and expanded polytetrafluoroethylene grafts in infrainguinal arterial reconstructions. *Journal of Vascular Surgery*. 1986;3:104-114.
63. Cho KR, Kim J-S, Jae-Sung C and Kim K-B. Serial angiographic follow-up of grafts one year and five years after coronary artery bypass surgery. *European journal of cardio-thoracic surgery*. 2006;29:511-516.
64. Motwani JG and Topol EJ. Aortocoronary saphenous vein graft disease: pathogenesis, predisposition, and prevention. *Circulation*. 1998;97:916-931.
65. DE BAKEY ME, Cooley DA, Crawford ES and MORRIS GC. Clinical application of a new flexible knitted Dacron arterial substitute. *AMA archives of surgery*. 1958;77:713-724.
66. Campbell C, Brooks D, Webster M and Bahnson H. The use of expanded microporous polytetrafluoroethylene for limb salvage: a preliminary report. *Surgery*. 1976;79:485-491.
67. Hoenig MR, Campbell GR, Rolfe BE and Campbell JH. Tissue-engineered blood vessels: alternative to autologous grafts? *Arteriosclerosis, thrombosis, and vascular biology*. 2005;25:1128-1134.
68. Benrashid E, McCoy CC, Youngwirth LM, Kim J, Manson RJ, Otto JC and Lawson JH. Tissue engineered vascular grafts: Origins, development, and current strategies for clinical application. *Methods*. 2016;99:13-19.
69. Manson RJ, Unger JM, Ali A, Gage SM and Lawson JH. Tissue-Engineered Vascular Grafts: Autologous Off-the-Shelf Vascular Access? *Seminars in Nephrology*. 2012;32:582-591.
70. Strobel HA, Calamari EL, Alphonse B, Hookway TA and Rolle MW. Fabrication of Custom Agarose Wells for Cell Seeding and Tissue Ring Self-assembly Using 3D-Printed Molds. *Journal of visualized experiments: JoVE*. 2018.

71. Gwyther TA, Hu JZ, Billiar KL and Rolle MW. Directed Cellular Self-Assembly to Fabricate Cell-Derived Tissue Rings for Biomechanical Analysis and Tissue Engineering. *Journal of Visualized Experiments : JoVE*. 2011.
72. Wang Y, Hu J, Jiao J, Liu Z, Zhou Z, Zhao C, Chang L-J, Chen YE, Ma PX and Yang B. Engineering vascular tissue with functional smooth muscle cells derived from human iPS cells and nanofibrous scaffolds. *Biomaterials*. 2014;35:8960-8969.
73. A Strobel H, Dikina A, Levi K, Solorio L, Alsberg E and Rolle M. *Cellular self-assembly with microsphere incorporation for growth factor delivery within engineered vascular tissue rings*; 2016.
74. Metz RP, Patterson JL and Wilson E. Vascular smooth muscle cells: isolation, culture, and characterization *Cardiovascular Development*: Springer; 2012: 169-176.
75. Rensen S, Doevendans P and Van Eys G. Regulation and characteristics of vascular smooth muscle cell phenotypic diversity. *Netherlands Heart Journal*. 2007;15:100-108.
76. Chamley-Campbell JH and Campbell GR. What controls smooth muscle phenotype? *Atherosclerosis*. 1981;40:347-357.
77. Beamish JA, He P, Kottke-Marchant K and Marchant RE. Molecular regulation of contractile smooth muscle cell phenotype: implications for vascular tissue engineering. *Tissue Engineering Part B: Reviews*. 2010;16:467-491.
78. Dahl SL, Kypson AP, Lawson JH, Blum JL, Strader JT, Li Y, Manson RJ, Tente WE, DiBernardo L and Hensley MT. Readily available tissue-engineered vascular grafts. *Science translational medicine*. 2011;3:68ra9-68ra9.
79. McAllister TN, Maruszewski M, Garrido SA, Wystrychowski W, Dusserre N, Marini A, Zagalski K, Fiorillo A, Avila H and Manglano X. Effectiveness of haemodialysis access with an autologous tissue-engineered vascular graft: a multicentre cohort study. *The Lancet*. 2009;373:1440-1446.
80. Wystrychowski W, McAllister TN, Zagalski K, Dusserre N, Cierpka L and L'Heureux N. First human use of an allogeneic tissue-engineered vascular graft for hemodialysis access. *Journal of Vascular Surgery*. 2014;60:1353-1357.
81. Best C, Strouse R, Hor K, Pepper V, Tipton A, Kelly J, Shinoka T and Breuer C. Toward a patient-specific tissue engineered vascular graft. *Journal of Tissue Engineering*. 2018;9:2041731418764709.
82. Chen W, Yang J, Liao W, Zhou J, Zheng J, Wu Y, Li D and Lin Z. In vitro remodeling and structural characterization of degradable polymer scaffold-based tissue-engineered vascular grafts using optical coherence tomography. *Cell and tissue research*. 2017;370:417-426.
83. Dikina AD, Strobel HA, Lai BP, Rolle MW and Alsberg E. Engineered cartilaginous tubes for tracheal tissue replacement via self-assembly and fusion of human mesenchymal stem cell constructs. *Biomaterials*. 2015;52:452-462.
84. Ratner BD, Hoffman AS, Schoen FJ and Lemons J. Biomaterials science: a multidisciplinary endeavor. *Biomaterials science: an introduction to materials in medicine*. 2004:1-9.
85. Noviana D, Estuningsih S and Ulum MF. Animal Study and Pre-clinical Trials of Biomaterials *Biomaterials and Medical Devices*: Springer; 2016: 67-101.
86. McCreery RL. *Raman spectroscopy for chemical analysis*: John Wiley & Sons; 2005.
87. Perlaki CM, Liu Q and Lim M. Raman Spectroscopy Based Techniques in Tissue Engineering—An Overview. *Applied Spectroscopy Reviews*. 2014;49:513-532.
88. Mishchenko MI, Travis LD and Lacis AA. *Scattering, absorption, and emission of light by small particles*: Cambridge university press; 2002.
89. Maiman TH. Stimulated optical radiation in ruby. 1960.
90. Strutt JW. XV. On the light from the sky, its polarization and colour. *The London, Edinburgh, and Dublin Philosophical Magazine and Journal of Science*. 1871;41:107-120.
91. Rayleigh L. XXXIV. On the transmission of light through an atmosphere containing small particles in suspension, and on the origin of the blue of the sky. *The London, Edinburgh, and Dublin Philosophical Magazine and Journal of Science*. 1899;47:375-384.
92. Smekal A. Zur Quantentheorie der Dispersion. *Naturwissenschaften*. 1923;11:873-875.
93. Raman CV and Krishnan KS. A new type of secondary radiation. *Nature*. 1928;121:501-502.
94. Long DA. Raman spectroscopy. *New York*. 1977:1-12.
95. Gardiner DJ. Introduction to Raman scattering *Practical Raman Spectroscopy*: Springer; 1989: 1-12.
96. Harz M, Kiehntopf M, Stöckel S, Rösch P, Deufel T and Popp J. Analysis of single blood cells for CSF diagnostics via a combination of fluorescence staining and micro-Raman spectroscopy. *Analyst*. 2008;133:1416-1423.
97. Brauchle E, Thude S, Brucker SY and Schenke-Layland K. Cell death stages in single apoptotic and necrotic cells monitored by Raman microspectroscopy. *Scientific reports*. 2014;4.

98. Wold S, Albano C, Dunn III W, Edlund U, Esbensen K, Geladi P, Hellberg S, Johansson E, Lindberg W and Sjöström M. Multivariate data analysis in chemistry *Chemometrics*: Springer; 1984: 17-95.
99. Esbensen KH, Guyot D, Westad F and Houmoller LP. *Multivariate data analysis-in practice: an introduction to multivariate data analysis and experimental design*: Multivariate Data Analysis; 2002.
100. Hotelling H. Analysis of a complex of statistical variables into principal components. *Journal of educational psychology*. 1933;24:417.
101. Pearson K. LIII. On lines and planes of closest fit to systems of points in space. *The London, Edinburgh, and Dublin Philosophical Magazine and Journal of Science*. 1901;2:559-572.
102. Wold S, Esbensen K and Geladi P. Principal component analysis. *Chemometrics and intelligent laboratory systems*. 1987;2:37-52.
103. Næs T, Isaksson T, Fearn T and Davies T. *A user friendly guide to multivariate calibration and classification*: NIR publications; 2002.
104. Miljković M, Chernenko T, Romeo MJ, Bird B, Matthäus C and Diem M. Label-free imaging of human cells: algorithms for image reconstruction of Raman hyperspectral datasets. *Analyst*. 2010;135:2002-2013.
105. Strachan CJ, Rades T, Gordon KC and Rantanen J. Raman spectroscopy for quantitative analysis of pharmaceutical solids. *Journal of pharmacy and pharmacology*. 2007;59:179-192.
106. Ager III JW and Drory MD. Quantitative measurement of residual biaxial stress by Raman spectroscopy in diamond grown on a Ti alloy by chemical vapor deposition. *Physical Review B*. 1993;48:2601.
107. De Beer T, Burggraeve A, Fonteyne M, Saerens L, Remon JP and Vervaet C. Near infrared and Raman spectroscopy for the in-process monitoring of pharmaceutical production processes. *International Journal of Pharmaceutics*. 2011;417:32-47.
108. Wang Y, Alsmeyer DC and McCreery RL. Raman spectroscopy of carbon materials: structural basis of observed spectra. *Chemistry of Materials*. 1990;2:557-563.
109. Bower D. Investigation of molecular orientation distributions by polarized Raman scattering and polarized fluorescence. *Journal of Polymer Science: Polymer physics Edition*. 1972;10:2135-2153.
110. Fanconi B, Tomlinson B, Nafie LA, Small W and Peticolas WL. Polarized laser Raman studies of biological polymers. *Journal of Chemical Physics*. 1969;51:3993-4005.
111. Spiro TG and Strekas TC. Resonance Raman spectra of hemoglobin and cytochrome c: inverse polarization and vibronic scattering. *Proceedings of the National Academy of Sciences*. 1972;69:2622-2626.
112. Schrader B. *Infrared and Raman spectroscopy: methods and applications*: John Wiley & Sons; 2008.
113. Adar F, Delhaye M and DaSilva E. Evolution of instrumentation for detection of the Raman effect as driven by available technologies and by developing applications. *Journal of chemical education*. 2007;84:50.
114. Haka AS, Shafer-Peltier KE, Fitzmaurice M, Crowe J, Dasari RR and Feld MS. Diagnosing breast cancer by using Raman spectroscopy. *Proceedings of the National Academy of Sciences*. 2005;102:12371-12376.
115. Jermyn M, Mok K, Mercier J, Desroches J, Pichette J, Saint-Arnaud K, Bernstein L, Guiot M-C, Petrecca K and Leblond F. Intraoperative brain cancer detection with Raman spectroscopy in humans. *Science translational medicine*. 2015;7:274ra19-274ra19.
116. Brauchle E, Kasper J, Daum R, Schierbaum N, Falch C, Kirschniak A, Schäffer TE and Schenke-Layland K. Biomechanical and biomolecular characterization of extracellular matrix structures in human colon carcinomas. *Matrix Biology*. 2018.
117. Chan JW, Lieu DK, Huser T and Li RA. Label-free separation of human embryonic stem cells and their cardiac derivatives using Raman spectroscopy. *Analytical chemistry*. 2009;81:1324-1331.
118. Notingher I, Jell G, Lohbauer U, Salih V and Hench LL. In situ non‐invasive spectral discrimination between bone cell phenotypes used in tissue engineering. *Journal of cellular biochemistry*. 2004;92:1180-1192.
119. Oshima Y, Shinzawa H, Takenaka T, Furihata C and Sato H. Discrimination analysis of human lung cancer cells associated with histological type and malignancy using Raman spectroscopy. *Journal of biomedical optics*. 2010;15:017009.
120. Chan JW and Lieu DK. Label‐free biochemical characterization of stem cells using vibrational spectroscopy. *Journal of biophotonics*. 2009;2:656-668.

121. Brauchle E, Knopf A, Bauer H, Shen N, Linder S, Monaghan Michael G, Ellwanger K, Layland Shannon L, Brucker Sara Y, Nsair A and Schenke-Layland K. Non-invasive Chamber-Specific Identification of Cardiomyocytes in Differentiating Pluripotent Stem Cells. *Stem Cell Reports*. 2016;6:188-199.
122. Pascut FC, Kalra S, George V, Welch N, Denning C and Notingher I. Non-invasive label-free monitoring the cardiac differentiation of human embryonic stem cells in-vitro by Raman spectroscopy. *Biochimica et Biophysica Acta (BBA)-General Subjects*. 2013;1830:3517-3524.
123. Notingher I, Verrier S, Haque S, Polak J and Hench L. Spectroscopic study of human lung epithelial cells (A549) in culture: living cells versus dead cells. *Biopolymers: Original Research on Biomolecules*. 2003;72:230-240.
124. Delogne C, Lawford PV, Habesch SM and Carolan VA. Characterization of the calcification of cardiac valve bioprostheses by environmental scanning electron microscopy and vibrational spectroscopy. *Journal of microscopy*. 2007;228:62-77.
125. Otero EU, Sathaiah S, Silveira L, Pomerantzeff PMA and Pasqualucci CAG. Raman spectroscopy for diagnosis of calcification in human heart valves. *Journal of Spectroscopy*. 2004;18:75-84.
126. Römer TJ, Brennan III JF, Puppels GJ, Zwinderman AH, van Duinen SG, van der Laarse A, van der Steen AF, Bom NA and Bruschke AV. Intravascular ultrasound combined with Raman spectroscopy to localize and quantify cholesterol and calcium salts in atherosclerotic coronary arteries. *Arteriosclerosis, thrombosis, and vascular biology*. 2000;20:478-483.
127. Votteler M, Carvajal Berrio DA, Pudlas M, Walles H, Stock UA and Schenke‐Layland K. Raman spectroscopy for the non‐contact and non‐destructive monitoring of collagen damage within tissues. *Journal of biophotonics*. 2012;5:47-56.
128. Jozwik K and Karczemska A. The new generation Ti6Al4V artificial heart valve with nanocrystalline diamond coating on the ring and with Derlin disc after long-term mechanical fatigue examination. *Diamond and related materials*. 2007;16:1004-1009.
129. Ali N, Kousar Y, Okpalugo T, Singh V, Pease M, Ogwu A, Gracio J, Titus E, Meletis E and Jackson M. Human micro-vascular endothelial cell seeding on Cr-DLC thin films for mechanical heart valve applications. *Thin solid films*. 2006;515:59-65.
130. Rockwood DN, Woodhouse KA, Fromstein JD, Chase DB and Rabolt JF. Characterization of biodegradable polyurethane microfibers for tissue engineering. *Journal of Biomaterials Science, Polymer Edition*. 2007;18:743-758.
131. Liu Z, Cai W, He L, Nakayama N, Chen K, Sun X, Chen X and Dai H. In vivo biodistribution and highly efficient tumour targeting of carbon nanotubes in mice. *Nature nanotechnology*. 2007;2:47.
132. Saar BG, Contreras-Rojas LR, Xie XS and Guy RH. Imaging drug delivery to skin with stimulated Raman scattering microscopy. *Molecular pharmaceutics*. 2011;8:969-975.
133. Liu Z, Chen K, Davis C, Sherlock S, Cao Q, Chen X and Dai H. Drug delivery with carbon nanotubes for in vivo cancer treatment. *Cancer research*. 2008;68:6652-6660.
134. Tippavajhala VK, de Oliveira Mendes T and Martin AA. In Vivo Human Skin Penetration Study of Sunscreens by Confocal Raman Spectroscopy. *AAPS PharmSciTech*. 2018;19:753-760.
135. Caspers PJ, Williams AC, Carter EA, Edwards HG, Barry BW, Bruining HA and Puppels GJ. Monitoring the penetration enhancer dimethyl sulfoxide in human stratum corneum in vivo by confocal Raman spectroscopy. *Pharmaceutical research*. 2002;19:1577-1580.
136. Ascencio SM, Choe C, Meinke MC, Müller RH, Maksimov GV, Wigger-Alberti W, Lademann J and Darvin ME. Confocal Raman microscopy and multivariate statistical analysis for determination of different penetration abilities of caffeine and propylene glycol applied simultaneously in a mixture on porcine skin ex vivo. *European journal of pharmaceutics and biopharmaceutics*. 2016;104:51-58.
137. Mélot M, Pudney PD, Williamson A-M, Caspers PJ, Van Der Pol A and Puppels GJ. Studying the effectiveness of penetration enhancers to deliver retinol through the stratum cornum by in vivo confocal Raman spectroscopy. *Journal of controlled release*. 2009;138:32-39.
138. Boyd RW. *Nonlinear optics*: Elsevier; 2003.
139. Zoumi A, Yeh A and Tromberg BJ. Imaging cells and extracellular matrix in vivo by using second-harmonic generation and two-photon excited fluorescence. *Proceedings of the National Academy of Sciences*. 2002;99:11014-11019.
140. Koehler MJ, König K, Elsner P, Bückle R and Kaatz M. In vivo assessment of human skin aging by multiphoton laser scanning tomography. *Optics letters*. 2006;31:2879-2881.
141. Helmchen F and Denk W. Deep tissue two-photon microscopy. *Nature methods*. 2005;2:932.

142. Zipfel WR, Williams RM, Christie R, Nikitin AY, Hyman BT and Webb WW. Live tissue intrinsic emission microscopy using multiphoton-excited native fluorescence and second harmonic generation. *Proceedings of the National Academy of Sciences*. 2003;100:7075-7080.
143. Franken eP, Hill AE, Peters Ce and Weinreich G. Generation of optical harmonics. *Physical Review Letters*. 1961;7:118.
144. Perry SW, Burke RM and Brown EB. Two-photon and second harmonic microscopy in clinical and translational cancer research. *Annals of biomedical engineering*. 2012;40:277-291.
145. Georgiou E, Theodossiou T, Hovhannisyan V, Politopoulos K, Rapti G and Yova D. Second and third optical harmonic generation in type I collagen, by nanosecond laser irradiation, over a broad spectral region. *Optics Communications*. 2000;176:253-260.
146. Campagnola PJ and Loew LM. Second-harmonic imaging microscopy for visualizing biomolecular arrays in cells, tissues and organisms. *Nature biotechnology*. 2003;21:1356.
147. Dombeck DA, Kasischke KA, Vishwasrao HD, Ingelsson M, Hyman BT and Webb WW. Uniform polarity microtubule assemblies imaged in native brain tissue by second-harmonic generation microscopy. *Proceedings of the National Academy of Sciences*. 2003;100:7081-7086.
148. Chen G, Chen J, Zhuo S, Xiong S, Zeng H, Jiang X, Chen R and Xie S. Nonlinear spectral imaging of human hypertrophic scar based on two‐photon excited fluorescence and second‐harmonic generation. *British Journal of Dermatology*. 2009;161:48-55.
149. Roberts MS, Dancik Y, Prow TW, Thorling CA, Lin LL, Grice JE, Robertson TA, König K and Becker W. Non-invasive imaging of skin physiology and percutaneous penetration using fluorescence spectral and lifetime imaging with multiphoton and confocal microscopy. *European Journal of Pharmaceutics and Biopharmaceutics*. 2011;77:469-488.
150. König K and Riemann I. High-resolution multiphoton tomography of human skin with subcellular spatial resolution and picosecond time resolution. *Journal of biomedical optics*. 2003;8:432-440.
151. Brown CM, Rivera DR, Ouzounov DG, Webb WW, Xu C, Pavlova IP, Williams WO and Mohanan S. In vivo imaging of unstained tissues using a compact and flexible multiphoton microendoscope. *Journal of biomedical optics*. 2012;17:040505.
152. Horton NG, Wang K, Kobat D, Clark CG, Wise FW, Schaffer CB and Xu C. In vivo three-photon microscopy of subcortical structures within an intact mouse brain. *Nature photonics*. 2013;7:205.
153. Katona G, Szalay G, Maák P, Kaszás A, Veress M, Hillier D, Chiovini B, Vizi ES, Roska B and Rózsa B. Fast two-photon in vivo imaging with three-dimensional random-access scanning in large tissue volumes. *Nature methods*. 2012;9:201.
154. Schenke-Layland K, Riemann I, Opitz F, König K, Halbhuber K and Stock U. Comparative study of cellular and extracellular matrix composition of native and tissue engineered heart valves. *Matrix biology*. 2004;23:113-125.
155. Joyce EM, Liao J, Schoen FJ, Mayer Jr JE and Sacks MS. Functional collagen fiber architecture of the pulmonary heart valve cusp. *The Annals of thoracic surgery*. 2009;87:1240-1249.
156. Misfeld M and Sievers H-H. Heart valve macro-and microstructure. *Philosophical Transactions of the Royal Society of London B: Biological Sciences*. 2007;362:1421-1436.
157. Ramachandran G, Bansal M and Bhatnagar R. A hypothesis on the role of hydroxyproline in stabilizing collagen structure. *Biochimica et Biophysica Acta (BBA)-Protein Structure*. 1973;322:166-171.
158. Shoulders MD and Raines RT. Collagen structure and stability. *Annual review of biochemistry*. 2009;78:929-958.
159. Martin C and Sun W. Biomechanical characterization of aortic valve tissue in humans and common animal models. *Journal of biomedical materials research Part A*. 2012;100:1591-1599.
160. Brockbank KG, Schenke-Layland K, Greene ED, Chen Z, Fritze O, Schleicher M, Kaulitz R, Riemann I, Fend F and Albes JM. Ice-free cryopreservation of heart valve allografts: better extracellular matrix preservation in vivo and preclinical results. *Cell and tissue banking*. 2012;13:663-671.
161. Liao J, Joyce EM and Sacks MS. Effects of decellularization on the mechanical and structural properties of the porcine aortic valve leaflet. *Biomaterials*. 2008;29:1065-1074.
162. Christie GW and Barratt-Boyes BG. Age-dependent changes in the radial stretch of human aortic valve leaflets determined by biaxial testing. *The Annals of thoracic surgery*. 1995;60:S156-S159.
163. Lee C-H, Zhang W, Liao J, Carruthers Christopher A, Sacks Jacob I and Sacks Michael S. On the Presence of Affine Fibril and Fiber Kinematics in the Mitral Valve Anterior Leaflet. *Biophysical Journal*. 2015;108:2074-2087.
164. Hwang YJ and Lyubovitsky JG. The structural analysis of three‐dimensional fibrous collagen hydrogels by raman microspectroscopy. *Biopolymers: Original Research on Biomolecules*. 2013;99:349-356.

165. GĄSIOR-GŁOGOWSKA M, KOMOROWSKA M, Hanuza J, Ptak M and Kobielarz M. Structural alteration of collagen fibres–spectroscopic and mechanical studies. *strain*. 2010;19:20.
166. Unal M, Jung H and Akkus O. Novel Raman spectroscopic biomarkers indicate that postyield damage denatures bone's collagen. *Journal of Bone and Mineral Research*. 2016;31:1015-1025.
167. Nagase H, Visse R and Murphy G. Structure and function of matrix metalloproteinases and TIMPs. *Cardiovascular research*. 2006;69:562-573.
168. Giwa S, Lewis JK, Alvarez L, Langer R, Roth AE, Church GM, Markmann JF, Sachs DH, Chandraker A and Wertheim JA. The promise of organ and tissue preservation to transform medicine. *Nature biotechnology*. 2017;35:530.
169. Manji RA, Lee W and Cooper DK. Xenograft bioprosthetic heart valves: past, present and future. *International Journal of Surgery*. 2015;23:280-284.
170. Santos NC, Figueira-Coelho J, Martins-Silva J and Saldanha C. Multidisciplinary utilization of dimethyl sulfoxide: pharmacological, cellular, and molecular aspects. *Biochemical pharmacology*. 2003;65:1035-1041.
171. Galvao J, Davis B, Tilley M, Normando E, Duchen MR and Cordeiro MF. Unexpected low-dose toxicity of the universal solvent DMSO. *The FASEB Journal*. 2014;28:1317-1330.
172. Aye M, Di Giorgio C, De Mo M, Botta A, Perrin J and Courbiere B. Assessment of the genotoxicity of three cryoprotectants used for human oocyte vitrification: dimethyl sulfoxide, ethylene glycol and propylene glycol. *Food and chemical toxicology*. 2010;48:1905-1912.
173. Program NT. Toxicology and carcinogenesis studies of formamide (Cas No. 75-12-7) in F344/N rats and B6C3F1 mice (gavage studies). *National Toxicology Program technical report series*. 2008:1.
174. Carpenter JF and Dawson PE. Quantitation of dimethyl sulfoxide in solutions and tissues by high-performance liquid chromatography. *Cryobiology*. 1991;28:210-215.
175. Salomonsson ML, Bondesson U and Hedeland M. Quantification of dimethylsulfoxide (DMSO) in equine plasma and urine using HILIC‐MS/MS. *Drug testing and analysis*. 2017;9:935-941.
176. Gao S, Wilson DM, Edinboro LE, McGuire GM, Williams SG and Thomas Karnes H. Improvement of sensitivity for the determination of propylene glycol in rat plasma and lung tissue using HPLC/tandem MS and derivatization with benzoyl chloride. *Journal of liquid chromatography & related technologies*. 2003;26:3413-3431.
177. Liu J, Bu J, Bu W, Zhang S, Pan L, Fan W, Chen F, Zhou L, Peng W and Zhao K. Real‐Time In Vivo Quantitative Monitoring of Drug Release by Dual‐Mode Magnetic Resonance and Upconverted Luminescence Imaging. *Angewandte Chemie International Edition*. 2014;53:4551-4555.
178. Decot V, Houze P, Stoltz J-F and Bensoussan D. Quantification of residual dimethylsulfoxide after washing cryopreserved stem cells and thawing tissue grafts. *Bio-medical materials and engineering*. 2009;19:293-300.
179. Lakey JR, Helms LM, Moser G, Lix B, Slupsky CM, Rebeyka IM, Sykes BD and McGann LE. Dynamics of cryoprotectant permeation in porcine heart valve leaflets. *Cell transplantation*. 2003;12:123-128.
180. Shardt N, Al-Abbasi KK, Yu H, Jomha NM, McGann LE and Elliott JA. Cryoprotectant kinetic analysis of a human articular cartilage vitrification protocol. *Cryobiology*. 2016;73:80-92.
181. Takroni TA, Yu H, Laouar L, Adesida AB, Elliott JA and Jomha NM. Ethylene glycol and glycerol loading and unloading in porcine meniscal tissue. *Cryobiology*. 2017;74:50-60.
182. Corral A, Balcerzyk M, Parrado-Gallego Á, Fernández-Gómez I, Lamprea DR, Olmo A and Risco R. Assessment of the cryoprotectant concentration inside a bulky organ for cryopreservation using X-ray computed tomography. *Cryobiology*. 2015;71:419-431.
183. Vásquez-Rivera A, Sommer KK, Oldenhof H, Higgins AZ, Brockbank KG, Hilfiker A and Wolkers WF. Simultaneous monitoring of different vitrification solution components permeating into tissues. *Analyst*. 2018.
184. Rhys NH, Gillams RJ, Collins LE, Callear SK, Lawrence MJ and McLain SE. On the structure of an aqueous propylene glycol solution. *The Journal of chemical physics*. 2016;145:224504.
185. Dabkowska AP, Foglia F, Lawrence MJ, Lorenz CD and McLain SE. On the solvation structure of dimethylsulfoxide/water around the phosphatidylcholine head group in solution. *The Journal of chemical physics*. 2011;135:12B611.
186. Kirchner B and Reiher M. The Secret of Dimethyl Sulfoxide− Water Mixtures. A Quantum Chemical Study of 1DMSO− n Water Clusters. *Journal of the American Chemical Society*. 2002;124:6206-6215.
187. Bolen D and Baskakov IV. The osmophobic effect: natural selection of a thermodynamic force in protein folding1. *Journal of molecular biology*. 2001;310:955-963.

188. Kurobe H, Maxfield MW, Breuer CK and Shinoka T. Concise Review: Tissue-Engineered Vascular Grafts for Cardiac Surgery: Past, Present, and Future. *STEM CELLS Translational Medicine*. 2012;1:566-571.
189. Schmidt CE and Baier JM. Acellular vascular tissues: natural biomaterials for tissue repair and tissue engineering. *Biomaterials*. 2000;21:2215-2231.
190. Konig G, McAllister TN, Dusserre N, Garrido SA, Iyican C, Marini A, Fiorillo A, Avila H, Wystrychowski W and Zagalski K. Mechanical properties of completely autologous human tissue engineered blood vessels compared to human saphenous vein and mammary artery. *Biomaterials*. 2009;30:1542-1550.
191. Niklason L, Gao J, Abbott W, Hirschi K, Houser S, Marini R and Langer R. Functional arteries grown in vitro. *Science*. 1999;284:489-493.
192. Fodor SP, Copeland RA, Grygon CA and Spiro TG. Deep-ultraviolet Raman excitation profiles and vibronic scattering mechanisms of phenylalanine, tyrosine, and tryptophan. *Journal of the American Chemical Society*. 1989;111:5509-5518.
193. Klein K, Gigler AM, Aschenbrenner T, Monetti R, Bunk W, Jamitzky F, Morfill G, Stark RW and Schlegel J. Label-free live-cell imaging with confocal Raman microscopy. *Biophysical journal*. 2012;102:360-368.
194. Nan X, Cheng J-X and Xie XS. Vibrational imaging of lipid droplets in live fibroblast cells with coherent anti-Stokes Raman scattering microscopy. *Journal of lipid research*. 2003;44:2202-2208.
195. Frid MG, Shekhonin BV, Koteliansky VE and Glukhova MA. Phenotypic changes of human smooth muscle cells during development: Late expression of heavy caldesmon and calponin. *Developmental Biology*. 1992;153:185-193.
196. Ailawadi G, Moehle CW, Pei H, Walton SP, Yang Z, Kron IL, Lau CL and Owens GK. Smooth muscle phenotypic modulation is an early event in aortic aneurysms. *The Journal of thoracic and cardiovascular surgery*. 2009;138:1392-1399.
197. Doran AC, Meller N and McNamara CA. Role of smooth muscle cells in the initiation and early progression of atherosclerosis. *Arteriosclerosis, thrombosis, and vascular biology*. 2008;28:812-819.
198. Gabbiani G, Schmid E, Winter S, Chaponnier C, De Ckhastonay C, Vandekerckhove J, Weber K and Franke WW. Vascular smooth muscle cells differ from other smooth muscle cells: predominance of vimentin filaments and a specific alpha-type actin. *Proceedings of the National Academy of Sciences*. 1981;78:298-302.
199. Aikawa M, Sakomura Y, Ueda M, Kimura K, Manabe I, Ishiwata S, Komiyama N, Yamaguchi H, Yazaki Y and Nagai R. Redifferentiation of smooth muscle cells after coronary angioplasty determined via myosin heavy chain expression. *Circulation*. 1997;96:82-90.
200. Owens GK, Kumar MS and Wamhoff BR. Molecular regulation of vascular smooth muscle cell differentiation in development and disease. *Physiological reviews*. 2004;84:767-801.
201. Bargehr J, Low L, Cheung C, Bernard WG, Iyer D, Bennett MR, Gambardella L and Sinha S. Embryological origin of human smooth muscle cells influences their ability to support endothelial network formation. *Stem cells translational medicine*. 2016;5:946-959.
202. Opitz F, Schenke-Layland K, Cohnert TU and Stock UA. Phenotypical plasticity of vascular smooth muscle cells—effect of in vitro and in vivo shear stress for tissue engineering of blood vessels. *Tissue engineering*. 2007;13:2505-2514.
203. McDaniel DP, Shaw GA, Elliott JT, Bhadriraju K, Meuse C, Chung K-H and Plant AL. The Stiffness of Collagen Fibrils Influences Vascular Smooth Muscle Cell Phenotype. *Biophysical Journal*. 2007;92:1759-1769.
204. Glukhova MA, Kabakov AE, Frid MG, Ornatsky OI, Belkin AM, Mukhin DN, Orekhov AN, Koteliansky VE and Smirnov VN. Modulation of human aorta smooth muscle cell phenotype: a study of muscle-specific variants of vinculin, caldesmon, and actin expression. *Proceedings of the National Academy of Sciences*. 1988;85:9542-9546.
205. Owens GK. Regulation of differentiation of vascular smooth muscle cells. *Physiological reviews*. 1995;75:487-517.
206. Zhang X, Wang X, Zhou X, Ma X, Yao Y and Liu X. Phenotypic transformation of smooth muscle cells from porcine coronary arteries is associated with connexin 43. *Molecular medicine reports*. 2016;14:41-48.
207. Chadjichristos CE, Morel S, Derouette J-P, Sutter E, Roth I, Brisset AC, Bochaton-Piallat M-L and Kwak BR. Targeting Connexin 43 Prevents Platelet-Derived Growth Factor-BB–Induced Phenotypic Change in Porcine Coronary Artery Smooth Muscle Cells. *Circulation research*. 2008.

208. Yamamoto M, Yamamoto K and Noumura T. Type I collagen promotes modulation of cultured rabbit arterial smooth muscle cells from a contractile to a synthetic phenotype. *Experimental cell research*. 1993;204:121-129.
209. Wen J, Wang P, Smith SV, Haller CA and Chaikof EL. Syndecans are differentially expressed during the course of aortic aneurysm formation. *Journal of vascular surgery*. 2007;46:1014-1025.
210. Li L and Chaikof EL. Mechanical stress regulates syndecan-4 expression and redistribution in vascular smooth muscle cells. *Arteriosclerosis Thrombosis and Vascular Biology*. 2002;22:61-68.
211. Wu K-C and Jin J-P. Calponin in non-muscle cells. *Cell biochemistry and biophysics*. 2008;52:139.
212. Timraz SB, Farhat IA, Alhussein G, Christoforou N and Teo JC. In-depth evaluation of commercially available human vascular smooth muscle cells phenotype: Implications for vascular tissue engineering. *Experimental cell research*. 2016;343:168-176.
213. Appel AA, Anastasio MA, Larson JC and Brey EM. Imaging challenges in biomaterials and tissue engineering. *Biomaterials*. 2013;34:6615-6630.
214. Harrison BS and Atala A. Carbon nanotube applications for tissue engineering. *Biomaterials*. 2007;28:344-353.
215. Dash BC, Levi K, Schwan J, Luo J, Bartulos O, Wu H, Qiu C, Yi T, Ren Y and Campbell S. Tissue-engineered vascular rings from human iPSC-derived smooth muscle cells. *Stem cell reports*. 2016;7:19-28.
216. Luo J, Qin L, Kural MH, Schwan J, Li X, Bartulos O, Cong X-q, Ren Y, Gui L and Li G. Vascular smooth muscle cells derived from inbred swine induced pluripotent stem cells for vascular tissue engineering. *Biomaterials*. 2017;147:116-132.
217. Strobel HA, Dikina AD, Levi K, Solorio LD, Alsberg E and Rolle MW. Cellular self-assembly with microsphere incorporation for growth factor delivery within engineered vascular tissue rings. *Tissue Engineering Part A*. 2017;23:143-155.
218. Stone N, Hart Prieto MC, Crow P, Uff J and Ritchie AW. The use of Raman spectroscopy to provide an estimation of the gross biochemistry associated with urological pathologies. *Analytical and bioanalytical chemistry*. 2007;387:1657-1668.
219. Buschman HP, Deinum G, Motz JT, Fitzmaurice M, Kramer JR, van der Laarse A, Bruschke AV and Feld MS. Raman microspectroscopy of human coronary atherosclerosis: biochemical assessment of cellular and extracellular morphologic structures in situ. *Cardiovascular pathology*. 2001;10:69-82.
220. Ellis R, Green E and Winlove CP. Structural analysis of glycosaminoglycans and proteoglycans by means of Raman microspectrometry. *Connective tissue research*. 2009;50:29-36.
221. Desmoulière A, Geinoz A, Gabbiani F and Gabbiani G. Transforming growth factor-beta 1 induces alpha-smooth muscle actin expression in granulation tissue myofibroblasts and in quiescent and growing cultured fibroblasts. *The Journal of cell biology*. 1993;122:103-111.
222. Camejo G, Fager G, Rosengren B, Hurt-Camejo E and Bondjers G. Binding of low density lipoproteins by proteoglycans synthesized by proliferating and quiescent human arterial smooth muscle cells. *Journal of Biological Chemistry*. 1993;268:14131-14137.
223. Evanko SP, Angello JC and Wight TN. Formation of hyaluronan-and versican-rich pericellular matrix is required for proliferation and migration of vascular smooth muscle cells. *Arteriosclerosis, thrombosis, and vascular biology*. 1999.
224. Suna G, Wojakowski W, Lynch M, Barallobre-Barreiro J, Yin X, Mayr U, Baig F, Lu R, Fava M and Hayward R. Extracellular matrix proteomics reveals interplay of aggrecan and aggrecanases in vascular remodeling of stented coronary arteries. *Circulation*. 2017:CIRCULATIONAHA. 116.023381.
225. Cikach FS, Koch CD, Mead TJ, Galatioto J, Willard BB, Emerton KB, Eagleton MJ, Blackstone EH, Ramirez F and Roselli EE. Massive aggrecan and versican accumulation in thoracic aortic aneurysm and dissection. *JCI insight*. 2018;3.
226. Timchenko EV, Timchenko PE, Lichtenberg A, Assmann A, Aubin H, Akhyari P, Volova LT and Pershutkina SV. Assessment of decellularization of heart bioimplants using a Raman spectroscopy method. *Journal of biomedical optics*. 2017;22:091511.
227. Chung YG, Tu Q, Cao D, Harada S, Eisen HJ and Chang C. Raman spectroscopy detects cardiac allograft rejection with molecular specificity. *Clinical and translational science*. 2009;2:206-210.
228. Abu‐Absi NR, Kenty BM, Cuellar ME, Borys MC, Sakhamuri S, Strachan DJ, Hausladen MC and Li ZJ. Real time monitoring of multiple parameters in mammalian cell culture bioreactors

using an in‐line Raman spectroscopy probe. *Biotechnology and bioengineering*. 2011;108:1215-1221.
229. Mathur A, Loskill P, Shao K, Huebsch N, Hong S, Marcus SG, Marks N, Mandegar M, Conklin BR and Lee LP. Human iPSC-based cardiac microphysiological system for drug screening applications. *Scientific reports*. 2015;5:8883.
230. Grosberg A, Alford PW, McCain ML and Parker KK. Ensembles of engineered cardiac tissues for physiological and pharmacological study: heart on a chip. *Lab on a chip*. 2011;11:4165-4173.
231. Huber A and Badylak SF. Phenotypic changes in cultured smooth muscle cells: limitation or opportunity for tissue engineering of hollow organs? *Journal of Tissue Engineering and Regenerative Medicine*. 2012;6:505-511.
232. Lau AY, Lee LP and Chan JW. An integrated optofluidic platform for Raman-activated cell sorting. *Lab on a Chip*. 2008;8:1116-1120.
233. Li M, Xu J, Romero-Gonzalez M, Banwart SA and Huang WE. Single cell Raman spectroscopy for cell sorting and imaging. *Current opinion in biotechnology*. 2012;23:56-63.
234. König K. Multiphoton microscopy in life sciences. *Journal of microscopy*. 2000;200:83-104.
235. Monaghan MG, Kroll S, Brucker SY and Schenke-Layland K. Enabling Multiphoton and Second Harmonic Generation Imaging in Paraffin-Embedded and Histologically Stained Sections. *Tissue Engineering Part C: Methods*. 2016;22:517-523.
236. Zoumi A, Lu X, Kassab GS and Tromberg BJ. Imaging coronary artery microstructure using second-harmonic and two-photon fluorescence microscopy. *Biophysical journal*. 2004;87:2778-2786.
237. Tilbury KB, Hocker JD, Wen BL, Sandbo N, Singh V and Campagnola PJ. Second harmonic generation microscopy analysis of extracellular matrix changes in human idiopathic pulmonary fibrosis. *Journal of biomedical optics*. 2014;19:086014.
238. Garcia AA, Haudenschild AK and Marcu L. Label-free Fluorescence Lifetime Imaging for Assessment of Carotid Artery Grafts. *Clinical and Translational Biophotonics*. 2018:CW4B. 4.
239. Baria E, Nesi G, Santi R, Maio V, Massi D, Pratesi C, Cicchi R and Pavone FS. Improved label‐free diagnostics and pathological assessment of atherosclerotic plaques through nonlinear microscopy. *Journal of biophotonics*. 2018:e201800106.
240. Bec J, Phipps JE, Gorpas D, Ma D, Fatakdawala H, Margulies KB, Southard JA and Marcu L. In vivo label-free structural and biochemical imaging of coronary arteries using an integrated ultrasound and multispectral fluorescence lifetime catheter system. *Scientific Reports*. 2017;7:8960.
241. Fatakdawala H, Griffiths LG, Wong ML, Julien M and Marcu L. Multimodal imaging of vascular grafts using time-resolved fluorescence and ultrasound. *Photonic Therapeutics and Diagnostics XI*. 2015;9303:930335.
242. Heuke S, Vogler N, Meyer T, Akimov D, Kluschke F, Röwert‐Huber HJ, Lademann J, Dietzek B and Popp J. Multimodal mapping of human skin. *British Journal of Dermatology*. 2013;169:794-803.
243. Lin J, Lu F, Zheng W, Huang Z, Xu S, Tai DC and Yu H. Assessment of liver steatosis and fibrosis in rats using integrated coherent anti-Stokes Raman scattering and multiphoton imaging technique. *Journal of biomedical optics*. 2011;16:116024.
244. Guo S, Pfeifenbring S, Meyer T, Ernst G, von Eggeling F, Maio V, Massi D, Cicchi R, Pavone FS and Popp J. Multimodal image analysis in tissue diagnostics for skin melanoma. *Journal of Chemometrics*. 2018;32:e2963.
245. Hench LL and Thompson I. Twenty-first century challenges for biomaterials. *Journal of The Royal Society Interface*. 2010;7:S379-S391.
246. Lim M, Ye H, Panoskaltsis N, Drakakis EM, Yue X, Cass AEG, Radomska A and Mantalaris A. Intelligent bioprocessing for haemotopoietic cell cultures using monitoring and design of experiments. *Biotechnology Advances*. 2007;25:353-368.
247. Notingher I, Gough JE and Hench LL. Study of osteoblasts mineralisation in vitro by Raman micro-spectroscopy. *Key Engineering Materials*. 2004;254:769-772.
248. Swain RJ, Jell G and Stevens MM. Non‐invasive analysis of cell cycle dynamics in single living cells with Raman micro‐spectroscopy. *Journal of cellular biochemistry*. 2008;104:1427-1438.
249. Pudlas M, Brauchle E, Klein TJ, Hutmacher DW and Schenke‐Layland K. Non‐invasive identification of proteoglycans and chondrocyte differentiation state by Raman microspectroscopy. *Journal of biophotonics*. 2013;6:205-211.
250. Liang X, Graf BW and Boppart SA. Imaging engineered tissues using structural and functional optical coherence tomography. *Journal of biophotonics*. 2009;2:643-655.

251. Kotecha M, Klatt D and Magin RL. Monitoring cartilage tissue engineering using magnetic resonance spectroscopy, imaging, and elastography. *Tissue Engineering Part B: Reviews*. 2013;19:470-484.
252. Papantoniou I, Sonnaert M, Geris L, Luyten FP, Schrooten J and Kerckhofs G. Three-dimensional characterization of tissue-engineered constructs by contrast-enhanced nanofocus computed tomography. *Tissue Engineering Part C: Methods*. 2013;20:177-187.
253. Kneipp K, Kneipp H, Itzkan I, Dasari RR and Feld MS. Ultrasensitive chemical analysis by Raman spectroscopy. *Chemical reviews*. 1999;99:2957-2976.
254. Maker PD and Terhune RW. Study of Optical Effects Due to an Induced Polarization Third Order in the Electric Field Strength. *Physical Review*. 1965;137:A801-A818.
255. Evans CL and Xie XS. Coherent anti-Stokes Raman scattering microscopy: chemical imaging for biology and medicine. *Annu Rev Anal Chem*. 2008;1:883-909.
256. Begley RF, Harvey AB and Byer RL. Coherent anti‐Stokes Raman spectroscopy. *Applied Physics Letters*. 1974;25:387-390.
257. Hashimoto M, Araki T and Kawata S. Molecular vibration imaging in the fingerprint region by use of coherent anti-Stokes Raman scattering microscopy with a collinear configuration. *Optics Letters*. 2000;25:1768-1770.
258. Kano H and Hamaguchi H-o. Ultrabroadband (> 2500 cm− 1) multiplex coherent anti-Stokes Raman scattering microspectroscopy using a supercontinuum generated from a photonic crystal fiber. *Applied Physics Letters*. 2005;86:121113.
259. Liu Y, Lee YJ and Cicerone MT. Broadband CARS spectral phase retrieval using a time-domain Kramers–Kronig transform. *Optics letters*. 2009;34:1363-1365.
260. Jeanmaire DL and Van Duyne RP. Surface Raman spectroelectrochemistry: Part I. Heterocyclic, aromatic, and aliphatic amines adsorbed on the anodized silver electrode. *Journal of Electroanalytical Chemistry and Interfacial Electrochemistry*. 1977;84:1-20.
261. Albrecht MG and Creighton JA. Anomalously intense Raman spectra of pyridine at a silver electrode. *Journal of the American Chemical Society*. 1977;99:5215-5217.
262. Fleischmann M, Hendra PJ and McQuillan A. Raman spectra of pyridine adsorbed at a silver electrode. *Chemical Physics Letters*. 1974;26:163-166.
263. Stöckle RM, Suh YD, Deckert V and Zenobi R. Nanoscale chemical analysis by tip-enhanced Raman spectroscopy. *Chemical Physics Letters*. 2000;318:131-136.
264. Cialla D, März A, Böhme R, Theil F, Weber K, Schmitt M and Popp J. Surface-enhanced Raman spectroscopy (SERS): progress and trends. *Analytical and bioanalytical chemistry*. 2012;403:27-54.
265. Liu Z, Tabakman S, Welsher K and Dai H. Carbon nanotubes in biology and medicine: in vitro and in vivo detection, imaging and drug delivery. *Nano research*. 2009;2:85-120.
266. Brackmann C, Esguerra M, Olausson D, Delbro D, Krettek A, Gatenholm P and Enejder A. Coherent anti-Stokes Raman scattering microscopy of human smooth muscle cells in bioengineered tissue scaffolds. *Journal of biomedical optics*. 2011;16:021115-021115-6.
267. Wang H-W, Le TT and Cheng J-X. Label-free Imaging of Arterial Cells and Extracellular Matrix Using a Multimodal CARS Microscope. *Optics communications*. 2008;281:1813-1822.
268. Schlücker S, Küstner B, Punge A, Bonfig R, Marx A and Ströbel P. Immuno‐Raman microspectroscopy: In situ detection of antigens in tissue specimens by surface‐enhanced Raman scattering. *Journal of Raman Spectroscopy: An International Journal for Original Work in all Aspects of Raman Spectroscopy, Including Higher Order Processes, and also Brillouin and Rayleigh Scattering*. 2006;37:719-721.
269. Schütz M, Steinigeweg D, Salehi M, Kömpe K and Schlücker S. Hydrophilically stabilized gold nanostars as SERS labels for tissue imaging of the tumor suppressor p63 by immuno-SERS microscopy. *Chemical Communications*. 2011;47:4216-4218.
270. Keren S, Zavaleta C, Cheng Zd, de La Zerda A, Gheysens O and Gambhir S. Noninvasive molecular imaging of small living subjects using Raman spectroscopy. *Proceedings of the National Academy of Sciences*. 2008;105:5844-5849.
271. Socrates G. *Infrared and Raman characteristic group frequencies: tables and charts*: John Wiley & Sons; 2004.
272. Movasaghi Z, Rehman S and Rehman IU. Raman spectroscopy of biological tissues. *Applied Spectroscopy Reviews*. 2007;42:493-541.
273. De Gelder J, De Gussem K, Vandenabeele P and Moens L. Reference database of Raman spectra of biological molecules. *Journal of Raman Spectroscopy*. 2007;38:1133-1147.
274. Lippert J, Tyminski D and Desmeules P. Determination of the secondary structure of proteins by laser Raman spectroscopy. *Journal of the American Chemical Society*. 1976;98:7075-7080.

275. Pelton JT and McLean LR. Spectroscopic methods for analysis of protein secondary structure. *Analytical biochemistry*. 2000;277:167-176.
276. You AY, Bergholt MS, St-Pierre J-P, Kit-Anan W, Pence IJ, Chester AH, Yacoub MH, Bertazzo S and Stevens MM. Raman spectroscopy imaging reveals interplay between atherosclerosis and medial calcification in the human aorta. *Science advances*. 2017;3:e1701156.
277. Frushour BG and Koenig JL. Raman scattering of collagen, gelatin, and elastin. *Biopolymers*. 1975;14:379-391.
278. Hu S, Smith KM and Spiro TG. Assignment of Protoheme Resonance Raman Spectrum by Heme Labeling in Myoglobin. *Journal of the American Chemical Society*. 1996;118:12638-12646.
279. Abe M, Kitagawa T and Kyogoku Y. Resonance Raman spectra of octaethylporphyrinato‐Ni (II) and meso‐deuterated and 15N substituted derivatives. II. A normal coordinate analysis. *The Journal of Chemical Physics*. 1978;69:4526-4534.
280. Stone N, Kendall C, Smith J, Crow P and Barr H. Raman spectroscopy for identification of epithelial cancers. *Faraday discussions*. 2004;126:141-157.
281. Notingher I, Green C, Dyer C, Perkins E, Hopkins N, Lindsay C and Hench LL. Discrimination between ricin and sulphur mustard toxicity in vitro using Raman spectroscopy. *Journal of the Royal Society Interface*. 2004;1:79-90.
282. Cheng WT, Liu MT, Liu HN and Lin SY. Micro‐Raman spectroscopy used to identify and grade human skin pilomatrixoma. *Microscopy research and technique*. 2005;68:75-79.
283. Ruiz-Chica AJ, Medina MA, Sánchez-Jiménez F and Ramírez FJ. Characterization by Raman spectroscopy of conformational changes on guanine–cytosine and adenine–thymine oligonucleotides induced by aminooxy analogues of spermidine. *Journal of Raman Spectroscopy*. 2004;35:93-100.
284. Naumann D. Infrared and NIR Raman spectroscopy in medical microbiology. *Infrared spectroscopy: new tool in medicine*. 1998;3257:245-258.
285. Krimm S and Bandekar J. Vibrational Spectroscopy and Conformation of Peptides, Polypeptides, and Proteins. In: C. B. Anfinsen, J. T. Edsall and F. M. Richards, eds. *Advances in Protein Chemistry*: Academic Press; 1986(38): 181-364.
286. Miura T and Thomas Jr GJ. Raman spectroscopy of proteins and their assemblies *Proteins: Structure, Function, and Engineering*: Springer; 1995: 55-99.
287. Hanlon E, Manoharan R, Koo TW, Shafer K, Motz J, Fitzmaurice M, Kramer J, Itzkan I, Dasari R and Feld M. Prospects for in vivo Raman spectroscopy. *Physics in medicine and biology*. 2000;45:R1.
288. Dukor RK. Vibrational Spectroscopy in the Detection of Cancer *Handbook of Vibrational Spectroscopy*: John Wiley & Sons, Ltd; 2006.
289. Huang Z, McWilliams A, Lui H, McLean DI, Lam S and Zeng H. Near‐infrared Raman spectroscopy for optical diagnosis of lung cancer. *International journal of cancer*. 2003;107:1047-1052.
290. Neault JF, Naoui M, Manfait M and Tajmir-Riahi HA. Aspirin-DNA interaction studied by FTIR and laser Raman difference spectroscopy. *FEBS Letters*. 1996;382:26-30.
291. Krafft C, Neudert L, Simat T and Salzer R. Near infrared Raman spectra of human brain lipids. *Spectrochimica Acta Part A: Molecular and Biomolecular Spectroscopy*. 2005;61:1529-1535.
292. Shetty G, Kendall C, Shepherd N, Stone N and Barr H. Raman spectroscopy: elucidation of biochemical changes in carcinogenesis of oesophagus. *Br J Cancer*. 2006;94:1460-1464.
293. Chan JW, Taylor DS, Zwerdling T, Lane SM, Ihara K and Huser T. Micro-Raman Spectroscopy Detects Individual Neoplastic and Normal Hematopoietic Cells. *Biophysical Journal*. 2006;90:648-656.
294. Lakshmi RJ, Kartha V, Murali Krishna C, R. Solomon J, Ullas G and Uma Devi P. Tissue Raman spectroscopy for the study of radiation damage: brain irradiation of mice. *Radiation research*. 2002;157:175-182.
295. Yue KT, Martin CL, Chen D, Nelson P, Sloan DL and Callender R. Raman spectroscopy of oxidized and reduced nicotinamide adenine dinucleotides. *Biochemistry*. 1986;25:4941-4947.

Acknowledgements

An dieser Stelle möchte ich mich ganz besonders bei meiner Doktormutter Prof. Dr. Katja Schenke-Layland für die fachliche und menschliche Unterstützung, die Aufnahme in ihrer Arbeitsgruppe sowie die fortwährende Motivation, insbesondere bei der Anfertigung der Publikationen bedanken.

Bei Prof. Dr. Ulrich Stock bedanke ich mich für seine Unterstützung als zweiter Berichterstatter. Außerdem möchte ich mich bei Prof. Dr. Ulrich Stock sowie Anna Biermann für die ausgezeichnete Zusammenarbeit im DFG-Projekt, die Durchführung der Tierstudien und das Zurverfügungstellen der Herzklappengewebe bedanken.

Prof. Dr. Marsha Rolle danke ich für ihre Vorarbeit und Anregungen, ohne die das SMC-Projekt nicht entstanden wäre.

Ein großer Dank geht ebenfalls an Dr. Eva Brauchle für die Betreuung meiner Doktorarbeit und ihre ständige Diskussions- und Hilfsbereitschaft.

Daniel Carvajal Berrio und Simone Liebscher danke ich für ihre geduldige Einarbeitung und ständige Unterstützung, insbesondere bei technischen und histologischen Fragen. Shannon Lee Layland möchte ich ganz besonders für die stets humorvolle Unterstützung beim Korrekturlesen der Abstracts, Poster und Publikationen danken. Auch allen anderen Mitarbeitern der AG Schenke-Layland gilt ein herzliches Dankeschön für ihre Hilfsbereitschaft, wertvolle Anregungen, die Organisation des Labors und die freundschaftliche Arbeitsatmosphäre.

Bei meinen lieben Freunden und Kollegen Aline Zbinden, Silke Keller, Lisa Rebers und Isabel Jesswein bedanke ich mich für die vielen anregenden Diskussionen, Motivationsschübe und diverse Abwechslungen vom Arbeitsalltag.
Schließlich gilt ein besonderer Dank meiner Familie und meinem Freund für die vielseitige Motivation und uneingeschränkte Unterstützung.

Declaration

Ich erkläre hiermit, dass ich die zur Promotion eingereichte Arbeit mit dem Titel: ”*Quality assessment in cardiovascular cells and tissues by Raman microspectroscopy and imaging*” selbständig verfasst, nur die angegebenen Quellen und Hilfsmittel benutzt und wörtlich oder inhaltlich übernommene Zitate als solche gekennzeichnet habe. Ich erkläre, dass die Richtlinien zur Sicherung guter wissenschaftlicher Praxis der Universität Tübingen beachtet wurden. Ich versichere an Eides statt, dass diese Angaben wahr sind und dass ich nichts verschwiegen habe. Mir ist bekannt, dass die falsche Angabe einer Versicherung an Eides statt mit Freiheitsstrafe bis zu drei Jahren oder mit Geldstrafe bestraft wird.

Tübingen, 04.03.2019

Julia Marzi

Appendices

Appendix I: A.C. Biermann & J. Marzi, E.M. Brauchle, J.L.Wichmann, C.T. Arendt, V. Puntmann, E. Nagel, S. Abdelaziz, A.G. Winter, K.G.M. Brockbank, S.L. Layland, K. Schenke-Layland, U.A. Stock, *Improved long-term durability of allogeneic heart valves*, European Journal of Cardiothoracic Surgery, 2019; 55(3): 484-493

European Journal of Cardio-Thoracic Surgery 55 (2019) 484–493
doi:10.1093/ejcts/ezy292 Advance Access publication 24 August 2018

ORIGINAL ARTICLE

Cite this article as: Biermann AC, Marzi J, Brauchle E, Wichmann JL, Arendt CT, Puntmann V *et al.* Improved long-term durability of allogeneic heart valves in the orthotopic sheep model. Eur J Cardiothorac Surg 2019;55:484–93.

Improved long-term durability of allogeneic heart valves in the orthotopic sheep model

Anna Christina Biermann[a,b,c,*,†], Julia Marzi[c,†], Eva Brauchle[c], Julian Lukas Wichmann[d], Christophe Theo Arendt[d], Valentina Puntmann[d], Eike Nagel[d], Sherif Abdelaziz[a], Andreas Gerhard Winter[a], Kelvin Gordon Mashader Brockbank[e,f], Shannon Layland[c], Katja Schenke-Layland[c,g,h] and Ulrich Alfred Stock[a,b,i,j]

[a] Department of Thoracic and Cardiovascular Surgery, University Hospital Frankfurt, Goethe University, Frankfurt am Main, Germany
[b] Department of Cardiothoracic Surgery, Royal Brompton and Harefield Foundation Trust, Harefield, UK
[c] Department of Women's Health, Research Institute for Women's Health, Eberhard-Karls-University Tuebingen, Tuebingen, Germany
[d] Department of Diagnostic and Interventional Radiology, University Hospital Frankfurt, Goethe University, Frankfurt am Main, Germany
[e] Tissue Testing Technologies LLC, North Charleston, SC, USA
[f] Department of Bioengineering, Clemson University, North Charleston, SC, USA
[g] Department of Medicine/Cardiology, Cardiovascular Research Laboratories, David Geffen School of Medicine at UCLA, Los Angeles, CA, USA
[h] Natural and Medical Sciences Institute at the University of Tuebingen (NMI), Reutlingen, Germany
[i] Faculty of Medicine, Imperial College London, London, UK
[j] Magdi Yacoube Institute, Heart Science Center, Harefield, UK

* Corresponding author. Royal Brompton and Harefield Hospital, Heart Science Centre, Hill End Road, Harefield, UB9 6JH, UK. Tel: +44-01895-828715; fax: +44-01895-829382; e-mail: annabiermann@hotmail.com (A. C. Biermann).

Received 12 May 2018; received in revised form 16 July 2018; accepted 20 July 2018

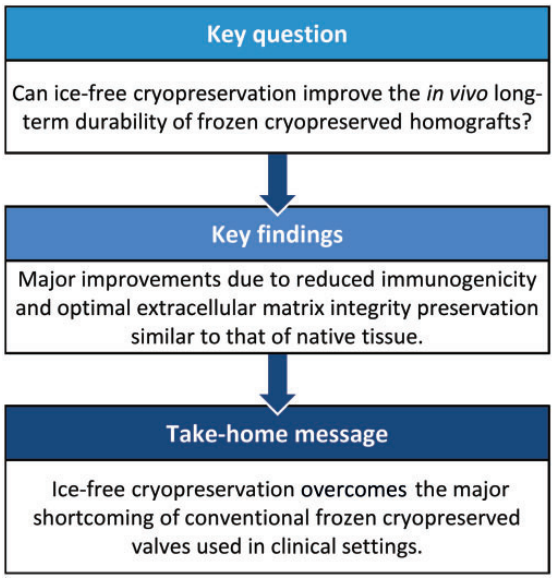

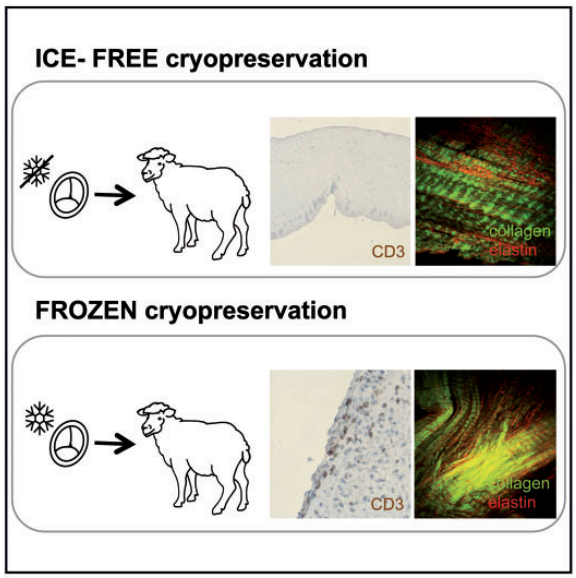

Downloaded from https://academic.oup.com/ejcts/article-abstract/55/3/484/5079309 by Klinikbibliothek Schnarrenberg user on 26 February 2019

Reprinted with permission from A.C. Biermann & J. Marzi, E.M. Brauchle, J.L. Wichmann, C.T. Arendt, V. Puntmann, E. Nagel, S. Abdelaziz, A.G. Winter, K.G.M. Brockbank, S.L. Layland, K. Schenke-Layland, U.A. Stock, *Improved long-term durability of allogeneic heart valves*, European Journal of Cardiothoracic Surgery, 2019; 55(3): 484-493. Copyright 2019 Oxford University Press

Abstract

OBJECTIVES: Frozen cryopreservation (FC) with the vapour phase of liquid nitrogen storage (-135°C) is a standard biobank technique to preserve allogeneic heart valves to enable a preferable allograft valve replacement in clinical settings. However, their long-term function is limited by immune responses, inflammation and structural degeneration. Ice-free cryopreserved (IFC) valves with warmer storage possibilities at -80°C showed better matrix preservation and decreased immunological response in preliminary short-term *in vivo* studies. Our study aimed to assess the prolonged performance of IFC allografts in an orthotopic pulmonary sheep model.

METHODS: FC ($n = 6$) and IFC ($n = 6$) allografts were transplanted into juvenile Merino sheep. After 12 months of implantation, functionality testing via 2-dimensional echocardiography and histological analyses was performed. In addition, multiphoton autofluorescence imaging and Raman microspectroscopy analysis were applied to qualitatively and quantitatively assess the matrix integrity of the leaflets.

RESULTS: Six animals from the FC group and 5 animals from the IFC group were included in the analysis. Histological explant analysis showed early inflammation in the FC valves, whereas sustainable, fully functional, devitalized acellular IFC grafts were obtained. IFC valves showed excellent haemodynamic data with fewer gradients, no pulmonary regurgitation, no calcification and acellularity. Structural remodelling of the leaflet matrix structure was only detected in FC-treated tissue, whereas IFC valves maintained matrix integrity comparable to that of native controls. The collagen crimp period and amplitude and elastin structure were significantly different in the FC valve cusps compared to IFC and native cusps. Collagen fibres in the FC valves were less aligned and straightened.

CONCLUSIONS: IFC heart valves with good haemodynamic function, reduced immunogenicity and preserved matrix structures have the potential to overcome the known limitations of the clinically applied FC valve.

Keywords: Ice-free cryopreservation • Frozen cryopreservation • Heart valve • Allograft • Transplantation

INTRODUCTION

Human allogeneic heart valves have been described as almost perfect heart valve replacements [1]. First introduced in 1962 [2], they have optimal haemodynamic properties, outstanding resistance to infections and require no anticoagulation [3]. Their clinical application is, however, limited due to a worldwide organ donor shortage and long-term failure because of degeneration. Due to logistical issues, valves were cryopreserved with controlled-rate freezing and stored in the gas phase of liquid nitrogen [4], enabling a long-term storage time of up to 5 years. Frozen cryopreservation (FC) has been the choice of preservation of human heart valves worldwide for the last 50 years [5].

Other major shortcomings of cryopreserved allograft heart valves are their cost-intensive vapour phase liquid nitrogen storage and their limited long-term function due to immune responses, inflammation and subsequent structural deterioration [6–8]. Allograft failure is seen more frequently in paediatric patients with increased calcium metabolism resulting in early reintervention procedures [9, 10]. An alternative ice-free cryopreservation (IFC) method was developed on the basis of vitrification principles avoiding ice crystal formation by using high concentrations of cryoprotectants and circumventing the economical disadvantages of liquid nitrogen storage. In a preliminary *in vivo* animal study, the initial preservation of the extracellular matrix (ECM) was verified after 7 months with superior haemodynamic properties compared to those achieved with standard cryopreservation [11].

The objective of this study was to evaluate the prolonged (1 year) performance of implanted IFC and FC pulmonary valves in an orthotopic pulmonary sheep model, including the integrity of the ECM. We applied multiphoton imaging to detect ECM damage caused by interstitial ice formation in FC heart valves [12, 13]. Furthermore, Raman spectroscopy was used as a novel analysis tool for in depth analysis of collagen structures [14].

METHODS

Tissue preparation

Hearts of 12 adult sheep (Dorset cross, ~1 year old, obtained from a slaughterhouse in Carlson Meats, Grove City, MN, USA) were obtained using aseptic conditions, rinsed with ice-cold lactated Ringer's solution (B. Braun, Melsungen, Germany) and placed in sterile Dulbecco's modified Eagle medium (DMEM, Invitrogen, Carlsbad, CA, USA) for overnight shipment to the processing laboratory (Cell & Tissue Systems, North Charleston, SC, USA). Pulmonary heart valves were excised and stored for 24 h at 4°C in 100 ml antibiotic solution (DMEM containing 4.5 g/l glucose with 126 mg/l lincomycin, 52 mg/l vancomycin, 157 mg/l cefoxitin and 117 mg/l polymyxin). Following the antibiotic treatment, the valves were randomly assigned to the FC and IFC groups. The individual valves of the FC group were cryopreserved, stored in the vapour phase of liquid nitrogen (-135°C) and thawed according to the American Association of Tissue Banks guidelines and as previously described by Lisy *et al.* [11]. For the IFC group, valve preservation, storage at -80°C in a mechanical freezer and rewarming were conducted via the protocol of Brockbank *et al.* [15]. After rewarming, the valves were stored in ice-cold lactated Ringer's solution until implantation (B. Braun).

Implantation/explantation

Twelve juvenile Merino sheep (average age 39 ± 3 weeks, weight 47 ± 4 kg) underwent pulmonary heart valve replacement with either IFC ($n = 6$) or FC ($n = 6$) allogeneic valves according to a previously described protocol [16]. Deaths due to perioperative complications due to valve implantation were excluded. All animals were kept in an indoor housing facility and received humane care in compliance with the *Guide for the Care and Use of Laboratory Animals* published by the National Institutes of Health

Downloaded from https://academic.oup.com/ejcts/article/55/3/484/5079309 by Klinikbibliothek Schnarrenberg user on 26 February 2019

(NIH publication no. 85-23 revised 1985). Animals were euthanized after 12 months of implantation using an intravenous application of embutramide. The valves were explanted and, following inspection for gross morphology, they were further processed.

Cardiovascular imaging studies

Echocardiography. Two weeks prior to explantation, each animal underwent a Doppler echocardiographic (CX50, Philips, Hamburg, Germany) examination with an S5-1 (iPx-7) probe to evaluate valve function. A blinded 2-dimensional echocardiographic-Doppler examination was performed of the right ventricular outflow tract, conduit and distal main pulmonary artery. In addition, the competence of the pulmonary valve was evaluated using colour-flow Doppler mapping.

In vivo *computed tomography and cardiac magnetic resonance imaging.* Two representative anaesthetized animals from both groups were used for *in vivo* computed tomography (CT) and cardiac magnetic resonance imaging (MRI) scans to visualize possible calcification and evaluate the valve function *in vivo*. Settings and equipment are described in detail in Supplementary Materials Methods.

Histological analysis

After being implanted for 12 months, the heart valve explants were embedded in paraffin (Merck, Darmstadt, Germany). For general morphological analysis, representative 3 µm sections were stained with haematoxylin-eosin, Elastica van Gieson and Movat pentachrome Verhoeff stains. Van Kossa stain was used to detect calcium deposits. CD3 (DCS, Hamburg, Germany) and chloracetate esterase stain were performed to identify T cells and leukocytes, respectively.

Near-infrared multiphoton imaging

One leaflet of each explant was placed individually in 100-ml volumes of ice-cold DMEM with 4.5 g/l glucose and antibiotic mix (1.2 g/l amikacin, 3 g/l flucytosine, 1.2 g/l vancomycin, 0.3 g/l ciprofloxacin, 1.2 g/l metronidazole). Tissues were analysed within 72 h after explantation. A custom-build multiphoton laser system (JenLab GmbH, Jena, Germany) as previously described [17] was used for simultaneous autofluorescence and second harmonic generation imaging. Photomultiplier tube settings for each measurement were 1000 V for contrast and 52.7% for brightness. The attenuator power of the laser was set to 20 mW and the chosen excitation wavelength was 760 nm. The leaflets were placed in a glass-bottom dish (ibidi GmbH, Martinsried, Germany) with phosphate-buffered saline (PBS) and put on the microscope sample holder (40× oil immersion objective; N.A. 1.3; Carl Zeiss, Jena, Germany). Three spots in the ventricularis and fibrosa layers of each tissue were imaged. Crimp amplitude and period were determined for collagen fibre characterization in the fibrosa.

Raman spectroscopy

A customized Raman spectrometer [18] was used to obtain spectra of all leaflets that were used for multiphoton imaging obtained within 48 h after explanation as previously described [14]. In addition, native control pulmonary leaflets and a non-transplanted leaflet of IFC and FC were measured. Leaflets were dissected from the pulmonary root and placed in a glass-bottom dish (ibidi GmbH) in phosphate-buffered saline, with the fibrosa layer facing the bottom. Measurements were taken with a 60× water immersion objective (N.A. 1.2; Olympus, Japan). Collagen structures were targeted by the confocal brightfield imaging function of the microscope (cellB; Olympus Soft Imaging Solutions, Muenster, Germany) and 30 spots per tissue of the collagen fibres were randomly selected. Laser power was set to 85 mW, and spectra were acquired at an exposure time of 100 sec. Spectral data were processed prior to multivariate data analysis by spectroscopy software OPUS 4.2 (Bruker Optik GmbH, Ettlingen, Germany).

Enzyme-linked immunosorbent assay

Segments of each leaflet were used for the enzyme-linked immunosorbent assay (ELISA). ETDA-free protease inhibitor cocktail (complete mini, Roche Diagnostics, Mannheim, Germany) was added to the radioimmunoprecipitation assay lysis buffer (Thermo Fisher Scientific, Waltham, MA, USA) in the ratio 1:10. Tissue and lysis solution (15 µl/mg tissue) were put in innuSpeed lysis tubes (Analytik Jena AG, Jena, Germany) and processed for 2 × 4 min in a SpeedMill Plus homogenizer (Analytik Jena AG). After 2 h of incubation on ice, lysates were centrifuged, and supernatants were frozen at -80°C. The supernatants were utilized for sheep collagen I ELISA (Neobiolab, Cambridge, MA, USA).

Statistical analysis

Statistical analyses were conducted with Prism 6 (GraphPad, La Jolla, CA, USA). Data are represented as the median and the interquartile range due to the small sample size. Data were checked for normality. Unpaired parametric *t*-tests or the non-parametric Mann–Whitney tests were performed for 2-sample comparisons. Differences between the 3 groups were assessed with an ordinary non-matched analysis of variance or the Kruskal–Wallis test. Pairwise comparisons were done with the Bonferroni correction for multiple comparisons. All statistical tests were 2-sided, and *P*-values of 0.05 or less were considered statistically significant.

Spectral data analysis to identify matrix-specific peak shifts and spectral differences was performed by principal component analysis (PCA) using the multivariate data analysis software, The Unscrambler® (CAMO, Oslo, Norway). Data were vector normalized, and PCA calculated 7 principal components (PCs) based on a non-linear iterative partial least squares algorithm. Each PC defines certain spectral information describing spectral similarities or differences. The score values and the loadings plot were compared to define the most relevant PC for ECM-related spectral characteristics.

RESULTS

Twelve successful pulmonary heart valve transplantations were performed. After 7 months with the implanted heart valves, 1 animal of the IFC group was excluded due to bacterial endocarditis.

Downloaded from https://academic.oup.com/ejcts/article-abstract/55/3/484/5079309 by Klinikbibliothek Schnarrenberg user on 26 February 2019

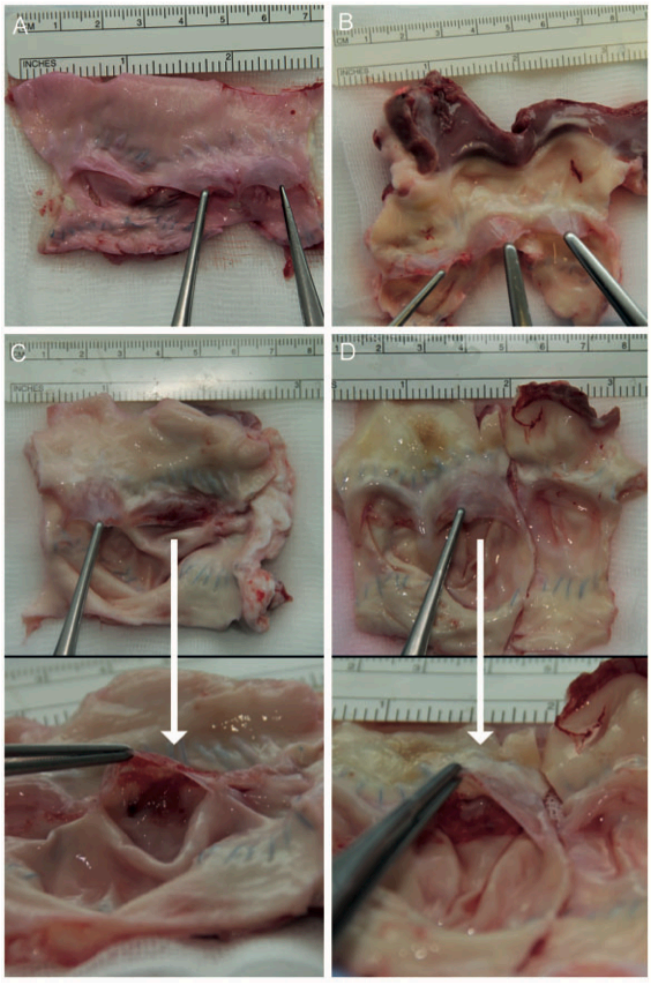

Figure 1: Gross morphology of representative ice-free cryopreserved (**A**, **B**) and frozen cryopreservation (**C**, **D**) heart valves after explantation. The leaflets in both groups were thin with translucent leaflets (**A**, **C**). One heart valve from each group showed a slightly thickened and inflamed cusp (indicated with arrows) (**C**, **D**).

Six animals of the FC and 5 animals of the IFC group survived the entire 12 months.

Gross morphology

For both groups, thin and translucent leaflets were obtained (Fig. 1A and C). Minor inflammation in 1 valve of each group was detectable on the arterial side of the leaflet (Fig. 1B and D).

Cardiovascular imaging results

No valvular stenosis with subsequent right heart failure was observed in either group. All animals developed minimal pulmonary insufficiency (50 ± 6% weight gain between implantation and explantation). Elevated values for the maximum flow velocity out of the right ventricle outflow tract, for peak pressure gradients, and for the right ventricular end-diastolic diameter were detected for the FC group. However, only right ventricular end-diastolic diameter values were increased with statistical significance compared to the IFC group (Fig. 2A–D, Supplementary Material, Table S1). Additional individual *in vivo* cardiac MRI scans confirmed the maximum flow velocity out of the right ventricle outflow tract and very small regurgitation fractions, indicating a minimal or rather a physiological pulmonary insufficiency [19] for the representative animals of each group.

Histology

Histological analysis revealed FC valves to be more frequent (3/6) and more severely inflamed compared to IFC valves. Although the IFC heart valve leaflets were virtually acellular, FC inflamed leaflets were infiltrated, and a mild to moderate pannus formed on the ventricularis side (Fig. 3A–P). Leaflet tip thickening was detected in the FC group, whereas the IFC leaflet tip diameter

Downloaded from https://academic.oup.com/ejcts/article/55/3/484/5079309 by Klinikbibliothek Schnarrenberg user on 26 February 2019

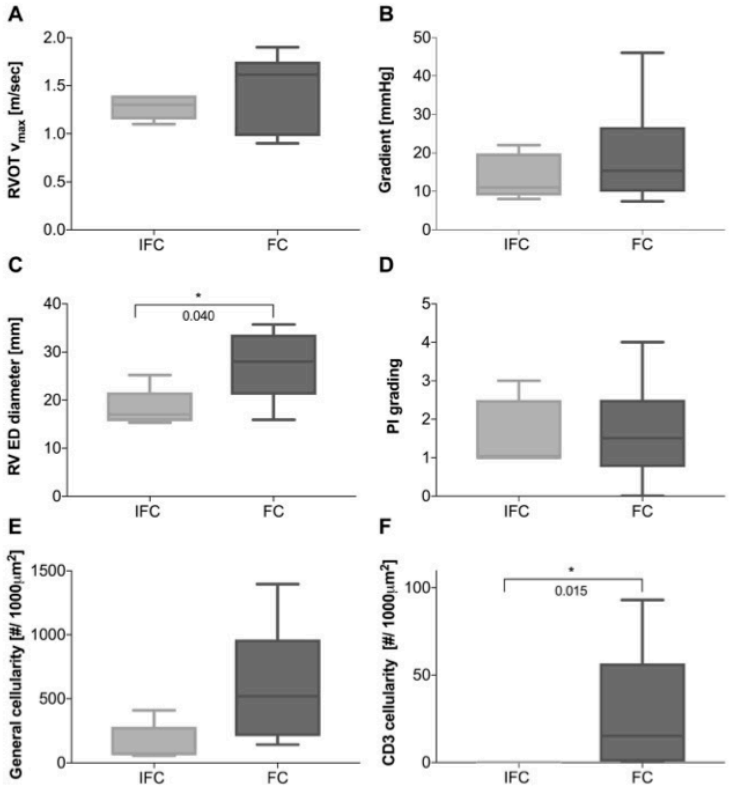

Figure 2: Haemodynamic and histomorphological data of IFC ($n = 5$) and FC ($n = 6$) valves. Haemodynamic *in vivo* function was evaluated with Doppler echocardiography (CX50, Philips, Hamburg, Germany). The maximum blood flow through the RVOT v_{max} (**A**), the peak pressure gradient (**B**), the RV ED diameter (**C**) and the graded PI (**D**) (categories: 0 = none, 1 = minimal, 2 = mild, 3 = moderate, 4 = severe) are displayed. For the histomorphological analysis, the area of the leaflet with the general and CD3 positive cell count of each representative valve was determined with AxioVision Software for routine bright-field light microscopy (Axio Observer Z1, Carl Zeiss, Göttingen, Germany). The general (**E**) and CD3 (**F**) cellularity is presented as cells per 1000 µm^2. *P-values of 0.05 or less were considered statistically significant. FC: frozen cryopreservation; IFC: ice-free cryopreserved; PI: pulmonary insufficiency; RV ED: right ventricular end diastolic; RVOT v_{max}: maximum flow velocity out of the right ventricle outflow tract.

was reduced (leaflet tip diameter: native: 207.4 ± 4 µm; FC: 233.8 ± 96.3 µm; IFC: 96.3 ± 43.5 µm). The thickened FC leaflets had a less condensed pars fibrosa and pars ventricularis. In contrast, the IFC leaflets had a more condensed pars fibrosa and pars ventricularis with condensed elastin fibres (Fig. 3F, G, J, K).

CD3 staining was performed to identify T cells (Fig. 4). Comparable to the native control (Fig. 4A), no CD3-positive T cells were found in the acellular IFC leaflets (Fig. 2E, F; Fig. 4B; Supplemental Table 1). Moderate T-cell infiltration was detected in the thickened areas of the infiltrated FC valves with sporadic T cells present in the pannus (Fig. 4D). Sporadic T cells were observed in the hinge region near the former muscle band and the sutures for both groups (Fig. 4E–H). T cells were present in the conduit in the tunica externa with signs of neovascularization. Infiltration by leukocytes was analysed using chloracetate esterase stain. No granulocytes or monocytes were found in valve leaflets of either group. Sporadic monocytes with a granulated cytoplasm were detected near the former suture points for both groups, as shown in the representative IFC section (Fig. 4I).

Neither group had calcifications in the leaflet or hinge region. Minor calcifications were detected next to the sutures. *In vivo* CT scans confirmed these findings (Supplementary Material, Fig. S1).

Multiphoton imaging

Multiphoton laser-induced autofluorescence imaging and second harmonic generation microscopy were used to image collagen and elastic fibres (Fig. 5). In comparison to microscopic bright-field images (Fig. 5A–C), the main ECM components were clearly distinguishable. In all tissues, the fibrosa was characterized by parallel alignment of collagen bundles with disorganized structures in the ventricularis. Native and IFC leaflets showed similar matrix structures. Less aligned, deteriorated and straightened collagen fibre structures were found in FC-treated tissues (Fig. 5D–F). The fibrosa of the FC leaflets showed significant differences in the crimp period and amplitude, which were comparable for native and IFC leaflets (Fig. 5K and I). The ventricularis layer revealed a more disorganized overall pattern in FC than in IFC (Fig. 5G–I).

Elastin structures were visibly more disrupted in the FC group and better preserved in IFC-treated tissues. Increased density of elastic fibres was observed in the IFC-treated leaflets on the ventricularis side compared to the native tissue. Despite the less aligned structures, the signal intensity remained similar for the native, FC and IFC tissues. Multiphoton autofluorescence imaging

Downloaded from https://academic.oup.com/ejcts/article-abstract/55/3/484/5079309 by Klinikbibliothek Schnarrenberg user on 26 February 2019

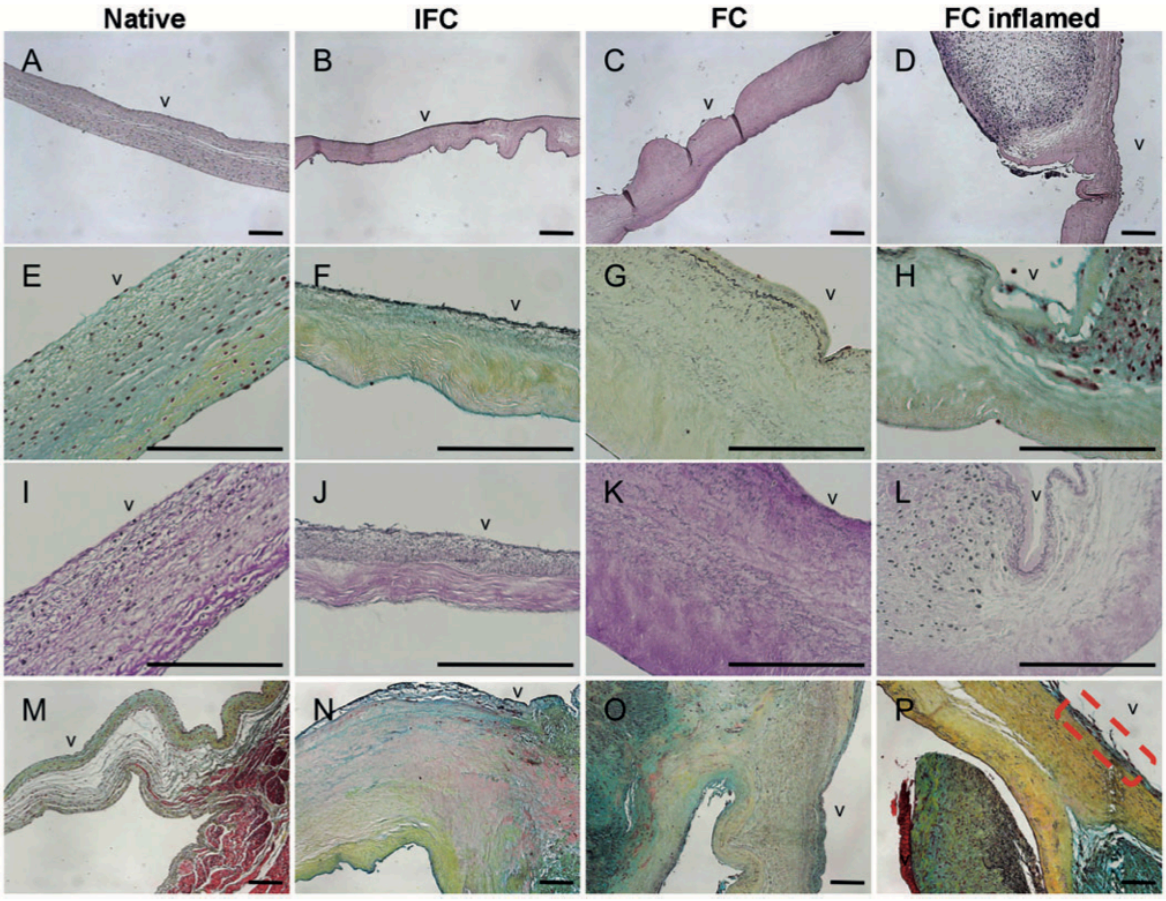

Figure 3: Histomorphological data of representative native control, IFC and FC leaflets. The leaflet belly (**A–L**) with the arterial and ventricular (v) side and the hinge region (**M–P**) were displayed. Haematoxylin-eosin (**A–D**), movat pentachrome (**E–H**, **M–P**) and elastica von Gieson (**I–L**) staining were performed. IFC valves showed thin, acellular leaflets (**B**, **F**, **J**, **N**). Three out of 6 FC valves had cell-free, thin leaflets with sporadic cells on the borders (**C**, **G**, **K**, **O**). The other 3 leaflets (**D**, **H**, **L**, **P**) showed thickened and severely infiltrated regions. A mild to moderate pannus formation, correlating to the intensity of leaflet infiltration, was detected for these valves (**P**: dashed rectangle). IFC leaflets were more condensed, whereas FC leaflets had thickened leaflets with looser structures. Scale bar equals 200 μm. FC: frozen cryopreservation; IFC: ice-free cryopreserved.

only allowed a qualitative interpretation of the ventricularis integrity, revealing structural damages, especially in the FC group.

Raman analysis of fibrosa extracellular matrix structures

Raman spectroscopic analyses of the ECM structures of the fibrosa of native control pulmonary valves and of transplanted and non-transplanted IFC and FC valves were performed for an in-depth study of changes in the collagen. PCA was applied to evaluate spectral differences between the individual groups. PC2 revealed distinct clustering of overlapping native and IFC tissue data in the negative range and FC tissue data in the positive range (Fig. 6A). The mean score values of PC2 indicated significant differences between FC and native data but not between IFC and native tissues (Fig. 6B). Five peaks correlating to a certain molecular bond in the collagen molecule [20] were identified in the loadings plot (Fig. 6C) and displayed the most influencing peaks on spectral differences in the fingerprint region. Single peak shifts but no decrease in the overall ECM fingerprint intensity were detected. These results were consistent with no decreased Col I content in FC leaflets quantified by Col I ELISA (Fig. 6D).

PCA of native, non-transplanted and transplanted tissues showed distinctly higher scores for the non-transplanted tissues compared to the transplanted equivalents (Supplementary Material, Fig. S2). Transplanted and non-transplanted IFC tissues showed no significant differences in their scores. The differences in the transplanted and non-transplanted FC tissues were highly significant. A general shift towards the native molecular pattern of collagen structures was seen in both transplanted groups. Importantly, the IFC group was more similar to the native group than the FC group.

DISCUSSION

Structural deterioration and inflammatory processes are long-term obstacles of the current state-of-the-art frozen

Downloaded from https://academic.oup.com/ejcts/article/55/3/484/5079309 by Klinikbibliothek Schnarrenberg user on 26 February 2019

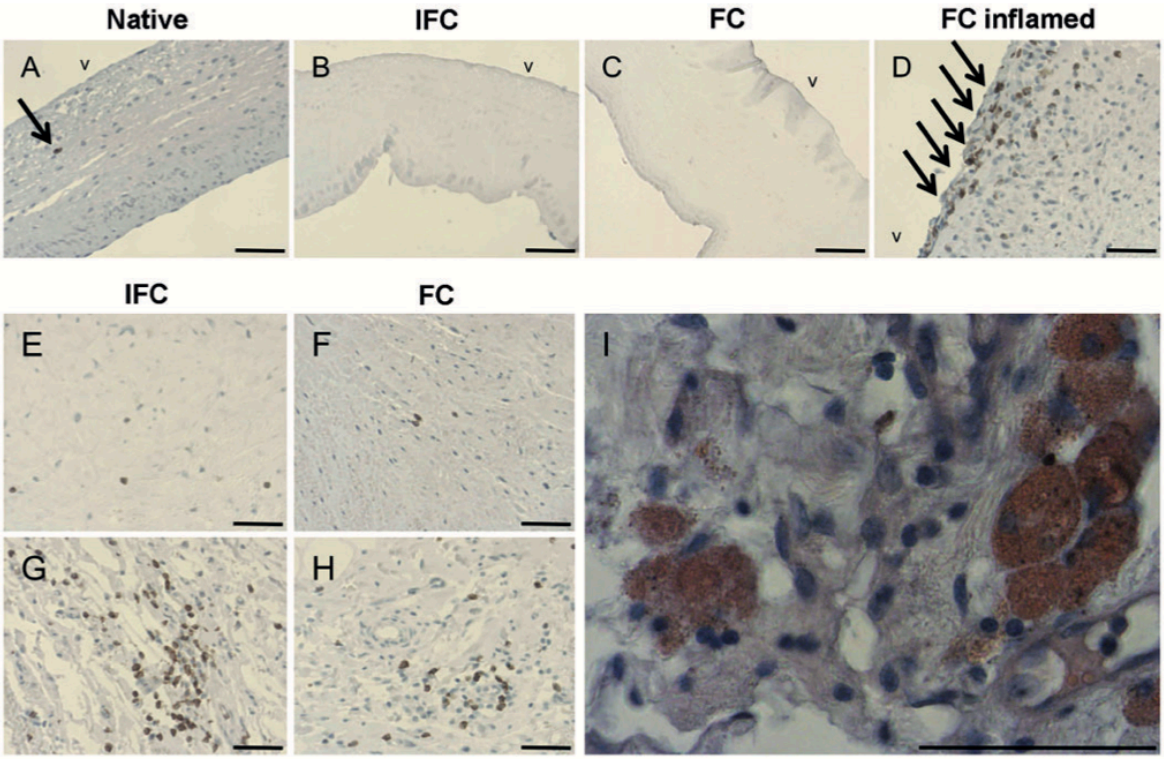

Figure 4: CD3 (**A–H**) and chloracetate esterase (**I**) representative sections of the native control (**A**) and the IFC (**B**, **E**, **F**, **I**) and FC (**C**, **D**, **F**, **H**) valves. T cells were abundantly present in the leaflet belly (**A–D**) of the FC-inflamed valve (**D**). Both groups had similar levels of T-cell infiltration in the hinge region (**E**, **F**) and near the sutures lines (**G**, **H**). No granulocytes, but sporadic monocytes near the suture lines, were detected for both groups (**I**). Scale bar equals 50 µm. FC: frozen cryopreservation; IFC: ice-free cryopreserved.

cryopreserved heart valves used in clinical practice. This study demonstrated that these shortcomings can be overcome by using IFC valves due to the protection and maintenance of natural ECM structures, resulting in outstanding long-term function of acellular grafts. We implanted IFC and FC heart valves in an orthotropic sheep model, a common cardiovascular model for biological heart valves [21]. Our extended *in vivo* testing over 1 year correlates to approximately 40 million wear cycles [22, 23] and corresponds to roughly 18 years of implantation in humans. Different sheep strains (donor: Dorset cross sheep; recipient: Merino sheep) were used to obtain a true allogeneic model, which better simulates the naturally occurring, more extensive genetic differences among humans. According to the American Association of Tissue Banks guidelines, the standard protocol was applied for FC to ensure state-of-the-art preservation for heart valve transplants.

At the time of explantation, IFC heart valves showed well-preserved ECM integrity. IFC valves exhibited excellent function with leaflets remaining acellular and a sporadically cellularized conduit wall, indicating that recellularization was not fundamentally important for long-term function. Three out of 6 FC valves revealed early signs of long-term graft failure. Leaflet thickening and moderate T-cell infiltration were detected, both of which are known to be responsible for early degeneration [24, 25]. Deep tissue analysis of FC valves revealed no signs of remaining native cells.

The ECM of the leaflets has to withstand extreme biomechanical demands due to major deformation processes and large sheer stresses [23, 26]. Therefore, we focused on the analysis of the architecture of leaflet ECM fibres. We hypothesized that, by maintaining the structural integrity of the ECM, the degeneration processes can be reduced or even avoided, thereby preventing long-term failure of heart valve implants [6, 27]. Multiphoton imaging demonstrated collagen and elastin degradation similar to that found in mid-term implanted (7 months) FC valves [11]. Consequently, previously described destructive effects of standard cryopreservation due to intratissue ice formation [28] were detected in the FC group even 1 year after implantation. Moreover, a severely impaired collagen crimp structure of the FC valves with a crimp altitude decrease of 2.4-fold and a 2.2-fold increase in the crimp period, indicated long-term failure and loss of biomechanical sustainability. The loss of the characteristic crimp structure of collagen Type I in the fibrosa has previously been associated with reduced flexural rigidity of tissue valves [29]. In contrast to FC leaflets, native-like matrix structures in the IFC leaflets were detected after explantation. Additional PCA results

Downloaded from https://academic.oup.com/ejcts/article-abstract/55/3/484/5079309 by Klinikbibliothek Schnarrenberg user on 26 February 2019

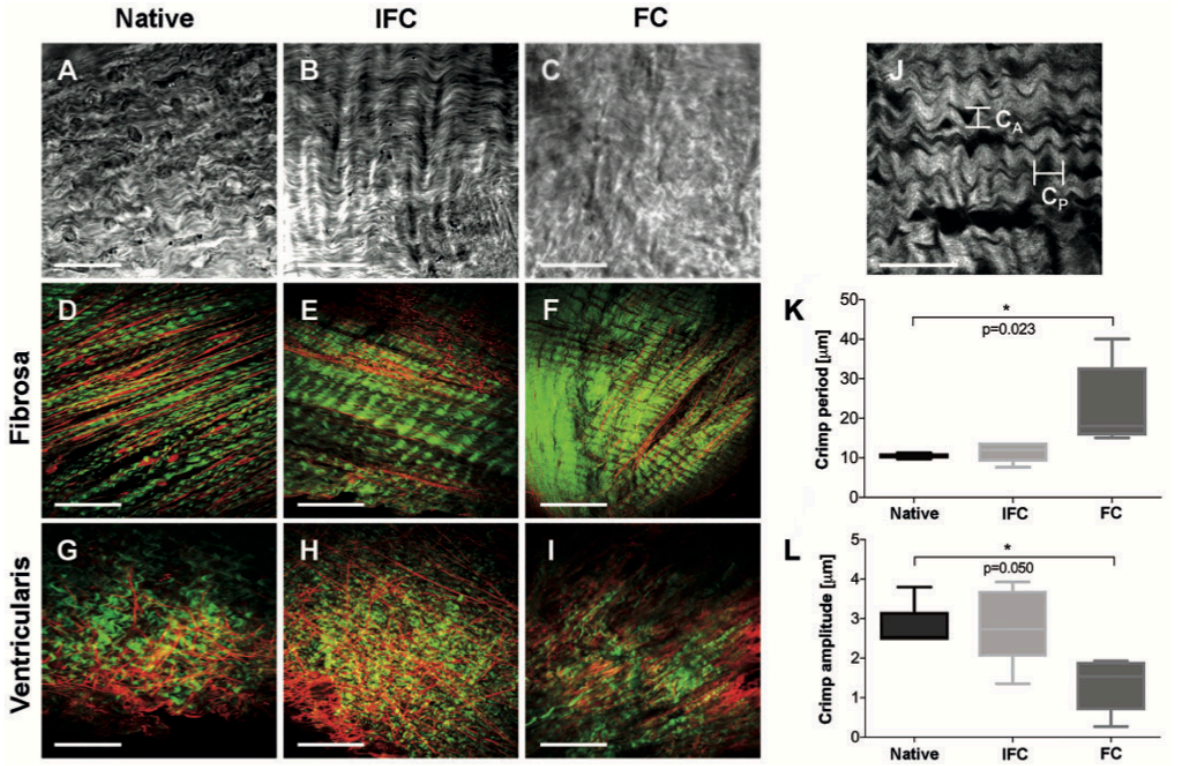

Figure 5: Brightfield (**A–C**) and multiphoton (**D–I**) images of fibrosa and ventricularis of native and transplanted leaflets. Collagen and elastic fibres of the fibrosa showed parallel alignment (**A–F**); there was no ordered structure in the ventricularis (**G–I**). FC leaflets (**C**, **F**, **I**) showed deteriorated collagen structures. IFC leaflets (**B**, **E**, **H**) resembled the arrangement of the native matrix structures (**A**, **D**, **G**). (**J**) Crimp period (C_P) and crimp amplitude (C_A) were determined and showed significant differences for FC-treated leaflets; $n = 5$ (**K**, **L**). Green: collagen, red: elastic fibres, cells; Scale bar: brightfield equals 20 µm, multiphoton equals 60 µm. *P-values of 0.05 or less were considered statistically significant. FC: frozen cryopreservation; IFC: ice-free cryopreserved.

of Raman spectroscopy analysis of collagen confirmed that the IFC group had native-like collagen structures after being implanted for 12 months, whereas the FC group showed a lack of integrity of the matrix. Raman enabled the non-destructive detection of ECM changes at the molecular level. Specific changes in certain molecular bonds in collagen instead of general collagen degeneration were shown, with PCA loading plots indicating no degradation processes in the FC leaflet. Additional collagen quantification determined by applying ELISA demonstrated that the overall collagen content was not reduced after 12 months in FC allografts compared to IFC grafts.

PCA including non-transplanted leaflets showed distinct differences between native and non-transplanted preserved tissues with a shift towards native-like PC2 score values after implantation in both groups. Those results need to be analysed carefully because of the lack of statistical significance due to of the lack of non-transplanted tissues. Nevertheless, we hypothesize that this shift can be observed due to dehydration of tissue during FC and IFC cryopreservation. The tissue might not be fully hydrated after thawing. Additional passive mechanically driven rearrangements of collagen might also occur over time due to the major deformation processes and large sheer stresses. Additional Raman analyses of tissue hydration processes and potential *ex vivo* bioreactor experiments might offer deeper insight.

CONCLUSION

In summary, IFC offers a preferable preservation method compared to FC. Despite the small number of animals in this expensive large-animal model and limited cardiac MRI data sets for all animals, we successfully demonstrated a distinct improvement in long-term function with regard to immunogenicity and true ECM preservation. Moreover, our preservation method has additional economical, financial, logistical and processing advantages because it involves less complex and less expensive equipment. Processing and storage at only -80°C, shipment in dry ice and easier preservation protocols result in a cost effective method applicable even in developing countries. We are convinced that transplanted IFC pulmonary heart valves will be superior in a clinical setting compared to standard FC grafts. This hypothesis is supported by Neumann *et al.* [30], who observed favourable long-term haemodynamic results over 8 years of follow-up and no cellular immune responses over 36 months for fresh decellularized allografts in young adults and children. We postulate that the remaining cells or the repopulation of cells is not required for good long-term function of the allogeneic valves. Possible devitalization or even decellularization processes with the aid of the IFC solution should be elucidated in the future due to its ease and cost-effectiveness. IFC represents a promising new technique for maintaining a more natural ECM makeup and minimizing the immunological reactions *in vivo*.

Downloaded from https://academic.oup.com/ejcts/article/55/3/484/5079309 by Klinikbibliothek Schnarrenberg user on 26 February 2019

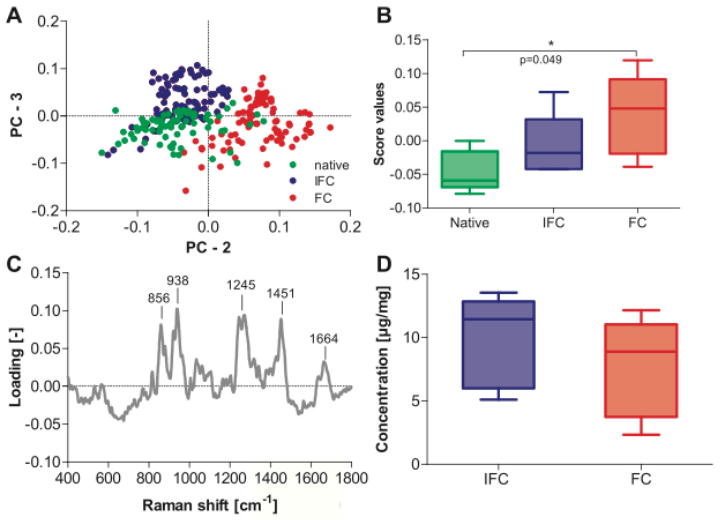

E

molecular group	C-C (hydroxyprolin)	C-C (col backbone)	amid III	CH2/CH3 deformation	amid I
position [cm^{-1}]	856	938	1245	1451	1664

Figure 6: Multivariate data analysis. (**A**) Principal component analysis scores plot; FC tissue data were clustered, whereas IFC and native tissue data overlapped. Each spot correlates with a single spectrum. (**B**) Score values of PC2. Significant difference between FC and native tissue but not between IFC and native leaflet is shown. *$P = 0.05$, $n = 5$. (**C**) Loadings plot of PC2 identified outstanding peaks characterizing certain molecular bonds specific in collagen. (**D**) Collagen I enzyme-linked immunosorbent assay (µg collagen/mg tissue) showed no significant decrease in FC leaflets compared to IFC leaflets. (**E**) Significant collagen peaks of the loadings plots and their correlating molecular groups. FC: frozen cryopreservation; IFC: ice-free cryopreserved; PC: principal component.

SUPPLEMENTARY MATERIAL

Supplementary material is available at *EJCTS* online.

ACKNOWLEDGEMENTS

We thank Harald Keller and Eva Knoepfler for technical assistance with the cardiopulmonary perfusion.

Funding

This work was supported by the German Research Foundation [Sto 359/10-1 to U.A.S., SCHE 701/10-1 and INST 2388/30-1 to K.S.-L.] and the Ministry of Baden-Wuerttemberg for Sciences, Research and Arts [33-729.55-3/214 and SI-BW 01222-91]. K.G.M.B. was supported by the National Institute of Allergy and Infectious Disease, National Institutes of Health [grant R43 AI114486].

Conflict of interest: Julian L. Wichmann received speaker fees from GE Healthcare and Siemens Healthcare. Kelvin GM Brockbank is the owner and the employee of Tissue Testing Technologies LLC.

REFERENCES

[1] Mayer JE. In search of the ideal valve replacement device. J Thorac Cardiovasc Surg 2001;122:8–9.
[2] Ross D. Homograft replacement of the aortic valve. Lancet 1962;2:487.
[3] Tuna IC, Orszulak TA, Schaff HV, Danielson GK. Results of homograft aortic valve replacement for active endocarditis. Ann Thorac Surg 1990; 49:619–24.
[4] Stock UA. Searching for the optimal heart valve. Biotechnol J 2013;8: 286–7.
[5] American Association of Tissue Banks. Standard for Tissue Banking. American Association of Tissue Banks, 2012. http://aatb.kma.net/aatb/files/ccLibraryFiles/Filename/000000001225/AATB%20Standards%20for%20Tissue%20Banking%2013th%20edition%202-17-16.pdf (1 August 2018, date last accessed).
[6] Mitchell RN, Jonas RA, Schoen FJ. Pathology of explanted cryopreserved allograft heart valves: comparison with aortic valves from orthotopic heart transplants. J Thorac Cardiovasc Surg 1998;115:118–27.
[7] Brown JW, Ruzmetov M, Rodefeld MD, Vijay P, Turrentine MW. Right ventricular outflow tract reconstruction with an allograft conduit in non-Ross patients: risk factors for allograft dysfunction and failure. Ann Thorac Surg 2005;80:655–64.
[8] Mayer JE. Uses of homograft conduits for right ventricle to pulmonary artery connections in the neonatal period. Semin Thorac Cardiovasc Surg 1995;7:130–2.
[9] Bonhoeffer P, Boudjemline Y, Saliba Z, Merckx J, Aggoun Y, Bonnet D *et al.* Percutaneous replacement of pulmonary valve in a right-ventricle to pulmonary-artery prosthetic conduit with valve dysfunction. Lancet 2000;356:1403–5.
[10] Joudinaud TM, Baron F, Raffoul R, Pagis B, Vergnat M, Parisot C *et al.* Redo aortic root surgery for failure of an aortic homograft is a major technical challenge. Eur J Cardiothorac Surg 2008;33:989–94.
[11] Lisy M, Pennecke J, Brockbank KG, Fritze O, Schleicher M, Schenke-Layland K *et al.* The performance of -free cryopreserved heart valve allografts in an orthotopic pulmonary sheep model. Biomaterials 2010;31:5306–11.
[12] Schenke-Layland K, Madershahian N, Riemann I, Starcher B, Halbhuber K-J, König K *et al.* Impact of cryopreservation on extracellular matrix structures of heart valve leaflets. Ann Thorac Surg 2006;81:918–26.
[13] Schenke-Layland K, Xie J, Heydarkhan-Hagvall S, Hamm-Alvarez SF, Stock UA, Brockbank KG *et al.* Optimized preservation of extracellular matrix in cardiac tissues: implications for long-term graft durability. Ann Thorac Surg 2007;83:1641–50.

Downloaded from https://academic.oup.com/ejcts/article-abstract/55/3/484/5079309 by Klinikbibliothek Schnarrenberg user on 26 February 2019

[14] Votteler M, Carvajal Berrio DA, Pudlas M, Walles H, Stock UA, Schenke-Layland K. Raman spectroscopy for the non-contact and non-destructive monitoring of collagen damage within tissues. J Biophoton 2012;5:47–56.
[15] Brockbank KG, Chen Z, Greene ED, Campbell LH. Vitrification of heart valve tissues. In Wolkers WF, Oldenhof H (eds). Cryopreservation and Freeze-Drying Protocols. New York, NY: Springer, 2015, pp. 399–421.
[16] Stock UA, Nagashima M, Khalil PN, Nollert GD, Herdena T, Sperling JS *et al.* Tissue-engineered valved conduits in the pulmonary circulation. J Thorac Cardiovasc Surg 2000;119:732–40.
[17] Monaghan MG, Kroll S, Brucker SY, Schenke-Layland K. Enabling multiphoton and second harmonic generation imaging in paraffin-embedded and histologically stained sections. Tissue Eng Part C Methods 2016;22:517–23.
[18] Pudlas M, Berrio DAC, Votteler M, Koch S, Thude S, Walles H *et al.* Non-contact discrimination of human bone marrow-derived mesenchymal stem cells and fibroblasts using Raman spectroscopy. Med Laser Appl 2011;26:119–25.
[19] Zoghbi WA, Adams D, Bonow RO, Enriquez-Sarano M, Foster E, Grayburn PA *et al.* Recommendations for noninvasive evaluation of native valvular regurgitation: a report from the American Society of Echocardiography developed in collaboration with the Society for Cardiovascular Magnetic Resonance. J Am Soc Echocardiogr 2017;30:303–71.
[20] Frushour BG, Koenig JL. Raman scattering of collagen, gelatin, and elastin. Biopolymers 1975;14:379–91.
[21] DiVincenti J, Westcott R, Lee C. Sheep (*Ovis aries*) as a model for cardiovascular surgery and management before, during, and after cardiopulmonary bypass. J Am Assoc Lab Anim Sci 2014;53:439–48.
[22] Lisy M, Kalender G, Schenke-Layland K, Brockbank KG, Biermann A, Stock UA. Allograft heart valves: current aspects and future applications. Biopreserv Biobank 2017;15:148–57.
[23] Joyce EM, Liao J, Schoen FJ, Mayer JE, Sacks MS. Functional collagen fiber architecture of the pulmonary heart valve cusp. Ann Thorac Surg 2009;87:1240–9.
[24] Legare JF, Lee TD, Creaser K, Ross DB. T lymphocytes mediate leaflet destruction and allograft aortic valve failure in rats. Ann Thorac Surg 2000;70:1238–45.
[25] Biermann AC, Marzi J, Brauchle E, Schneider M, Kornberger A, Abdelaziz S *et al.* Impact of T-cell-mediated immune response on xenogeneic heart valve transplantation: short-term success and mid-term failure. Eur J Cardiothorac Surg 2017;53:784–92.
[26] Nejad SP, Blaser MC, Santerre JP, Caldarone CA, Simmons CA. Biomechanical conditioning of tissue engineered heart valves: too much of a good thing? Adv Drug Deliv Rev 2016;96:161–75.
[27] Schoen F. Aortic valve structure-function correlations: role of elastic fibers no longer a stretch of the imagination. J Heart Valve Dis 1997;6:1.
[28] Brockbank K, Lightfoot F, Song YC, Taylor M. Interstitial ice formation in cryopreserved homografts: a possible cause of tissue deterioration and calcification in vivo. J Heart Valve Dis 2000;9:200–6.
[29] Sacks MS, Schoen FJ. Collagen fiber disruption occurs independent of calcification in clinically explanted bioprosthetic heart valves. J Biomed Mater Res 2002;62:359–71.
[30] Neumann A, Sarikouch S, Breymann T, Cebotari S, Boethig D, Horke A *et al.* Early systemic cellular immune response in children and young adults receiving decellularized fresh allografts for pulmonary valve replacement. Tissue Eng Part A 2014;20:1003–11.

Downloaded from https://academic.oup.com/ejcts/article/55/3/484/5079309 by Klinikbibliothek Schnarrenberg user on 26 February 2019

Appendix II: A.C. Biermann, J Marzi, E.M. Brauchle, M Schneider, A Kornberger, S Abdelaziz, J.L. Wichmann, C.T. Arendt, E Nagel, K.G.M. Brockbank, M Seifert, K Schenke-Layland, U.A. Stock, *Impact of T-cell-mediated immune response on xenogeneic heart valve transplantation: short-term success and mid-term failure*, European Journal of Cardiothoracic Surgery, 2018; 53(4): 784-792

European Journal of Cardio-Thoracic Surgery 53 (2018) 784–792
doi:10.1093/ejcts/ezx396 Advance Access publication 27 November 2017

ORIGINAL ARTICLE

Cite this article as: Biermann AC, Marzi J, Brauchle E, Schneider M, Kornberger A, Abdelaziz S *et al.* Impact of T-cell-mediated immune response on xenogeneic heart valve transplantation: short-term success and mid-term failure. Eur J Cardiothorac Surg 2018;53:784–92.

Impact of T-cell-mediated immune response on xenogeneic heart valve transplantation: short-term success and mid-term failure

Anna C. Biermann[a,b,c,*], Julia Marzi[c,d], Eva Brauchle[c,d], Maria Schneider[e,f], Angela Kornberger[g], Sherif Abdelaziz[a], Julian L. Wichmann[h], Christophe T. Arendt[h], Eike Nagel[h], Kelvin G.M. Brockbank[i,j], Martina Seifert[e,f], Katja Schenke-Layland[c,d,k] and Ulrich A. Stock[a,b,l,m]

[a] Department of Thoracic and Cardiovascular Surgery, University Hospital Frankfurt, Goethe University, Frankfurt am Main, Germany
[b] Department of Cardiothoracic Surgery, Royal Brompton and Harefield Foundation Trust, Harefield, UK
[c] Department of Women's Health, Research Institute for Women's Health, Eberhard-Karls-University, Tuebingen, Germany
[d] Department of Cell and Tissue Engineering, Fraunhofer Institute for Interfacial Engineering and Biotechnology (IGB), Stuttgart, Germany
[e] Institue of Medical Immunology, Charité – Universitätsmedizin Berlin, corporate member of Freie Universität Berlin, Humboldt-Universität zu Berlin, Berlin Institute of Health, Berlin, Germany
[f] Berlin-Brandenburg Center of Regenerative Therapies (BCRT), Charité – Universitätsmedizin Berlin, corporate member of Freie Universität Berlin, Humboldt-Universität zu Berlin, Berlin Institute of Health, Berlin, Germany
[g] Department of Cardiothoracic and Vascular Surgery, Johannes Gutenberg-University, Mainz, Germany
[h] Department of Diagnostic and Interventional Radiology, University Hospital Frankfurt, Goethe University, Frankfurt am Main, Germany
[i] Tissue Testing Technologies LLC, North Charleston, SC, USA
[j] Department of Bioengineering, Clemson University, North Charleston, SC, USA
[k] Department of Medicine / Cardiology, Cardiovascular Research Laboratories, David Geffen School of Medicine at UCLA, Los Angeles, CA, USA
[l] Faculty of Medicine, Imperial College London, London, UK
[m] Magdi Yacoub Institute, Heart Science Centre, Harefield, UK

* Corresponding author. Department of Thoracic and Cardiovascular Surgery, University Hospital Frankfurt, Goethe University, Theodor-Stern-Kai 7, Frankfurt am Main, Germany. Tel: +49-69-63016500; fax: +49-69-63017108; e-mail: annabiermann@hotmail.com (A.C. Biermann).

Received 20 July 2017; received in revised form 11 October 2017; accepted 23 October 2017

Abstract

OBJECTIVES: Allogeneic frozen cryopreserved heart valves (allografts or homografts) are commonly used in clinical practice. A major obstacle for their application is the limited availability in particular for paediatrics. Allogeneic large animal studies revealed that alternative ice-free cryopreservation (IFC) results in better matrix preservation and reduced immunogenicity. The objective of this study was to evaluate xenogeneic (porcine) compared with allogeneic (ovine) IFC heart valves in a large animal study.

METHODS: IFC xenografts and allografts were transplanted in 12 juvenile merino sheep for 1–12 weeks. Immunohistochemistry, *ex vivo* computed tomography scans and transforming growth factor-β release profiles were analysed to evaluate postimplantation immunopathology. In addition, near-infrared multiphoton imaging and Raman spectroscopy were employed to evaluate matrix integrity of the leaflets.

RESULTS: Acellular leaflets were observed in both groups 1 week after implantation. Allogeneic leaflets remained acellular throughout the entire study. In contrast, xenogeneic valves were infiltrated with abundant T-cells and severely thickened over time. No collagen or elastin changes could be detected in either group using multiphoton imaging. Raman spectroscopy with principal component analysis focusing on matrix-specific peaks confirmed no significant differences for explanted allografts. However, xenografts demonstrated clear matrix changes, enabling detection of distinct inflammatory-driven changes but without variations in the level of transforming growth factor-β.

CONCLUSIONS: Despite short-term success, mid-term failure of xenogeneic IFC grafts due to a T-cell-mediated extracellular matrix-triggered immune response was shown.

Keywords: Ice-free cryopreservation • Heart valve transplantation • Allograft • Xenograft • T-cell-mediated immune response • Organ scarcity

Downloaded from https://academic.oup.com/ejcts/article-abstract/53/4/784/4662953 by Klinikbibliothek Schnarrenberg user on 26 February 2019

Reprinted with permission from A.C. Biermann, J Marzi, E.M. Brauchle, M Schneider, A Kornberger, S Abdelaziz, J.L. Wichmann, C.T. Arendt, E Nagel, K.G.M. Brockbank, M Seifert, K Schenke-Layland, U.A. Stock, *Impact of T-cell-mediated immune response on xenogeneic heart valve transplantation: short-term success and mid-term failure*, European Journal of Cardiothoracic Surgery, 2018; 53(4): 784-792.Copyright 2019 Oxford University Press

INTRODUCTION

Human allogeneic heart valves are almost perfect heart valve replacements, offering optimal haemodynamic properties, outstanding resistance to infections without anticoagulation [1]. In the early 1960s, allografts were directly transplanted, as the so-called homovitals [2]. Since 1968, valves were cryopreserved with controlled-rate freezing and stored in vapour-phase liquid nitrogen due to logistic issues with fresh tissues [3], enabling long-term storage times up to 5 years. Frozen cryopreservation (FC) remains the preservation method of choice for human heart valves worldwide.

Shortcomings of FC valves include intensive and logistically unfavourable storage in the vapour phase of liquid nitrogen, as well as their limited long-term function due to inflammation, immune response, and subsequent structural deterioration [4]. In particular, early reinterventions in paediatrics occur due to allograft failure within the first 5 years [5], demonstrating the need for new optimized preservation methods. To overcome these limitations, an alternative ice-free cryopreservation (IFC) method was developed. This method prevents interstitial ice formation [6] and enables optimal preservation of the extracellular matrix (ECM) structures. A mid-term large animal study [7] and an unpublished long-term study confirmed preserved ECM integrity and excellent haemodynamics compared with standard cryopreserved valves.

Despite these promising results, the worldwide organ shortage remains unchanged. Therefore, the objective of this study was to explore the potential of IFC for xenogeneic pulmonary valves, by comparing xenogeneic (porcine) with allogeneic (ovine) valves in a sheep model.

METHODS

Tissue preparation

Seven porcine (domestic pig, ~3-month-old, Laboratory animal facility in Frankfurt, Germany) and 7 control ovine hearts (Dorset Cross, ~1-year-old, slaughterhouse in Minnesota, USA) were obtained using aseptic conditions, rinsed with ice-cold lactated Ringer's solution. Pulmonary heart valves were excised aseptically and placed individually in 100 ml volumes of Dulbecco's modified Eagle's medium (Invitrogen, Carlsbad, CA, USA) containing 4.5 g/l glucose with 126 mg/l lincomycin, 52 mg/l vancomycin, 157 mg/l cefoxitin and 117 mg/l polymixin for overnight storage at 4 °C.

Ice-free cryopreservation

All valves were preserved using IFC. They were individually placed and cooled in sterile polyester bags containing 100 ml VS83 solution (4.65 mol/l dimethyl sulfoxide, 4.65 mol/l formamide and 3.31 mol/l propylene glycol in 1× EuroCollins solution) as previously described [8]. Valves were stored at -80 °C. After a total storage time of 10.6 ± 0.8 months (ovine) and 12 ± 1.8 months (porcine) at -80 °C, valves were implanted.

Warming procedure

Individual ice-free cryopreserved valves were directly warmed in a 37 °C water bath without external manipulation until the solution moved freely. Bags were cleansed externally with 70% ethanol, and cryoprotectant solution was removed in 5 steps by placing the valve for 5 min each in ice-cold EuroCollins solution. Subsequently, valves were stored in ice-cold lactated Ringer's solution (Ringerlösung, B.Braun, Melsungen, Germany) until implantation.

Implantation

Twelve juvenile merino sheep (average age 16 ± 2 weeks; weight 35 ± 5 kg) underwent pulmonary heart valve replacement as previously described [9]. In brief, the right ventricular outflow tract was exposed by a left anterolateral thoracotomy through the fourth intercostal space. Normothermic cardiopulmonary bypass was established using femoral arterial and right atrial venous cannulation. With the heart beating, the pulmonary artery was transected and a segment of the artery and all 3 leaflets were removed. The trimmed heart valves were subsequently implanted using running 5-0 monofilament sutures (Fig. 1E). The cardiovascular sheep model was applied due to the similar heart size, frequency, stoke volume and pressure ratios as humans. Six xenogeneic and 6 allogeneic IFC valves were implanted. All animals were kept in an indoor housing facility and received care in compliance with the 'Guide for the Care and Use of Laboratory Animals' published by the National Institute of Health (NIH publication no. 85-23 revised 2011).

Explantation

After 1, 2, 3, 4, 8 and 12 weeks, 2 animals, 1 from each group, were euthanized. Valves were explanted and the following gross inspection further processed.

Ex vivo computed tomography

Ex vivo computed tomography (CT) phantom scans were performed for paraffin-embedded heart valve blocks before tissue sectioning. Examinations were performed with a third-generation dual-source CT system (SOMATOM Force, Siemens Healthcare, Forchheim, Germany), equipped with a fully integrated circuit detector system (Stellar Infinity; Siemens) and 2 X-ray tubes (Vectron; Siemens). All studies were reconstructed with advanced modelled iterative reconstruction (ADMIRE; Siemens) at a standard strength level of 3 using a medium-sharp convolution kernel (Bv36), 0.6 mm section thickness and 0.4 mm increment.

Histology

One leaflet of each heart valve was formalin fixed for 24 h and paraffin embedded (Merck, Darmstadt, Germany). For general morphology, representative 3-µm-thick sections were stained with standard Hematoxylin-Eosin, Elastica van Gieson and Movat Pentachrome nach Verhoeff stains. Calcium deposits were detected via von Kossa stain. CD3 (DCS, Hamburg, Germany) stain was performed to identify T-cell infiltration.

Transforming growth factor-β1 cytokine release

Tissue punches of the second leaflet with 5 mm thickness of each explanted valve were obtained for the cytokine release

Downloaded from https://academic.oup.com/ejc/article/doi/10.1093/ejcts/ezy662953 by Klinikbibliothek Schnarrenberg user on 26 February 2019

TRANSLATIONAL RESEARCH

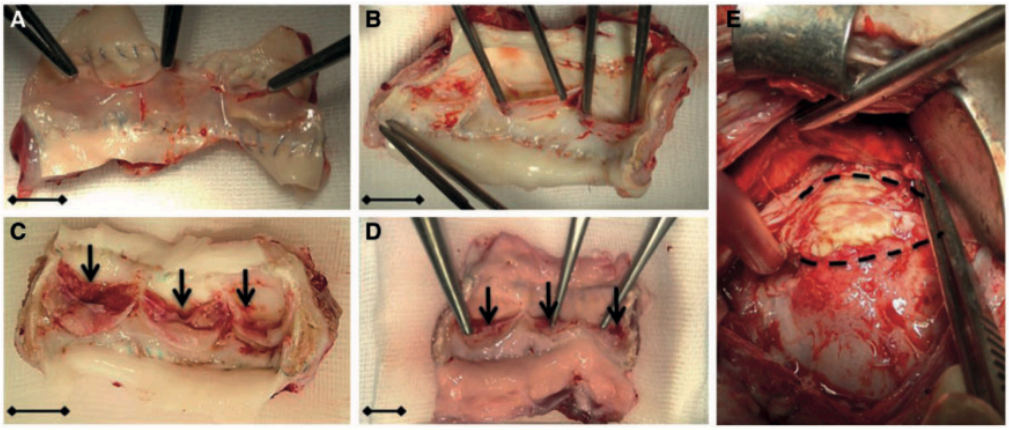

Figure 1: Gross morphology of allogeneic and xenogeneic pulmonary heart valves. (**A**) Allogeneic leaflets were thin and translucent as the representative explant after 8 weeks displays. (**B**) Early xenogeneic explants, as well as the representative explant after 8 weeks, had thin and translucent leaflets. Strong inflammation was detected for (**C**) xenogeneic explant at 4 weeks (**D**) and at 12 weeks. The inflamed inside of leaflets as well as thickened leaflets vegetation are indicated with black arrows. (**E**) Lateral thoracotomy with implanted xenogeneic porcine heart valve with running 5-0 monofilament sutures before the excision of the valve at 2 weeks after implantation.

assessment ($n = 2–3$). Excised native leaflets and preserved but not implanted leaflets served as additional controls. Punches were washed twice in ice-cold phosphate-buffered saline and incubated individually in 24 well plates with 500 µl Dulbecco's modified Eagle's medium (Biochrom, Berlin, Germany) for 4 days at 37 °C and 5% carbon dioxide. Coculture supernatants were centrifuged (1 min, 1000*g*) and stored at -80 °C until further analysis. Active and inactive transforming growth factor (TGF)-β1 in supernatants were analysed using LEGEND MAX™ Total TGF-β1 ELISA Kit (Biolegend, Fell, Germany) according to the manufacturer's protocol. Mean ± standard deviation was determined and a non-parametric 1-way analysis of variance was conducted with Prism 6 (GraphPad, La Jolla, CA, USA). Differences with *P*-value <0.05 were considered statistically significant.

Near-infrared multiphoton imaging

The third leaflet was placed individually in 100 ml ice-cold Dulbecco's modified Eagle's medium with 4.5 g/l glucose and antibiotics (1.2 g/l amikacin, 3 g/l flucytosin, 1.2 g/l vancomycin, 0.3 g/l ciprofloxacin and 1.2 g/l metronidazol). Autofluorescence and second harmonic generation imaging were performed within 72 h. Leaflets were placed in a glass bottom dish (ibidi GmbH, Martinsried, Germany) and assessed on the microscope stage (40× oil immersion objective; N.A. 1.3; Carl Zeiss, Jena, Germany) of a multiphoton laser system (JenLab GmbH, Jena, Germany), as previously described [10]. Samples were excited with a laser power of 20 mW and a wavelength of 760 nm. Detector settings were 1000 V contrast and 52.7% brightness.

Raman spectroscopy

Explanted native ovine, porcine pulmonary and non-transplanted (NT) IFC leaflets were analysed within 48 h, as described previously [11]. Samples were measured with a custom-built confocal Raman microspectroscope [12]. In each tissue, 30 randomly selected spots, focusing on collagen structures, were measured through a 60× water immersion objective (N.A. 1.2; Olympus, Japan). Spectra were acquired at 85 mW laser power during 100 s exposures. Data sets were pretreated by baseline correction, background subtraction and pursued by the spectroscopy software OPUS 4.2 (Bruker Optik GmbH, Ettlingen, Germany). Multivariate data analysis software, The Unscrambler® (Camo, Oslo, Norway), was used for principal component analysis, including spectral differences and peak shifts. Mean ± standard deviation score values were determined and an analysis of variance with a Tukey's test was performed ($n = 30$) with OriginPro 9.1G software (OriginLab, Northampton, MA, USA). Differences with *P*-values <0.05 were considered statistically significant.

RESULTS

All animals survived heart valve replacement. One allogeneic heart valve required explantation due to an acute severe infection (pneumonia) at 18 days instead of 4 weeks.

Gross morphology

Gross morphology revealed thin and translucent leaflets for all allogeneic valves (Fig. 1A). Xenogeneic valves generally had thicker leaflets (Fig. 1B). After 4 weeks, the arterial side of xenogeneic leaflet became severely inflamed (Fig. 1C), and at 12 weeks, additional severe vegetations on the ventricularis (Fig. 1D) were observed.

Ex vivo computed tomography

Ex vivo CT scans of formalin-fixed and paraffin-embedded explanted valves indicated increasing calcium deposition restricted to the conduit wall for both groups starting at 3 weeks after implantation. Allogeneic tissue calcifications were limited to the hinge region near the former annulus muscle and the suture lines. In contrast, the entire conduit wall in xenogeneic tissue was severely calcified after 12 weeks (Fig. 2B).

Downloaded from https://academic.oup.com/ejcts/article-abstract/53/4/784/4662953 by Klinikbibliothek Schnarrenberg user on 26 February 2019

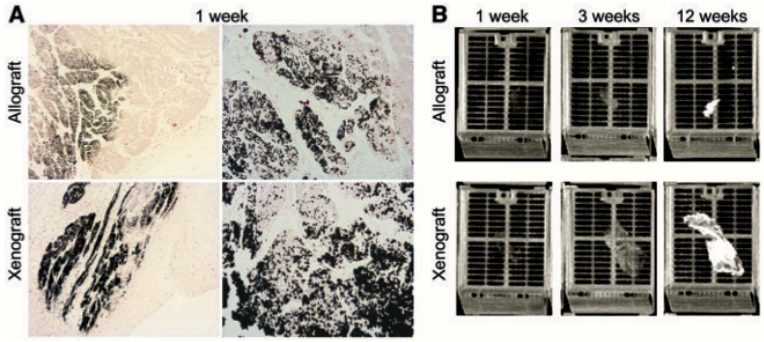

Figure 2: Calcium depositions in explanted allogeneic and xenogeneic heart valves. Calcium depositions were demonstrated with (**A**) van Kossa stain for 1 week implanted allograft and xenograft in the former annulus muscle and (**B**) computed tomography phantom scans of formalin-fixed and paraffin-embedded heart valves. Bright white areas indicate calcium depositions in the tissue.

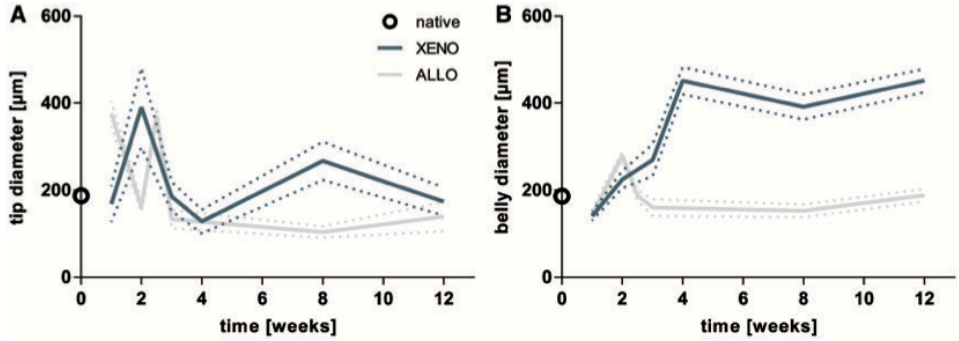

Figure 3: Leaflet diameters of allogeneic and xenogeneic heart valves. The mean ± standard deviation ($n = 5$) of (**A**) leaflet tip and (**B**) belly diameters of transplanted ice-free cryopreserved allogeneic and xenogeneic pulmonic heart valves are displayed. Native leaflet tip and belly diameter (open circle) is shown as a control. ALLO: allograft; XENO: xenograft.

Histology

No thickening of allogeneic leaflets was observed. In contrast, severe leaflet thickening of all xenogeneic leaflets was observed by 4 weeks of implantation (Fig. 3). Hinge regions including the annulus and lumen of allogeneic valves were almost completely acellular after 1 week and remained virtually cell free throughout the 12-week study (Fig. 4V, VI, IX, X). Sporadic CD3-positive cells were observed at 12 weeks in the hinge region (Fig. 4XI). A few T-cells could be seen after 1 week near the annulus (Fig. 4VIII). Small numbers of CD3-positive T-cells surrounded but never infiltrated the former muscular annulus (Fig. 4VIII, XII). Increased cellularity, with abundant CD3-positive cells, was detected at the suture lines. In addition, changes in the proteoglycan and collagen make-up of ECM were detected over the 12-week period. Increasing proteoglycan deposition and decreasing collagen content in the valves annulus were detected over time using Movat Pentachrome after Verhoeff staining (Fig. 4II, VI, X). Leaflet tissue appeared slightly more condensed, particularly elastin fibres in the lamina ventricularis (data not shown).

Acellular leaflets and hinge regions were also observed after 1 week for xenogeneic valves (Fig. 5AII, V and BI). In contrast to allogeneic tissues, subsequently, severe immune response characterized by cell infiltration and leaflet thickening was detected. After 4, 8 and 12 weeks, 33, 50 and 66% of the leaflets were infiltrated with abundant CD3-positive T-cells (Fig. 5AI) initiating from the hinge region. Explants at 4 and 12 weeks had the most thickened and inflamed leaflets, consistent with gross morphology (Fig. 5AV, IV). Importantly, the donor leaflet tissue was not generally infiltrated with cells. Neotissue formation of 2 thick cell-rich layers with abundant CD3-positive T-cells on arterial and ventricularis sides were detected (Fig. 5AIV and BIV). The lamina ventricularis with elastin fibres was overgrown and localized inside acellular leaflet tissue (Fig. 5AVIII).

In general, multiple foci of inflammatory infiltration with subsequent structural changes were found to a much greater extent compared with allogeneic tissue. The former annulus muscle was surrounded rapidly by abundant CD3-positive cells (Fig. 5BIII, VI). CD3-positive cells also infiltrated the cell-rich tunica externa of the conduit starting 1 week after implantation (Fig. 5BII, V). New microvessel formation was detected in the cell-rich tunica externa and slow degradation of the transplanted acellular conduit tissue was observed at 12 weeks originating from the tunica externa. Strong CD3-positive T-cell infiltration was observed at these degradation sites. Additionally, proteoglycan-rich neointima formation on the luminal surface of the allograft wall was found after 4 weeks of implantation. As observed in allogeneic tissue, similar structural changes of increasing proteoglycan depositions and decreasing collagen amounts were detected in the annulus over time. The xenogeneic annulus lost its original appearance and shrank dramatically (Fig. 5AIX–XII).

Downloaded from https://academic.oup.com/ejc/article-abstract/doi/10.1016/j.ejcts.2011.10.019/662953 by Klinikbibliothek Schnarrenberg user on 26 February 2019

TRANSLATIONAL RESEARCH

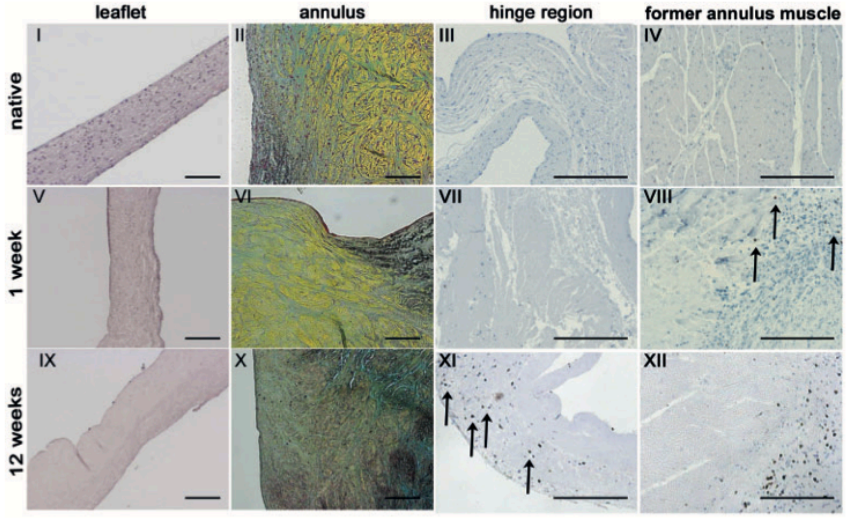

Figure 4: Histology of representative explanted allogeneic ice-free cryopreservation pulmonic valves and native control sections. Acellular leaflets were observed using Haematoxylin-Eosin stain (I, V, IX), Movat Pentachrome nach Verhoeff stain (II, VI, X) showed extracellular matrix changes, detected in the valves annulus. Minimal CD3-positive T-cell infiltration over time of the hinge region (III, VII, XI) and around the former annulus muscle (IV, VIII, XII) was found. Scale bars equal 100 μm.

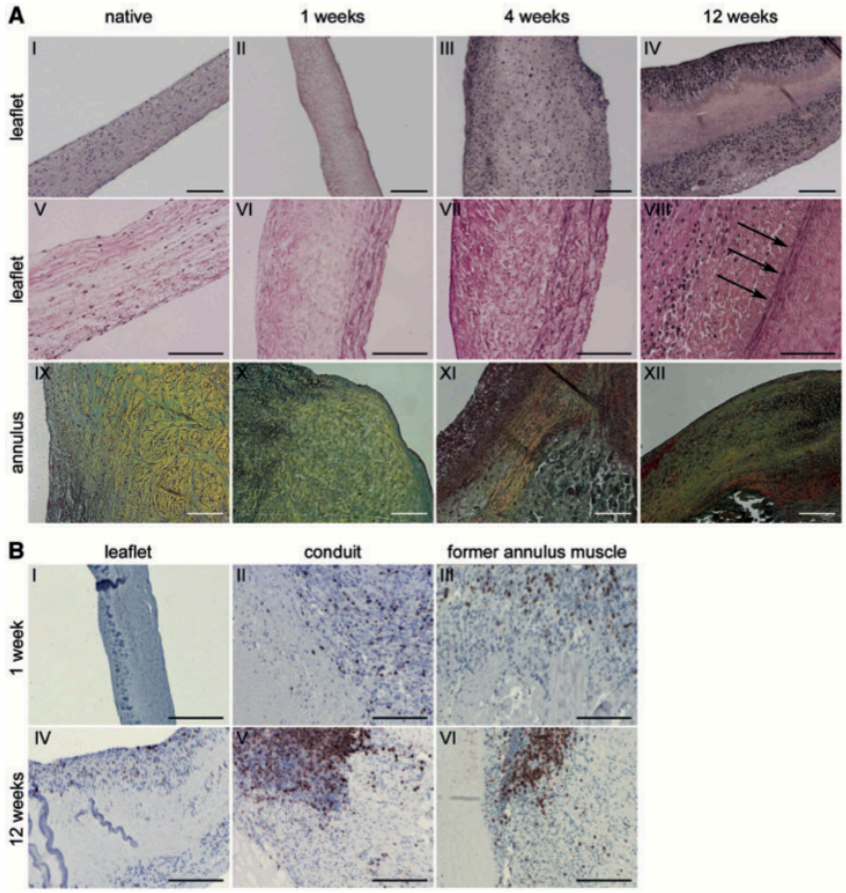

Figure 5: Histology of representative explanted xenogeneic ice-free cryopreservation pulmonic valves and native control sections. (**A**) Acellular leaflets were rapidly and severely infiltrated and overgrown with neotissue as indicated with the Haematoxylin-Eosin stain (I–IV), Elastica van Gieson stain (V–VIII). Black arrow indicates elastin fibres in the overgrown former lamina ventricularis. Extracellular matrix changes were detected in the annulus (IX–XII) using a Movat Pentachrome nach

Downloaded from https://academic.oup.com/ejcts/article-abstract/53/4/784/4662953 by Klinikbibliothek Schnarrenberg user on 26 February 2019

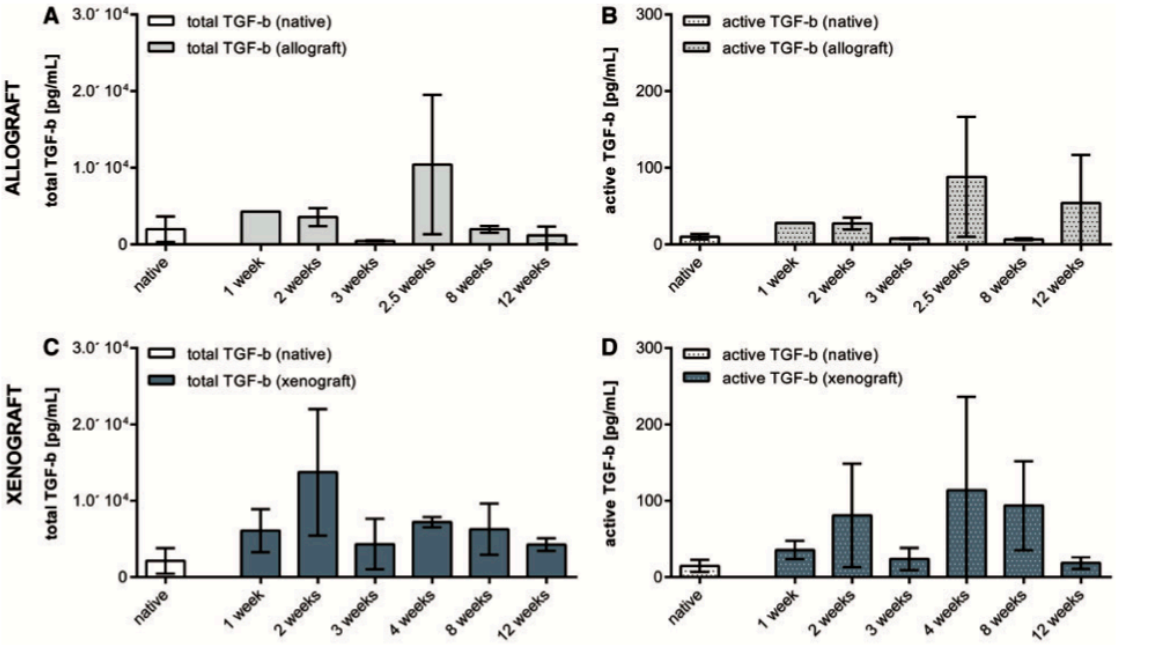

Figure 6: TGF-β1 release profiles of leaflet tissue punches**.** Total latent and active TGF-β1 (**A, C**) and the active TGF-β1 (**B, C**) release profiles for ovine allogeneic (**A**, **B**) and porcine xenogeneic (**C**, **D**) leaflets are presented. The mean ± standard deviation is displayed ($n = 3$). TGF-β: transforming growth factor beta.

Calcifications

Von Kossa stains revealed no calcification in the leaflets of either groups. However, microcalcifications in the former muscular annulus of both groups were more abundant in xenogeneic valves (Fig. 2A). Stronger calcifications throughout the entire xenogeneic conduit wall were consistent with CT scans (Fig. 2B).

Transforming growth factor-β1 cytokine release

TGF-β1 is highly conserved across mammalian species and exists in a latent and active form. This cytokine is an important mediator and an indicator of tissue remodelling, inflammation and fibrosis. For native (ovine) leaflet tissue, a total (latent and active) TGF-β1 release of around 2500 pg/ml with 1% active TGF-β was detected (Fig. 6). The xenogeneic leaflets had slightly elevated total TGF-β levels compared with the allogeneic release profiles. No significant differences in TGF-β release profiles were observed for at different explant times.

Near-infrared multiphoton imaging

Autofluorescence and second harmonic generation images revealed no elastin or collagen changes in either allogeneic or xenogeneic tissues compared with the native controls (Fig. 7).

Raman spectroscopy

Raman spectroscopic analyses and multivariate data analysis of excised native, NT and explanted ice-free ovine and porcine leaflets analysis (Fig. 8A) revealed a clustering between all 4 groups. However, native and NT data of ovine tissues clustered more closely than porcine tissues, where a clear separation between native and NT tissues was shown.

Principal component analysis of allogeneic leaflets (Fig. 8C) demonstrated significant differences between mean score values of PC3 compared with native tissue for the first 3 weeks. The 8- and 12-week implants were not statistically different. Corresponding loadings plot for allogeneic valves showed 5 typical influencing peaks on the spectral differences in the fingerprint region all correlated with certain molecular bonds in the collagen molecule (Fig. 8E) [13, 14]. In contrast, more pronounced statistically significant differences between the mean score valves of PC1 of xenogeneic and native tissues were detected, particularly at 12 weeks (Fig. 8D). Although the characteristic collagen peaks were still found in the loading plot, a clear shift of the peak intensities was observed, as indicated in Fig. 8F.

DISCUSSION

The objective of this study was to evaluate the potential of xenogeneic ice-free cryopreserved heart valves in comparison with ice-free allogeneic valves with natural unaltered ECM structures to overcome organ scarcity. Our results demonstrated an almost immediate and complete loss of cellular elements in the 1st and 2nd week after implantation. Acellular allogeneic heart valves revealed no immune rejection leaflet architecture and ECM preservation compared with native tissues. The loss of cellular components in IFC grafts was previously described after 7 months *in vivo* [7, 8]. The IFC procedure uses highly concentrated chemicals resulting in grafts without cell viability [8, 15, 16]. Based on the fast disappearance of cells, we hypothesized a passive washout of cell remnants. Sheer stress due to blood flow, as well as constant stretching and contraction of tissue, may enable

Downloaded from https://academic.oup.com/ejc/article-abstract/53/6/662953 by Klinikbibliothek Schnarrenberg user on 26 February 2019

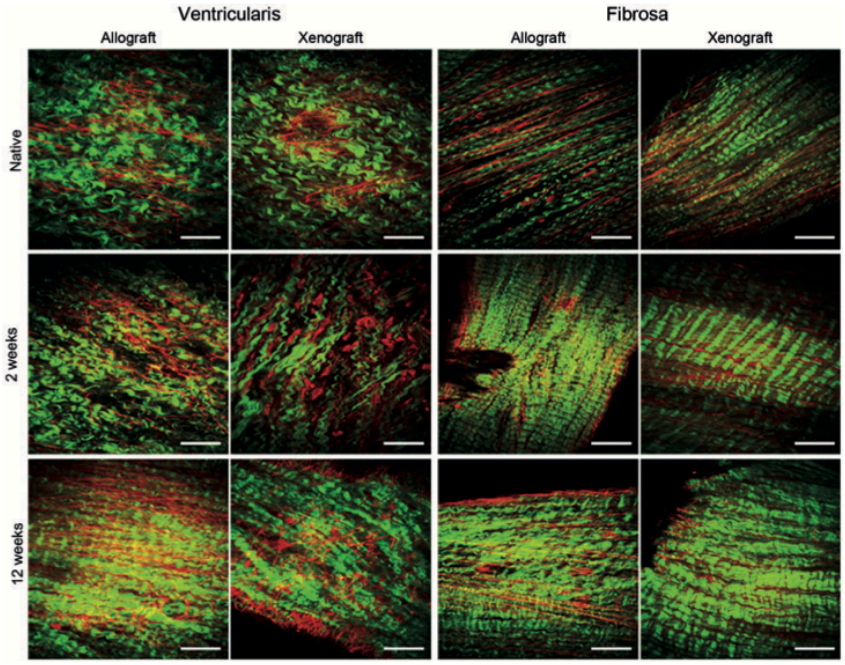

Figure 7: Multiphoton and second harmonic generation images of fibrosa and ventricularis of control and explanted heart valve leaflets. Collagen and elastic fibres of the fibrosa show parallel alignment. Scale bars represent 60 μm.

washout of cellular debris. However, the acute cell removal process requires further in-depth investigation to evaluate possible early macrophage involvement within the 1st week. In contrast to allogeneic valves, an early and elevated T-cell infiltration was detected after 1 week in xenogeneic valves turning into a T-cell-mediated immune response with subsequent structural degeneration, which was observed to start after 4 weeks.

Compared with xenogeneic implanted valves, allogeneic valves show less adverse immune responses, consistent with previous mid-term results [7]. We postulate that the immediate cell loss and the lack of triggering soluble mediators prevented infiltration and activation of T-cells. In particular, cell-mediated T-cell activation by endothelial or dendritic cells [17] is unlikely in acellular grafts. The minimal T-cell infiltration restricted to the conduit wall is most likely caused by remaining cell remnants. Possibly, the additional washing processes prior to implantation using pulsatile bioreactors [18] might enable complete elimination of cell remnants and avoid subsequent T-cell infiltration.

As opposed to allografts, we observed an active rejection of xenogeneic valves. Multiple foci of inflammatory infiltrations, predominantly CD3-positive T lymphocytes, as well as pannus formation on the luminal side, indicate an ongoing rejection as previously described by others [19]. The inflammation that occurred was predominantly extravascular similar to glutaraldehyde-fixed bioprosthetic heart valves [20]. The immediate acute severe T-cell infiltration of acellular xenogeneic tissue confirms recent observations that the xenogeneic matrix itself is the culprit for the immunogenicity [19, 21]. Because of the fact that T-cell infiltration has been linked to ECM destruction, especially collagen fibres [22], this could partly explain the fast structural deterioration of T-cell-infiltrated xenogeneic tissues already after 4 weeks. Even though T-cell infiltration has always been seen as a major contributing factor for heart valve failure [21, 23], further in-depth studies into other immune cells of the innate immunity, such as granulocytes and macrophages, are warranted.

Despite clear differences of T-cell infiltration for allografts and xenografts, no influenced immunological response profiles for the different explanation time points in neither of the groups were observed. Release of TGF-β1, an important mediator and indicator of tissue remodelling, as well as inflammation and fibrosis modulation, was analysed. Despite a high variability, similar active and inactive (latent) TGF-β1 levels were seen. A constant TGF-β release from transplanted and acellular leaflets indicate a prolonged leakage of matrix-bound TGF-β. Slightly increased absolute values for xenogeneic tissue might be related to an increased leaflet thickness and infiltrating TGF-β1 producing T-cells or macrophages. Other TGF-β isoforms, and especially their relative ratios, influence tissue regeneration [24]. Although TGF-β3 shares a similar structure to TGF-β1, it shows different effects on immune responses [25]. Furthermore, TGF-β3 is anti-fibrotic and might be involved in fibrosis modulation [26]. Whether other isoforms of TGF-β are also detectable and involved in immune responses to implanted IFC heart valves have to be elucidated in the future.

Additional in-depth structural analysis was performed because T-cell infiltration is known to be associated with ECM destruction, especially of collagen [22]. Near-infrared multiphoton imaging did not detect structural changes of collagen or elastin, unlike Raman spectroscopy analysis. Principal component analyses of the Raman showed native-like results for allograft. Although xenogeneic score values for longer implanted valves were more different compared with native fresh control tissues. Clear collagen

Downloaded from https://academic.oup.com/ejcts/article-abstract/53/4/784/4662953 by Klinikbibliothek Schnarrenberg user on 26 February 2019

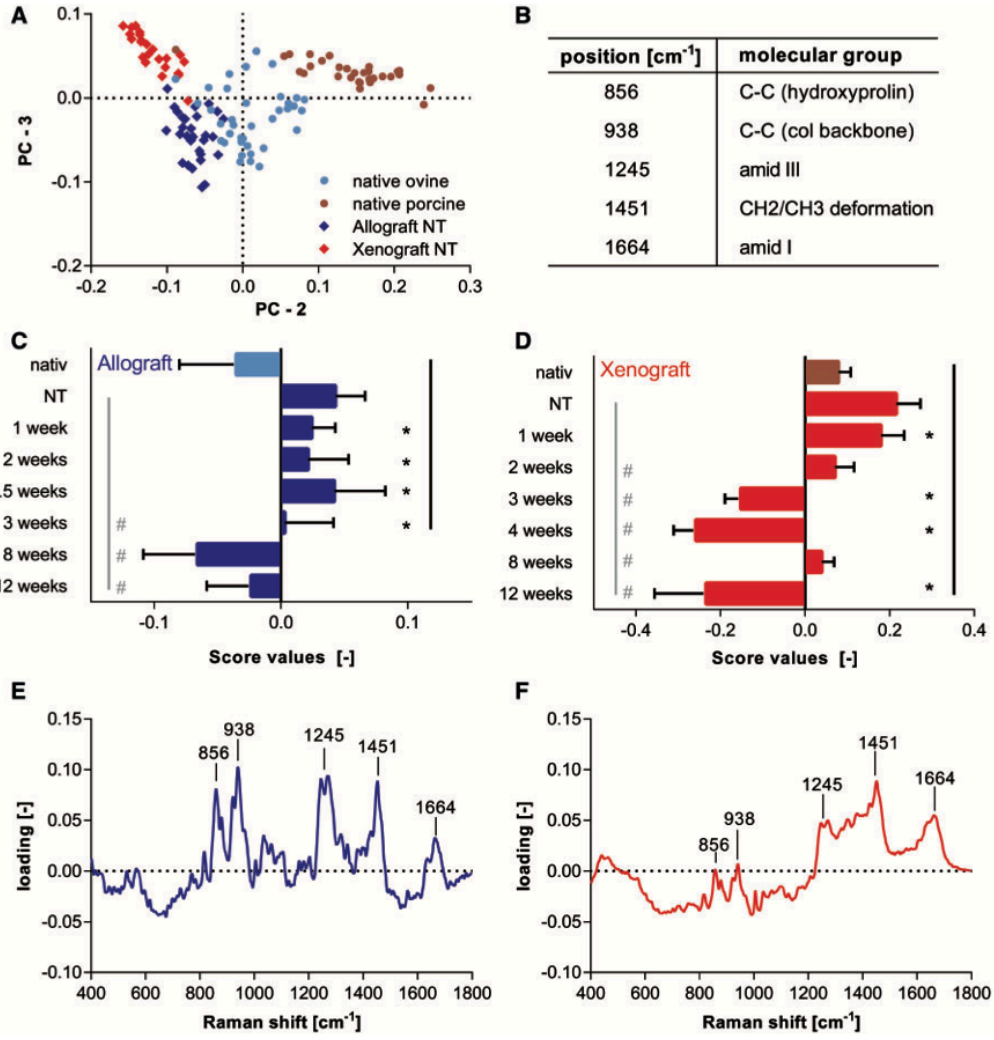

Figure 8: Multivariate data analysis. (**A**) Principal component analysis scores plot of native and NT porcine and ovine data sets: ovine native and NT data clusters overlap, while porcine native and NT differ more. (**B**) Significant collagen peaks of the loadings plots and their correlating molecular groups. (**C**) Score values of PC3 for allogeneic and (**D**) of PC1 for xenogeneic explants. **P*-value ≤0.001 (*n* = 30). Loading plot (**E**) of PC3 of allogeneic explants and (**F**) of PC1 of xenogeneic explants. The mean ± standard deviation is displayed. NT: non-transplanted.

changes, possibly caused by leucocytes, were found for xenogeneic tissue, particularly for the more severely infiltrated and inflamed leaflets after 4 and 12 weeks. A clear shift in the loading plot for the xenogeneic tissue away from typical collagen-associated loading plots seen in allogeneic tissues also indicated collagen changes. A limitation of our study is the lack of haemodynamic data, which could have underlined possible valvular dysfunction due to the structural ECM alterations.

Surprisingly, early microcalcifications were detected in both groups starting from 1 week after implantation in the muscular annulus. No calcifications in the conduit wall were found in mid-term or long-term implanted IFC valves [7]. Microcalcifications are formed at sites of cell death. These cytoskeletal remnants allow nodule formation and calcium deposition [27]. The phospholipids-rich membranous debris is linked to nucleate apatite [20, 28] and calcium phosphate crystal deposition has been identified as the source of calcification [28]. They are found especially close to smooth muscle cells, as these cells commonly form matrix vesicles to attract calcium, leading to microcalcifications [27]. Destruction of cardiomyocytes in the annulus may have caused an acute release of these plasma membrane-derived matrix vesicles causing microcalcifications [27–29]. Possible elevated calcium levels, which induce mineralization of cardiomyocytes, might accelerate rapid calcification [28]. Inflammatory reactions, connected with pathogenesis of acquired calcifications in valves [27, 30] as well as α-Gal antibodies interacting with the Gal epitope (galactose-α(1, 3)-galactose antigen) accelerate calcification in heart valves [22] and therefore favour a progression of the calcification processes, particularly in xenogeneic tissues. The potential elimination of α-Gal antibodies using knock-out models are the current focus of the ongoing xenogeneic IFC heart valve studies.

Downloaded from https://academic.oup.com/ejc/article-abstract/662953 by Klinikbibliothek Schnarrenberg user on 26 February 2019

CONCLUSION

In summary, our data implicate that xenogeneic ECM in wild-type porcine tissue elicits an immune response rendering ice-free cryopreserved xenogeneic valves unsuitable for heart valve replacement. Allograft transplantation still remains the current preferable choice of replacement until new alternatives such as porcine α-Gal knock-out, human CD46 transgenic porcine xenograft valves or tissue-engineered valves can overcome these limitations and organ scarcity in the future. In contrast, IFC allografts perform well *in vivo* in sheep and are ready for evaluation in human patients.

Funding

This work was supported by the German Research Foundation [Sto 359/10-1 to U.S., SE 657/9-1 to M.S., SCHE 701/10-1 to K.S.-L. and INST 2388/30-1 to K.S.-L.] and the Ministry of Baden-Wuerttemberg for Sciences, Research and Arts (33-729.55-3/214 and SI-BW 01222-91). KGMB was supported by the National Institute of Allergy and Infectious Disease, National Institutes of Health grant R43 AI114486.

Conflict of interest: Julian L. Wichmann received speaker fees from GE Healthcare and Siemens Healthcare. Kelvin G.M. Brockbank is the owner and employee of Tissue Testing Technologies LLC.

REFERENCES

[1] O'Brien M, Stafford E, Gardner M, Pohlner P, McGiffin D. A comparison of aortic valve replacement with viable cryopreserved and fresh allograft valves, with a note on chromosomal studies. J Thorac Cardiovasc Surg 1987;94:812–23.
[2] Gonzalez-Lavin L, McGrath LB, Amini S, Graf D. Homograft valve preparation and predicting viability at implantation. J Card Surg 1988;3:309–12.
[3] Watts LK, Duffy P, Field RB, Stafford E, O'Brien MF. Establishment of a viable homograft cardiac valve bank: a rapid method of determining homograft viability. Ann Thorac Surg 1976;21:230–6.
[4] Brown JW, Ruzmetov M, Rodefeld MD, Vijay P, Turrentine MW. Right ventricular outflow tract reconstruction with an allograft conduit in non-Ross patients: risk factors for allograft dysfunction and failure. Ann Thorac Surg 2005;80:655–64.
[5] Joudinaud TM, Baron F, Raffoul R, Pagis B, Vergnat M, Parisot C *et al.* Redo aortic root surgery for failure of an aortic homograft is a major technical challenge. Eur J Cardiothorac Surg 2008;33:989–94.
[6] Schenke-Layland K, Xie J, Heydarkhan-Hagvall S, Hamm-Alvarez SF, Stock UA, Brockbank KG *et al.* Optimized preservation of extracellular matrix in cardiac tissues: implications for long-term graft durability. Ann Thorac Surg 2007;83:1641–50.
[7] Lisy M, Pennecke J, Brockbank KG, Fritze O, Schleicher M, Schenke-Layland K *et al.* The performance of ice-free cryopreserved heart valve allografts in an orthotopic pulmonary sheep model. Biomaterials 2010;31:5306–11.
[8] Brockbank KG, Chen Z, Greene ED, Campbell LH. Vitrification of heart valve tissues. Methods Mol Biol 2015;1257:399–421.
[9] Stock UA, Nagashima M, Khalil PN, Nollert GD, Herdena T, Sperling JS *et al.* Tissue-engineered valved conduits in the pulmonary circulation. J Thorac Cardiovasc Surg 2000;119:732–40.
[10] Monaghan MG, Kroll S, Brucker SY, Schenke-Layland K. Enabling multiphoton and second harmonic generation imaging in paraffin-embedded and histologically stained sections. Tissue Eng Part C Methods 2016;22:517–23.
[11] Votteler M, Carvajal Berrio DA, Pudlas M, Walles H, Stock UA, Schenke-Layland K. Raman spectroscopy for the non-contact and non-destructive monitoring of collagen damage within tissues. J Biophotonics 2012;5:47–56.
[12] Pudlas M, Berrio DAC, Votteler M, Koch S, Thude S, Walles H *et al.* Non-contact discrimination of human bone marrow-derived mesenchymal stem cells and fibroblasts using Raman spectroscopy. Med Laser Appl 2011;26:119–25.
[13] Frushour BG, Koenig JL. Raman scattering of collagen, gelatin, and elastin. Biopolymers 1975;14:379–91.
[14] Frank CJ, McCreery RL, Redd D. Raman spectroscopy of normal and diseased human breast tissues. Anal Chem 1995;67:777–83.
[15] Huber AJ, Brockbank KG, Riemann I, Schleicher M, Schenke-Layland K, Fritze O *et al.* Preclinical evaluation of ice-free cryopreserved arteries: structural integrity and hemocompatibility. Cells Tissues Organs 2012;196:262–70.
[16] Campbell L, Brockbank K. Cryopreservation of porcine aortic heart valve leaflet-derived myofibroblasts. Biopreserv Biobank 2010;8:211–7.
[17] Hogan P, Duplock L, Green M, Smith S, Gall KL, Frazer IH *et al.* Human aortic valve allografts elicit a donor-specific immune response. J Thorac Cardiovasc Surg 1996;112:1260–7.
[18] Schleicher M, Sammler G, Schmauder M, Fritze O, Huber AJ, Schenke-Layland K *et al.* Simplified pulse reactor for real-time long-term in vitro testing of biological heart valves. Ann Biomed Eng 2010;38:1919–27.
[19] Vogt PR, Stallmach T, Niederhäuser U, Schneider J, Zünd G, Lachat M *et al.* Explanted cryopreserved allografts: a morphological and immunohistochemical comparison between arterial allografts and allograft heart valves from infants and adults. Eur J Cardiothorac Surg 1999;15:639–45.
[20] Manji RA, Zhu LF, Nijjar NK, Rayner DC, Korbutt GS, Churchill TA *et al.* Glutaraldehyde-fixed bioprosthetic heart valve conduits calcify and fail from xenograft rejection. Circulation 2006;114:318–27.
[21] Neumann A, Sarikouch S, Breymann T, Cebotari S, Boethig D, Horke A *et al.* Early systemic cellular immune response in children and young adults receiving decellularized fresh allografts for pulmonary valve replacement. Tissue Eng Part A 2014;20:1003–11.
[22] Manji RA, Lee W, Cooper DK. Xenograft bioprosthetic heart valves: past, present and future. Int J Surg 2015;23:280–4.
[23] Legare JF, Lee TD, Ross DB. Cryopreservation of rat aortic valves results in increased structural failure. Circulation 2000;102:III75–8.
[24] Gilbert RW, Vickaryous MK, Viloria-Petit AM. Signalling by transforming growth factor beta isoforms in wound healing and tissue regeneration. J Dev Biol 2016;4:21.
[25] Lee Y, Awasthi A, Yosef N, Quintana FJ, Xiao S, Peters A *et al.* Induction and molecular signature of pathogenic TH17 cells. Nat Immunol 2012;13:991–9.
[26] Okamura T, Morita K, Iwasaki Y, Inoue M, Komai T, Fujio K *et al.* Role of TGF-beta3 in the regulation of immune responses. Clin Exp Rheumatol 2015;33:63–9.
[27] Leopold JA. Cellular mechanisms of aortic valve calcification. Circ Cardiovasc Interv 2012;5:605–14.
[28] Yiu AJ, Callaghan D, Sultana R, Bandyopadhyay BC. Vascular calcification and stone disease: a new look towards the mechanism. J Cardiovasc Dev Dis 2015;2:141–64.
[29] Kovacic JC, Mercader N, Torres M, Boehm M, Fuster V. Epithelial-to-mesenchymal and endothelial-to-mesenchymal transition. Circulation 2012;125:1795–808.
[30] Wallby L, Janerot-Sjöberg B, Steffensen T, Broqvist M. T lymphocyte infiltration in non-rheumatic aortic stenosis: a comparative descriptive study between tricuspid and bicuspid aortic valves. Heart 2002;88:348–51.

Downloaded from https://academic.oup.com/ejcts/article-abstract/53/4/784/4662953 by Klinikbibliothek Schnarrenberg user on 26 February 2019

Appendix III: J. Marzi, A.C. Biermann, E.M. Brauchle, K.G.M Brockbank, U.A. Stock, K. Schenke-Layland, *In situ quantitative assessment of residual cryoprotectant effects on cardiac tissues*, Analytical chemistry, 2019; 91(3): 2266-2272

analytical chemistry

Article

Cite This: *Anal. Chem.* XXXX, XXX, XXX−XXX

pubs.acs.org/ac

Marker-Independent In Situ Quantitative Assessment of Residual Cryoprotectants in Cardiac Tissues

Julia Marzi,[†] Anna C. Biermann,[‡,§] Eva M. Brauchle,[†,∥] Kelvin G. M. Brockbank,[⊥,#] Ulrich A. Stock,[‡,§,○,□] and Katja Schenke-Layland*[,†,∥,△]

[†]Department of Women's Health, Research Institute for Women's Health, Eberhard Karls University Tübingen, 72076 Tübingen, Germany

[‡]Department for Thoracic and Cardiovascular Surgery, Johann Wolfgang Goethe University, 60596 Frankfurt am Main, Germany

[§]Department of Cardiothoracic Surgery, Royal Brompton and Harefield Foundation Trust; Harefield UB96JH, United Kingdom

[∥]Natural and Medical Sciences Institute (NMI) at the University of Tübingen, 72770 Reutlingen, Germany

[⊥]Tissue Testing Technologies LLC., North Charleston, South Carolina 20406, United States

[#]Department of Bioengineering, Clemson University, Clemson, South Carolina 29634, United States

[○]Imperial College London, London SW72AZ, United Kingdom

[□]Magdi Yacoub Institute, Harefield UB96JH, United Kingdom

[△]Department of Medicine, Cardiovascular Research Laboratories, David Geffen School of Medicine at UCLA, Los Angeles, California 90095, United States

Supporting Information

ABSTRACT: Cryomedium toxicity is a major safety concern when transplanting cryopreserved organs. Therefore, thorough removal of potentially toxic cryoprotective agents (CPAs) is required before transplantation. CPAs such as dimethylsulfoxide (DMSO), propylene glycol (PG), and formamide (FMD), routinely employed in ice-free cryopreservation (IFC), have advantages in long-term preservation of tissue structures compared with conventional cryopreservation employing lower CPA concentrations. This study evaluated the impact of potential residual CPAs on human cardiac valves. Raman microspectroscopy and Raman imaging were established as nondestructive marker-independent techniques for in situ quantitative assessment of CPA residues in IFC valve tissues. In detail, IFC valve leaflets and supernatants of the washing solutions were analyzed to determine the washing efficiency. A calibration model was developed according to the CPA's characteristic Raman signals to quantify DMSO, PG and FMD concentrations in the supernatants. Single point Raman measurements were performed on the intact tissues to analyze penetration properties. In addition, Raman imaging was utilized to visualize potential CPA residues. Our data showed that washing decreased the CPA concentration in the final washing solution by 99%, and no residues could be detected in the washed tissues, validating the multistep CPA removal protocol routinely used for IFC valves. Raman analysis of unwashed tissues showed different permeation characteristics depending on each CPA and their concentration. Our results demonstrate a great potential of Raman microspectroscopy and Raman imaging as marker-independent in situ tissue quality control tools with the ability to assess the presence and concentration of different chemical agents or drugs in preimplantation tissues.

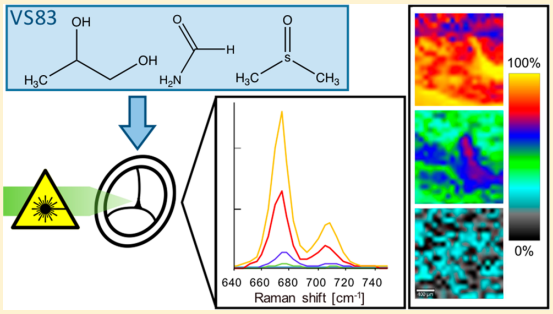

Donor organ scarcity and restricted long-term organ viability are limiting factors for transplantation medicine.[1] Cryopreservation is a critical technology with numerous applications in cell and tissue banking. Chemical additives, so-called cryoprotective agents (CPAs), allow for a better post-thaw recovery of cells and tissues.[2] CPAs play a fundamental role to guide, reduce, or prevent ice crystal formation and protect the biological structures during preservation. They determine the post-thaw condition of the graft and extracellular matrix (ECM) integrity. At the same time, their metabolic and biophysical effects bear the risk of potentially damaging the biological system.[3−5] It is a continuing challenge to balance the application of sufficiently concentrated but potentially toxic concentrations of CPAs.[6]

In clinical practice, standard frozen cryopreservation (FC) of human cardiac valves has been applied for over three decades.

Received: October 23, 2018
Accepted: January 2, 2019
Published: January 2, 2019

ACS Publications © XXXX American Chemical Society

DOI: 10.1021/acs.analchem.8b04861
Anal. Chem. XXXX, XXX, XXX−XXX

Reprinted with permission from J. Marzi, A.C. Biermann, E.M. Brauchle, K.G.M Brockbank, U.A. Stock, K. Schenke-Layland, *In situ quantitative assessment of residual cryoprotectant effects on cardiac tissues*, Analytical chemistry, 2019; 91(3): 2266-2272. Copyright 2019 American Chemical Society

However, a limited long-term function of FC valves due to immune responses, inflammation, and subsequent structural deterioration has been observed.[7−9] An alternative preservation method, ice-free cryopreservation (IFC), was established that showed promising results due to the avoidance of ice-crystal formation and preservation of natural ECM structures.[10,11] In order to achieve an ice-free vitreous state, high CPA concentrations of dimethyl sulfoxide (DMSO), propylene glycol (PG), and formamide (FMD) are required. CPA concentrations in the IFC formulation are eight times higher than in FC medium with 83% penetrating CPAs. Hence, the formulation is known as vitrification solution 83 (VS83).[12] Despite the improved long-term endurance of IFC valves in vivo,[13] the potential toxicity of the remaining CPAs needs to be addressed before pursuing clinical trials. DMSO and PG are broadly used as cryoprotectants and penetration enhancers.[14,15] However, they show dose-dependent toxic effects.[16−18] FMD is widely used as a solvent in industrial use. Its impact on the metabolism of human cells and tissues is still unknown, and the chemical has potential mutagenic and carcinogenic activities.[19,20]

Previous studies characterized CPA diffusion, permeation, and efflux kinetics. The measurement of osmolalities and complex techniques such as capillary zone electrophoresis, HPLC, or NMR spectroscopy[21−25] provided diffusion coefficients that enabled mathematical modeling. This allows for the better understanding and optimization of cryopreservation procedures. However, diffusion strongly depends on temperature, concentration, applied CPAs, and structural composition of the treated tissues. Rather than determining the properties for every different CPA in every single tissue, a technique that allows for in situ CPA quantification would be beneficial, especially if there is the possibility to simultaneously monitor different chemicals.

Here, we aimed to implement Raman microspectroscopy and Raman imaging as tools for quantitative safety assessment of cryopreserved, intact, preimplantation tissues. Raman spectroscopy has been applied before for the identification of chemicals and drugs in tissues or biofluids,[26−28] as well as for characterization of the penetration of DMSO and PG in skin.[29−31] Although, Raman spectroscopy is well established for the quantitative assessment of individual substances in complex mixtures in pharmaceutical and material sciences,[32−34] its utility as a quantitative analysis tool for biological samples is still under investigation. Vasquez-Rivera et al. investigated the tissue permeation of VS83 using near-infrared spectroscopy.[35] They reported simultaneous measurements of CPA diffusion kinetics in aortic tissue at room temperature.[35] Our study focused on the quantification of CPAs in rewarmed tissues prior and during the washing procedure toward the establishment of a protocol that guarantees implantation of CPA-free tissues. Therefore, Raman microspectroscopic measurements were performed on IFC valve tissues and on the supernatants of the washing solutions.

■ EXPERIMENTAL SECTION

Ice-Free Cryopreservation. VS83, applied for cryopreservation of cardiac valves, contained 4.65 M DMSO, 3.31 M PG, and 4.65 M FMD in Euro-Collins (EC) solution.[12]

Supernatants. Tissues, VS83, and washing solution samples were collected from a previously reported large animal study.[13] VS83 and EC solution supernatants were obtained during the rewarming procedure of IFC ovine pulmonary valves (Dorset Cross, ∼1 year old, slaughterhouse in Minnesota, U.S.A., n = 7), which were then transplanted into juvenile sheep (merino, ∼10 months old, animal testing institution Frankfurt am Main, Germany, n = 5). The cryopreserved valves were rewarmed and underwent a defined washing procedure in order to remove the CPAs before transplantation.[12] Valves stored in VS83 were washed five times for 5 min in 1× EC solution. Supernatants of storage and washing solutions were collected and frozen at −80 °C prior further analyses. Fresh VS83 was diluted with 1× EC solution to concentrations ranging between 0.2−100% VS83 to serve as calibration solutions. Those values corresponded to molarities of 0.009−4.65 mol/L for DMSO and FMD, and 0.007−3.31 mol/L for PG.

Tissue Samples. Fresh ovine pulmonary leaflets were obtained from juvenile sheep (merino, ∼ 10 months, animal testing institution Frankfurt am Main, Germany). The excised leaflets were IFC preserved in diluted VS83/phosphate buffered saline mixtures as previously described[12] in order to analyze the tissue permeability of the VS83 solution. Mixtures ranged from 5 to 100% VS83.

Raman Microspectroscopy. Single point measurements of tissues and CPA solutions were acquired with a customized Raman microspectroscopy system.[36] System calibration was performed with a silicon wafer that demonstrated a characteristic peak at 521 cm^{-1}. After every reboot, the Raman microspectroscope was validated by measuring the silicon wafer. The unprocessed, intact heart valve leaflet tissue samples were placed in a glass bottom μ-dish (ibidi GmbH, Martinsried, Germany) and put on the microscope stage with a 60× water immersion objective (N.A. 1.4; Olympus, Tokyo, Japan). For detection of CPA residues in the tissues, the collagen-rich fibrosa layer of the cardiac valve leaflets[12] was assessed. A total of 30 spots per tissue were randomly selected and measured over an acquisition time of 10 s and 10 accumulations. For all liquid samples, 20 μL were placed onto a coverslip and 5 spectra were taken at an acquisition time of 10 s and 10 accumulations. Laser settings were 783 nm excitation wavelength and an output laser power of 80 mW. In addition, background spectra were recorded from the glass bottom dishes and glass coverslips with the same acquisition settings as for the sample measurements.

Spectral Analysis. Spectral data were pretreated with the spectra processing software OPUS (Bruker, Ettlingen, Germany). Background spectra were subtracted from the sample spectra and a baseline correction was performed. Peaks, classified as noise, light or cosmic rays were removed by the straight line generation function. Mean spectra of repeated measurements were calculated for supernatants (n = 5) and tissues (n = 30).

Quantification. All analyses were performed with the Unscrambler X (Camo Software AS, Oslo, Norway). A partial least-squares (PLS) regression model was used to analyze and predict the CPA concentrations in the supernatants according to their identified characteristic peaks. The data were mean-centered and the PLS regression was based on a NIPALS algorithm and a cross-validation. Spectral data of the calibration solutions were used to establish the model. The calibration for DMSO was performed at the maximum spectral intensity in the range of 640−780 cm^{-1}, for PG in the range of 780−860 cm^{-1}, and for FMD in the range of 1370−1410 cm^{-1} (see Supporting Information, Figure S1). For each CPA, the first component of the PLS regression described the

DOI: 10.1021/acs.analchem.8b04861
Anal. Chem. XXXX, XXX, XXX−XXX

concentration-dependent information (99% explained variance). All data are presented as mean ± standard deviation. Statistical analysis was performed with GraphPad Prism 6 (GraphPad Software Inc., La Jolla, CA, U.S.A.). *P*-values ≤0.05 were considered statistically significant.

Raman Imaging. Raman imaging was performed on unwashed and washed leaflets that were preserved in VS83. Measurements were acquired with a confocal Raman microspectroscope (WiTec alpha 3000, WiTec GmbH, Ulm, Germany). Ovine pulmonary leaflets were rewarmed and placed in a glass bottom μ-dish (ibidi GmbH). A green laser (532 nm) was utilized at a power of 40 mW. A 10× objective (Zeiss GmbH) was applied for all measurements. Images of an area of 2000 × 2000 μm were acquired at a low resolution of 100 × 100 μm and an integration time of 0.5 s for fast detection of CPA residues. To simulate the washing steps, the leaflets were rinsed in 1x EC solution and immediately imaged. Images were analyzed as intensity heat maps at selected spectral bandwidths and by principal component analysis (PCA). PCA of the spectral maps was performed with the Project FIVE 5.1 Software (WiTec GmbH) by the calculation of a covariance matrix and the corresponding eigenvectors (principal components) and eigenvalues (loadings). PCA resulted in false color intensity distribution images of the weightings of the selected principal component (PC).

■ RESULTS AND DISCUSSION

It has been shown that the use of highly concentrated CPAs for IFC of valves results in grafts without the presence of viable cells.[13] Nevertheless, IFC valves outperform postimplantation conventional FC valves as shown in previous animal studies.[13,37] Therefore, it is safe to conclude that the cytotoxic nature of the VS83 solution does not impact general graft function. However, the potential residual CPAs inside a valvular graft may influence the adjacent cells and ECM structures in the recipient tissue, which has to be addressed to guarantee transplant safety. Here, we utilized Raman microspectroscopy and imaging to quantify CPA residues in valve tissues and supernatants of the washing solutions.

Raman Spectra of the Cryoprotective Agents. Reference spectra of VS83 and the single cryoprotectant components were acquired and peaks of DMSO, PG, and FMD were identified (Table 1). The most prominent peaks at 677 and 711 cm^{-1} were assigned to DMSO,[38] and characteristic peaks of PG were detected at 806 and 841 cm^{-1}. For FMD, the two peaks at 1317 and 1393 cm^{-1} were most dominant. Additional peaks were identified that refer to dextrose in the EC solution.[39] However, peaks of the CPAs, especially the DMSO bands, had much higher intensities when compared with the peaks assigned to the dextrose and salts in the EC solution. The EC solution-related peaks were negligible for the overall VS83 spectrum (Figure 1), and a characteristic Raman shift region for each CPA was defined without significant interference with the other components. The calibration for each CPA was performed according to these spectral bandwidths.

Table 1. Characteristic Peaks in VS83 and Their Molecular Assignment

Raman shift (cm^{-1})	molecular assignment	component
677	CS symmetric stretch	DMSO
711	CS antisymmetric stretch	DMSO
806	CH_2 bending	PG
840	CCO stretching	PG
953	HCH rocking	DMSO
1023	CH deformation	EC (dextrose)
1087	COH deformation	EC (dextrose)
1316	CH deformation	FMD
1392	CH rocking	FMD
1418	HCH deformation	DMSO
1460	CH_3 bending	PG

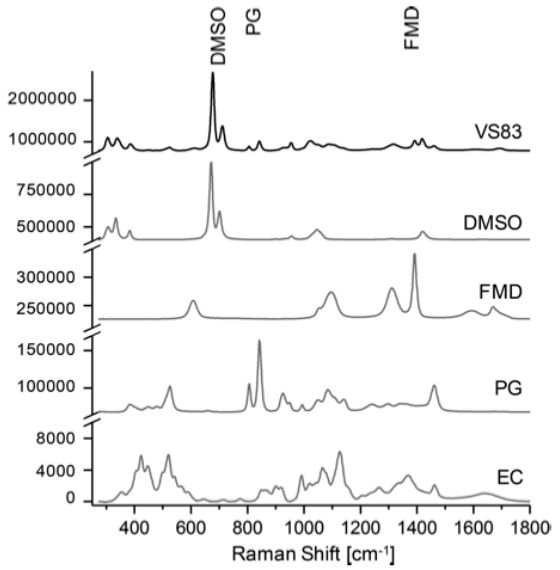

Figure 1. Raman spectra of the VS83 solution and its different components dimethyl sulfoxide (DMSO), formamide (FMD), propylene glycol (PG), and Euro-Collins (EC) solution. The most characteristic peaks are highlighted in blue.

Quantitative Assessment of the Washing Efficacy. VS83 contains higher CPA concentrations than standard cryopreservation solutions. Therefore, washing efficacy was assessed to ensure complete removal of the CPAs within the preimplantation tissues. Supernatants of each washing steps were measured to monitor the diffused CPAs, with washing solution 1 corresponding to the cryopreservation solution after rewarming, solutions 2–5 represent the washing steps with fresh EC solution for 5 min each, and washing solution 6 is the solution the tissues were kept in until implantation.

Average spectra of the supernatants identified a significant decrease of CPAs after the first washing step (Figure 2a). In detail, quantification of the spectral intensities of the supernatant samples according to the calibration model showed a significant ($p < 0.0001$) decrease after washing steps 1 and 2 (Figure 2b–d). After washing step 3, the initial CPA concentrations in the supernatants were decreased by 99.2% ± 0.15% for DMSO and PG and by 98.9% ± 0.43% for formamide. No statistically significant changes in CPA concentrations were detected. The CPA concentrations remained in a millimolar range; however, diffusion kinetics behaved differently depending on the CPA. DMSO and PG concentrations decreased faster than FMD concentrations. After the final washing step (step 5), DMSO concentrations were 0.02 ± 0.004 mol/L, PG concentrations were 0.01 ±

DOI: 10.1021/acs.analchem.8b04861
Anal. Chem. XXXX, XXX, XXX−XXX

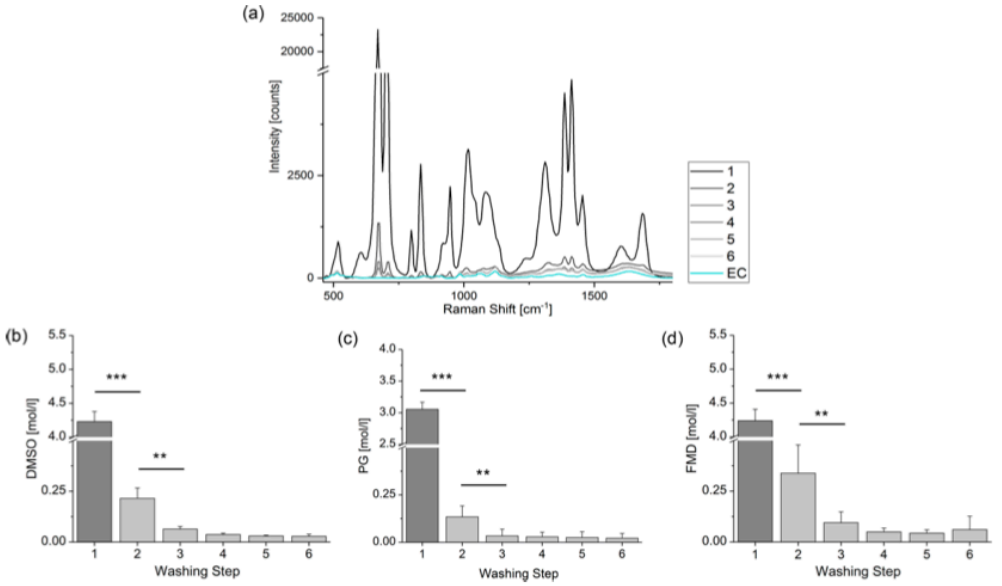

Figure 2. Quantification of CPAs in washing supernatants. (a) Average spectra of washing supernatants of each washing step and pure Euro-Collins (EC) solution. (b–d) Quantification of DMSO, PG, and FMD concentrations according to a calibration model in a defined spectral range. Each $n = 6$; $^{**}p \leq 0.01$; $^{***}p \leq 0.001$.

0.009 mol/L and FMD decreased to 0.04 ± 0.02 mol/L. Higher FMD concentrations of 0.06 ± 0.07 mol/L were still detectable in the storage solution (step 6). CPA quantification in the washing supernatants demonstrated that the washing protocol was efficient to remove the CPAs from the tissues. Our results indicate that an adaption of the washing protocol to shorten the procedure would be feasible. Three washing steps instead of six would be sufficient to ensure the absence of harmful CPA concentrations.

CPA Residues in Rewarmed Leaflets. Quantification of different CPAs and characterization of diffusion kinetics have been performed on supernatants before by other methods.[21,22] Here, we aimed to establish a technique to identify CPAs within tissues. Spectra of single point measurements of cryopreserved and washed valve leaflets were investigated before and after washing in order to identify peaks that are related to the CPAs. No DMSO-, PG-, or FMD-specific peaks could be detected in the Raman spectra of the preserved and washed leaflets. In contrast, the Raman spectra of unwashed leaflets clearly showed peaks in the Raman shift region of DMSO and also FMD (Figure 3a). PG peaks of low concentration VS83 were overlapped by the ECM collagen signals in the same Raman shift region.

Tissue Permeation Depends on CPA Concentration. Leaflets treated with different VS83 dilutions were analyzed to define the sensitivity of Raman microspectroscopy as a detection method for CPAs in tissues. Rewarmed, unwashed leaflets were measured. CPA-related peaks were detectable in all leaflets. Leaflets preserved in 5% VS83, corresponding to 0.2 M DMSO, still showed CPA-related peaks in their spectra. Interestingly, no proportional correlation between peak intensity and VS83 concentration was detected at higher VS83 concentration ranges. Leaflets stored in 100% VS83 showed interstitial CPA concentrations similar to leaflets stored in 25% VS83 and lower interstitial CPA concentrations when compared with leaflets stored in 50% and 75% VS83

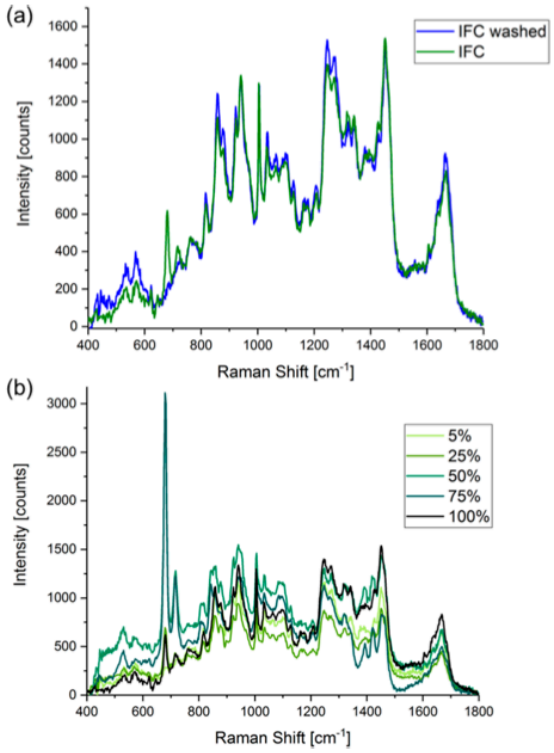

Figure 3. Detection of CPA residues in cardiac valve tissues. (a) Spectral data of rewarmed and washed (blue) or unwashed (green) IFC tissues show detectable CPA peaks. Spectra of washed tissues only show peaks related to the valve's ECM. (b) Analysis of leaflets that were cryopreserved in different concentrations of VS83 (5–100%) reveals a concentration-dependent tissue penetration of the CPAs.

DOI: 10.1021/acs.analchem.8b04861
Anal. Chem. XXXX, XXX, XXX−XXX

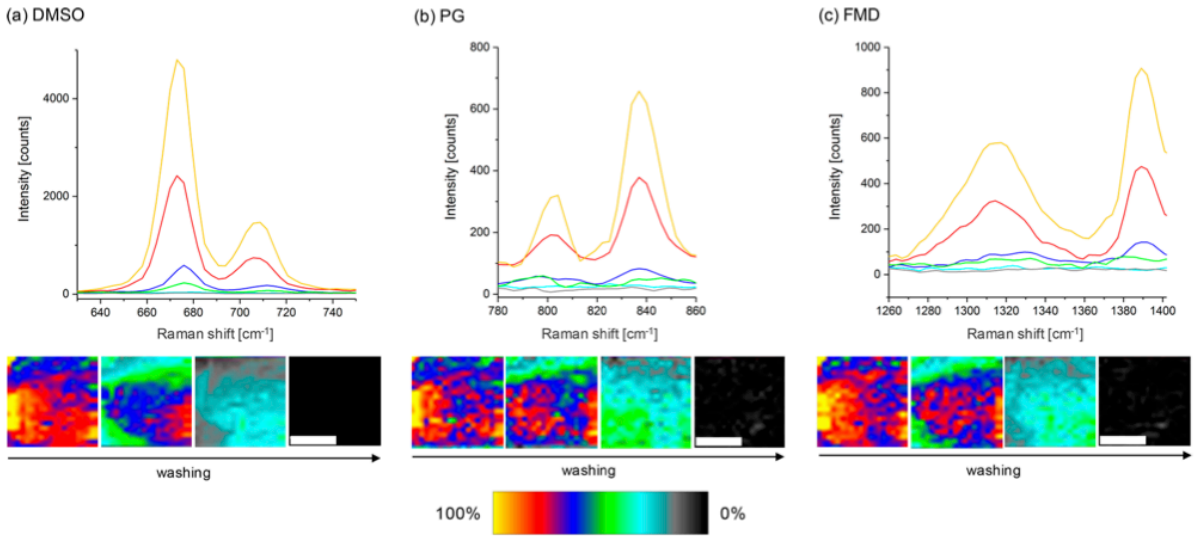

Figure 4. Raman imaging of CPA residues in unwashed and washed VS83-cryopreserved valve leaflets. Intensity heat maps and the correlating average spectral intensities at the different characteristic bandwidths for DMSO (a), PG (b), and FMD (c) indicate the CPA residues in the tissues. Color coding defines the relative spectral intensity. Scale bars equal 1 mm.

(Figure 3b). These findings could be explained by the underlying mechanism of the cryoprotective effect of the CPAs. IFC leaflets shrink and compact due to the treatment, as high CPA concentrations cause an efflux of interstitial fluid, resulting in dehydration and loss of weight as described for VS83 before.[35] At high CPA concentrations, intermolecular interactions between the different CPAs and an association with water might play a dominant role when compared to the interaction of the CPAs with the tissue. Self-association of PG occurs in the presence of water.[40] DMSO replaces water and forms stable DMSO−water clusters that have an effect on the freezing, and self-associate in the presence of lipids. Furthermore, DMSO tends to bind to water before it binds to proteins.[41,42] FMD prefers to self-associate into α-helix tertiary structures.[43] The formation of overall big complexes with neighboring molecules will reduce the permeability into the tissue.[4,44] In the presence of higher concentrations of water, the tissues remained hydrated and allowed a deeper penetration of the CPAs, resulting in higher interstitial CPA concentrations than in the dehydrated and condensed tissues. Previous studies mainly described CPA diffusion at temperatures above 0 °C. The diffusion coefficient is a temperature-dependent variable and it has been shown that CPA diffusion decreased with decreasing temperature.[22,24] Lower temperatures employed for the stepwise cooling of the valves during cryopreservation might enhance the influence of the interactions of the CPAs by decreasing the diffusion. We hypothesize that the different penetration kinetics can be explained due to the concentration-dependent binding properties of the CPAs. Notably, highly concentrated CPAs are essential to reach a cryopreservative effect that eliminates interstitial water and avoids deep infiltration with potentially toxic chemicals at the same time.

Raman Imaging of CPA Residues in Tissues. Raman imaging was performed on excised leaflets that were cryopreserved in VS83 solution to determine the tissue penetration of the CPAs. The first steps of the washing procedure were simulated by rinsing the leaflet in EC solution, as performed for the preimplantation valves. Figure 4 depicts the intensity heat maps of the CPA distribution in the leaflet tissue at the characteristic bandwidths of DMSO, PG, and FMD. Concentrations were significantly reduced after the first two washing steps for all CPAs, and after the third washing, no significant CPA residues were detectable. Spectra correlating to the average spectral intensity of each color labeling did not show significant CPA peaks in the light blue to gray color-coded range. DMSO, PG, and FMD differed in tissue efflux. In the freshly rewarmed, unwashed samples, DMSO and FMD showed a similar distribution within the tissue, whereas PG showed slightly lower CPA concentration levels. After the first washing step, all CPAs were significantly reduced. DMSO demonstrated the fastest diffusion out of the tissue. The regions at the tissue borders equilibrated faster to the concentration in the surrounding medium when compared to the regions in the tissue center, where higher concentrations were detected. For PG, a homogeneous distribution throughout the tissue was visible in the Raman imaging data after the first washing step. A similar tendency was observed in the data of the second washing step. All CPA concentrations continuously decreased. However, PG showed concentrations of 30−40% compared to the unwashed tissues, whereas FMD was reduced to 20−30% and DMSO diffused to a remaining CPA concentration of 10−20%. These diffusion results for the washing process are in accordance with the findings of an IR study determining the penetration kinetics of VS83 into aortic tissue, indicating the highest diffusion coefficient for DMSO, followed by FMD and PG.[35] For the third washing step, no differences between the three CPAs and also no differences between tissues and the washing solution were detectable. No CPA spectra were found in the tissues.

Raman imaging allowed for the simultaneous detection and quantification of DMSO, PG and FMD. Few techniques are capable of noninvasive, marker-independent imaging of chemicals in non-processed, intact tissues. Corral et al. applied X-ray computed tomography to quantify CPAs in liver tissue.[45] However, only DMSO quantification was successful due to the

DOI: 10.1021/acs.analchem.8b04861
Anal. Chem. XXXX, XXX, XXX−XXX

lack of significantly different attenuation levels for PG and other tested CPAs in comparison with water.

A PCA was performed on the Raman imaging data for a detailed analysis of the CPA distribution (Figure 5a). PC5-

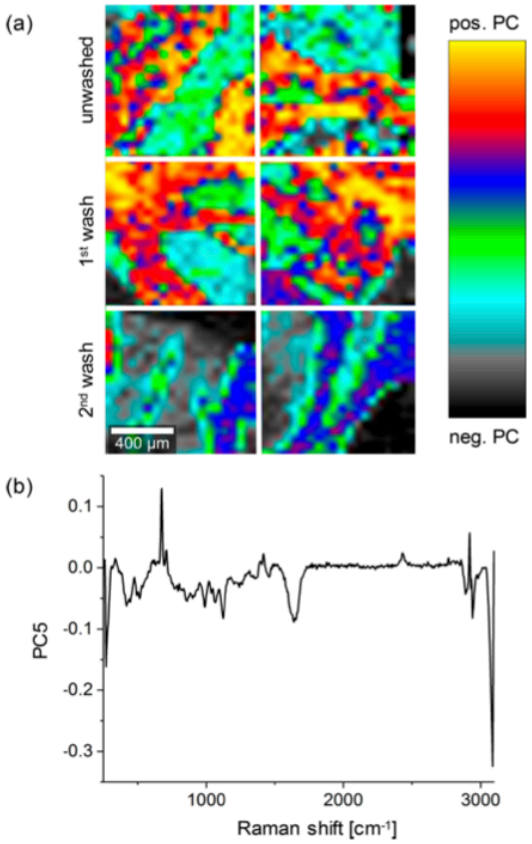

Figure 5. PCA of washed and unwashed tissues. (a) Intensity heat map of PC5. (b) Analysis of identified CPA-related spectral information in the positive range of PC5 and components related to the leaflet tissue in the negative range of PC5.

separated spectral information related to the CPAs in the positive range of the PC and tissue-related peaks in the negative range of the PC (Figure 5b). Peaks at 677 and 1392 cm^{-1} showed information related to DMSO and FMD in the VS83 solution. Peaks at 856, 935, 1245, and 1664 cm^{-1} indicated a molecular assignment to the leaflet's ECM structures. Freshly rewarmed leaflets and tissues after the first washing step mainly showed areas described by positive PC values, indicating CPA residues. The imaging data after the second washing step was dominated by negative PC5 values, which correlated to the detection of tissue structures and showed only a few spots in the low positive PC range. Raman imaging was performed at very low resolution to achieve fast data generation of a large tissue area. Detailed tissue structures were not detectable with these settings; however, the technique was fast and precise enough to monitor CPA residues and their diffusion properties.

CONCLUSIONS

IFC is an advantageous method for long-term cryopreservation of cardiac valves with the preservation of ECM structures.[10,13] Removal of cytotoxic CPA concentrations before implantation was demonstrated by an established multistep washing protocol. This work presents Raman microspectroscopy and Raman imaging as valuable techniques for the fast, noninvasive, and marker-independent in situ quantification of chemicals employed in IFC. Simultaneous detection of DMSO, PG, and FMD was performed in IFC valves and their supernatants. Raman microspectroscopy detected millimolar CPA concentrations in both washing supernatants and tissue samples, suggesting a future role for this technique in quality assessment. Raman imaging was successfully employed for the detection of CPAs in IFC tissues. In future applications, Raman microspectroscopy and Raman imaging may be promising tools for the quantitative study of chemical compounds or drug penetration and diffusion within tissues.

ASSOCIATED CONTENT

Supporting Information

The Supporting Information is available free of charge on the ACS Publications website at DOI: 10.1021/acs.analchem.8b04861.

Regression coefficient plots of the CPA quantification (PDF).

AUTHOR INFORMATION

Corresponding Author

*E-mail: katja.schenke-layland@med.uni-tuebingen.de.

ORCID

Katja Schenke-Layland: 0000-0001-8066-5157

Author Contributions

J.M. and K.S.-L. wrote the manuscript. Tissues and supernatants were provided by A.C.B. and U.A.S. J.M. conducted all experiments and data analyses. E.M.B., K.G.M.B., U.A.S., and K.S.-L. provided conceptual input and supervised the research.

Notes

The authors declare the following competing financial interest(s): K.G.M. Brockbank is an owner and employee of Tissue Testing Technologies LLC. The company is interested in the advance-ment of the VS83 solution for general tissue treatment. There are no further conflicts to declare.

ACKNOWLEDGMENTS

The authors thank Shannon Lee Layland (University of Tübingen) for his helpful comments. This work was supported by the German Research Foundation [Deutsche Forschungsgemeinschaft Sto 359/10-1 (to U.A.S.), as well as SCHE 701/10-1 and INST 2388/64-1 (both to K.S.-L.)], the Peter and Traudel Engelhorn foundation (Postdoc fellowship to E.M.B.), and the Ministry of Science, Research and the Arts of Baden-Württemberg (33-729.55-3/214 and SI-BW 01222-91 (to K.S.-L.)). K.G.M.B. was supported by the U.S. Army Medical Research and Materiel Command (Contract No. W81XWH-16-C-0174). The views, opinions, and findings contained in this report are those of the authors and should not be construed as an official Department of the Army position, policy, or decision unless so designated by other documentation.

DOI: 10.1021/acs.analchem.8b04861
Anal. Chem. XXXX, XXX, XXX−XXX

REFERENCES

(1) Giwa, S.; Lewis, J. K.; Alvarez, L.; Langer, R.; Roth, A. E.; Church, G. M.; Markmann, J. F.; Sachs, D. H.; Chandraker, A.; Wertheim, J. A. *Nat. Biotechnol.* **2017**, *35* (6), 530.
(2) Karow, A. M. *J. Pharm. Pharmacol.* **1969**, *21* (4), 209−223.
(3) Elliott, G. D.; Wang, S.; Fuller, B. J. *Cryobiology* **2017**, *76*, 74−91.
(4) Best, B. P. *Rejuvenation Res.* **2015**, *18* (5), 422−436.
(5) Fahy, G. M. *Cryobiology* **1986**, *23* (1), 1−13.
(6) Fahy, G. M.; Wowk, B.; Wu, J. *Rejuvenation Res.* **2006**, *9* (2), 279−291.
(7) Brown, J. W.; Ruzmetov, M.; Rodefeld, M. D.; Vijay, P.; Turrentine, M. W. *Annals of Thoracic Surgery* **2005**, *80* (2), 655−664.
(8) Mitchell, R. N.; Jonas, R. A.; Schoen, F. J. *J. Thorac. Cardiovasc. Surg.* **1998**, *115* (1), 118−127.
(9) Mayer, J. *Semin Thorac Cardiovasc Surg.* **1995**, *7* (3), 130−132.
(10) Schenke-Layland, K.; Xie, J.; Heydarkhan-Hagvall, S.; Hamm-Alvarez, S. F.; Stock, U. A.; Brockbank, K. G.; MacLellan, W. R. *Annals of thoracic surgery* **2007**, *83* (5), 1641−1650.
(11) Schenke-Layland, K.; Madershahian, N.; Riemann, I.; Starcher, B.; Halbhuber, K.-J.; König, K.; Stock, U. A. *Annals of thoracic surgery* **2006**, *81* (3), 918−926.
(12) Brockbank, K. G.; Chen, Z.; Greene, E. D.; Campbell, L. H., Vitrification of heart valve tissues. In *Cryopreservation and Freeze-Drying Protocols*; Springer: New York, NY, 2015; pp 399−421.
(13) Biermann, A. C.; Marzi, J.; Brauchle, E.; Wichmann, J. L.; Arendt, C. T.; Puntmann, V.; Nagel, E.; Abdelaziz, S.; Winter, A. G.; Brockbank, K. G. M.; Layland, S.; Schenke-Layland, K.; Stock, U. A. *European Journal of Cardio-Thoracic Surgery* **2018**, ezy292−ezy292.
(14) Williams, A. C.; Barry, B. W. *Adv. Drug Delivery Rev.* **2012**, *64*, 128−137.
(15) Santos, N. C.; Figueira-Coelho, J.; Martins-Silva, J.; Saldanha, C. *Biochem. Pharmacol.* **2003**, *65* (7), 1035−1041.
(16) Galvao, J.; Davis, B.; Tilley, M.; Normando, E.; Duchen, M. R.; Cordeiro, M. F. *FASEB J.* **2014**, *28* (3), 1317−1330.
(17) Brayton, C. F. *Cornell Veterinarian* **1986**, *76* (1), 61−90.
(18) Aye, M.; Di Giorgio, C.; De Mo, M.; Botta, A.; Perrin, J.; Courbiere, B. *Food Chem. Toxicol.* **2010**, *48* (7), 1905−1912.
(19) Program, N. T. *National Toxicology Program Technical Report Series* **2008**, No. 541, 1.
(20) Kennedy, G. L.; Short, R. D. *CRC critical reviews in toxicology* **1986**, *17* (2), 129−182.
(21) Decot, V.; Houze, P.; Stoltz, J.-F.; Bensoussan, D. *Bio-Med. Mater. Eng.* **2009**, *19* (4−5), 293−300.
(22) Lakey, J. R.; Helms, L. M.; Moser, G.; Lix, B.; Slupsky, C. M.; Rebeyka, I. M.; Sykes, B. D.; McGann, L. E. *Cell transplantation* **2003**, *12* (2), 123−128.
(23) Shardt, N.; Al-Abbasi, K. K.; Yu, H.; Jomha, N. M.; McGann, L. E.; Elliott, J. A. *Cryobiology* **2016**, *73* (1), 80−92.
(24) Takroni, T. A.; Yu, H.; Laouar, L.; Adesida, A. B.; Elliott, J. A.; Jomha, N. M. *Cryobiology* **2017**, *74*, 50−60.
(25) Lawson, A.; Mukherjee, I. N.; Sambanis, A. *Cryobiology* **2012**, *64* (1), 1−11.
(26) Rohleder, D.; Kiefer, W.; Petrich, W. *Analyst* **2004**, *129* (10), 906−911.
(27) Zhai, F.; Huang, Y.; Li, C.; Wang, X.; Lai, K. *J. Agric. Food Chem.* **2011**, *59* (18), 10023−10027.
(28) Zaleski, S.; Clark, K. A.; Smith, M. M.; Eilert, J. Y.; Doty, M.; Van Duyne, R. P. *Anal. Chem.* **2017**, *89* (4), 2497−2504.
(29) Freudiger, C. W.; Min, W.; Saar, B. G.; Lu, S.; Holtom, G. R.; He, C.; Tsai, J. C.; Kang, J. X.; Xie, X. S. *Science* **2008**, *322* (5909), 1857−1861.
(30) Liu, P.; Huang, Y.; Guo, Z.; Wang, J.; Zhuang, Z.; Liu, S. *J. Biomed. Opt.* **2013**, *18* (2), 020507.
(31) Ascencio, S. M.; Choe, C.; Meinke, M. C.; Müller, R. H.; Maksimov, G. V.; Wigger-Alberti, W.; Lademann, J.; Darvin, M. E. *Eur. J. Pharm. Biopharm.* **2016**, *104*, 51−58.
(32) Strachan, C. J.; Rades, T.; Gordon, K. C.; Rantanen, J. *J. Pharm. Pharmacol.* **2007**, *59* (2), 179−192.
(33) Ager, J. W., III; Drory, M. D. *Phys. Rev. B: Condens. Matter Mater. Phys.* **1993**, *48* (4), 2601.
(34) Szostak, R.; Mazurek, S. *Analyst* **2002**, *127* (1), 144−148.
(35) Vásquez-Rivera, A.; Sommer, K. K.; Oldenhof, H.; Higgins, A. Z.; Brockbank, K. G.; Hilfiker, A.; Wolkers, W. F. *Analyst* **2018**, *143* (2), 420−428.
(36) Pudlas, M.; Koch, S.; Bolwien, C.; Thude, S.; Jenne, N.; Hirth, T.; Walles, H.; Schenke-Layland, K. *Tissue Eng., Part C* **2011**, *17* (10), 1027−1040.
(37) Lisy, M.; Pennecke, J.; Brockbank, K. G.; Fritze, O.; Schleicher, M.; Schenke-Layland, K.; Kaulitz, R.; Riemann, I.; Weber, C. N.; Braun, J. *Biomaterials* **2010**, *31* (20), 5306−5311.
(38) Martens, W. N.; Frost, R. L.; Kristof, J.; Theo Kloprogge, J. *J. Raman Spectrosc.* **2002**, *33* (2), 84−91.
(39) Vasko, P.; Blackwell, J.; Koenig, J. *Carbohydr. Res.* **1972**, *23* (3), 407−416.
(40) Rhys, N. H.; Gillams, R. J.; Collins, L. E.; Callear, S. K.; Lawrence, M. J.; McLain, S. E. *J. Chem. Phys.* **2016**, *145* (22), 224504.
(41) Dabkowska, A. P.; Foglia, F.; Lawrence, M. J.; Lorenz, C. D.; McLain, S. E. *J. Chem. Phys.* **2011**, *135* (22), 12B611.
(42) Kirchner, B.; Reiher, M. *J. Am. Chem. Soc.* **2002**, *124* (21), 6206−6215.
(43) Bolen, D.; Baskakov, I. V. *J. Mol. Biol.* **2001**, *310* (5), 955−963.
(44) Naccache, P.; Sha'afi, R. *J. Gen. Physiol.* **1973**, *62* (6), 714−736.
(45) Corral, A.; Balcerzyk, M.; Parrado-Gallego, Á.; Fernández-Gómez, I.; Lamprea, D. R.; Olmo, A.; Risco, R. *Cryobiology* **2015**, *71* (3), 419−431.

DOI: 10.1021/acs.analchem.8b04861
Anal. Chem. XXXX, XXX, XXX−XXX

Appendix IV: J. Marzi, E.M. Brauchle, K. Schenke-Layland, M. Rolle, *Non-invasive functional molecular phenotyping of human smooth muscle cells utilized in cardiovascular tissue engineering*, Acta Biomaterialia, 2019; 89: 193-205

Acta Biomaterialia 89 (2019) 193–205

Contents lists available at ScienceDirect

Acta Biomaterialia

journal homepage: www.elsevier.com/locate/actabiomat

Full length article

Non-invasive functional molecular phenotyping of human smooth muscle cells utilized in cardiovascular tissue engineering

Julia Marzi [a], Eva M. Brauchle [a,b], Katja Schenke-Layland [a,b,c,*,1], Marsha W. Rolle [a,d,1]

[a] Department of Women's Health, Research Institute for Women's Health, Eberhard Karls University, Tübingen, Germany
[b] The Natural and Medical Sciences Institute (NMI) at the University of Tübingen, Reutlingen, Germany
[c] Department of Medicine/Cardiology, Cardiovascular Research Laboratories, David Geffen School of Medicine at UCLA, Los Angeles, CA, USA
[d] Department of Biomedical Engineering, Worcester Polytechnic Institute, Worcester, MA, USA

ARTICLE INFO

Article history:
Received 25 November 2018
Received in revised form 8 March 2019
Accepted 12 March 2019
Available online 13 March 2019

Keywords:
Smooth muscle cell heterogeneity
Phenotypic switching
Blood vessel
Raman microspectroscopy
Marker-independent imaging

ABSTRACT

Smooth muscle cell (SMC) diversity and plasticity are limiting factors in their characterization and application in cardiovascular tissue engineering. This work aimed to evaluate the potential of Raman microspectroscopy and Raman imaging to distinguish SMCs of different tissue origins and phenotypes. Cultured human SMCs isolated from different vascular and non-vascular tissues as well as fixed human SMC-containing tissues were analyzed. In addition, Raman spectra and images of tissue-engineered SMC constructs were acquired. Routine techniques such as qPCR, histochemistry, histological and immunocytological staining were performed for comparative gene and protein expression analysis. We identified that SMCs of different tissue origins exhibited unique spectral information that allowed a separation of all groups of origin by multivariate data analysis (MVA). We were further able to non-invasively monitor phenotypic switching in cultured SMCs and assess the impact of different culture conditions on extracellular matrix remodeling in the tissue-engineered ring constructs. Interestingly, we identified that the Raman signature of the human SMC-based ring constructs was similar to the one obtained from native aortic tissue.

We conclude that Raman microspectroscopic methods are promising tools to characterize cells and define cellular and extracellular matrix components on a molecular level. In this study, in situ measurements were marker-independent, fast, and identified cellular differences that were not detectable by established routine techniques. Perspectively, Raman microspectroscopy and MVA in combination with artificial intelligence can be suitable for automated quality monitoring of (stem) cell and cell-based tissue engineering products.

Statement of Significance

The accessibility of autologous blood vessels for surgery is limited. Tissue engineering (TE) aims to develop functional vascular replacements; however, no commercially available TE vascular graft (TEVG) exists to date. One limiting factor is the availability of a well-characterized and safe cell source. Smooth muscle cells (SMCs) are generally used for TEVGs. To engineer a TEVG, proliferating SMCs of the synthesizing phenotype are essential, whereas functional, sustainable TEVGs require SMCs of the contractile phenotype. SMC diversity and plasticity are therefore limiting factors, also for their quality monitoring and application in TE. In this study, Raman microspectroscopy and imaging combined with machine learning tools allowed the non-destructive, marker-independent characterization of SMCs, smooth muscle tissues and TE SMC-constructs. The spectral information was specific enough to distinguish for the first time the phenotypic switching in SMCs in real-time, and monitor the impact of culture conditions on ECM remodeling in the TE SMC-constructs.

© 2019 Acta Materialia Inc. Published by Elsevier Ltd. This is an open access article under the CC BY-NC-ND license (http://creativecommons.org/licenses/by-nc-nd/4.0/).

1. Introduction

Pre-existing vascular diseases, re-operations and the shifting indication to an elderly population limit the accessibility of suitable autologous vessels in about 30% of the patients undergoing

* Corresponding author at: Department of Women's Health, Research Institute for Women's Health, Eberhard Karls University, Silcherstrasse 7/1, 72076 Tübingen, Germany.
E-mail address: katja.schenke-layland@med.uni-tuebingen.de (K. Schenke-Layland).
[1] Authors contributed equally.

https://doi.org/10.1016/j.actbio.2019.03.026
1742-7061/© 2019 Acta Materialia Inc. Published by Elsevier Ltd.
This is an open access article under the CC BY-NC-ND license (http://creativecommons.org/licenses/by-nc-nd/4.0/).

coronary artery bypass surgery [1,2]. Vascular tissue engineering aims to develop functional, persisting vascular replacements. However, no commercially available tissue-engineered vascular graft (TEVG) exists to date. Synthetic grafts as well as TEVG approaches failed due to the development of stenosis or atherosclerosis [3,4]. Smooth muscle cells (SMCs) are used in tissue engineering for construction of vascular grafts or the assembly of other organs [5–7] and play a crucial role in vascular pathologies, due to their phenotypic switching ability [8–10]. SMCs of the contractile type are spindle-shaped, provide mainly contractile filaments and are less proliferative. SMCs of the proliferative or synthetic type show a rhomboid, fibroblast-like shape, dominate in protein synthesizing organelles and have a higher proliferation rate [11,12]. To populate and seed a tissue-engineered construct, proliferating SMCs of the synthesizing phenotype are essential, whereas functional, sustainable TEVGs require SMCs of the contractile phenotype. Phenotypic switching and its stimuli and regulating factors are extensively described in basic research [13–16] and the relevance for tissue engineering has been discussed by others [17,18]. Despite detailed mechanistic studies, most research regarding SMC behavior is observational and lack an approach to control and direct SMC plasticity in tissue-engineering constructs. Moreover, there are no methods for the reliable, consistent and quantitative characterization of SMC phenotypes in situ, as well as their differentiation within tissue constructs [17].

SMC tissue origin is another area that needs addressing for cell-based biomaterial design. Smooth muscle tissue is prevalent in distinct anatomic body compartments. It is well known that the vasculature contains a smooth muscle layer; however lesser known tissues such as the urinary, uterine and gastrointestinal tracts are composed of smooth muscle tissue as well. Although these tissues differ in their function and appearance, all of them are formed by SMCs. To date very little is known regarding the tissue-specific characteristics of primary SMCs. Very few studies have compared SMCs of different tissue origin [19,20]. Quantitative distinction between SMCs of distinct anatomical regions and the impact of the selected tissue origin of SMCs applied for tissue engineering have not been thoroughly investigated.

In the present study, we employed a technique that enables marker-independent, non-destructive in situ microscopy that provides molecular information of cell and tissue samples. Raman microspectroscopy is a laser-based technique that induces photon-molecule interactions. Combined with a confocal microscope, sample structures can be targeted to acquire biochemical information. In Raman microspectroscopy, a sample is excited with a laser source to induce molecular vibrations. The spectrometer with a charge coupled device (CCD) camera converts the backscattered light, so-called incoherent Raman scattering, to a single spectrum of the targeted spot. The resulting spectra are comparable to a biochemical fingerprint. Every peak is assigned to a molecular vibration and allows for the characterization and analysis of the sample. Raman spectroscopy is well established in material science and pharmaceuticals [21–23] and is gaining broader recognition in the biological and biomedical field [24,25]. Raman spectroscopy is used in cancer diagnostics [26–28] as well as skin and cardiovascular research [29,30]. Raman spectroscopy has been applied to detect lipids in atherosclerosis [29], image SMCs on scaffolds [31] and to test vascular SMC response in fresh arteries [32]. A recent study by Molony et al. applied vibrational spectroscopy to distinguish de-differentiated SMCs from undifferentiated stem cells and their progenitors [33]. These studies performed analyses at the cellular level, but no subcellular SMC structures were analyzed.

The objective of this study was to identify and characterize SMCs applied in tissue engineering on a molecular level. We assessed the sensitivity and selectivity of Raman microspectroscopy as a quality control tool to detect differences between cell phenotype and populations. Furthermore, we monitored extracellular matrix (ECM) remodeling in tissue-engineered rings comprised of human SMCs, similar to rat aortic SMC rings previously described [34], and compared it to native human tissue.

2. Materials & methods

2.1. Human cell culture

Primary human SMCs isolated from non-vascular [trachea (HTSMC), uterus (HUtSMC)] and vascular [coronary artery (HCASMC), pulmonary artery (HPASMC) and aorta (HAoSMC)] tissues were purchased (PromoCell, Heidelberg, Germany). Cells were thawed and seeded in culture flasks at a density of 6500 cells per cm^2 in SMC Growth Medium 2 (PromoCell), supplemented with 1% Penicillin/Streptomycin (Thermo Fisher Scientific, Waltham, MA, USA) and SMC supplement mix (PromoCell). Cells were cultured 48–72 h up to a confluency of 80%, detached with EDTA-Trypsin 0.05% (Thermo Fisher Scientific), and seeded up to passage 20 for further experiments.

2.2. Tissue-engineered rings

Engineered vascular tissue rings derived from hCASMCs and hAoSMCs (LifeLine Cell Technology LLC, Frederick, MD, USA) were cultured for 14 days, as described previously [35]. Briefly, hSMCs were seeded into ring-shaped, non-adhesive agarose wells (400,000 cells/ring) to form 2 mm diameter rings [36]. The rings were seeded and cultured in growth medium (GM, LifeLine Cell Technology LLC) for 24 h, then cultured in differentiation medium (DMEM, 1% FBS, 1% ITS, 1% Penicillin/Streptomycin [35]), quiescence medium (QM) or GM supplemented with 10 ng/ml transformation growth factor β1 (TGF-β) for 14 days with medium exchanged daily. Rings were fixed with 4% formalin, paraffin-embedded and sectioned for Raman measurements and routine histochemistry (hematoxylin and eosin (H&E), fast green/picrosirius red), as previously described [35].

2.3. Human tissues

Native formalin-fixed and paraffin-embedded human tissues from pulmonary artery, aorta, trachea and uterus (purchased from amsbio LLC, Cambridge, MA, USA) were sectioned and mounted onto cover glasses for Raman measurements.

2.4. Immunocytochemistry (ICC)

Cells were seeded on 1% gelatin coated glass bottom μ-dishes (ibidi GmbH, Martinsried, Germany) and incubated for 24–48 h. After fixation with 4% PFA (Affymetrics/Thermo-Fisher Scientific) for 20 min, cells were washed with PBS (Thermo Fisher Scientific), treated with Triton X-100 0.05% (Fluka/Sigma-Aldrich, St. Louis, MO, USA) and blocked with goat block (Vector Laboratories, Burlingame, CA, USA). Cells were stained for calponin (CNN1 (1:200)), smooth muscle myosin heavy chain (MYH11 (1:100)), syndecan (SYN4 (1:400), collagen I (COL1A1 (1:75) and connexin (CX43 (1:200) (Sigma-Aldrich) and stored at 4 °C over night. Immunofluorescence labeling was performed with IgG goat anti-rabbit AlexaFluor 488 secondary antibody (Thermo Fisher Scientific) for 30 min at room temperature. Cell nuclei were stained with DAPI (Roche, Basel, Switzerland). Samples were washed and mounted with Prolong Gold Antifade (Thermo Fisher Scientific).

2.5. Real-Time quantitative polymerase chain reaction (qPCR)

Cells of passage 6 were trypsinized and washed with PBS. The cell pellet (500.000–1.000.000 cells) was suspended in 350 µl RLT lysis buffer, homogenized (QIAShredder, Qiagen, Hilden, Germany) and stored at −80 °C until all cell lysates were collected for further proceeding to total RNA isolation with the RNeasy micro kit (Qiagen). Isolated RNA was quantified and qualified using a NanoDrop spectrometer (Thermo Fisher Scientific) and the Experion® automated electrophoresis system (Bio-Rad, Hercules, CA, USA). First strand cDNA was generated in a thermal block cycler (C1000; Bio-Rad) using reversed transcriptase, a mixture of anchored dT and random hexamer primer (Qiagen) and 1 µg of total RNA. Real-time PCR for contractile and synthetic phenotype SMC genes was performed with the QuantiFast SYBR Green Kit (Qiagen) in the thermal block cycler combined with a real time system (CFX96, BioRad). *CNN1* (QT00067718), caldesmon (*CALD1* (QT00997899)), α-smooth muscle actin (*ACTA2* (QT00088102)), *MYH11* (QT00069391) and *COL1A1* (QT00037793) and *COL3A1* (QT00058233) served as primer and *GAPDH* (QT01192646) was used as housekeeping gene (all Qiagen). All data were normalized to hAoSMC gene expression levels for comparison of gene expression within the different types of SMC origin. Experiments were conducted at least as triplicates.

2.6. Raman microspectroscopy and single spectra acquisition

Raman measurements of single cells were obtained with a custom-build confocal Raman microspectroscope, combining a confocal microscope with a near-infrared laser source (783 nm) as previously described [37]. Human tissues and tissue-engineered rings were cut (10 µm thickness). Sections were collected on gelatin-coated coverslips as previously described [38]. The tissues were deparaffinized and kept humid with PBS during the entire measurement procedure to prevent sample dehydration and burning. The coverslip was placed on the microscope stage on a 60x water immersion objective (N.A. 1.2, Olympus, Shinjuku, Japan). The samples were targeted on the wavy structures of collagen bundles [37] and the laser power was set to 85 mW. Raman measurements were initiated with the Andor iDus spectra acquisition software (Andor Technology Ltd, Belfast, UK). Spectra were measured in the Raman fingerprint region from 0 to 2000 cm^{-1}. Each spectrum was averaged by the acquisition of 10 spectra. Acquisition time was 10 s per spectrum, resulting in a total acquisition time of 100 s per spot. 30 spots within each tissue were randomly selected and measured. Cells were detached with Trypsin – EDTA 0.05% and washed with PBS by centrifugation (3 min, 1000 rpm). The cell pellet was suspended in PBS at a concentration of 1×10^5 cells/ml and 250 µl of the suspension was transferred to a glass bottom dish. The dish was placed on the microscope stage and cells were targeted in the middle of the cell. Microscope and acquisition settings were the same as for the SMC tissues. 30 cells of each passage and origin type were measured. Background spectra were collected of the glass bottom dish with only PBS (Fig. 1). In addition, lyophilized aggrecan from bovine articular cartilage (Merck, Darmstadt, Germany) was used to acquire a proteoglycan reference spectrum at an acquisition time of 1s and a laser power of 60 mW.

2.7. Raman mapping and imaging

Raman imaging was performed with a customized Raman system (WiTec alpha 300 R, Ulm, Germany) equipped with a green laser (532 nm) and a 63× Apochromat water dipping objective (N.A. 1.0; Carl Zeiss GmbH). The device is equipped with a CCD

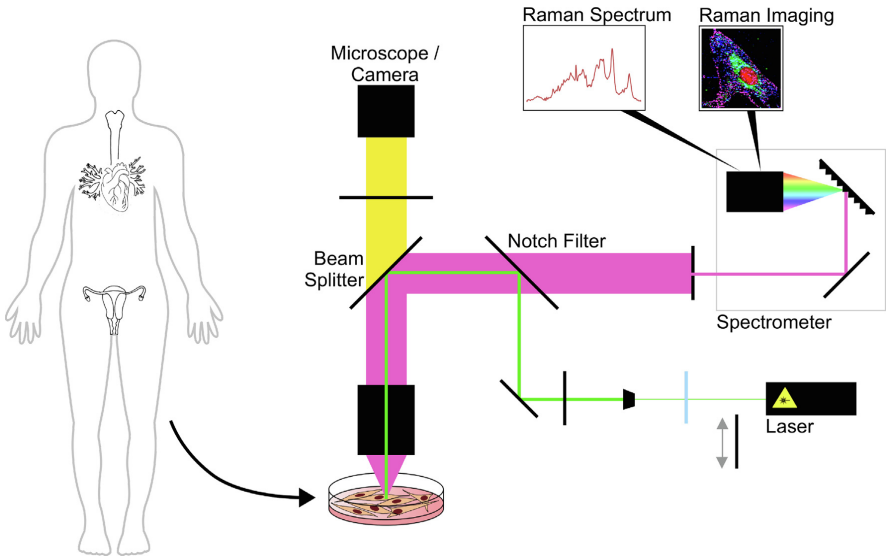

Fig. 1. Principle of Raman microspectroscopy. Isolated human SMC tissues and cells were measured (fixed or in situ). A laser source providing a green (532 nm) or near-infrared (735 nm) laser passes an optical isolator over a deflection mirror. The laser is led into a beam expander and a downstream polarizer. Afterwards it is directed through a notch filter and a beam splitter into the objective lens of the microscope and focuses on the sample. Due to molecular interaction, the light is scattered, collected by the lens, and only the light with a wavelength shift (Raman shift) passes the notch filter and is directed into the spectrometer. In the spectrometer, the light is led through a pinhole aperture and the different wavelength shifts are separated over a diffraction grating and detected by a change-coupled device camera. The acquisition of a single spectrum or a spectral map of a defined area and resolution is possible. green: incident laser source; pink: spontaneous Raman scattering; yellow: bright-field setting of the microscope. (For interpretation of the references to colour in this figure legend, the reader is referred to the web version of this article.)

camera. A spectrograph with a grating of 600 g/mm was chosen for spectral detection. Laser power was set to 39 mW. Samples were treated the same as for single spectrum acquisition. Images of SMC rings were acquired at a resolution of 1 μm/pixel and 0.5 s acquisition time per spectrum. This implied that every μm^2 was described by a single spectrum (Fig. 1).

2.8. Spectral analysis

Single spectral data were pretreated with the spectra processing software OPUS (Bruker, Ettlingen, Germany). Background spectra were subtracted from the sample spectra and the baseline was corrected. Principal component analysis (PCA) was applied to define and analyze spectral differences within every spectral dataset, as described before for the discrimination of different cells [38,39]. The multivariate data analysis (MVA) software 'The Unscrambler X' (CAMO Software AS, Oslo, Norway) was used. A PCA identifies spectral differences and similarities on a vector based algorithm [40–42]. Every vector describes a principal component (PC). PC1 is the vector explaining the main variance in spectral information; however, it often describes differences in baseline or background. PC2 describes the second most influencing information and so on. The variance explained by each PC is indicated as percentage number. For every PCA performed in this study, 7 PCs were calculated based on a nonlinear iterative partial least square (NIPALS) algorithm. For analysis of the data sets, the scores plots and the loadings plots of the PCAs were examined. The scores describe every single spectrum, which can then be displayed as a spot in a two-dimensional vector plot based on two selected PCs. A clustering of the data is shown in the scores plot if the PC demonstrates spectral differences within the groups. The loadings plot shows the Raman shift values describing the information of the selected PC. Peaks shown in the loadings plot allow to identify the molecular assignments relevant for clustering of the data in the corresponding PC. Spectra with score values in the positive range of the PC contained molecular information correlating to the peaks in the positive range of the loadings plot. Spectra with score values in the negative range of the PC contained information related to the peaks in the negative range of the loadings plot.

Raman images of the SMC rings were analyzed using Project FIVE 5.0 software (WiTec). True Component Analysis (TCA) allowed for identification of single components characterizing the sample. This method defined similar spectra as the same component and identified all pixels that provided these spectral characteristics in an intensity distribution image. Average spectra of the components were extracted to identify the molecular information of each component.

An overview of all samples, experiments and performed analyses is provided in the Supporting Information (Supplementary Table 1).

2.9. Second harmonic generation imaging

HAoSMC rings and aortic tissue samples were analyzed using second harmonic generation (SHG) of collagen fibers. SHG imaging was performed with a laser scanning microscope (LSM 880; Carl Zeiss GmbH, Jena, Germany) combined with a pulsing titanium sapphire laser (MaiTai, Spectra Physics, Santa Clara, CA, USA). Tissue sections of 10 μm were collected on gelatin-coated glass cover slips. Paraffin was removed in different washing steps with Xylol. Images were acquired with a 20x objective (N.A. 0.8, Carl Zeiss GmbH). The laser power was set to 4%. The SHG signal of collagen fibers was detected at 800 nm excitation wavelength and a detector range of 385–410 nm.

2.10. Statistical analysis

Statistical analyses were performed with Prism 6 (GraphPad, La Jolla, CA, USA). Data are represented as mean ± standard deviation. Differences were assessed with an analysis of variance (ANOVA). P values of 0.05 or less were considered statistically significant.

3. Results

3.1. Raman microspectroscopy allows to distinguish hSMCs of different origins on a single cell-level

Single spectrum acquisition of passage 6 SMCs of different tissue origins in suspension was performed. Representative Raman spectra of each SMC subtype are shown in Supplementary Fig. 1 (S1). PCA analysis of the data showed that all groups of cells could be distinguished according to their biological Raman fingerprint (Fig. 2). PC2/PC3 scores plot showed clustering between all groups. A clear separation between non-vascular and vascular cells was observed. However, a clustering within the groups was also present (Fig. 2A). Loadings of PC2 and PC3 (Fig. 2C, D) explained spectral differences within the cell types. Peaks in the loadings plot correlated to molecular information of the samples. PC2 explained nucleus related differences, described by peaks assigned to DNA (720 cm^{-1}), DNA bases (e.g. Uracil at 778 cm^{-1}) and DNA backbone (1090 cm^{-1}). PC3, separating non-vascular and vascular SMCs, correlated to cellular components such as membrane related proteins (775 cm^{-1}), proteins (1250 and 1650 cm^{-1}) and lipids (1125 and 1339 cm^{-1}). Characteristic peaks of all analyses performed in this study and their molecular assignment are shown in Table 1.

In contrast to the Raman results, routine techniques for gene and protein expression assessment in cells were not precise enough to distinguish between the five hSMC groups and to assign the hSMCs to a certain type of tissue. Real time qPCR for contractile (*ACTA2*, *CNN1*, *CALD* and *MYH11*) and synthetic (*COL1A1* and *COL3A1*) SMC phenotype markers showed differences in gene expression levels (Fig. 3A–F). However, those results did not enable a clear and fast differentiation and separation of HSMCs from the different tissues. Compared to the gene expression in HAoSMCs, that was used as internal standard, significantly increased levels were only detected for *ACTA2* in HCASMCs (Fig. 3A), for *CNN1* in the non-vascular SMCs (Fig. 3B) and for *CALD1* in HCASMCs and HUtSMCs (Fig. 3C). *MYH11* expression levels did not significantly differ from each other (Fig. 3D). Collagen expression levels of both *COL1A1* and *COL3A1* were modest and did not differ in between the different types of origin. Solely HTSMCs showed a significant increase in *COL3A1* when compared to the other HSMCs (Fig. 3E, F). Detailed statistics and multiple comparison of the gene expression levels are provided in the supporting information (Supplementary Table 2). Immunofluorescence staining for contractile SMC markers CNN1 and MYH11 was positive for all SMC types of origin. However, ICC did not allow for a quantitative assessment of the protein expression levels or a discrimination of the distinct SMCs (Fig. 3G).

3.2. Non-invasive monitoring of phenotypic switching in hSMCs

SMCs of a non-vascular (uterus) and vascular (coronary artery) origin were cultured for 20 passages and Raman spectroscopic measurements were taken of 30 cells at every other passage. Comparison of similarly composed samples often results in not more than small spectral changes, peak shifts or intensity differences. These differences were minimal in the spectral graphs themselves (Fig. 4A, B). Therefore, spectral data were analyzed by PCA to define minor spectral alterations. Both populations indicated a shift in their spectral information over culture time. A shift in score values

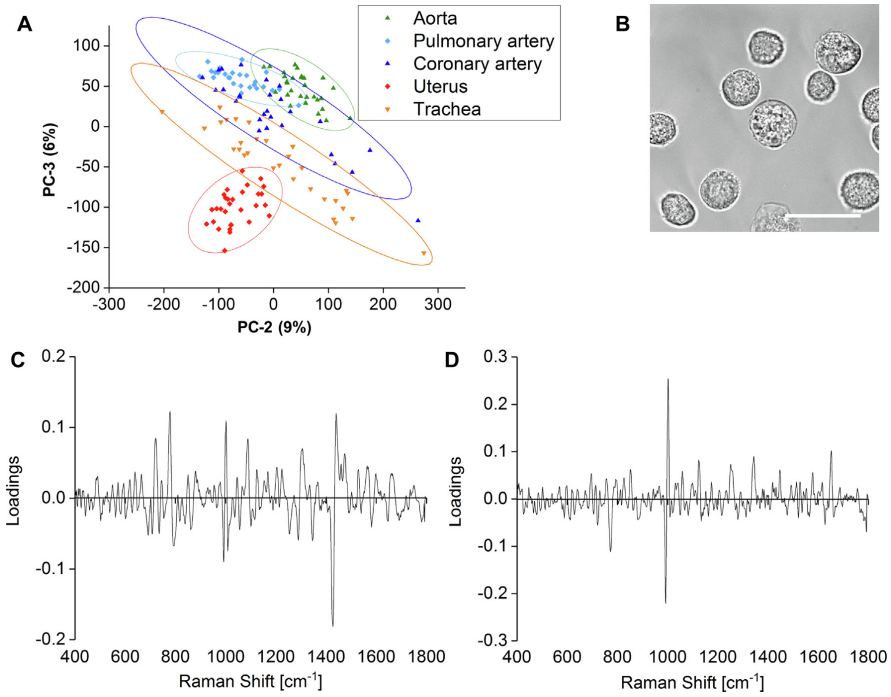

Fig. 2. Raman spectrum analysis of single human SMCs in suspension. (A) Scores plot of normalized and 2nd derivative Raman spectra shows the clustering of all cells of different tissue origins. In PC3, a separation of vascular SMCs can be detected in the positive range, and non-vascular SMCs in the negative range. Thirty cells were measured per group. Ellipses indicate a confidence interval of 95%. (B) Phase-contrast bright-field image of targeted cells. Scale bar equals 20 μm. (C, D) Loadings plots of PC2 and PC3 show the spectral ranges that explain the differences within the samples.

Table 1
Raman peaks and their molecular assignments identified by PCAs.

Peak [cm^{-1}]	Molecular assignment	Analysis
623	C–C twisting (proteins) [39]	Fig. 6E
720	DNA [74]	Fig. 2C
775	Phosphatidylinositol [75]	Fig. 2D
778	Uracil [76]	Fig. 2C
785	DNA [39]	Fig. 4E, Fig. 6A
939	Proline (collagen) [44]	Fig. 7B
1008	Proteoglycans [55]	Fig. 6E
1090	DNA backbone. Phosphate [43]	Fig. 2C, Fig. 6A
1099	DNA bases [40]	Fig. 4E
1102	DNA bases [40]	Fig. 4F
1125	acyl backbone (lipids) [77]	Fig. 2D
1128	C-N stretching (proteins) [44]	Fig. 4F
1246	Tyrosine (collagen) [44]	Fig. 6E
1250	amide III (proteins) [41]	Fig. 2D, Fig. 7B
1263	protein band (collagens) [42,43]	Fig. 4F
1294	Cytosine [78]	Fig. 2C
1297	CH_2 deformation (Collagen backbone) [44]	Fig. 7B
1299	CH_2 deformation (lipids) [39]	Fig. 4F
1310	C-N stretching (amines) [41]	Fig. 4E
1339	CH_2/CH_3 twisting (lipids) [77]	Fig. 2D
1373	DNA bases [51]	Fig. 6A
1434	CH_2 deformation [39]	Fig. 2C
1440	CH_2 bending [42,75,79]	Fig. 4D
1446	CH_3/CH_2 scissoring [27]	Fig. 6E
1454	CH_2 scissoring/CH_3 bending (collagen) [44]	Fig. 6E, Fig. 7B
1650	Proteins amide I [40]	Fig. 2D
1654	amide I [44]	Fig. 4E
1657	C=O stretching, C=lipids) [42,43]	Fig. 4E
1663	amide I [44]	Fig. 6E

was detected in PC3 for HUtSMCs (Fig. 4C) and a shift in PC2 was shown for HCASMCs (Fig. 4D).

Both SMC types showed a significant difference between early and later passages. In HUtSMC spectra, a significant shift was detected after passage 6 and passage 12, whereas a continuous alteration occurred in HCASMCs. HUtSMCs retained a phenotype intermediate for 2–3 passages and then significantly altered. HCASMCs up to passage 10 did not differ in their spectral information. A significant shift occurred between passage 10 and 12 and again between passage 16 and 20. According to the loadings plot, changes in HUtSMCs were mostly based on intensity changes and peak shifts at 785, 1099, 1310 and 1657 cm^{-1}. These peaks relate to cellular structures such as the DNA bases in the nucleus [39 40], amino acids [41] and amide I in proteins and C=C and CH_2 bonds in lipids [42,43]. Changes in HCASMCs were mainly linked to peaks at 1102, 1128, 1263 and 1299 cm^{-1}. Similar cellular structures as for HUtSMCs were identified by those peaks, however, different molecular bonds were affected. Peaks of the PC2 loadings plot of HCASMC data referred to amino acids and the C–C backbone in collagen [42,43], amide III in proteins [44], DNA bases in the nucleus [40] and the acyl backbone in lipids [39].

In parallel to Raman measurements, standard ICC for proteins corresponding to synthetic phenotype markers was performed (Fig. 5). Morphological alterations throughout culture time were visible in bright field images. Whereas low passage HUtSMCs clearly showed the spindle-shaped morphology of contractile SMCs and low passage HCASMCs were less differentiated in their morphology. HUtSMCs significantly shifted in morphology to a

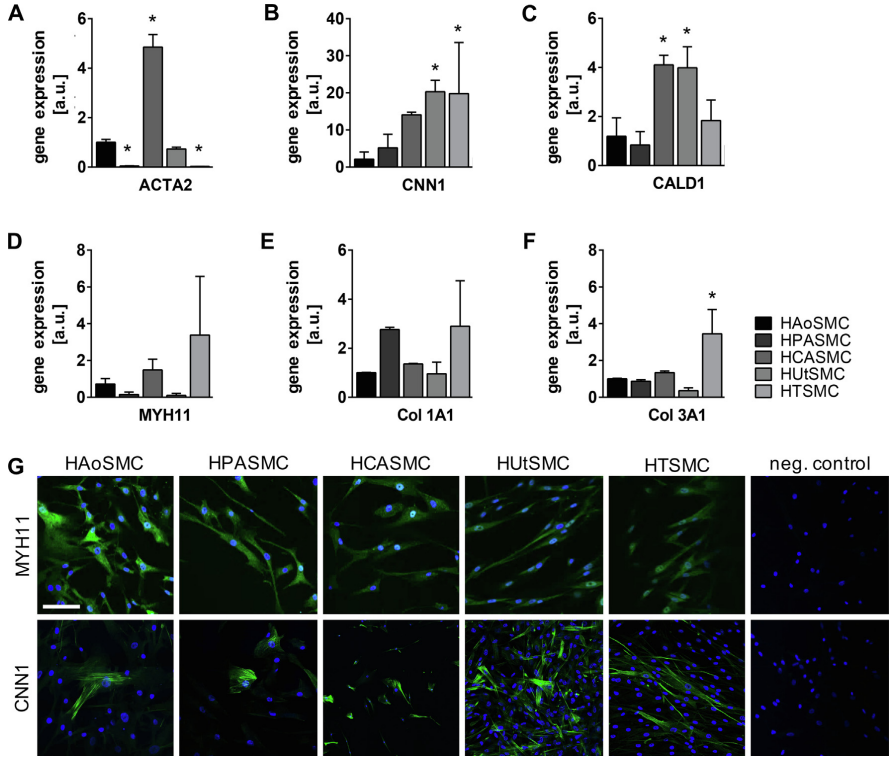

Fig. 3. Protein and gene expression analysis. Real-time quantitative PCR for maker genes expressed in contractile SMCs [*ACTA2* **(A)**, *CNN1* **(B)**, *CALD1* **(C)**, *MYH11* **(D)**] and synthetic [*COL1A1* **(E)**, *COL3A1* **(F)**]. Relative gene expression levels were normalized to HAoSMC levels. *$p < 0.05$ compared to HAoSMCs, each n = 3. **(G)** Immunofluorescence staining of HSMCs of different tissue origins showing nuclei in blue (DAPI) and MYH11 or CNN1 in green. Scale bar equals 50 μm. (For interpretation of the references to colour in this figure legend, the reader is referred to the web version of this article.)

rhomboid, fibroblast-like shape in high passage (Fig. 5A). HCASMCs also depicted a synthetic phenotype in higher passages. However, over passage time they did not alter significantly in their morphological appearance, compared to their low passage shape (Fig. 5B). Cells of low (4 & 6) and high (20) passage were stained for the contractile phenotype marker CNN1 and three other markers related to the synthetic SMC phenotype. CX43, COL1A1 and SYN4 are mainly expressed in SMCs of the synthetic phenotype [15,45] and have been reported in relation to phenotypic switching in coronary artery SMCs [46,47], ECM production [48] and aortic aneurisms [49,50]. ICC for CNN1 showed a decrease of protein expression over passaging in HUtSMCs (Fig. 5C). Cells of early passages stained positive for CNN1, in passage 20 only few cells expressed the contractile marker protein. In HCASMCs no significantly different CNN1 expression patterns between high and low passage cells were found (Fig. 5D). ICC for synthetic SMC phenotype proteins was positive in vascular and non-vascular SMCs in low and high passage. However, COL1A1 was more expressed in HCASMCs of higher passage, indicating a switch to the synthetic SMC phenotype.

3.3. Raman microspectroscopy as quality control tool for tissue engineering approaches

Raman analyses were applied to compare the tissue structures of tissue-engineered SMC rings to native tissue. SMC rings were formed by vascular SMCs and can be assembled to a vascular graft tube with the option to incorporate microspheres or microbeads to allow supplementation with drugs or growth factors [6,35]. Raman spectroscopic measurements were performed to non-invasively analyze the tissue structures of these SMC rings. First, SMC rings that were cultured under different conditions were compared. Raman data were acquired from three different groups of rings constructed out of passage 7 HCASMCs that were cultured for 14 days. SMC rings were cultured in i) growth medium (GM), ii) quiescence medium (QM) and iii) GM supplemented with TGF β (GM + TGFβ). Raman imaging and single spectra acquisition were performed to identify the influence of the culture conditions on the ECM formation of the SMC rings (Fig. 6). Raman imaging and TCA identified and localized two ECM components and as well as cell nuclei (Fig. 6A). Peaks related to DNA (785, 1090, 1373 cm^{-1}) [43,51] could define the structures, that were detected in one component of the TCA. One of the remaining components showed peak assignments reported before for contractile proteins, particularly actin, in coronary artery and bladder tissue [52,53]. Contractile proteins were more expressed in SMC rings cultured in QM when compared to the other culture conditions. SMC rings cultured in GM showed less collagen structures as well. Supplementation with TGFβ increased contractile protein expression in SMC rings cultured in GM, as observed in SMCs and other cell types [15,35,54]. The third component identified by TCA showed peak assignments related to a dissolved and dried aggrecan proteoglycan reference

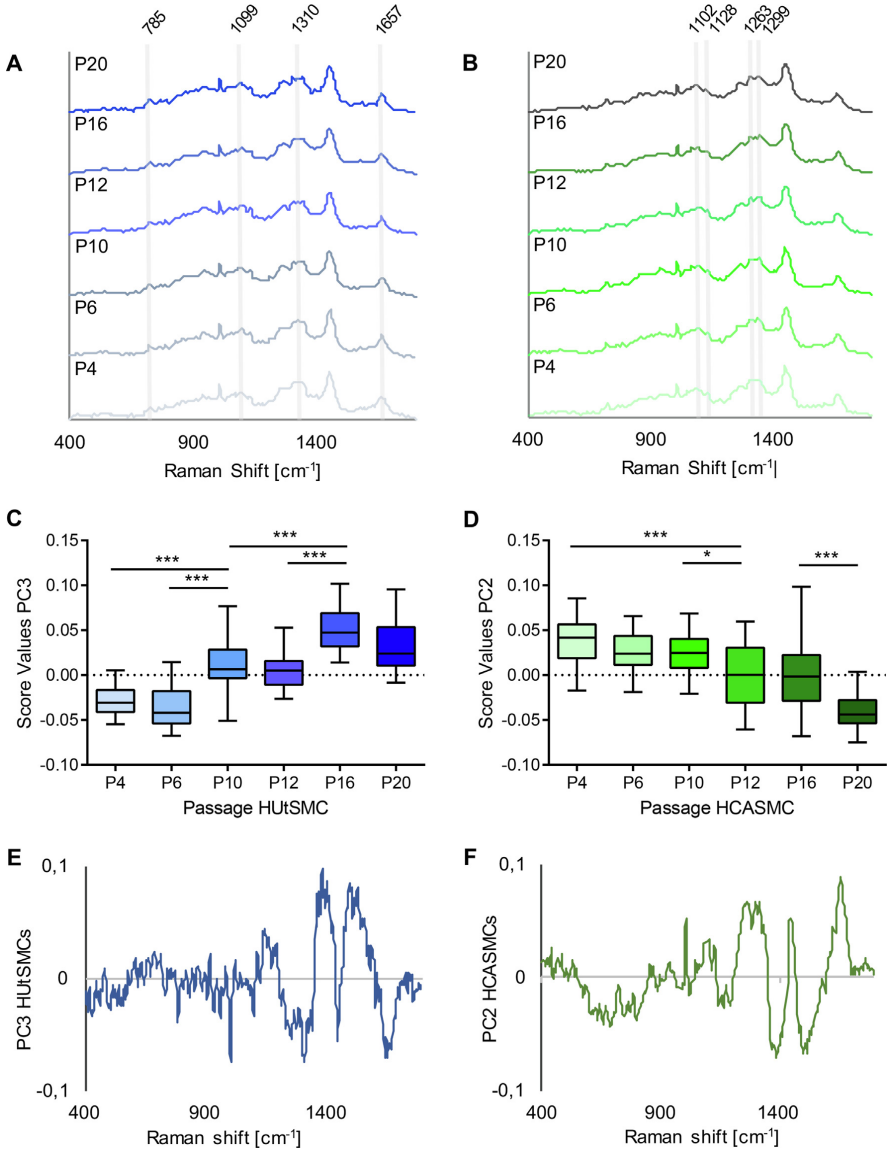

Fig. 4. PCA of phenotypic switching in HUtSMCs and HCASMCs. Average spectra of HUtSMCs **(A)** and HCASMCs **(B)** in different passages (passages 4–20). Spectral regions indicate differences explained by the PCA (highlighted in grey) at the corresponding Raman shift wavenumbers. (**C**) PC3 score values of HUtSMCs show a shift in spectral information over culture time. (**D**) Passage-dependent alterations are detected in HCASMCs in PC2. Loadings plots of the relevant PCs explain spectral differences within the HUtSMC **(E)** and the HCASMC **(F)** data. n = 30, $^{*}p < 0.05$, $^{***}p < 0.001$.

(Fig. 6B) and to peaks reported before in proteoglycans and glycosaminoglycans [55]. The proteoglycan component was distinctively expressed in rings in GM culture, TGFβ supplementation did not induce a significant alteration in the expression pattern. SMC rings cultured in QM only showed modest proteoglycan deposition.

A PCA was performed on single point measurements of the rings for detailed analysis of spectral differences and to search for specific Raman fingerprints, identifying the SMC rings of QM, GM and GM + TGF culture conditions. A distinct clustering for each culture condition was detected (Fig. 6C). While PC3 allowed for a significant separation between each group, PC 5 allowed for a separation

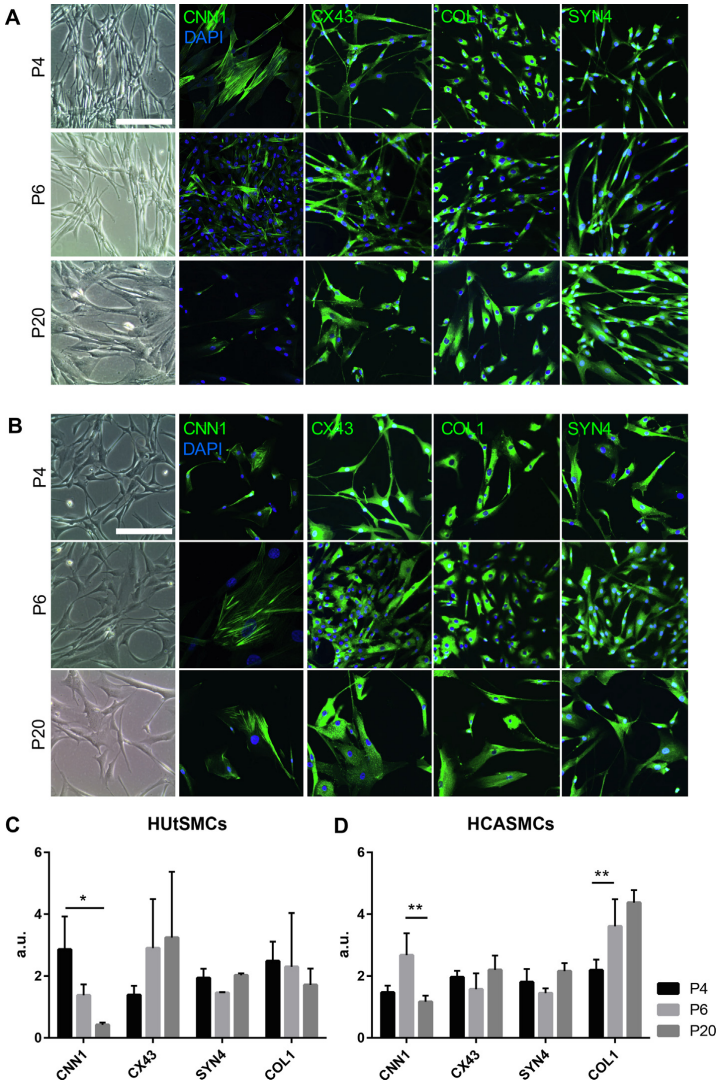

Fig. 5. ICC of HUtSMC (A) and HCASMC (B) of different passages. Bright-field images of adherent cells in culture and fixed SMCs of passage 4, 6 and 20, stained for markers expressed in contractile SMCs (calponin (CNN1)) and synthetic SMCs [connexin (CX43), collagen I (COL1A1) and syndecan (SYN4)] visualized with AlexaFluor488 (green). Nuclei were stained with DAPI (blue). Mean gray value intensity (GVI) quantification **(C, D)** showed a significant decrease of CNN1 in HUtSMCs. Scale bars equal 50 μm; n = 3, $^{*}p < 0.05$, $^{**}p < 0.005$. (For interpretation of the references to colour in this figure legend, the reader is referred to the web version of this article.)

of the rings cultured in QM from the rings cultured in GM (Fig. 6D). Peaks indicating the major spectral differences within the PCs are shown in the loadings plot (Fig. 6E). PC3 indicated differences in the peaks at 623, 1446 and 1667 cm^{-1} assigned to amino acids and amides in proteins [39,40]. PC5 explained alterations in collagen, described by peaks at 1246, 1401 and 1450 cm^{-1} [44]. Proteoglycans show a significant peak in the Raman shift region of 1008 cm^{-1} [55]. PC3 and PC5 both showed this peak in the positive range of their loadings plots. GM and GM + TGF data were mainly described by positive PC3 values and GM data as well by positive PC5 data, indicating higher proteoglycan levels in tissue samples of those culture conditions. PCA results of ECM protein expression in the differently cultured rings correlated to the Raman imaging data.

3.4. Assessment of ECM composition in human smooth muscle tissue and tissue-engineered SMC constructs

Single Raman spectra acquisition of human smooth muscle tissue sections and PCA were performed to determine spectral infor-

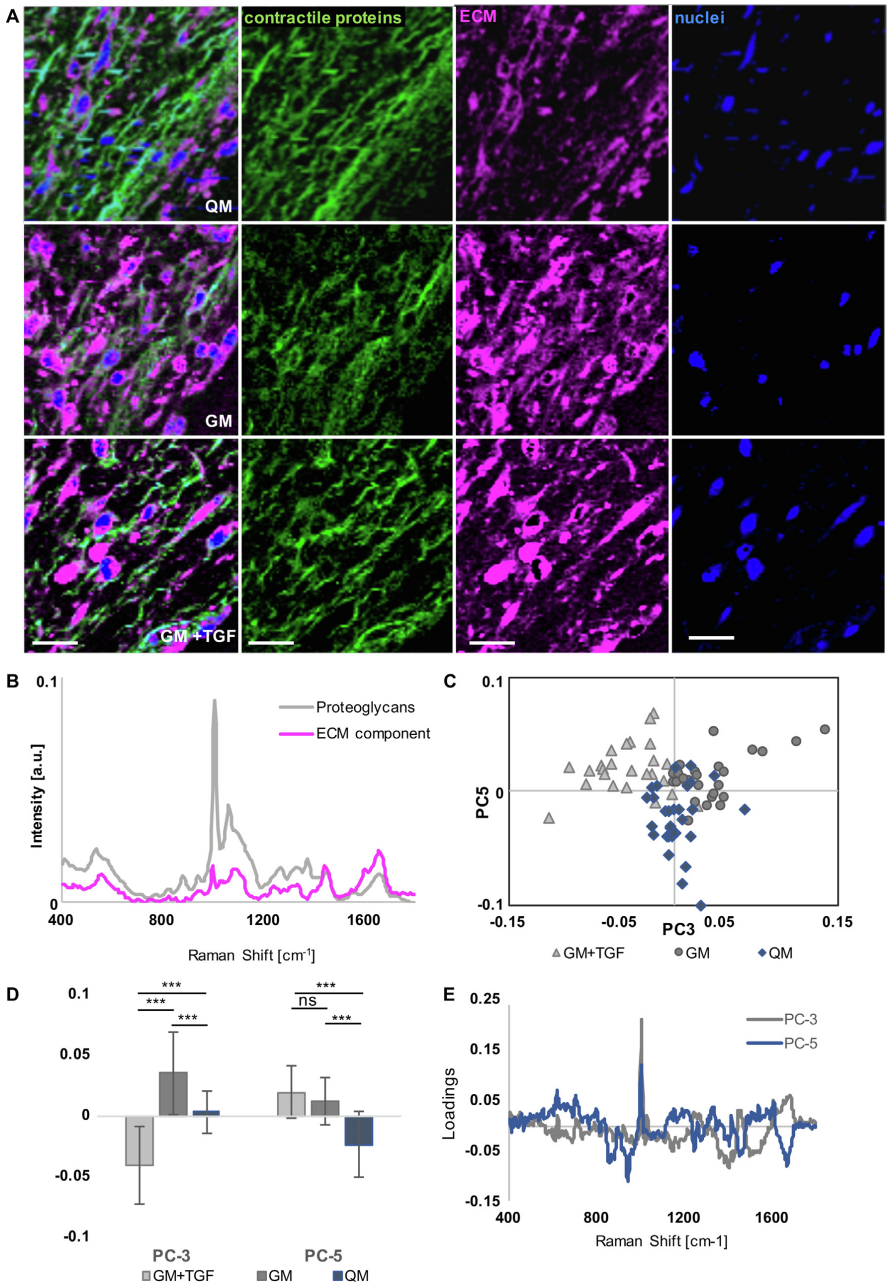

Fig. 6. Raman imaging and PCA of tissue-engineered SMC rings. **(A)** Raman images of hCASMC rings cultured in quiescence medium (QM), growth medium (GM) and growth medium that was supplemented with TFG-β (GM + TGF). TCA identified contractile proteins (green), ECM (pink) and nuclei (blue). **(B)** Comparison of the ECM component (pink) with a proteoglycan (aggrecan) reference spectrum (grey) identified overlapping peaks. PCA analysis showed differences in the SMC rings depending on the culture conditions. **(C)** PC3 vs PC5 scores plot separates the SMC ring groups. **(D)** Analysis of the single score values for PC3 and PC5 showed a significant difference between all ring types in PC3, and a significant difference between the two groups cultured in GM and the rings cultured in QM in PC5. **(E)** The loadings plot indicates peaks that explain the separation of spectral information in the corresponding PC. Scale bars equal 20 µm. PC score values ± SD, n = 30, $^{***}p < 0.001$. (For interpretation of the references to colour in this figure legend, the reader is referred to the web version of this article.)

mation and to evaluate the sensitivity of the Raman spectral fingerprint to separate different tissue types. All tissues showed distinct clustering in the PC2/PC3 scores plot (Fig. 7A). Differences could be found in PC2 and PC3 score values. The non-vascular tissues clustered in the positive range of PC2, whereas the vascular tissues clustered in the negative PC2 range. Loadings plot indicating the main spectral differences within the corresponding PC were used to analyze the molecular differences between the groups. Loadings for PC2 and PC3 (Fig. 7B) described matrix related peaks. The peak at 939 cm^{-1} was assigned to proline in collagen [44], 1250 cm^{-1} corresponds to amide III [41] and peaks at 1297 and 1453 cm^{-1} correlated to the collagen backbone [44]. The PCA identified differences in the overall matrix structure composition and collagen content between vascular and non-vascular tissues in PC2. Smaller differences within the vascular and non-vascular group were explained by PC3. Each tissue had a characteristic biological Raman fingerprint, which allowed for separation of all tissues.

Furthermore, to evaluate the influence of the selection of a cell type for tissue engineering approaches, Raman data were acquired from an engineered SMC tissue ring sample (Fig. 8A, C, E) constructed out of self-assembled HAoSMCs, and compared to native human aortic tissue (Fig. 8B, D). SHG imaging identified collagen fibers in both, native and tissue-engineered tissues (Fig. 8D, E). Analysis of the SHG signals demonstrated a higher collagen content in the aortic tissue (Fig. 8F). A PCA comparing HAoSMC data to human aortic tissue data (Fig. 8G) identified a clear similarity of the structural composition between native and the tissue-engineered vascular tissues. PC2/PC3 scores plot showed no clustering, although the loadings plots (Fig. 8H) explained matrix related differences similar to the loadings plots found for the PCA

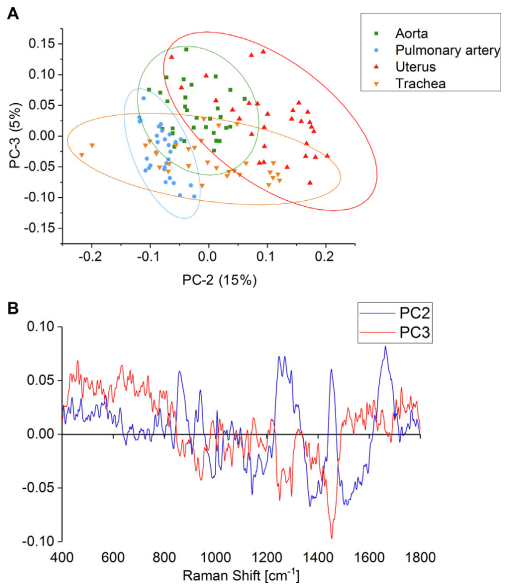

Fig. 7. PCA of Raman single spectrum acquisition of human SMC tissues. **(A)** Scores plot of normalized Raman spectra shows clustering of the different tissues. Aortic tissues are in the PC2 negative and PC3 positive range. Pulmonary artery tissue cluster in the PC2 negative and PC3 negative range. Uterus and trachea tissues are both in the PC2 positive range, whereas uterus spectra cluster in positive PC3 and trachea in PC3 negative range. Thirty spots per tissue were measured. **(B)** Loadings plots of PC2 and PC3 indicate the spectral ranges explaining the differences within the score values.

of aortic, uterine, trachea and pulmonary artery tissues. Spectral differences within the tissues had a bigger influence on the PCA than differences between the two samples. Although quantitative differences in collagen content were detected, single spectrum acquisition showed that the ring construct out of HAoSMCs provided ECM structures comparable to the native aortic tissue composition.

4. Discussion

This study showed a marker-independent approach for the non-destructive analysis of SMCs and its promising application in tissue engineering. Raman microspectroscopy allowed for a fast and marker-independent biochemical characterization and identification based on the endogenous spectral fingerprint of cells and tissues. Furthermore, Raman imaging performed on tissue-engineered SMC constructs enabled non-destructive imaging and monitoring of ECM remodeling under different culture conditions. Combined with MVA this technique provided a strong tool for fast identification and discrimination of SMCs as it has been shown for the analysis of bone cell phenotypes, cell death stages and stem cell differentiation [56–58].

PCA results showed that for both tissues and cells, differences between non-vascular and vascular origin were larger than differences within these groups. In tissues, non-vascular and vascular samples were separated due to spectral information on the overall ECM content. Separation within these groups was described by minor differences in the biochemical ECM composition. In cells, differences between non-vascular and vascular SMCs were corresponding to changes in cellular structures such as proteins and lipids. Differences in DNA content and composition discriminated the cells within the non-vascular and vascular group of origin. Differences of vascular and non-vascular SMCs have also been described by Gabbiani et al. [19]. They reported predominance of vimentin filaments and αSMA in vascular SMCs, whereas mainly desmin was expressed in non-vascular SMCs. Similar specificity was described for smoothelin isotypes that have been reported to be found exclusively in vascular SMCs of the contractile phenotype (smoothelin B) or in visceral SMCs (smoothelin A) [59]. Although highly specific marker proteins were used in this study, they only allow to separate non-vascular and vascular SMCs but are not suitable to further differentiate vascular SMCs of different origins. However, those findings correlated to the Raman results explaining different cellular protein composition as one characteristic of separation between non-vascular and vascular cell type.

Moreover, Raman spectroscopy enabled marker-free characterization and identification of de-differentiation. HUtSMCs and HCASMCs appeared to differ in their phenotypic switching. HUTSMCs demonstrated a first phenotypic alteration after passage 6, whereas a significant change of the cell composition was not detected before passage 10 for HCASMCs. In addition, it was shown that HUtSMCs underwent a stepwise phenotypic switching, while HCASMCs indicated a smooth transition to the synthetic phenotype. Routine techniques such as PCR or ICC lack reliable markers to distinguish SMC phenotypes. Moreover, PCR requires precise sample preparation steps and is highly sensitive to handling accuracy, whereas Raman instrumentation and sample processing is very robust. Huber and Badylak analyzed phenotypic changes in SMCs of three different tissue origins [20]. They reported difficulties in clearly defining a contractile or synthetic phenotype with marker proteins such as CNN1, CALD1 and ACTA2. There exists a broad number of markers related to SMCs, which are dominantly expressed in either the synthetic or contractile SMC phenotype [15]. However, this does not imply that those markers are not completely missing in the other phenotype and can also be expressed

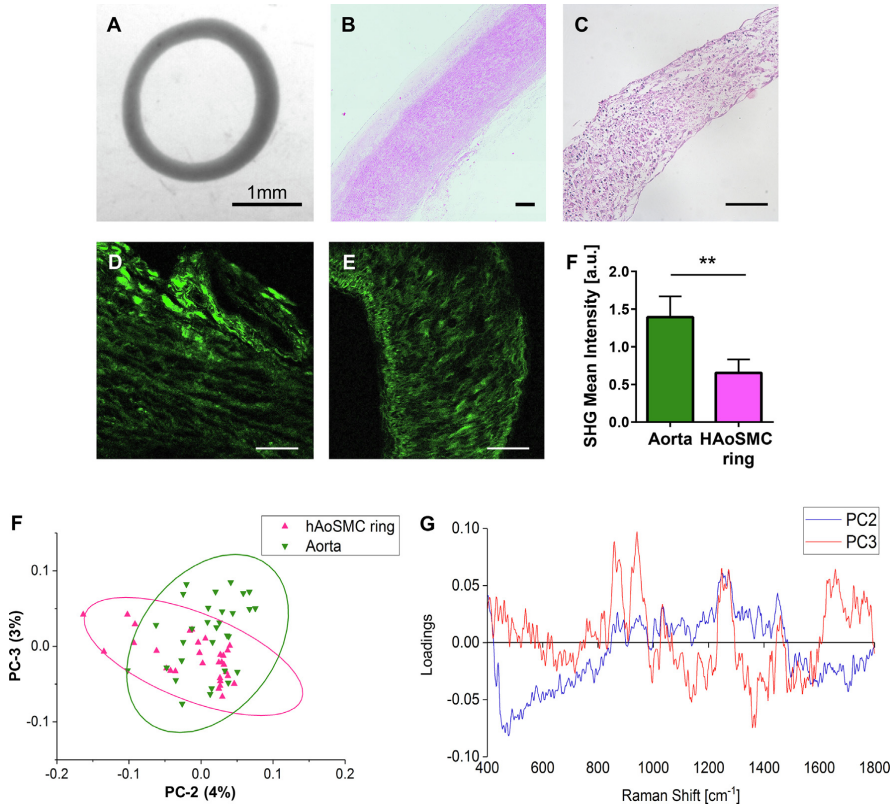

Fig. 8. Comparison of tissue-engineered SMC rings **(A, C, E)** and human aorta **(B, D)** stained with H&E **(B, C)**, and second harmonic generation (SHG) microscopy to visualize collagen fibers **(D, E)**. Scale bars equal 100 μm. **(F)** Collagen structures showed higher SHG signal intensities in native aortic tissue when compared with HAoSMC rings $^{**}p < 0.01$; n = 5 **(G)** PCA of normalized hAoSMC ring and native aortic tissue data. PC2/PC3 scores plot, based on principal components describing tissue ECM structures **(H)**, do not show a separation between tissue-engineered and native data sets.

in other cell types such as fibroblast or other cardiovascular cells [60–62]. Moreover, there exist transition states between the synthetic and contractile phenotype. In contrary, Raman microspectroscopy did not focus on one defined marker but provided the overall biomolecular fingerprint of the cell, containing marker-free molecular information describing the overall cellular composition and enabling the detection of cellular changes and the definition of the time point of switching. According to our results, we conclude that SMCs applied for tissue engineering should be of passage 6–7 or below to guarantee the dominance of SMCs of functional, contractile phenotype. A study by Timraz et al. investigated the behavior of HAoSMCs in culture and reported similar results [63]. Based on the analysis of cell morphology, IHC on MYH11, αSMA, COL1 and COL3A1 and marker gene expression they identified passage 7 as the intermediate state between contractile and synthetic phenotype.

In tissue engineering, there is a need for non-destructive, non-invasive real-time methods to characterize cells and to monitor cell-material interactions. A major obstacle for rapidly evolving tissue engineering approaches is to control and monitor the development, degeneration and functionality of the biomaterial [64,65]. We showed that Raman spectroscopy provided the desired features for a fast determination of the properties of tissue engineered constructs. Raman imaging and single spectrum acquisition results of SMC rings in different culture conditions lead to the conclusion that GM induced an increased proteoglycan production, while QM helped to maintain the SMCs contractile phenotype with modest ECM remodeling and proteoglycan expression, but contractile protein expression. Proteoglycans seemed to play an important role in vascular SMC-derived ECM expression. These findings were confirmed by the results of previous studies that reported higher expression of lipoprotein-binding proteoglycans in proliferative vascular SMCs compared to quiescent SMCs [66] and the relevance of proteoglycans (hyaluronan and versican) for vascular SMC migration and proliferation [67]. Extensive aggrecan and versican accumulation has recently been reported in thoracic aortic aneurysm [68] and Suna et al. described the impact of aggrecan in ECM remodeling in vasculature and reported aggrecan gene expression specifically in vascular SMCs, whereas vascular endothelial cells lacked aggrecan gene expression [69]. Raman imaging marker-independently demonstrated that TGFβ supplementation supported culture conditions to form a tissue ring that develops intact ECM and contractile protein structures which are necessary to sustain the physiological demands of a native vessel. Tissue-engineered rings grown in medium with TGFβ supplementation or incorporated with gelatin beads containing TGFβ have already

been shown to comply with the biomechanical properties of native tissue [35]. Moreover, the tissue-engineered HAoSMC ring sample showed molecular information similar to the Raman fingerprint of the native aorta and differed from other smooth muscle tissues. The role of the selected SMC type for tissue engineering approaches has been previously investigated [20,70]. It was discussed that any SMC type could be applied as long as the regulation of the phenotype is controlled, regardless of the smooth muscle organ that should be reconstructed in vitro. However, our results showed that except for contractile and synthetic phenotype characteristics, there are other cellular properties discriminating SMCs of different tissue origins. There exist significant differences especially between vascular and non-vascular SMCs. Raman spectroscopy may help in the assessment and monitoring of variable factors in tissue engineering such as maturation, dedifferentiation, degradation and assembly of cells or biomaterials. An increasingly important approach is the derivation of SMCs from stem cells and their application for tissue engineering [71–73]. Further work will focus on the analysis of stem cell derived tissue engineering approaches in comparison to native vascular tissues.

5. Conclusion

Raman microspectroscopy and Raman imaging combined with MVA allowed in this study the non-destructive, marker-independent identification and characterization of SMCs, smooth muscle tissues and tissue-engineered SMC constructs. The spectral information was specific enough to distinguish for the first time the phenotypic switching in SMCs in real-time, and monitor the impact of culture conditions on ECM remodeling in the tissue-engineered SMC constructs. Raman spectroscopy, especially in combination with machine learning and artificial intelligence tools, has not only the potential to be employed for the assessment of cellular properties and the characterization of disease-related modifications in cells and tissues, but also for the non-destructive and marker-free assessment of cellular quality and phenotype stability when dealing with cell manufacturing. It can further be very useful for the in situ analysis of biomaterials, cell-(bio)material interactions and to monitor molecular and biochemical changes in tissue-engineered products.

Acknowledgements

The authors thank Shannon Lee Layland for his helpful comments on the manuscript (Dept. of Women's Health, Eberhard Karls University Tübingen, Germany). Hannah Strobel (Worcester Polytechnic Institute, USA) provided the tissue-engineered SMC ring samples.

Source of funding

This work was supported by a DAAD Faculty Research Visit Fellowship (to MWR), as well as the Deutsche Forschungsgemeinschaft (SCHE701/14-1, INST 2388/30-1 and INST 2388/64-1), and the Ministry of Science, Research and Arts of Baden Württemberg (Az.: SI-BW 01222-91, 33-729.55-3/214-8) (all to KS-L).

Disclosures

None.

Appendix A. Supplementary data

Supplementary data to this article can be found online at https://doi.org/10.1016/j.actbio.2019.03.026.

References

[1] X. Wang, P. Lin, Q. Yao, C. Chen, Development of small-diameter vascular grafts, World J. Surg. 31 (4) (2007) 682–689.
[2] H.R. Laube, J. Duwe, W. Rutsch, W. Konertz, Clinical experience with autologous endothelial cell–seeded polytetrafluoroethylene coronary artery bypass grafts, J. Thoracic Cardiovasc. Surgery 120 (1) (2000) 134–141.
[3] N. Hibino, E. McGillicuddy, G. Matsumura, Y. Ichihara, Y. Naito, C. Breuer, T. Shinoka, Late-term results of tissue-engineered vascular grafts in humans, J. Thoracic Cardiovasc. Surgery 139 (2) (2010) 431–436. e2.
[4] M.R. Hoenig, G.R. Campbell, B.E. Rolfe, J.H. Campbell, Tissue-engineered blood vessels: alternative to autologous grafts?, Arterioscler Thromb. Vasc. Biol. 25 (6) (2005) 1128–1134.
[5] X. Zhang, X. Wang, V. Keshav, X. Wang, J.T. Johanas, G.G. Leisk, D.L. Kaplan, Dynamic culture conditions to generate silk-based tissue-engineered vascular grafts, Biomaterials 30 (19) (2009) 3213–3223.
[6] A.D. Dikina, H.A. Strobel, B.P. Lai, M.W. Rolle, E. Alsberg, Engineered cartilaginous tubes for tracheal tissue replacement via self-assembly and fusion of human mesenchymal stem cell constructs, Biomaterials 52 (2015) 452–462.
[7] Y. Nakase, A. Hagiwara, T. Nakamura, S. Kin, S. Nakashima, T. Yoshikawa, K.-I. Fukuda, Y. Kuriu, K. Miyagawa, C. Sakakura, Tissue engineering of small intestinal tissue using collagen sponge scaffolds seeded with smooth muscle cells, Tissue Eng. 12 (2) (2006) 403–412.
[8] S.A. Steitz, M.Y. Speer, G. Curinga, H.-Y. Yang, P. Haynes, R. Aebersold, T. Schinke, G. Karsenty, C.M. Giachelli, Smooth muscle cell phenotypic transition associated with calcification, Circ. Res. 89 (12) (2001) 1147–1154.
[9] G. Ailawadi, C.W. Moehle, H. Pei, S.P. Walton, Z. Yang, I.L. Kron, C.L. Lau, G.K. Owens, Smooth muscle phenotypic modulation is an early event in aortic aneurysms, J. Thoracic Cardiovasc. Surgery 138 (6) (2009) 1392–1399.
[10] M. Aikawa, Y. Sakomura, M. Ueda, K. Kimura, I. Manabe, S. Ishiwata, N. Komiyama, H. Yamaguchi, Y. Yazaki, R. Nagai, Redifferentiation of smooth muscle cells after coronary angioplasty determined via myosin heavy chain expression, Circulation 96 (1) (1997) 82–90.
[11] H. Hao, G. Gabbiani, M.-L. Bochaton-Piallat, Arterial smooth muscle cell heterogeneity, Arterioscler. Thromb. Vasc. Biol. 23 (9) (2003) 1510–1520.
[12] J.H. Chamley-Campbell, G.R. Campbell, What controls smooth muscle phenotype?, Atherosclerosis 40 (3–4) (1981) 347–357
[13] M.G. Frid, B.V. Shekhonin, V.E. Koteliansky, M.A. Glukhova, Phenotypic changes of human smooth muscle cells during development: late expression of heavy caldesmon and calponin, Dev. Biol. 153 (2) (1992) 185–193.
[14] M.A. Glukhova, A.E. Kabakov, M.G. Frid, O.I. Ornatsky, A.M. Belkin, D.N. Mukhin, A.N. Orekhov, V.E. Koteliansky, V.N. Smirnov, Modulation of human aorta smooth muscle cell phenotype: a study of muscle-specific variants of vinculin, caldesmon, and actin expression, Proc. Natl. Acad. Sci. 85 (24) (1988) 9542–9546.
[15] S. Rensen, P. Doevendans, G. Van Eys, Regulation and characteristics of vascular smooth muscle cell phenotypic diversity, Netherlands Heart J. 15 (3) (2007) 100–108.
[16] F. Opitz, K. Schenke-Layland, T.U. Cohnert, U.A. Stock, Phenotypical plasticity of vascular smooth muscle cells—effect of in vitro and in vivo shear stress for tissue engineering of blood vessels, Tissue Eng. 13 (10) (2007) 2505–2514.
[17] J.A. Beamish, P. He, K. Kottke-Marchant, R.E. Marchant, Molecular regulation of contractile smooth muscle cell phenotype: implications for vascular tissue engineering, Tissue Eng. Part B: Rev. 16 (5) (2010) 467–491.
[18] M.B. Chan-Park, J.Y. Shen, Y. Cao, Y. Xiong, Y. Liu, S. Rayatpisheh, G.C.W. Kang, H.P. Greisler, Biomimetic control of vascular smooth muscle cell morphology and phenotype for functional tissue-engineered small-diameter blood vessels, J. Biomed. Mater. Res. Part A 88 (4) (2009) 1104–1121.
[19] G. Gabbiani, E. Schmid, S. Winter, C. Chaponnier, C. De Ckhastonay, J. Vandekerckhove, K. Weber, W.W. Franke, Vascular smooth muscle cells differ from other smooth muscle cells: predominance of vimentin filaments and a specific alpha-type actin, Proc. Natl. Acad. Sci. 78 (1) (1981) 298–302.
[20] A. Huber, S.F. Badylak, Phenotypic changes in cultured smooth muscle cells: limitation or opportunity for tissue engineering of hollow organs?, J Tissue Eng. Regener. Med. 6 (7) (2012) 505–511.
[21] M.S. Dresselhaus, A. Jorio, M. Hofmann, G. Dresselhaus, R. Saito, Perspectives on carbon nanotubes and graphene Raman spectroscopy, Nano Lett. 10 (3) (2010) 751–758.
[22] D.S. Knight, W.B. White, Characterization of diamond films by Raman spectroscopy, J. Mater. Res. 4 (2) (1989) 385–393.
[23] T. De Beer, A. Burggraeve, M. Fonteyne, L. Saerens, J.P. Remon, C. Vervaet, Near infrared and Raman spectroscopy for the in-process monitoring of pharmaceutical production processes, Int. J. Pharm. 417 (1) (2011) 32–47.
[24] C.H. Camp Jr, Y.J. Lee, J.M. Heddleston, C.M. Hartshorn, A.R.H. Walker, J.N. Rich, J.D. Lathia, M.T. Cicerone, High-speed coherent Raman fingerprint imaging of biological tissues, Nat. Photonics 8 (8) (2014) 627–634.
[25] R. Smith, K.L. Wright, L. Ashton, Raman spectroscopy: an evolving technique for live cell studies, Analyst 141 (12) (2016) 3590–3600.
[26] X. Qian, X.-H. Peng, D.O. Ansari, Q. Yin-Goen, G.Z. Chen, D.M. Shin, L. Yang, A.N. Young, M.D. Wang, S. Nie, In vivo tumor targeting and spectroscopic detection with surface-enhanced Raman nanoparticle tags, Nat. Biotechnol. 26 (1) (2008) 83–90.
[27] Z. Huang, A. McWilliams, H. Lui, D.I. McLean, S. Lam, H. Zeng, Near-infrared Raman spectroscopy for optical diagnosis of lung cancer, Int. J. Cancer 107 (6) (2003) 1047–1052.

[28] E. Brauchle, J. Kasper, R. Daum, N. Schierbaum, C. Falch, A. Kirschniak, T.E. Schäffer, K. Schenke-Layland, Biomechanical and biomolecular characterization of extracellular matrix structures in human colon carcinomas, Matrix Biol. (2018).
[29] S.-H. Kim, E.-S. Lee, J.Y. Lee, E.S. Lee, B.-S. Lee, J.E. Park, D.W. Moon, Multiplex coherent anti-stokes raman spectroscopy images intact atheromatous lesions and concomitantly identifies distinct chemical profiles of atherosclerotic lipids, Circ. Res. 106 (8) (2010) 1332–1341.
[30] M. Pudlas, D.A.C. Berrio, M. Votteler, S. Koch, S. Thude, H. Walles, K. Schenke-Layland, Non-contact discrimination of human bone marrow-derived mesenchymal stem cells and fibroblasts using Raman spectroscopy, Med. Laser Appl. 26 (3) (2011) 119–125.
[31] C. Brackmann, M. Esguerra, D. Olausson, D. Delbro, A. Krettek, P. Gatenholm, A. Enejder, Coherent anti-Stokes Raman scattering microscopy of human smooth muscle cells in bioengineered tissue scaffolds, J. Biomed. Opt. 16 (2) (2011). 021115-021115-6.
[32] D. Zhang, W. Chen, H. Chen, H.-Q. Yu, G. Kassab, J.-X. Cheng, Chemical imaging of fresh vascular smooth muscle cell response by epi-detected stimulated Raman scattering, J. Biophoton. e201700005-n/a.
[33] C. Molony, J. McIntyre, A. Maguire, R. Hakimjavadi, D. Burtenshaw, G. Casey, M. Di Luca, B. Hennelly, H.J. Byrne, P.A. Cahill, Label-free discrimination analysis of de-differentiated vascular smooth muscle cells, mesenchymal stem cells and their vascular and osteogenic progeny using vibrational spectroscopy, Biochimica et Biophysica Acta (BBA)-Molecular Cell Res. 1865 (2) (2018) 343–353.
[34] T.A. Gwyther, J.Z. Hu, K.L. Billiar, M.W. Rolle, Directed cellular self-assembly to fabricate cell-derived tissue rings for biomechanical analysis and tissue engineering, J. Visualized Exp. : JoVE (57) (2011).
[35] H.A. Strobel, A.D. Dikina, K. Levi, L.D. Solorio, E. Alsberg, M.W. Rolle, Cellular self-assembly with microsphere incorporation for growth factor delivery within engineered vascular tissue rings, Tissue Eng. Part A 23 (3–4) (2017) 143–155.
[36] H.A. Strobel, E.L. Calamari, B. Alphonse, T.A. Hookway, M.W. Rolle, Fabrication of custom agarose wells for cell seeding and tissue ring self-assembly using 3D-printed molds, J. Visualized Exp.: JoVE (134) (2018).
[37] M. Votteler, D.A. Carvajal Berrio, M. Pudlas, H. Walles, U.A. Stock, K. Schenke-Layland, Raman spectroscopy for the non-contact and non-destructive monitoring of collagen damage within tissues, J. Biophotonics 5 (1) (2012) 47–56.
[38] E. Brauchle, H. Bauer, P. Fernes, A. Zuk, K. Schenke-Layland, G. Sengle, Raman microspectroscopy as a diagnostic tool for the non-invasive analysis of fibrillin-1 deficiency in the skin and in the in vitro skin models, Acta Biomater. 52 (2017) 41–48.
[39] N. Stone, C. Kendall, J. Smith, P. Crow, H. Barr, Raman spectroscopy for identification of epithelial cancers, Faraday Discuss. 126 (2004) 141–157.
[40] I. Notingher, C. Green, C. Dyer, E. Perkins, N. Hopkins, C. Lindsay, L.L. Hench, Discrimination between ricin and sulphur mustard toxicity in vitro using Raman spectroscopy, J. R. Soc. Interface 1 (1) (2004) 79–90.
[41] D. Naumann, Infrared and NIR Raman spectroscopy in medical microbiology, infrared spectroscopy: new tool in medicine, Int. Soc. Opt. Photonics (1998) 245–258.
[42] E. Hanlon, R. Manoharan, T.W. Koo, K. Shafer, J. Motz, M. Fitzmaurice, J. Kramer, I. Itzkan, R. Dasari, M. Feld, Prospects for in vivo Raman spectroscopy, Phys. Med. Biol. 45 (2) (2000) R1.
[43] R.K. Dukor, Vibrational Spectroscopy in the Detection of Cancer, Handbook of Vibrational Spectroscopy, John Wiley & Sons Ltd, 2006.
[44] B.G. Frushour, J.L. Koenig, Raman scattering of collagen, gelatin, and elastin, Biopolymers 14 (2) (1975) 379–391.
[45] G.K. Owens, Regulation of differentiation of vascular smooth muscle cells, Physiol. Rev. 75 (3) (1995) 487–517.
[46] X. Zhang, X. Wang, X. Zhou, X. Ma, Y. Yao, X. Liu, Phenotypic transformation of smooth muscle cells from porcine coronary arteries is associated with connexin 43, Mol. Med. Rep. 14 (1) (2016) 41–48.
[47] C.E. Chadjichristos, S. Morel, J.-P. Derouette, E. Sutter, I. Roth, A.C. Brisset, M.-L. Bochaton-Piallat, B.R. Kwak, Targeting connexin 43 prevents platelet-derived growth factor-bb–induced phenotypic change in porcine coronary artery smooth muscle cells, Circ. Res. (2008).
[48] M. Yamamoto, K. Yamamoto, T. Noumura, Type I collagen promotes modulation of cultured rabbit arterial smooth muscle cells from a contractile to a synthetic phenotype, Exp. Cell Res. 204 (1) (1993) 121–129.
[49] J. Wen, P. Wang, S.V. Smith, C.A. Haller, E.L. Chaikof, Syndecans are differentially expressed during the course of aortic aneurysm formation, J. Vasc. Surg. 46 (5) (2007) 1014–1025.
[50] L. Li, E.L. Chaikof, Mechanical stress regulates syndecan-4 expression and redistribution in vascular smooth muscle cells, Arterioscler. Thromb. Vasc. Biol. 22 (1) (2002) 61–68.
[51] J.W. Chan, D.S. Taylor, T. Zwerdling, S.M. Lane, K. Ihara, T. Huser, Micro-raman spectroscopy detects individual neoplastic and normal hematopoietic cells, Biophys. J. 90 (2) (2006) 648–656.
[52] N. Stone, M.C. Hart Prieto, P. Crow, J. Uff, A.W. Ritchie, The use of Raman spectroscopy to provide an estimation of the gross biochemistry associated with urological pathologies, Anal. Bioanal. Chem. 387 (5) (2007) 1657–1668.
[53] H.P. Buschman, G. Deinum, J.T. Motz, M. Fitzmaurice, J.R. Kramer, A. van der Laarse, A.V. Bruschke, M.S. Feld, Raman microspectroscopy of human coronary atherosclerosis: biochemical assessment of cellular and extracellular morphologic structures in situ, Cardiovasc. Pathol. 10 (2) (2001) 69–82.
[54] A. Desmoulière, A. Geinoz, F. Gabbiani, G. Gabbiani, Transforming growth factor-beta 1 induces alpha-smooth muscle actin expression in granulation tissue myofibroblasts and in quiescent and growing cultured fibroblasts, J. Cell Biol. 122 (1) (1993) 103–111.
[55] R. Ellis, E. Green, C.P. Winlove, Structural analysis of glycosaminoglycans and proteoglycans by means of Raman microspectrometry, Connect. Tissue Res. 50 (1) (2009) 29–36.
[56] I. Notingher, G. Jell, U. Lohbauer, V. Salih, L.L. Hench, In situ non-invasive spectral discrimination between bone cell phenotypes used in tissue engineering, J. Cell. Biochem. 92 (6) (2004) 1180–1192.
[57] E. Brauchle, S. Thude, S.Y. Brucker, K. Schenke-Layland, Cell death stages in single apoptotic and necrotic cells monitored by Raman microspectroscopy, Sci. Rep. 4 (2014).
[58] E. Brauchle, A. Knopf, H. Bauer, N. Shen, S. Linder, Michael G. Monaghan, K. Ellwanger, Shannon L. Layland, Sara Y. Brucker, A. Nsair, K. Schenke-Layland, Non-invasive chamber-specific identification of cardiomyocytes in differentiating pluripotent stem cells, Stem Cell Rep. 6 (2) (2016) 188–199.
[59] G.J. van Eys, P.M. Niessen, S.S. Rensen, Smoothelin in vascular smooth muscle cells, Trends Cardiovasc. Med. 17 (1) (2007) 26–30.
[60] E. Rabkin-Aikawa, M. Farber, M. Aikawa, F.J. Schoen, Dynamic and reversible changes of interstitial cell phenotype during remodeling of cardiac valves, J. Heart Valve Dis. 13 (5) (2004) 841–847.
[61] K. Schenke-Layland, I. Riemann, F. Opitz, K. König, K. Halbhuber, U. Stock, Comparative study of cellular and extracellular matrix composition of native and tissue engineered heart valves, Matrix Biol. 23 (2) (2004) 113–125.
[62] K.-C. Wu, J.-P. Jin, Calponin in non-muscle cells, Cell Biochem. Biophys. 52 (3) (2008) 139.
[63] S.B. Timraz, I.A. Farhat, G. Alhussein, N. Christoforou, J.C. Teo, In-depth evaluation of commercially available human vascular smooth muscle cells phenotype: implications for vascular tissue engineering, Exp. Cell Res. 343 (2) (2016) 168–176.
[64] A.A. Appel, M.A. Anastasio, J.C. Larson, E.M. Brey, Imaging challenges in biomaterials and tissue engineering, Biomaterials 34 (28) (2013) 6615–6630.
[65] B.S. Harrison, A. Atala, Carbon nanotube applications for tissue engineering, Biomaterials 28 (2) (2007) 344–353.
[66] G. Camejo, G. Fager, B. Rosengren, E. Hurt-Camejo, G. Bondjers, Binding of low density lipoproteins by proteoglycans synthesized by proliferating and quiescent human arterial smooth muscle cells, J. Biol. Chem. 268 (19) (1993) 14131–14137.
[67] S.P. Evanko, J.C. Angello, T.N. Wight, Formation of hyaluronan-and versican-rich pericellular matrix is required for proliferation and migration of vascular smooth muscle cells, Arterioscler. Thromb. Vasc. Biol. (1999).
[68] F.S. Cikach, C.D. Koch, T.J. Mead, J. Galatioto, B.B. Willard, K.B. Emerton, M.J. Eagleton, E.H. Blackstone, F. Ramirez, E.E. Roselli, Massive aggrecan and versican accumulation in thoracic aortic aneurysm and dissection, JCI Insight 3 (5) (2018).
[69] G. Suna, W. Wojakowski, M. Lynch, J. Barallobre-Barreiro, X. Yin, U. Mayr, F. Baig, R. Lu, M. Fava, R. Hayward, Extracellular matrix proteomics reveals interplay of aggrecan and aggrecanases in vascular remodeling of stented coronary arteries, Circulation (2017). CIRCULATIONAHA. 116.023381.
[70] J.-Y. Lai, P.-Y. Chang, J.-N. Lin, A comparison of engineered urinary bladder and intestinal smooth muscle for urinary bladder wall replacement in a rabbit model, J. Pediatr. Surg. 41 (12) (2006) 2090–2094.
[71] V.K. Bajpai, P. Mistriotis, Y.-H. Loh, G.Q. Daley, S.T. Andreadis, Functional vascular smooth muscle cells derived from human induced pluripotent stem cells via mesenchymal stem cell intermediates, Cardiovasc. Res. 96 (3) (2012) 391–400.
[72] Y. Wang, J. Hu, J. Jiao, Z. Liu, Z. Zhou, C. Zhao, L.-J. Chang, Y.E. Chen, P.X. Ma, B. Yang, Engineering vascular tissue with functional smooth muscle cells derived from human iPS cells and nanofibrous scaffolds, Biomaterials 35 (32) (2014) 8960–8969.
[73] K.L. Hill, P. Obrtlikova, D.F. Alvarez, J.A. King, S.A. Keirstead, J.R. Allred, D.S. Kaufman, Human embryonic stem cell– derived vascular progenitor cells capable of endothelial and smooth muscle cell function, Exp. Hematol. 38 (3e1) (2010) 246–257.
[74] G. Shetty, C. Kendall, N. Shepherd, N. Stone, H. Barr, Raman spectroscopy: elucidation of biochemical changes in carcinogenesis of oesophagus, Br. J. Cancer 94 (10) (2006) 1460–1464.
[75] C. Krafft, L. Neudert, T. Simat, R. Salzer, Near infrared Raman spectra of human brain lipids, Spectrochim. Acta Part A Mol. Biomol. Spectrosc. 61 (7) (2005) 1529–1535.
[76] S. Farquharson, C. Shende, F.E. Inscore, P. Maksymiuk, A. Gift, Analysis of 5-fluorouracil in saliva using surface-enhanced Raman spectroscopy, J. Raman Spectrosc. 36 (3) (2005) 208–212.
[77] W.T. Cheng, M.T. Liu, H.N. Liu, S.Y. Lin, Micro-Raman spectroscopy used to identify and grade human skin pilomatrixoma, Microsc. Res. Tech. 68 (2) (2005) 75–79.
[78] A.J. Ruiz-Chica, M.A. Medina, F. Sánchez-Jiménez, F.J. Ramírez, Characterization by Raman spectroscopy of conformational changes on guanine–cytosine and adenine–thymine oligonucleotides induced by aminooxy analogues of spermidine, J. Raman Spectrosc. 35 (2) (2004) 93–100.
[79] R.J. Lakshmi, V. Kartha, C. Murali Krishna, J.R. Solomon, G. Ullas, P. Uma Devi, Tissue Raman spectroscopy for the study of radiation damage: brain irradiation of mice, Radiat. Res. 157 (2) (2002) 175–182.

Appendix V: Raman peaks and their assignments – tissues

Peak [cm^{-1}]	molecular assignment			
	elastin (component 1)	collagens (component 2)	cells/DNA (component 3)	red blood cells (component 4)
529	Des/ Isodes[277]			
669				porphyrin deformation[278, 279]
729		tryptophane[280]		
751				porphyrin ring breathing[278, 279]
756			A[281]	
782		C-N stretching[277, 282]		
825		C-N stretching[277]		
966	Des/ Isodes[277]			
999				C-C[278, 279]
1101			DNA bases[281]	
1107	Des/ Isodes[277]			
1122				porphyrin half ring [278, 279]
1128	C-N stretching[277]		phosphodiester[283]	
1165	Tyr[282]			
1179	Tyr*[277]		G, C[283]	
1207			NH_2 G, C[283]	
1212	Tyr[277]			
1218				C-N stretching [284]
1233	amide III[285, 286]			
1246		Tyr[277]		
1245		amide III[277]	A, G[281]	
1263	protein band[287, 288]			
1266			G[280]	
1311	CH_2/CH_3 twisting, bending[282]			
1317			CH_2 deformation[281]	
1340		amide III[277]		
1343	CH_2 /CH_3 wagging[277]			
1347			deoxyribose[283]	
1369		amide III (α-helix)[282, 289]		
1397	CH_2 deformation[282]			
1400			C[283]	
1439		CH_2 /CH_3 twisting[277]		
1444				C-C[278, 279]
1454	CH_2 scissoring /CH_3 bending*[277]		C-C stretching[284]	
1508		CH_3 bending[288]		
1580		CH_2 scissoring /CH_3 bending[277]		
1593				C=N, C=C in quinoid ring [284]
1611	Tyr[277]			
1654	amide I[277]			
1663		amide I[277]	DNA[290]	

Appendix VI: Raman peaks and their assignments – cells

Peak [cm^{-1}]	molecular assignment			
	phospholipids (component 1)	lipids (component 2)	proteins (component 3)	cells/DNA (component 4)
715	C-N (phospholipid head)[280, 281, 291]	$CN^-(CH_3)_3$[281]		
720				DNA[292]
760			tryptophan[281]	
786				DNA[280]
824			Tyr[289]	
831				T[293]
869			proline[280]	
875	$N^+(CH_3)_3$ (choline)[291]			
878		C-C-N^+ stretching [281]		
890			protein assignment[287, 288]	
968		lipid assignment[288]		
1032	CH_3/CH_2 bending*[289]			
1057	lipids*[288]			
1080	phospholipids[291]			
1090				phosphate[288]
1123	C-C stretching*[280]		C-N, C-C stretch[289]	
1177				G, C[283]
1248			amide III[284]	
1251				NH_2 G, C[283]
1299		CH_2 deformation [280]		
1302	CH_2 twisting[289]			
1308			C-N stretching (amines)[284]	
1335			CH_3/CH_2 twisting, wagging[289]	
1340				A, G[281]
1372				DNA bases[293]
1440		CH_2 bending[287, 291, 294]		
1443			CH_2 deformation[280]	
1445	CH_3/CH_2 scissoring[289]			
1577				NADH[295], G[283]
1656	C=C[294]			
1657		C=O stretching, C=C[287, 288]		
1660			amide I[281]	
1663				DNA[290]

A: adenine, G: guanine T: thymine C: cytosine, Des/Isodes: desomsine/isodesmosine, Tyr: tyrosine

*peaks are present in two components